A Magic Frequency in Light-Matter Interaction of a Two-State System with Multiple Degeneracy

Thesis submitted in partial fulfillment of the requirements for the degree of Doctor of Philosophy

by:

Menachem Givon

Submitted to the Senate of Ben-Gurion University of the Negev

November 11, 2014

Beer-Sheva, Israel

A Magic Frequency in Light-Matter Interaction of a Two-State System with Multiple Degeneracy

Thesis submitted in partial fulfillment of the requirements for the degree of Doctor of Philosophy

by:

Menachem Givon

Submitted to the Senate of Ben-Gurion University of the Negev

Approved by the advisor on April 20, 2015 : Prof. Ron Folman _____

Approved by the Dean of the Kreitman School of Advanced Graduate Studies: Prof. Michal Shapira _____

Beer-Sheva, Israel

This work was carried out under the supervision of Dr. Ron Folman

In the Department of Physics

Faculty of Natural Sciences

Research-Student's Affidavit when Submitting the Doctoral Thesis for Judgment

I, Menachem Givon, whose signature appears below, hereby declare that:

I have written this Thesis by myself, except for the help and guidance offered by my Thesis Advisors.

The scientific materials included in this Thesis are products of my own research, culled from the period during which I was a research student. [1]

This Thesis incorporates research materials produced in cooperation with others, excluding the technical help commonly received during experimental work. Therefore, I am attaching another affidavit stating the contributions made by myself and the other participants in this research, which has been approved by them and submitted with their approval

Date: _____ Student's name: Menachem Givon Signature: _____

[1] Part of my research was conducted during the special leave of absence granted to me so that I will be able to take part in another research project at the university (see the preface).

Affidavit stating the contributions made by myself and by other participants in this research

I, Menachem Givon, whose signature appears below, hereby declare that the scientific materials included in this Thesis are products of my own research, except for the following parts, which were produced in cooperation with others: the modulated laser (App. A) was developed in cooperation with Amir Waxman; the detection of a two-photon transition (App. B.5) was done in cooperation with Gal Aviv; the method for the experimental demonstration of the magic frequency (Table 5.2), some aspects of the measuring method (Sec. 4.2), and calculations for alkali atoms other than rubidium (Fig. 3.4), were developed in cooperation with Yair Margalit.

Date: _____	Name: Menachem Givon	Signature: _____
Date: _____	Name: Amir Waxman	Signature: _____
Date: _____	Name: Gal Aviv	Signature: _____
Date: _____	Name: Yair Margalit	Signature: _____

Acknowledgments

At this point I would like to express my gratitude to all the people who contributed to this work, helped and encouraged me during my years with the AtomChip Group.

First and foremost I thank my advisor, Prof. Ron Folman, for taking me as a Ph.D student although more than 30 years have past since I received my M.Sc. degree. Ron provided guidance and help on the one hand, while on the other hand let me set my own course, and I am deeply thankful for both.

I owe a lot of thanks to David Groswasser, who introduced me to the devices and equipment of the AtomChip lab, most of which did not exist when I was an undergraduate student (back then, we used punch cards to program a computer...). I also thank David for his support and guidance throughout my work on this thesis.

Three M.Sc. students shared the experimental system with me: Amir Waxman, Gal Aviv and Yair Margalit. I deeply thank Amir for his support and cooperation during the construction of the experimental system and its initial operation; Gal for coming up with, and executing, the two-photon Rabi oscillations; Yair for his inquisitive mind, his innovative suggestions and dedicated work. Thank you – I am lucky to have worked with you!

I wish to thank deeply Yoni Japha, our theoretician. Yoni provided answers and clarifications that were essential to the understanding and interpretation of our experimental results. His endless arsenal of mathematical tools and simulation programs helped us verify our initial assumptions.

I owe special thanks to Mark Keil for his support and help during the writing of this thesis. Thank you, Mark!

I received support and had very fruitful discussions (over the eternal cup of coffee...) with Tal, Shimi and other members of the AtomChip group. Thanks!

The support of Zina Binshtock, our electronics engineer, is essential to the construction, operation, upgrades and modifications of the experimental system. Thank you, Zina!. I also thank Aharon, Alex, David and Avi – the machine shop team, and Yaniv Bar-Haim – our lab technician.

Last but not least, I deeply thank my wife Mindy, my sons Ayron and Alon and my daughter Tal for their support and understanding during all these years!

.

Preface

The work and findings described in this thesis were carried out in the AtomChip group [1] at Ben-Gurion University of the Negev, Beer-Sheva, Israel. At the time this work started, the AtomChip group was focused on an effort to establish a laboratory for ultra-cold atoms [2, 3, 4, 5, 6]. When I joined the group, my first task was to design and build a laser system that can provide two phase-coherent laser beams with a precise and tunable frequency difference of several GHz. Such a laser system, typically called a "Raman laser", is an important tool for manipulating both ultra-cold atoms (e.g. qubit rotations) and room-temperature alkali metal vapor in vapor cells (e.g. coherent population trapping). See, for example [7, 8] and references therein.

We realized the Raman laser (design, construction and operation) based on a modulation-enhanced external cavity diode laser (ECDL) (see App. A). In order to test its capabilities we decided to set up a versatile experimental system for studying the interaction of ^{87}Rb vapor with a variety of electromagnetic fields (light, MW, RF) in a well controlled environment of magnetic fields (see App. B and C).

Our work attracted the attention of the Israeli Aerospace Industries, and led to a 4-year joint R&D project for the development of optical magnetometry [9] technology. (Since my part in this project was substantial, the university granted me a three-year leave-of-absence from my Ph.D. work.)

During the development of our experimental setup, we came upon the need for a fast and accurate method to measure the population of hyperfine states of room-temperature alkali vapor – in our case, ^{87}Rb. Although the interaction of alkali vapor with light has been studied for more than 60 years, we could not find an accurate enough method in the literature, so we had to develop our own method. This development effort led us to the discovery of the *magic frequency*, which is the main subject of this thesis. At this magic frequency, the absorption of a linearly polarized light beam by alkali vapor atoms is independent of the population distribution amongst their Zeeman sub-levels and the angle between the light beam and an external magnetic field.

Using the magic frequency, we present and analyze a simplified absorption model in

Ch. 3, with a review of helpful background material in Secs. 2.8 – 2.11 and in App E. The magic frequency provides the basis for a novel method of measuring the population in the hyperfine ground states of alkali atoms, as described in Ch. 4, with helpful background material in Sec. 2.7.5 and in App. B.

In Chap. 5 we present an experimental demonstration of the magic frequency. The relevant background material can be found in Secs. 2.5 and 2.10.2 and in Apps. B and D.

A general theoretical introduction in presented in sections 2.1 – 2.7, and some related experimental work (modulated laser subsystem; vapor cell filling system) is presented in Apps. A and C.

Abstract

In this thesis I analyze theoretically and demonstrate experimentally the existence of a *magic frequency* for which the absorption of a linearly polarized light beam by alkali vapor atoms is independent of the population distribution amongst their Zeeman sub-levels and the angle between the light beam and an external magnetic field. I show that the phenomenon originates from a cancellation of the contributions of higher moments of the atomic density matrix, and is described using the Wigner-Eckart theorem and inherent properties of Clebsch-Gordan coefficients.

I present a simplified model for the absorption of a light beam by a vapor of alkali atoms and use it to numerically study the properties of the magic frequency. I find that the magic frequency is very weakly dependent on the vapor temperature, and demonstrate that absorption of a light beam within 10 MHz from the magic frequency is also independent of the population distribution amongst the Zeeman sub-levels and the angle between the beam and an external magnetic field.

Based on the magic frequency I build a measuring system for the hyperfine population, demonstrate that it can measure the population with a time resolution of a few microseconds, and validate that its stability and sensitivity are better than 1%.

A versatile experimental system was built for studying the interaction of ^{87}Rb vapor with a variety of electromagnetic fields (light, MW, RF) in a well-controlled environment of DC magnetic fields. I describe the design, construction and operation of the system, which includes an RF source, a MW generator, several coils that produce DC magnetic field and three lasers, one of which is a modulated Raman laser capable of producing two coherent beams with frequencies spaced by several GHz. The Raman laser employs an innovative method that enhances the amplitude of sidebands generated by the modulation of the feed current of the laser diode with a microwave current.

I also outline the design, construction and operation of a vapor cell-filling system that is capable of producing Rb and Cs vapor cells with paraffin wall-coating and/or with buffer gas. The system includes a demonstration of a cell filling method that may lead to low-cost, high-yield vapor cell production.

Publications Based on This Research

- M. Givon, Y. Margalit, A. Waxman, T. David, D. Groswasser, Y. Japha and R. Folman, 'Magic Frequencies in Atom-Light Interaction for Precision Probing of the Density Matrix', Phys. Rev Lett. **111**, 053004 (2013).
- American Physical Society Synopsis (spotlighting exceptional research): 'A Magic Frequency for Atomic Spectroscopy', http://physics.aps.org/synopsis-for/10.1103/PhysRevLett.111.053004
- A.Waxman, M. Givon, G. Aviv, D. Groswasser and R. Folman, 'Modulation enhancement of a laser diode in an external cavity', Appl. Phys. B. **95**, 301 (2009).
- D. Groswasser, A. Waxman, M. Givon, G. Aviv, Y. Japha, M. Keil, and R. Folman, 'Retroreflecting polarization spectroscopy enabling miniaturization' Rev. Sci. Instrum. **80**, 093103 (2009).

Patent applications:

- M. Givon and A. Waxman, WO2010041158: Phase locked sideband beams by bias modulation of an external cavity laser diode having a grating (2008)
- Y. Bar Haim, M. Givon and T. David, Israeli patent application 227584: A vapor cell and a method and system for fabrication thereof (2013)

Contents

List of Figures

List of Tables

List of Abbreviations

AC	alternating current
AOM	acousto-optic modulator
AR	anti-reflection
CG	Clebsch-Gordan
CPU	central processing unit
CPT	coherent population trapping
CW	continuous wave
DAC	data acquisition system
DC	direct current
ECDL	external cavity diode laser
EIT	electromagnetically induced transparency
FSR	free spectral range
FWHM	full width half maximum
GPIB	general-purpose interface bus
GUI	graphical user interface
MCP	main control program
MW	microwave
OD	optical density
PCB	printed circuit board
PM	polarization moments
PZT	piezoelectric transducer

RF radio frequency

RMS root mean square

RWA rotating wave approximation

SMA subminiature version a

TTL transistor-transistor logic

Chapter 1

Introduction

Interaction of light with alkali metal vapor has an important role both in the study of fundamental physics and in many technological applications. In 1950, A. Kastler proposed the idea of using photons to induce order in an atomic ensemble by scattering resonant light [10, 11]. By appropriately choosing the frequency and the polarization of the pumping light, it is possible to generate a desired distribution of population in the atomic energy sub-levels of the atoms. A sodium vapor cell was used by J. P. Barrat et al. to demonstrate spin-polarized optical pumping in 1954 [12]. Modulation of a light beam by a precessing magnetic moment created by optically-pumped alkali atoms was suggested and realized by H. G. Dehment [13]. Further work by W. L. Bell and A. L. Bloom [14, 15], R. H. Dicke [16] and others during the late 1950s paved the way for modern frequency standards and optical magnetometers.

One of the first technological applications is the vapor-cell frequency standard (atomic clock). Commercially available since the 1960s [17], these standards were used in the early space missions, and are still extensively used today. There is a constant, on-going R&D effort to both miniaturize them and improve their performance (see [18, 19, 20, 21, 22] and references therein).

The introduction of solid-state laser diodes in the late 1980s boosted both the applied and the fundamental research of light-matter interaction. Optical magnetometers, typically based on the interaction of several laser beams with an alkali vapor, became the most sensitive available magnetometers, and their improvement continues to this very day [9, 23, 24, 25, 26, 27].

Other important examples of related phenomena are macroscopic entanglement, which was demonstrated using cesium vapor cells [28]; the nonlinear light-matter phenomena known as electromagnetically induced transparency (EIT) [7], which led to slow and stopped light [29], and to the storing of pulses of light, as well as images, in alkali vapor cells [30, 31].

In view of the central role of alkali vapor cells, detailed understanding of the physics of the vapor and its interaction with light is important. Already in 1957, U. Fano introduced the density matrix and the polarization moments as the main tools needed to describe the state of the vapor and its evolution [32, 33]. Additional reviews of this approach can be found in W. Happer's 1972 paper [34] and in a 1977 paper by A. Omont [35].

The early studies of the state of the vapor were focused on measuring the degree of optical pumping and the relaxation processes. H. G. Dehmelt proposed in 1957 a scheme to

measure the spin-relaxation time of optically-pumped alkali vapor [36], reporting a relaxation time of $\sim 200\,\mathrm{ms}$. An improved method, known as "evolution in the dark" was described in 1959 by W. Franzen [37], followed by detailed studies conducted in France during the early 1960s, mainly by M. A. Bouchiat and J. Brossel (see [38] and references therein). A comprehensive summary of these early methods can be found in the 1972 review by W. Happer [34]. Such measurements are still done today, reporting relaxation and coherence times of up to one minute [39, 40].

High-rank polarization moments and associated high-order coherences have attracted considerable attention since the late 1990s (see [41] and references therein), and several methods were developed to address and measure them (e.g. [41, 42]). Knowing all the polarization moments is equivalent to full knowledge of the density matrix and, thereby, all the observables of the system. However, to the best of our knowledge, there are no methods to accurately measure the zero-order polarization moment (which is proportional to the relative population of the hyperfine ground state), so the picture is not complete.

The main difficulty in measuring the population of atoms in their hyperfine ground states is that the interaction of light with room-temperature alkali vapor depends not only on the population, but also on several other parameters including the distribution of the population between the Zeeman sub-levels. Thus, measuring the hyperfine population depends on assumptions regarding the population distribution amongst the Zeeman sub-levels. It was during the development and upgrade of our population measuring method that we discovered a *magic frequency* – a frequency at which absorption of linearly polarized light by alkali atoms depends only on the hyperfine population, and can serve as a basis for a fast and accurate population measuring method. This method has potential for probing the full density matrix and may even provide interesting insight concerning group theory.

The body of this thesis is devoted to the discovery of the magic frequency and its applications, as follows: In Ch. 2 we present the necessary theoretical background related to the features of two-state and multi-state systems, to the irreducible representation of the density matrix via polarization moments, and to the interaction of electromagnetic radiation with alkali atoms. Chapter 3 is devoted to the description of our relative absorption model and to the discovery of the magic frequency. Based on our model, we analyze the absorption of light by alkali vapor near the magic frequency both numerically and analytically, and study the properties of the magic frequency. In Ch. 4 we show how we utilize the magic frequency to develop a fast and accurate method to measure the population of the hyperfine states of alkali vapor and in Ch. 5 we present an experimental demonstration of the magic frequency. Ch. 6 summarizes our work and and provides an outlook for further studies in this field.

Supplementary parts of our work and results are presented in the appendices. We present the modulation-enhanced ECDL subsystem in App. A. Appendix B provides full details of the various features of our versatile experimental system, and in App. C we describe our vapor cell filling system. App. D describes our fast current shutters.

Chapter 2

Theory

In this chapter we present the necessary theoretical background related to our research. Our aim here is to provide a coherent summary of the relevant material and to establish the notation that we will use throughout this thesis.

In Secs. 2.1 –2.6 we provide a basic description of the main aspects of the interaction of electromagnetic radiation with two-state atoms. Following a review of the Schrödinger equation for a two-state atom subjected to a perturbative external field, we first present the simple case of population oscillations resulting from a Heaviside step function of the external field ("Majorana population oscillations", see Shore [43], §3.4). We then review briefly the concept of the density matrix, present the Bloch sphere, Rabi oscillations and Ramsey fringes, and then discuss the dressed states concept.

Next (Sec. 2.7) we introduce the three-state Λ scheme, and provide a deeper insight into electric dipole transitions, magnetic dipole transitions, and the Rabi frequency. After a short review of optical pumping, we present important three-state phenomena: Raman transitions and electromagnetically induced transparency (EIT). (Some parts of the material presented in this section are typically included in the discussion of two-state atoms, but we prefer to incorporate it into our three-states discussion).

In Secs. 2.8 – 2.9 we review angular momentum operators and angular momentum states, present the concept of irreducible tensor operators and introduce the Wigner-Eckart theorem. We then (Sec. 2.10) describe the state structure of the ^{87}Rb atom. Here we also review Doppler broadening, and calculate the fraction of ^{87}Rb atoms at a temperature T that interact with near-resonant light – a result needed for the presentation (in Sec. 3.1) of our simplified absorption model. We then present the polarization moments (Sec. 2.11) and use the state structure of the ^{87}Rb atom to demonstrate some of them.

In the last section of this chapter (Sec. 2.12) we present a calculation of the dependence of the absorption of near-resonant light by a two-state atom on the dipole matrix element – an additional result we need for the presentation of our simplified absorption model.

This chapter is based mainly on works of Profs. Bruce W. Shore [43, 44], Daniel A. Steck [45, 46] and Dmitry Budker *et al.* [9, 47, 48].

2.1 The Schrödinger equation for a two-state atom

Let us look at an isolated atom which can be described by a stationary Hamiltonian H^0 and a complete set of orthonormal eigenfunctions (or eigenstates) $|\psi_n\rangle$ of H^0 such that:

$$H^0|\psi_n\rangle = E_n^0|\psi_n\rangle \tag{2.1}$$

and

$$\langle\psi_n|\psi_m\rangle = \delta_{m,n}. \tag{2.2}$$

Any state $|\Psi\rangle$ of the system can then be described as a linear combination of the $|\psi_n\rangle$'s:

$$|\Psi(t)\rangle = \sum_n C_n(t)|\psi_n\rangle, \tag{2.3}$$

where

$$C_n(t) = \langle\psi_n|\Psi\rangle \equiv \langle n|\Psi\rangle. \tag{2.4}$$

The $C_n(t)$'s are complex numbers representing probability amplitudes. The probability $P_n(t)$ of finding the system in state $|\psi_n\rangle$ at time t is:

$$P_n(t) = |C_n(t)|^2 = |\langle n|\Psi\rangle|^2 \tag{2.5}$$

and, since $|\psi_n\rangle$ is a complete set,

$$\sum_n P_n(t) = 1. \tag{2.6}$$

Obviously, when there is no interaction between the isolated atom and its environment the system is stationary and all the $P_n(t)$'s are constants. It follows that only the phases of the $C_n(t)$'s change with time for an isolated system:

$$C_n(t) = C_n(0)e^{-iE_n^0 t/\hbar}. \tag{2.7}$$

When we study light-matter interaction, we are typically interested in situations where we manipulate the atom with controllable, time-dependent external fields. In most cases, interactions with such external fields are small relative to the internal forces that define the stationary eigenstates $|\psi_n\rangle$ of H^0. In other cases, those interactions are strong, but last a very short time. When these conditions are met, we may use the perturbative approach. (Descriptions of the perturbation theory can be found in most quantum mechanics reference texts; see, for example, [49], Ch. 8). With this approach, it is useful to define the Hamiltonian H, describing both the isolated atom and its interaction with the applied external fields, as:

$$H(t) = H^0 + V(t). \tag{2.8}$$

Then the Schrödinger equation

$$i\hbar\frac{\partial}{\partial t}\Psi(t) = H(t)\Psi(t) \tag{2.9}$$

describes the time evolution of the atomic state $|\Psi(t)\rangle$ under the influence of the external interaction $V(t)$, which may also be represented by its matrix elements $V_{nm}(t)$:

$$V_{nm}(t) = \langle\psi_n|V(t)|\psi_m\rangle \tag{2.10}$$

with, since $V(t)$ is Hermitian,

$$V_{nm} = V^*_{mn}. \tag{2.11}$$

Let us now focus our attention on an atomic two-state system. Such a system is, by definition, fully described by the two states: $|0\rangle \equiv |\psi_0\rangle$ and $|1\rangle \equiv |\psi_1\rangle$. Using Eq. (2.3) we can expand any wave function $|\Psi(t)\rangle$ in $|0\rangle$ and $|1\rangle$. Substituting this expansion in the Schrödinger equation [Eq. (2.9)] yields the following equation for the expansion coefficients:

$$i\hbar\frac{d}{dt}\begin{pmatrix}C_0(t)\\C_1(t)\end{pmatrix} = \begin{pmatrix}E_0^0 + V_{00}(t) & V_{01}(t)\\ V_{10}(t) & E_1^0 + V_{11}(t)\end{pmatrix}\begin{pmatrix}C_0(t)\\C_1(t)\end{pmatrix}. \tag{2.12}$$

Once $V(t)$ and the initial conditions are specified, Eq. (2.12) provides the time evolution of the two-state system subject to the external interaction.

2.2 Coherent interaction – Majorana population oscillations

An isolated two-state atom that at some time t_0 is in one of the eigenstates of its Hamiltonian remains indefinitely in its initial condition, as long as there is no interaction with its environment. Conversely, to illustrate some of the phenomena that occur when such an interaction is present, let us subject a two-state atom to a very simple external time-dependent potential: zero for $t \leq 0$ and constant afterwards. For example, consider an atomic beam that moves rapidly from a field-free region to an area with a constant electric or magnetic field (see [43], § 3.4). The potential presented in Eq. (2.13) may be a good approximation of the sudden change in the potential energy the atoms in that beam are subjected to:

$$V = \begin{cases} \begin{pmatrix}0 & 0\\ 0 & 0\end{pmatrix} & t \leq 0 \\ \begin{pmatrix}\frac{1}{2}\hbar(2\bar{\omega}-\omega_0) - E_0^0 & \frac{1}{2}\hbar\Omega\\ \frac{1}{2}\hbar\Omega & \frac{1}{2}\hbar(2\bar{\omega}+\omega_0) - E_1^0\end{pmatrix} & t > 0 \end{cases} \tag{2.13}$$

where $\hbar\omega_0$ is the energy difference between the two states, $\hbar\bar{\omega}$ is the average of the energies of the two states and Ω is a real number where $\hbar\Omega$ specifies the sudden change in the potential energy due to the external field. As we will see below [Eq. (2.16)], this change in the potential causes population oscillations, and the value of Ω is related to the frequency of those oscillations. This Ω is, in a sense, the static counterpart of the Rabi frequency (also marked Ω) that characterizes the interaction between a two-state atom and an oscillating external excitation (see Sec. 2.5).

Substituting Eq. (2.13) into Eq. (2.12) and setting $\hbar\bar{\omega} = 0$ (the zero point of the energy is arbitrary) we get:

$$i\frac{d}{dt}\begin{pmatrix}C_0(t)\\C_1(t)\end{pmatrix} = \frac{1}{2}\begin{pmatrix}-\omega_0 & \Omega\\ \Omega & +\omega_0\end{pmatrix}\begin{pmatrix}C_0(t)\\C_1(t)\end{pmatrix}, \tag{2.14}$$

which leads to:

$$\begin{aligned} \ddot{C}_1(t) &= -\frac{1}{4}\widetilde{\Omega}^2 C_1(t) \\ \text{and} \quad \widetilde{\Omega} &= \sqrt{\Omega^2 + \omega_0^2}. \end{aligned} \tag{2.15}$$

Solving Eq. (2.15) for the $C_n(t)$'s with the initial conditions $C_0(0) = 1,\ C_1(0) = 0$, and calculating the probability $P_1(t)$ of finding the system in the upper state we get:

$$P_1(t) = \frac{1}{2}\left(\frac{\Omega}{\widetilde{\Omega}}\right)^2 [1 - \cos(\widetilde{\Omega}t)]. \tag{2.16}$$

So we see that by adding this simple interaction, we cause periodic oscillations in the two-state probabilities. When the interaction is weak ($\Omega \ll \omega_0$) the oscillation amplitude is small, and its frequency is close to ω_0. When the interaction is strong ($\Omega \gg \omega_0$) the entire population moves periodically between each of the two states, and its oscillation frequency is close to Ω. Similar oscillations of the two-state atom (typically called "Rabi oscillations" – see Sec. 2.5) are produced by almost any external excitation.

2.3 Pure / mixed states and the density matrix

The periodic probability oscillations described in the previous section cannot be observed by one measurement of a single two-state atom. To notice these oscillations we need an ensemble of such atoms (and several other conditions that we will summarize at the end of the next section). In this section we describe the basic tools required to deal with an ensemble of quantum states, following Hideo Mabuchi's 2001 on-line course notes [50]. (Note that many observations of a single system constitute an ensemble).

Let's assume that at time $t = 0$ we can define an ensemble of two-state atoms through a set of wave functions $|\Psi_i(0)\rangle$, each representing a fraction p_i of the atoms in that ensemble ($\sum_i p_i = 1$). We can then define the density operator at time $t = 0$ as:

$$\hat{\rho}(0) = \sum_i p_i |\Psi_i(0)\rangle\langle\Psi_i(0)|. \tag{2.17}$$

It can be shown that the equation of motion of $\hat{\rho}(t)$ is given by the Liouville equation (see [46], § 4.1):

$$i\hbar\frac{\partial}{\partial t}\hat{\rho}(t) = [H, \hat{\rho}(t)] \tag{2.18}$$

and that the expectation value of any operator $\hat{A}$ is given by

$$\langle\hat{A}\rangle = Tr(\hat{\rho}\hat{A}). \tag{2.19}$$

If one of the p_i equals 1, say $p_1 = 1$, then $|\Psi_1\rangle$ represents all the atoms in the ensemble, and we have what is usually called a "pure state". Otherwise, we have a "mixed state". ("Pure ensemble" and "mixed ensemble" seem to be more suitable names, but we will stick with tradition.)

2.4 The Bloch sphere

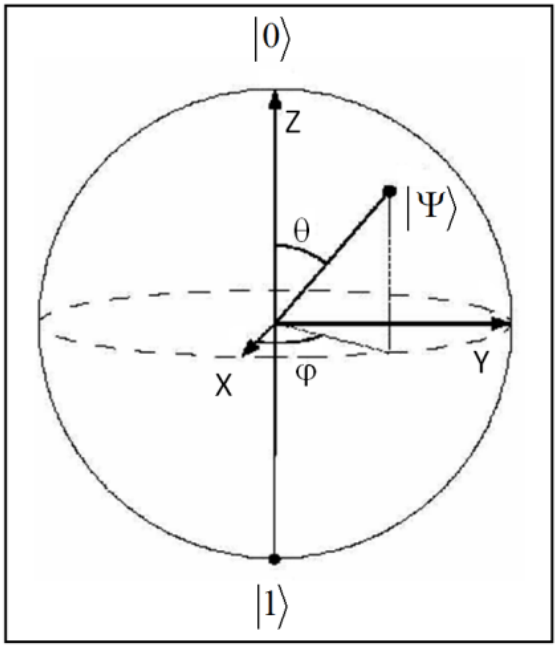

Figure 2.1: The Bloch sphere – a radius = 1 sphere with its center at the origin. The angles θ ans ϕ are the spherical coordinates of a point on the Block sphere.

We can geometrically represent any state of an ensemble of two-state systems on a three-dimensional unit sphere, known as the Bloch sphere (see Fig. 2.1). Any state $|\Psi\rangle$ of a two-state system can be written as [see Eq. (2.3)]:

$$|\Psi\rangle = C_0|0\rangle + C_1|1\rangle. \tag{2.20}$$

Ignoring the global phase, we can re-write Eq. (2.20) as:

$$\begin{aligned} |\Psi\rangle &= \cos\left(\frac{\theta}{2}\right)|0\rangle + e^{i\phi}\sin\left(\frac{\theta}{2}\right)|1\rangle \\ 0 &\leq \theta \leq \pi \\ 0 &\leq \phi \leq 2\pi. \end{aligned} \tag{2.21}$$

The two angles θ and ϕ represent both the pure state $|\Psi\rangle$ and a point on the Bloch sphere (Fig. 2.1). Thus we can represent the pure state $|\Psi\rangle$ as a point on the Bloch sphere.

The "north pole" ($\theta = 0$) represents the pure state $|0\rangle$ while the "south pole" ($\theta = \pi$) represents the pure state $|1\rangle$. Once we establish the correspondence between states and the Bloch sphere, we can use the Bloch sphere to visualize the system and demonstrate its evolution (both θ and ϕ may vary with time).

We now introduce the spin operator $\mathbf{S}$ and the Bloch vector $\mathbf{v}$, (which is the unit vector connecting the origin to a point (θ, ϕ) on the Bloch sphere) to link together the pure and

mixed states, the Bloch sphere, and the density operator:

$$\mathbf{S} \equiv \frac{\hbar}{2}\boldsymbol{\sigma} \equiv \frac{\hbar}{2}(\sigma_{\mathrm{x}}, \sigma_{\mathrm{y}}, \sigma_{\mathrm{z}}) \equiv \frac{\hbar}{2}\left[\begin{pmatrix} 0 & 1 \\ 1 & 0 \end{pmatrix}, \begin{pmatrix} 0 & -i \\ i & 0 \end{pmatrix}, \begin{pmatrix} 1 & 0 \\ 0 & -1 \end{pmatrix}\right]. \tag{2.22}$$

The Bloch vector components, in Cartesian coordinates, are:

$$\mathbf{v} = (v_{\mathrm{x}}, v_{\mathrm{y}}, v_{\mathrm{z}}) = (\sin\theta\cos\phi, \sin\theta\sin\phi, \cos\theta). \tag{2.23}$$

Calculating the expectation value $\langle\mathbf{S}\rangle$ for the pure state represented by (θ, ϕ) we get:

$$\langle\mathbf{S}\rangle = \frac{\hbar}{2}(\sin\theta\cos\phi, \sin\theta\sin\phi, \cos\theta). \tag{2.24}$$

Combining equations (2.19),(2.23) and (2.24) we see that for a pure state we may have:

$$\langle\mathbf{S}\rangle = Tr(\hat{\rho}\mathbf{S}) = \frac{\hbar}{2}\mathbf{v}, \text{ with } |\mathbf{v}| = 1. \tag{2.25}$$

Equation (2.25) motivates the definition of the generalized Bloch vector $\mathbf{v}_{\mathrm{B}}$ (both for pure and for mixed states) as:

$$\frac{\hbar}{2}\mathbf{v}_{\mathrm{B}} = Tr(\hat{\rho}\mathbf{S}). \tag{2.26}$$

Studying the properties of the density operator and the generalized Bloch vector, we learn the following:

- The density operator can be written as:

$$\hat{\rho} = \frac{1}{2}(1 + \mathbf{v}_{\mathrm{B}} \cdot \boldsymbol{\sigma}). \tag{2.27}$$

- The diagonal matrix elements of $\langle i|\hat{\rho}|i\rangle$ of the density operator are real; they give the relative populations of the two basis states $|0\rangle$ and $|1\rangle$ for the ensemble represented by $\hat{\rho}$. Therefore, their sum is 1, or $Tr(\hat{\rho}) = 1$. (This property of the density matrix is valid for any number of basis states.)

- The off-diagonal elements of $\hat{\rho}$ ($\rho_{ij} = \rho_{ji}^{*}$) represent the coherence between the states.

- The equation of motion for $\mathbf{v}_{\mathrm{B}}$ is:

$$i\hbar\frac{d}{dt}\mathbf{v}_{\mathrm{B}} = \frac{1}{2}Tr(\boldsymbol{\sigma}[H, (1 + \mathbf{v}_{\mathrm{B}} \cdot \boldsymbol{\sigma})]). \tag{2.28}$$

  Example: when a static magnetic field B_{z} is applied, the solution of this equation shows that the Bloch vector precesses about the z axis at the Larmor frequency, given by $\omega_L = \gamma B_{\mathrm{z}}$, where γ is the gyromagnetic ratio of the atom. For simplicity, the dynamics of $\mathbf{v}_{\mathrm{B}}$ may be calculated in a reference frame that rotates about the z axis at the Larmor frequency.

- Finally, the Bloch vector can represent dissipation and dephasing. For that purpose, we define 3 additional parameters: the longitudinal relaxation time T_1, the transverse relaxation time T_2 and v_{z}^0, which is the z component of the Bloch vector at thermal equilibrium. Adding these parameters to the equation of motion for $\mathbf{v}_{\mathrm{B}}$, and solving in the rotating-frame with no field except B_{z}, we obtain the following results for the components of the Bloch vector (see [50], lecture notes 12):

$$\begin{aligned} v_{\mathrm{x}}(t) &= v_{\mathrm{x}}(0)e^{-\frac{t}{T_2}} \\ v_{\mathrm{y}}(t) &= v_{\mathrm{y}}(0)e^{-\frac{t}{T_2}} \\ v_{\mathrm{z}}(t) &= [v_{\mathrm{z}}(0) - v_{\mathrm{z}}^0]e^{-\frac{t}{T_1}} + v_{\mathrm{z}}^0. \end{aligned} \tag{2.29}$$

This result is valid only in a very simple case, but it does present the general picture. We see that if the system starts at $t = 0$ at some pure state on the surface of the Bloch sphere, the projection of the Bloch vector on the xy plane will start to shrink to zero at a rate governed by the T_2 time constant, representing a dephasing (or decoherence) process. In parallel, but at a different rate defined by T_1, the z component of the Bloch vector will decay towards its thermal equilibrium value v_z^0.

Let us briefly return to the Majorana population oscillations described in Sec. 2.2. We now see that there are several requirements if we wish to actually observe the probability oscillations:

- We need an ensemble of measurements, which can be realized by repeated measurements on a single two-state atom (each time repeating the same preparation), or by a single measurement of a group of such atoms, or some combination of these two methods.

- We have to prepare the ensemble so that its initial state is as close as possible to a pure state. Otherwise, the atoms in the ensemble will have random phases relative to each other. This will mask any observation of the probability oscillations. Typically, the ensemble is prepared by some type of optical pumping [51].

- All the operations, including final measurements, must be completed well before the shorter of the two relaxation times T_1 and T_2. Failing to do this will again lead to averaging out the probability oscillations.

- The initial state of the system at $t = 0$ should not be an eigenstate of the full Hamiltonian. If it is, the system will remain in that state indefinitely.

All of these conditions are required if we wish to observe the Majorana population oscillations, or any other coherent phenomena.

2.5 Rabi oscillations and Ramsey fringes

The two-state atom is described by the Hamiltonian H^0, the eigenvalues E_0^0, E_1^0 and the eigenstates $|0\rangle$, $|1\rangle$ (see Sec. 2.1). When we subject the atom to external periodic excitation

(e.g., as caused by electromagnetic radiation), the atom is instead described by the full Hamiltonian $\hat{H}(t) = H^0 + \hat{V}(t)$ [see Eq. (2.12)]. For electromagnetic radiation that can be described as single frequency plane wave with circular polarization we have (see Shore [43], §3.7):

$$\begin{aligned} V_{00}(t) &= V_{11}(t) = 0 \\ V_{01}(t) &= V_{10}^*(t) = -\frac{\hbar}{2}|\Omega|e^{-i(\omega t+\phi)}, \end{aligned} \tag{2.30}$$

where ω is the radiation angular frequency and $|\Omega|$ is the Rabi frequency. We already introduced the symbol Ω as a measure of a static change of the potential (see Sec. 2.2); here $|\Omega|$ is a measure of the strength of the atom-radiation interaction. We use the same name "Rabi frequency" and the same symbol since the results of the interaction in both cases are population oscillations at a frequency that is related to $|\Omega|$. Details of the atom-radiation interaction and the exact definition of the Rabi frequency are presented in Sec. 2.7.2.

Now we can substitute Eq. (2.30) into the time dependent Schrödinger equation in the form presented by Eq. (2.12) and solve the resulting equations for the probability amplitudes $C_0(t)$ and $C_1(t)$. At this point we wish to introduce Shore's phase-choice method (see [43] §3.7): we can modify the probability amplitudes by writing the wave function as $|\Psi\rangle = \sum \overline{C}_i(t)e^{-i\zeta_i(t)}|i\rangle$, $i = 0, 1$, and still have $P_i = \langle i|\Psi\rangle = |\overline{C}_i(t)|^2 = |C_i(t)|^2$ although $C_i(t)$ and $\overline{C}_i(t)$ are different functions of time. A proper choice of the phases ζ_i may lead to equations that can be solved analytically. Using this method, we get the following equations for the probability amplitudes ([43], §3.7):

$$i\frac{d}{dt}\begin{pmatrix}\overline{C}_0(t)\\ \overline{C}_1(t)\end{pmatrix} = \frac{1}{2}\begin{pmatrix}\omega-\omega_0 & |\Omega| \\ |\Omega| & -(\omega-\omega_0)\end{pmatrix}\begin{pmatrix}\overline{C}_0(t)\\ \overline{C}_1(t)\end{pmatrix}, \tag{2.31}$$

where $\hbar\omega_0$ is the energy difference between the states. Solving these equations with the initial condition that at $t = 0$ all the population is in the state $|0\rangle$, and calculating the probabilities, we get:

$$P_1(t) = 1 - P_0(t) = \frac{1}{2}\left(\frac{|\Omega|}{\widetilde{\Omega}}\right)^2[1-\cos(\widetilde{\Omega}t)], \text{ with } \widetilde{\Omega} = \sqrt{|\Omega|^2+(\omega-\omega_0)^2}. \tag{2.32}$$

We see that the probability of finding the atom in the state $|1\rangle$ oscillates indefinitely (Rabi oscillations) with a frequency that is the square root of the sum of the squares of the Rabi frequency and the detuning $\delta = \omega - \omega_0$ of the radiation frequency from the frequency of the atomic transition.

This behavior is similar to the Majorana population oscillations presented in Sec. 2.2. However, while the amplitude of the Majorana population oscillations depends mainly on Ω, the amplitude of the Rabi oscillations depends only on the detuning. At $\delta = 0$ the amplitude is maximal and it drops as the excitation frequency moves away from this resonance point. Figure 2.2 presents the Rabi probability oscillations for $|\Omega| = 2$ rad/sec and several values of the detuning. In Fig. 2.3 we plot $\langle P_1\rangle$, the average population in the excited state as a function of the detuning. The average population $\langle P_1\rangle$ can serve as a measure of the interaction strength (as a function of the detuning). Figure 2.3 shows that $\langle P_1\rangle$ has a Lorentzian shaped peak at the resonance frequency. The width of the peak [full width half maximum (FWHM)] is $2|\Omega|$. This is called the power broadening, since $|\Omega|$ depends on the radiation power (see Sec. 2.7.2).

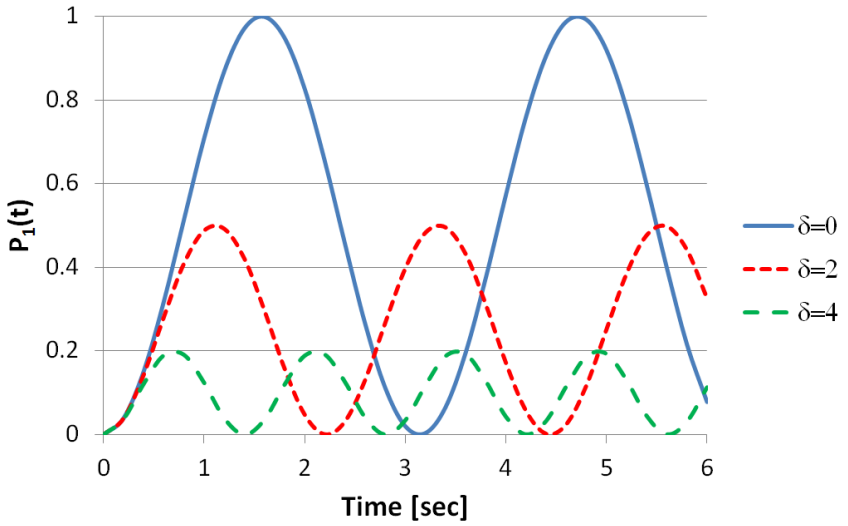

Figure 2.2: Rabi oscillations of the probability $P_1(t)$ for finding a two-state atom in the state $|1\rangle$ when the atom is excited by a circularly polarized single frequency plane wave at angular frequency ω ($\hbar\omega_0$ is the energy difference between the two states). The Rabi frequency used for this figure is $|\Omega| = 2$ rad/sec, and the Rabi oscillations are shown for three values of the detuning from resonance δ, measured in units of $|\Omega|$: $\delta = (\omega - \omega_0)/|\Omega|$.

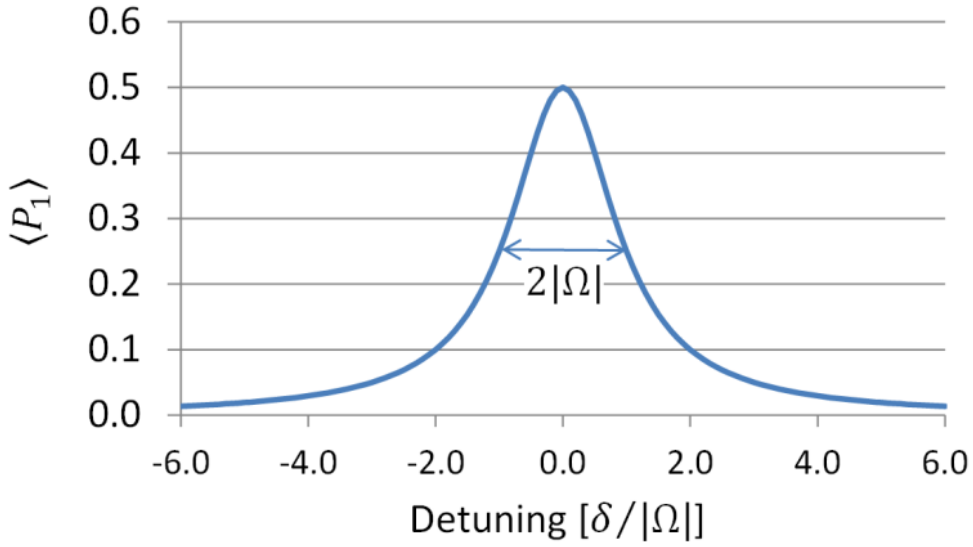

Figure 2.3: The average population $\langle P_1\rangle$ in the excited state of a two-state atom, plotted as a function of the detuning $\delta = \omega - \omega_0$ (the detuning is given in units of $|\Omega|$). The average population $\langle P_1\rangle$ can serve as a measure of the interaction strength. The plot is a Lorentzian and its FWHM is $2|\Omega|$.

2.5.1 Rabi pulses

Focusing our attention on the resonance case (the excitation frequency $\omega = \omega_0$), and following Kuhr [52], we can represent the effect of the Rabi pulse of duration time t on the Bloch vector $\mathbf{v}_{\mathrm{B}}(0)$ [see Eq. (2.26)] by the following 3×3 matrix:

$$\begin{aligned} \mathbf{v}_{\mathrm{B}}(t) &= \begin{pmatrix} 1 & 0 & 0 \\ 0 & \cos\theta(t) & \sin\theta(t) \\ 0 & -\sin\theta(t) & \cos\theta(t) \end{pmatrix} \mathbf{v}_{\mathrm{B}}(0) \equiv \widehat{\Theta}_{\theta(t)} \mathbf{v}_{\mathrm{B}}(0) \\ \theta(t) &= \int_0^t |\Omega(t')| dt'. \end{aligned} \tag{2.33}$$

In other words, a Rabi pulse rotates the Bloch vector about the x axis by an angle $\theta(t)$. (Note: In general, rotation about any axis is possible). For $\theta(t) = \pi/2$ and $\theta(t) = \pi$ the matrices become very simple:

$$\widehat{\Theta}_{\pi/2} = \begin{pmatrix} 1 & 0 & 0 \\ 0 & 0 & 1 \\ 0 & -1 & 0 \end{pmatrix} \text{ and } \widehat{\Theta}_{\pi} = \begin{pmatrix} 1 & 0 & 0 \\ 0 & -1 & 0 \\ 0 & 0 & -1 \end{pmatrix}. \tag{2.34}$$

$\widehat{\Theta}_{\pi}$ is called a π pulse, or Rabi flipping pulse, and $\widehat{\Theta}_{\pi/2}$ is called a $\pi/2$ pulse.

The matrix representation for free precession $\widehat{\Theta}_{\mathrm{free}}(t)$ of the Bloch vector is ($|\Omega| = 0$):

$$\begin{aligned} \widehat{\Theta}_{\mathrm{free}}(t) &= \begin{pmatrix} \cos\phi(t) & \sin\phi(t) & 0 \\ -\sin\phi(t) & \cos\phi(t) & 0 \\ 0 & 0 & 1 \end{pmatrix} \\ \phi(t) &= \int_0^t \delta(t') dt' = \int_0^t (\omega(t') - \omega_0) dt', \end{aligned} \tag{2.35}$$

where $\phi(t)$ is the accumulated phase as viewed in a reference frame that rotates with an angular frequency ω, typically referred to as the "rotating-frame" (see Sec. 2.7.3). Note: if $\omega(t) = \omega_0$ then the accumulated phase is zero and $\widehat{\Theta}_{\mathrm{free}}(t)$ reduces to the unit matrix.

In Fig. 2.4 we present some examples of Rabi pulses. The Rabi pulses may be utilized directly to manipulate our two-state atomic system. However, the two-state atom is usually just an approximate model, where we pick two of its many states and set them to be the states that will be used to realize a qubit or any other useful device. Depending on this choice, the frequency of the Rabi pulse may be in the radio frequency (RF) range (typically when the radiation links two Zeeman sub-levels of an alkali atom) in the microwave (MW) range (when two hyperfine levels are addressed) or in the optical domain.

2.5.2 Ramsey fringes

Consider the following sequence of operations, performed on an ensemble of two-state atoms (with an energy separation E between the states):

- prepare the ensemble in the pure state $\Psi(0) = |0\rangle$.

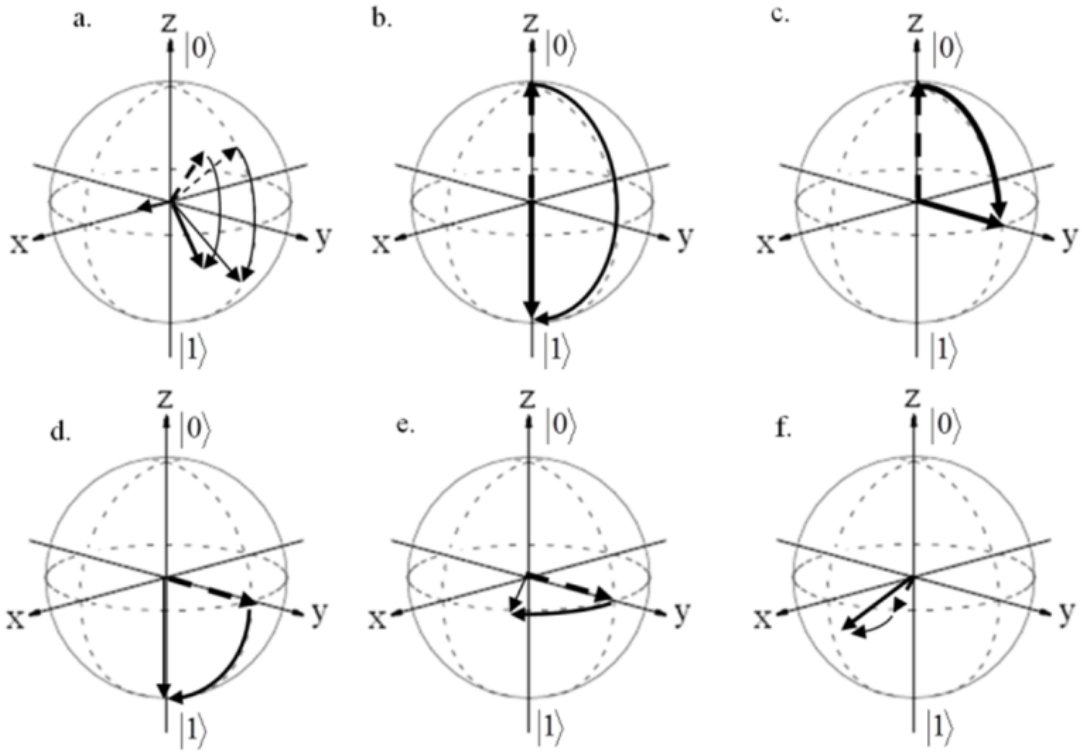

Figure 2.4: Some examples of Rabi pulses. ⇢ is the Bloch vector before the pulse, ⟶ is the vector after the pulse. In (a) we present a general Rabi pulse. The x component of the Bloch vector is preserved, while its projection on the yz plane is rotated by θ. Case (b) presents the operation of a π pulse on $|0\rangle$: it flips the population from $|0\rangle$ to $|1\rangle$, which explains its name – Rabi flipping pulse. In (c) a $\pi/2$ pulse takes the population from $|0\rangle$ to a point on the equator representing a coherent equal superposition of the two base states with no phase difference between them ($\phi = 0$). In (d) another $\pi/2$ pulse that is applied immediately takes the population from that point to $|1\rangle$. Case (e) shows free precession of the Bloch vector in the xy plane. Finally, (f) shows how a $\pi/2$ pulse affects the Bloch vector after being allowed to precess for some time.

- apply a $\pi/2$ Rabi pulse using a coherent, monochromatic radiation with angular frequency $\omega \approx \omega_0$ ($\omega_0 = E/\hbar$).
- block the radiation for time T. (The time T is also referred to as the "integration time" or "interrogation time").
- apply a second $\pi/2$ Rabi pulse using the same radiation.
- measure the population $P_1(T)$ of level $|1\rangle$.

In terms of the Bloch vectors and the matrices defined in Eq. (2.34) and Eq. (2.35), we can summarize the sequence described above as measuring the z component of $\mathbf{v}_{\text{Ramsey}}(T)$ defined below:

$$\mathbf{v}_{\text{Ramsey}}(T) = \Theta_{\pi/2} \cdot \Theta_{\text{free}}(T) \cdot \Theta_{\pi/2} \cdot \mathbf{v}_{\text{B}}^0, \tag{2.36}$$

where $\mathbf{v}_{\mathrm{B}}^{0}$ is the Bloch vector representing the state $|0\rangle$. Multiplying these matrices we obtain the z component of $\mathbf{v}_{\mathrm{Ramsey}}(T)$:

$$\mathbf{v}_{\mathrm{Ramsey}}(T)_z = -\cos\phi(T) = -\cos\left(\int_0^T \delta(t)dt\right). \tag{2.37}$$

Based on the above and on the examples presented in Fig. 2.4, it is clear that the population in level $|1\rangle$, $P_1(T)$, is a periodic function of the accumulated phase ϕ(T). Even a small value of $\delta(t)$ can change $P_1(T)$ drastically, provided that the integration time T is long enough.

The Ramsey fringes represented by Eq. (2.37) provide a very delicate interferometeric tool. The interferometeric nature can be revealed if we look at a $\pi/2$ pulse as a 50/50 optical beamsplitter. The first pulse splits the atomic wave function into a superposition of the two states. During the integration time T the relative phase $\phi(T)$ is accumulated. The second pulse recombines the two states, interferometrically comparing the accumulated relative phase. Thus, Ramsey fringes constitute a very sensitive probe to compare an external frequency to atomic transition frequency and to investigate other phenomena related to the two-state system.

2.6 Dressed states

Our unperturbed two-state atom is described by the Hamiltonian H^0, the eigenvalues E_0^0, E_1^0, and the eigenstates $|0\rangle$, $|1\rangle$ (see Sec. 2.1). When we add external interaction, the atom is described by the full Hamiltonian $\widehat{H}(t)$. It is of interest to study the full Hamiltonian eigenstates. Let the interaction with the external excitation (such as a monochromatic laser beam with angular frequency ω) be:

$$\widehat{V}(t) = \frac{\hbar}{2}\begin{pmatrix} 0 & \Omega^* e^{i\omega t} \\ \Omega e^{-i\omega t} & 0 \end{pmatrix}, \tag{2.38}$$

where Ω is the Rabi frequency (see Sec. 2.7.2). The state of the system in the rotating-frame (see Sec. 2.7.3) is:

$$\Psi(t) = C_0(t)|0\rangle e^{i\omega t/2} + C_1(t)|1\rangle e^{-i\omega t/2}. \tag{2.39}$$

Note that the energy zero is midway between the states. Substituting Eq.(2.38) and Eq. (2.39) into the time-dependent Schrödinger equation (2.12) leads to:

$$i\hbar\frac{d}{dt}\begin{pmatrix} C_0(t) \\ C_1(t) \end{pmatrix} = \frac{\hbar}{2}\begin{pmatrix} -\delta & \Omega^* \\ \Omega & \delta \end{pmatrix}\begin{pmatrix} C_0(t) \\ C_1(t) \end{pmatrix}, \tag{2.40}$$

where $\delta = \omega - \omega_0$ and $\hbar\omega_0 = E_1^0 - E_0^0$. We can see that in the rotating-frame the matrix representation of $\widehat{H}(t)$ is time independent, and so are its eigenvalues, given by:

$$E_{\pm} = \pm\frac{\hbar}{2}\sqrt{|\Omega|^2 + \delta^2} = \pm\frac{\hbar\widetilde{\Omega}}{2}. \tag{2.41}$$

Calculating the eigenvectors we get (excluding a global phase):

$$\begin{aligned}\Phi_+(t) &= e^{i\omega t/2}\sqrt{\frac{1}{2}\left(1+\frac{\delta}{\widetilde{\Omega}}\right)}|0\rangle + e^{-i\omega t/2}\sqrt{\frac{1}{2}\left(1-\frac{\delta}{\widetilde{\Omega}}\right)}|1\rangle \\ \Phi_-(t) &= e^{i\omega t/2}\sqrt{\frac{1}{2}\left(1-\frac{\delta}{\widetilde{\Omega}}\right)}|0\rangle - e^{-i\omega t/2}\sqrt{\frac{1}{2}\left(1+\frac{\delta}{\widetilde{\Omega}}\right)}|1\rangle.\end{aligned} \tag{2.42}$$

The states $\Phi_\pm$ are called "dressed states", as opposed to the "bare states" $|0\rangle$, $|1\rangle$. Thus, addition of an external perturbation mixes the bare states.

We can utilize the dressed states to manipulate our system of two-state atoms:

- from Eq. (2.42) we can see that $|\Phi_-(t)\rangle$ is mainly $|0\rangle$ for far-red detuning, while $|\Phi_+(t)\rangle$ is mainly $|0\rangle$ for far-blue detuning.
- we note that if a system is represented at some time by either one of the dressed states, it will remain in this state indefinitely, as this state is an eigenstate of the full Hamiltonian.
- it turns out that if we change the frequency of the exciting field slowly, a system that is in a pure dressed state will remain in this dressed state. Such changes changes are adiabatic and can be characterized by [53]:

$$\gamma = \frac{|\Omega|^2}{d\delta/dt}. \tag{2.43}$$

The probability that an atom will make a transition to another dressed state is $P = e^{-2\pi\gamma}$ so that with large enough γ we can assume that no atom will make a transition to another dressed state. There are several procedures that utilize adiabaticity to manipulate atomic ensembles.

2.6.1 Chirped pulses

To demonstrate one such adiabatic procedure, let us start with an ensemble in which all the atoms are in the ground state $|0\rangle$. Then we slowly ramp up the intensity of a far-red detuned laser field. Since the $\Phi_-(t)$ dressed state is thereby mainly $|0\rangle$, all the atoms will be in this state initially. Then we sweep the frequency adiabatically up to a far-blue detuned value, whereby the $\Phi_-(t)$ dressed state is mainly $|1\rangle$. At this point we adiabatically ramp the intensity down to zero, leaving almost all the atoms in $|1\rangle$. Thus we have a chirped pulse method to manipulate the state of an ensemble of atoms.

2.7 Adding other states - the Λ scheme

Typically, our two-state atom has many other states that are ignored at this level of approximation. Sometimes, however, it is advantageous to bring more states into the game, as well as additional parameters that may be used to manipulate our two-state system; these can

facilitate otherwise forbidden transitions and bring to light some hidden properties of the system. A frequently-used three-state configuration is presented in Fig. 2.5 and is known as the Λ scheme.

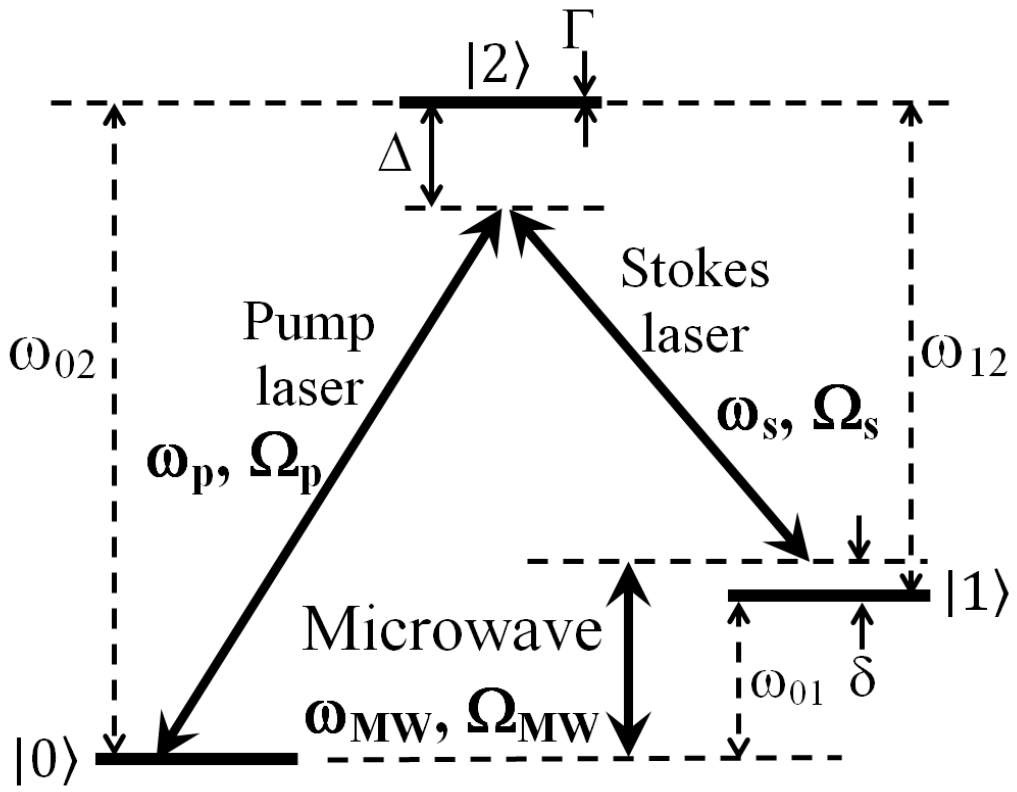

Figure 2.5: The Λ scheme – a three-state configuration. States $|0\rangle$ (the ground state) and $|1\rangle$ make up the two-state system, with energy separation $\hbar\omega_{01}$. Typically, these states have the same parity, so that the $|0\rangle \leftrightarrow |1\rangle$ transition is an electric-dipole-forbidden transition (see text). The linewidth of these states is usually very narrow. State $|2\rangle$ is the auxiliary state with linewidth Γ, and its parity is opposite to the parity of $|0\rangle$ and $|1\rangle$. Two light fields are shown with angular frequencies $\omega_{\rm p}$ and $\omega_{\rm s}$, while $\Omega_{\rm p}$, $\Omega_{\rm s}$ are the Rabi frequencies (see text). The terms "Pump laser" or "Pump beam" and "Stokes laser" or "Stokes beam" are the common terms used in the field of Raman spectroscopy [54]. Also shown is a MW field with angular frequency $\omega_{\rm MW}$ and Rabi frequency $\Omega_{\rm MW}$. $\delta = |\omega_{\rm p} - \omega_{\rm s}| - \omega_{01}$ is the Rabi detuning and Δ, the difference between $\omega_{\rm p}$ and the angular frequency of the $|0\rangle \leftrightarrow |2\rangle$ transition, is the Raman detuning.

To define a Λ scheme we need to choose three states from the many states that a real atom has (see, for example the rubidium atom, Sec. 2.10). Once we choose those states, we need to analyze the response of the atom to two or more light fields. Deeper understanding of the nature of the interaction of atoms with electromagnetic radiation is needed for these tasks, and we provide the relevant material (the multipole expansion, the Rabi frequency and the rotating-frame) in Secs. 2.7.1 – 2.7.4. (Note: parts of the material presented in these sections are typically included in the discussion of two-state atoms, but we prefer to

incorporate it into our three-state discussion.) Using that deeper understanding we analyze some of the applications of the Λ scheme: we describe the method of optical pumping, review Raman transitions and briefly present the EIT phenomenon.

2.7.1 Multipole expansion

The Hamiltonian of an atom interacting with external fields may be written as (see Sec. 2.1):

$$\begin{aligned} H(t) &= H^0 + V(t) \\ H^0|\psi_n\rangle &= E_n^0|\psi_n\rangle, \end{aligned} \tag{2.44}$$

where the matrix elements of $V(t)$ are:

$$V_{nm}(t) = \langle\psi_n|V(t)|\psi_m\rangle. \tag{2.45}$$

In this section we outline a method that relates the perturbation term $V(t)$ to the interaction of the atom with external electromagnetic fields.

Let us consider a collection of particles (electrons, protons and neutrons that make up an atom). Each particle has charge e_α and is at position $\mathbf{r}(\alpha)$ relative to the location $\mathbf{R}$ of the center of mass (Fig 2.6). Our aim is to evaluate the energy that these particles possess when they are subjected to external electric and magnetic fields (external fields are those that originate in charges and currents outside of the atom).

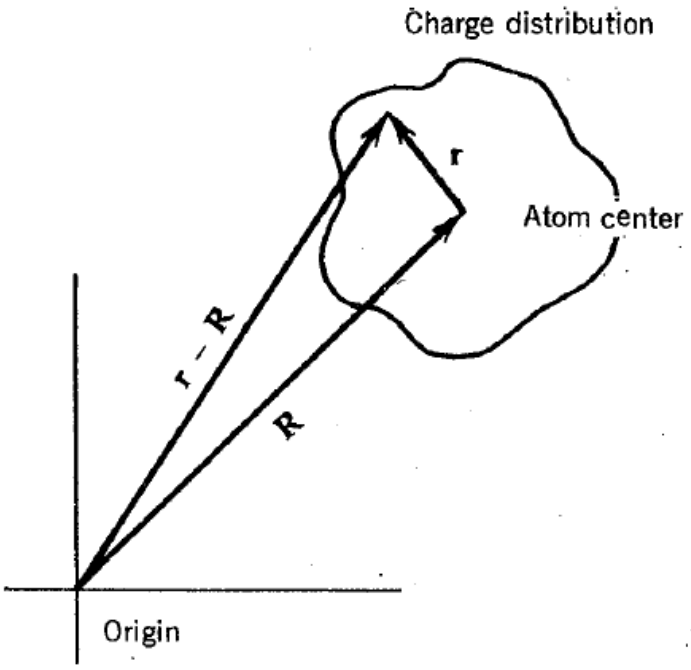

Figure 2.6: Multipole Coordinates. R – the position the center of mass (atomic center); r-position of a particle relative to the center of mass. Taken from Shore [43].

To proceed, we introduce the multipole expansion of the desired energy. This expansion has two parts: one series for the electric energy V^{elec}, and another for the magnetic one V^{magn}.

Following Shore's notation ([43], § 2.8) the series for V^{elec} is:

$$V^{\text{elec}}(t) = \left[\sum_\alpha e_\alpha\right]\phi(\mathbf{R},t) - \sum_i \left[\sum_\alpha e_\alpha r_i(\alpha)\right] E_i(\mathbf{R},t) - \frac{1}{2}\sum_{ij}\left[\sum_\alpha e_\alpha r_i(\alpha) r_j(\alpha)\right]\frac{\partial}{\partial R_j}E_i(\mathbf{R},t) + \cdots \tag{2.46}$$

or, in a shorter notation:

$$V^{\text{elec}}(t) = V^{\text{E0}}(t) + V^{\text{E1}}(t) + V^{\text{E2}}(t) + \cdots ,$$

where $\phi(\mathbf{R},t)$ is the external electrostatic potential, $E_i(\mathbf{R},t)$ are the components the external electric field, the indexes i,j stand for the three spatial direction and the index α runs over all the particles that compose the atom. The terms in the large square brackets in Eq. (2.46) are the first three electric multipole moments – the electric monopole, the electric dipole and the electric quadrupole. Note: the monopole moment in Eq.(2.46) is just the total charge, which vanishes for a neutral atom.

In a similar way, the energy V^{magn} of the interaction of the atom with the magnetic field can be written as:

$$V^{\text{magn}}(t) = -\sum_i \left[\sum_\alpha \mu(\alpha)\left[g_l(\alpha) l_i(\alpha) + g_s(\alpha) s_i(\alpha)\right]\right] B_i(\mathbf{R},t) + \cdots$$

or, in a shorter notation:

$$V^{\text{magn}}(t) = V^{\text{M1}}(t) + \cdots , \tag{2.47}$$

where for electrons $\mu(\alpha) = -e\hbar/2m_e c = -\mu_{\text{B}}$ (Bohr magenton), for protons and neutrons $\mu(\alpha) = e\hbar/2m_{\text{p}}c = \mu_{\text{N}}$ (nuclear magneton), and $B_i(\mathbf{R},t)$ are the components the external magnetic field. The term in the large square brackets in Eq. (2.47) is the first magnetic multipole moment – the magnetic dipole moment [see [43], § 2.8 for additional terms and for the values of the $g_s(\alpha)$]. Note that the nuclear magnetron μ_{N} is about 2000 times smaller than the Bohr magneton μ_{B} due to the ratio between mass of the electron to that of the proton.

Typically, almost-monochromatic lasers and/or RF fields interact with the atoms. Therefore we assume that these fields can be described as a single frequency plane wave:

$$\begin{aligned}\mathbf{E}(\mathbf{R},t) &= \text{Re}\left[\hat{\epsilon}_{\text{E}} E_0 e^{i(\mathbf{k}\cdot\mathbf{R}-\omega t)}\right] \\ \mathbf{B}(\mathbf{R},t) &= \text{Re}\left[\hat{\epsilon}_{\text{B}} B_0 e^{i(\mathbf{k}\cdot\mathbf{R}-\omega t)}\right],\end{aligned} \tag{2.48}$$

where $\hat{\epsilon}_{\text{E}}, \hat{\epsilon}_{\text{B}}$ are the polarization unit vectors, E_0, B_0 are the amplitudes and $\mathbf{k}, \omega$ are the wave vector and the angular frequency of the fields ($|\mathbf{k}| = 2\pi/\lambda$, where λ is the wavelength of the field). We further assume (the "small atom" assumption) that the size of the atom ($\sim 0.3\,\text{nm}$) is much smaller than λ ($\sim 500\,\text{nm}$). Note that this assumption is not always valid (e.g., for Rydberg atoms with size on the order of $\sim 1000\,\text{nm}$).

When the "small atom" assumption holds, the spatial variation of the field inside the atom is small, and consequently so are the spatial derivatives of the field. These derivatives

multiply all the terms in the multipole expansions [Eq. (2.46) and (2.47)] with quadrupole or higher moments. Thus the multipole expansions are a good mathematical tool, where the higher terms contribute only minor corrections.

The electric dipole moment. The second term in large square brackets in Eq. (2.46) is the electric dipole moment $\mathbf{d}$, given below both for a collection of discrete charges and for a continuous charge distribution $\rho(\mathbf{r})$:

$$\mathbf{d} = \sum_{\alpha} e_{\alpha}\mathbf{r}(\alpha) = \int d^3r\rho(\mathbf{r})\mathbf{r}. \tag{2.49}$$

For a one-electron atom, the charge distribution of the electron in a state $\psi_n(\mathbf{r})$ is given by $\rho(\mathbf{r}) = -e\psi_n(\mathbf{r})^*\psi_n(\mathbf{r})$. Thus the matrix elements of the dipole moment operator $\mathbf{d}$ are (note that each element $\mathbf{d}_{nm}$ is a vector with three components):

$$\mathbf{d}_{nm} = -e\int d^3r\psi_n(\mathbf{r})^*\mathbf{r}\psi_m(\mathbf{r}) \equiv -e\langle n|\mathbf{r}|m\rangle. \tag{2.50}$$

In particular, the diagonal matrix elements are:

$$\mathbf{d}_{nn} = -e\int d^3r\psi_n(\mathbf{r})^*\mathbf{r}\psi_n(\mathbf{r}) \equiv -e\langle n|\mathbf{r}|n\rangle. \tag{2.51}$$

With this definition of the electric dipole moment and Eq. (2.46) we can obtain an expression for the energy of the electric dipole interaction:

$$V_{nm}^{\mathrm{E1}} = -\mathbf{d}_{nm}\cdot\mathbf{E}(\mathbf{R},t). \tag{2.52}$$

Parity and the electric dipole moment. The parity operator Π, which flips the sign of the space coordinates with respect to a given origin, is defined by:

$$\Pi|\mathbf{r}\rangle = |-\mathbf{r}\rangle. \tag{2.53}$$

It can be shown (see [46], §5.1.1) that Π is a unitary operator, that $\langle\mathbf{r}|\Pi = \langle-\mathbf{r}|$, that Π has two eigenvalues $\pi_{\pm} = \pm 1$ and that all even and odd states are eigenstates of Π. Also, Π commutes with the operators $\mathbf{r}^n$ and $\mathbf{p}^n$ for even n, and with $|\mathbf{r}|$. Recalling that the unperturbed Hamiltonian of an atom [Eq. (2.1) or Eq. (2.44)] is a function of $\mathbf{p}^2$ and $|\mathbf{r}|$ we have:

$$[H^0, \Pi] = 0. \tag{2.54}$$

Equation 2.54 implies that all the eigenstates ψ_n of H^0 are also eigenstates of Π and have either odd or even parity.

The parity operator can provide us with some information regarding the matrix elements $-e\langle n|\mathbf{r}|m\rangle$ of the dipole operator [Eq. (2.50)]. To see that, note that the anti-commutator of Π and $\mathbf{r}$, and its matrix element, vanishes:

$$[\Pi, \mathbf{r}]_+ = \Pi\mathbf{r} + \mathbf{r}\Pi = \Pi\mathbf{r} - \Pi\mathbf{r} = 0 \Rightarrow \langle n|[\Pi, \mathbf{r}]_+|m\rangle = 0. \tag{2.55}$$

On the other hand, we have:

$$0 = \langle n|[\Pi, \mathbf{r}]_+|m\rangle = \langle n|(\Pi\mathbf{r} + \mathbf{r}\Pi)|m\rangle = (\pi_n + \pi_m)\langle n|\mathbf{r}|m\rangle. \tag{2.56}$$

From Eq. 2.56 it follows that the diagonal elements d_{nn} of the dipole operator vanish. It also follows that if two states $|\psi_n\rangle$ and $|\psi_m\rangle$ have the same parity, then the dipole matrix element $\mathbf{d}_{nm}$ and the electric dipole interaction V^{E1}_{nm} vanish [see Eq. (2.52)]. We say that the electric dipole $|\psi_n\rangle \leftrightarrow |\psi_m\rangle$ transition is forbidden, because there is no electric dipole interaction to induce it. The electric dipole interaction term is much larger than any other term in Eqs. (2.46) and (2.47), so that any transition between equal parity states will be induced by much smaller terms (such as the magnetic dipole interaction V^{M1}) and will have much lower rate.

Going back to the Λ scheme (Fig. 2.5) we note that the states $|0\rangle$ and $|1\rangle$ have the same parity, so that $\mathbf{d}_{01} = 0$. We say that the $|0\rangle \leftrightarrow |1\rangle$ transition is electric-dipole-forbidden. Such pairs of states are found in the all the alkali elements: we can choose state $|0\rangle$ to be one of the lower hyperfine sub-levels of the ground state and $|1\rangle$ to be one of the higher hyperfine sub-levels of the ground state. (see Sec. 2.10 for the detailed level structure of one alkali element – the rubidium 87 atom). One consequence of the fact that the $|0\rangle \leftrightarrow |1\rangle$ transition is a dipole-forbidden transition is that the spontaneous emission rate of atoms in state $|1\rangle$ is very low, and the lifetime of state $|1\rangle$ is very long. Another consequence is that transitions between these states may be induced only by the much smaller magnetic dipole interaction (see below). The third state in Fig. 2.5, state $|2\rangle$, has opposite parity relative to $|0\rangle$ and $|1\rangle$, so that both $|0\rangle \leftrightarrow |2\rangle$ and $|1\rangle \leftrightarrow |2\rangle$ transitions can be induced by the electrical dipole interaction.

The magnetic dipole moment. The first term in Eq. (2.47), (the multipole expansion of the magnetic interaction) is V^{M1}, the magnetic interaction term:

$$V^{\mathrm{M1}} = -\sum_i \left[\sum_\alpha \mu(\alpha)\left[g_l(\alpha)l_i(\alpha) + g_s(\alpha)s_i(\alpha)\right]\right] B_i(\mathbf{R}, t), \tag{2.57}$$

where for electrons $\mu(\alpha) = -e\hbar/2m_e c = -\mu_{\mathrm{B}}$ (Bohr magenton), for protons and neutrons $\mu(\alpha) = e\hbar/2m_{\mathrm{p}}c = \mu_{\mathrm{N}}$ (nuclear magneton), $B_i(\mathbf{R}, t)$ are the components the external magnetic field, the index i stands for the three spatial components and the index α runs over all the particles that compose the atom.

In this work we focus an alkali atom, where we have only one outer-shell electron with charge $-e$, orbital angular momentum $\mathbf{L}$, and spin $\mathbf{S}$. This electron is bound to a massive core made up of all the nucleons and the inner electrons, with total charge $+e$ and nuclear spin $\mathbf{I}$. For this one-electron atom we can write V^{M1} as $\boldsymbol{\mu} \cdot \mathbf{B}(\mathbf{R}, t)$, where the magnetic dipole moment $\boldsymbol{\mu}$ is given by:

$$\boldsymbol{\mu} = \frac{e\hbar}{2m_e c}(g_L\mathbf{L} + g_S\mathbf{S} + g_I\mathbf{I}) = \mu_B(g_L\mathbf{L} + g_S\mathbf{S} + g_I\mathbf{I}), \tag{2.58}$$

where $g_L \approx 1, g_S \approx 2, g_I \approx -0.001$ (see [45]). We will address angular momentum states in Sec. 2.8. At this point we just note that the value of the matrix elements of the magnetic dipole moment $\boldsymbol{\mu} \cdot \mathbf{B}$ is typically more than 2 orders of magnitude (or 5 orders of magnitude

in the transition rate) smaller than the corresponding numbers for the electric dipole (see [43] § 2.8), so that the magnetic dipole interaction is typically neglected unless the electric dipole elements vanish. For more details on magnetic dipole transitions see [55], § 15.1.

2.7.2 Rabi frequencies in the Λ scheme

Both the electric dipole interaction [V^{E1}, Eq. (2.52)] term and the magnetic dipole interaction [V^{M1}, Eq. (2.57)] term include an oscillating part at the high angular frequency ω. In many cases, we can describe the system so that explicit time-dependent oscillating terms will not appear, via the combined application of the rotating wave approximation (RWA) and a rotating-frame of reference. Here we review the application of both of these methods to the electric dipole interaction and, as a part of this development, we define the Rabi frequencies for the Λ scheme (Fig. 2.5).

Let us go back to Fig. 2.5, and focus our attention on the $|0\rangle \leftrightarrow |2\rangle$ transition: a transition induced by the "probe laser" beam (with frequency ω_{p}) between two states separated by an energy of $\hbar\omega_{02}$. In this case, the probe beam is detuned by Δ from the transition frequency ω_{02}. When all the other fields indicated in Fig. 2.5 are turned off, we can treat these two states and the probe beam as a two-state atom, and its Hamiltonian can be written [in the dipole approximation, see Eq. (2.52)] as:

$$H(t) = H^0 + V^{\mathrm{E1}}(t) = H^0 - \mathbf{d}\cdot\mathbf{E}(\mathbf{R},t) \tag{2.59}$$

with $H^0 = \hbar\omega_{20}|2\rangle\langle 2|$, as the energy zero is fixed at state $|0\rangle$.

Applying the identity $|2\rangle\langle 2| + |0\rangle\langle 0| = 1$ on both sides of $\mathbf{d}$, and noting that $\langle n|\mathbf{d}|n\rangle = 0$, we obtain:

$$\mathbf{d} = \langle 0|\mathbf{d}|2\rangle|0\rangle\langle 2| + \langle 2|\mathbf{d}|0\rangle|2\rangle\langle 0| \equiv \mathbf{d}^{(+)} + \mathbf{d}^{(-)}. \tag{2.60}$$

Since the expectation value of $|0\rangle\langle 2|$ has the unperturbed time dependence $e^{-i\omega_{02}t}$, the time dependence of $\mathbf{d}^{(\pm)}$ is proportional to $e^{\mp i\omega_{02}t}$. We have thereby decomposed the dipole operator into positive and negative "rotating" parts.

The electric field of the radiation, given by Eq. (2.48)

$$\mathbf{E}(\mathbf{R},t) = Re\left[\hat{\epsilon}_{\mathrm{E}}E_0 e^{i(\mathbf{k}\cdot\mathbf{R}-\omega_{\mathrm{p}}t+\phi)}\right], \tag{2.61}$$

can be similarly decomposed. We will assume that $\mathbf{R} = 0$ ($\mathbf{R}$ is the position of the atomic center of mass), and that $\mathbf{k}\cdot\mathbf{R} \approx$ const. $= 0$ across the atom. We now decompose $\mathbf{E}$ into positive and negative "rotating" components:

$$\mathbf{E}(t) = \frac{\mathbf{E}_0}{2}(\hat{\epsilon}_{\mathrm{E}}e^{-i\omega_{\mathrm{p}}t} + \hat{\epsilon}^*_{\mathrm{E}}e^{i\omega_{\mathrm{p}}t}) = \mathbf{E}^{(+)} + \mathbf{E}^{(-)} \tag{2.62}$$

with

$$\mathbf{E}^{(\pm)} \equiv \mathbf{E}^{\pm}_0 e^{\mp i\omega_{\mathrm{p}}t}. \tag{2.63}$$

(Note that $\hat{\epsilon}_{\mathrm{E}}$ may be complex, that $\mathbf{E}^{\pm}_0$ includes the phase ϕ, and that $\mathbf{E}^{+}_0 = (\mathbf{E}^{-}_0)^*$).

Substituting $\mathbf{E}^{(\pm)}, \mathbf{d}^{(\pm)}$ in the last term of Eq. (2.59) we get:

$$\begin{aligned} V^{\mathrm{E1}} = -\mathbf{d}\cdot\mathbf{E}(\mathbf{R},t) &= -(\mathbf{d}^{(+)} + \mathbf{d}^{(-)})(\mathbf{E}^{(+)} + \mathbf{E}^{(-)}) \\ &= -\mathbf{d}^{(+)}\mathbf{E}^{(+)} - \mathbf{d}^{(-)}\mathbf{E}^{(-)} - \mathbf{d}^{(+)}\mathbf{E}^{(-)} - \mathbf{d}^{(-)}\mathbf{E}^{(+)}. \end{aligned} \tag{2.64}$$

The first two terms oscillate as $e^{\pm i(\omega_{02}+\omega_{\rm p})t}$, while the next two terms oscillate as $e^{\pm i(\omega_{02}-\omega_{\rm p})t}$. Since $|\omega_{02}+\omega_{\rm p}| \gg |\omega_{02}-\omega_{\rm p}|$, we can say that first two terms oscillate so rapidly compared to the other terms that we can replace them by their average value, which is 0. This is the RWA – the rotating wave approximation. Applying the RWA to Eq. (2.64) and substituting $\mathbf{E}^{(\pm)}, \mathbf{d}^{(\pm)}$ given by Eqs. (2.63) and (2.60), we get:

$$V^{\rm E1} = -e^{i\omega_{\rm p}t}\langle 0|\mathbf{d}\cdot\mathbf{E}_0^-|2\rangle|0\rangle\langle 2| - e^{-i\omega_{\rm p}t}\langle 2|\mathbf{d}\cdot\mathbf{E}_0^+|0\rangle|2\rangle\langle 0|. \tag{2.65}$$

We now define the Rabi frequencies Ω_{02}, Ω_{20} to be

$$\Omega_{02} \equiv \frac{\langle 0|\mathbf{d}\cdot\mathbf{E}_0^-|2\rangle}{\hbar} \equiv \Omega_{\rm p}; \quad \Omega_{20} \equiv \frac{\langle 2|\mathbf{d}\cdot\mathbf{E}_0^+|0\rangle}{\hbar} = \Omega_{\rm p}^*. \tag{2.66}$$

In most cases it is possible to choose a global phase so that Ω_{02} is real. The Rabi frequency $|\Omega_{\rm p}|$ is independent of both time and frequency and is a measure of the strength of the interaction between the electromagnetic radiation and the *electric* dipole of the atom.

In a similar way we can define $\Omega_{\rm s}$, which couples states $|1\rangle$ and $|2\rangle$ (see Fig 2.5). However, the definition of $\Omega_{\rm MW}$, linking states $|0\rangle$ and $|1\rangle$ is somewhat different. Since states $|0\rangle$ and $|1\rangle$ have the same parity (see caption of Fig. 2.5), the electric dipole matrix element vanishes. The next term, $V^{\rm M1}$ (the magnetic dipole interaction), is the term that can induce $|0\rangle \leftrightarrow |1\rangle$ transitions. In a way similar to Eq. (2.66), we define:

$$\Omega_{01} \equiv \frac{\langle 0|\mu\cdot\mathbf{B}_0^-|2\rangle}{\hbar} \equiv \Omega_{\rm MW}; \quad \Omega_{10} \equiv \frac{\langle 1|\mu\cdot\mathbf{B}_0^+|0\rangle}{\hbar} = \Omega_{\rm MW}^*. \tag{2.67}$$

$|\Omega_{\rm MW}|$ is a measure of the the strength of the interaction between the electromagnetic radiation and the *magnetic* dipole of the atom.

For a laser beam of intensity I (in W/cm^2), the Rabi frequencies $\Omega_{\rm p}$, $\Omega_{\rm s}$ are given by (see [43], § 3.3) :

$$\frac{|\Omega|}{2\pi}\ [\text{MHz}] = 70.24\frac{|\mathbf{d}_{i2}\cdot\boldsymbol{\epsilon}|}{ea_0}\sqrt{I\ [\text{W/cm}^2]}, \tag{2.68}$$

where a_0 is the Bohr radius, $\mathbf{d}_{i2}(i=0,1)$ is the dipole matrix element $\langle i|\mathbf{d}|2\rangle$ and $\boldsymbol{\epsilon}$ is the unit vector in the direction of the electric field of the laser light. The value of $|\mathbf{d}_{i2}\cdot\boldsymbol{\epsilon}|$ is typically in the same order of magnitude as ea_0. The value of $\Omega_{\rm MW}$, which depends on the interaction of the electromagnetic field with the magnetic moment of the atom, is typically more than 2 orders of magnitude smaller than $\Omega_{\rm p}$, $\Omega_{\rm s}$. The transition rate, which depends on $|\Omega_{\rm MW}|^2$, is typically 5 orders of magnitude smaller (for the same intensity of the field).

2.7.3 The rotating frame

Let us now focus our attention back to the $|0\rangle \leftrightarrow |2\rangle$ transition (Fig. 2.5). Combining Eqs. (2.59), (2.65) and (2.66), we can write the Hamiltonian of this sub-system (in the dipole approximation) as:

$$H_{\rm D}(t) = \hbar\omega_{20}|2\rangle\langle 2| - \frac{e^{i\omega_{\rm p}t}}{2}\hbar\Omega_{\rm p}|0\rangle\langle 2| - \frac{e^{-i\omega_{\rm p}t}}{2}\hbar\Omega_{\rm p}^*|2\rangle\langle 0|. \tag{2.69}$$

Substituting a general state $|\Psi\rangle = C_0|0\rangle + C_2|2\rangle$ in the time-dependent Schrödinger equation $i\hbar|\dot{\Psi}\rangle = H_{\rm D}(t)|\Psi\rangle$ we get:

$$\dot{C}_0|0\rangle + \dot{C}_2|2\rangle = -i\omega_{20}C_2|2\rangle - i\frac{\Omega_{\rm p}}{2}C_2e^{i\omega_{\rm p}t}|0\rangle - i\frac{\Omega_{\rm p}^*}{2}C_0e^{-i\omega_{\rm p}t}|2\rangle. \tag{2.70}$$

Projecting with $\langle 0|$ and $\langle 2|$ produces the equations of motion of the our sub-system:

$$\begin{aligned}\dot{C}_0 &= -i\frac{\Omega_{\rm p}}{2}C_2e^{i\omega_{\rm p}t}\\ \dot{C}_2 &= -i\omega_{20}C_2 - i\frac{\Omega_{\rm p}^*}{2}C_0e^{-i\omega_{\rm p}t}.\end{aligned} \tag{2.71}$$

Our next step is to transfer the above equations to a frame of reference that rotates at $\omega_{\rm p}$, via the rotating-frame amplitude:

$$\widetilde{C_2} = C_2e^{i\omega_{\rm p}t}. \tag{2.72}$$

In terms of the rotating-frame amplitudes, the equations of motion [Eq. (2.71)] now read:

$$\begin{aligned}\dot{C}_0 &= -i\frac{\Omega_{\rm p}}{2}\widetilde{C_2}\\ \dot{\widetilde{C_2}} &= -i(\omega_{20}-\omega_{\rm p})\widetilde{C}_2 - i\frac{\Omega_{\rm p}^*}{2}C_0 = -i\Delta\widetilde{C}_2 - i\frac{\Omega_{\rm p}^*}{2}C_0.\end{aligned} \tag{2.73}$$

Thus we have removed all the explicit time dependence from the equations of motion of our two-state sub-system. Several solutions to these equations (including Rabi oscillations) can be found in [46], § 5.

2.7.4 Validity of approximations

The time-independent equations of motion [Eq. (2.73)] describe the behavior of an atom subjected to an external oscillatory electromagnetic radiation field at frequency ω_p. In previous sections, we have used several approximations to develop these equations. We list them below, and briefly discuss the validity of each.

The "small perturbation" approximation. In the absence of external fields, the atom has a Hamiltonian H_0, with eigenvalues E_n^0 and eigenstates $|\psi_n^0\rangle$. We assume that the external radiation field is a small perturbation upon the internal structure of the atom, so that the eigenstates $|\psi_n^0\rangle$ still provide a good basis for the description of the combined system of atom + field. This small perturbation may be due to the fact that the interaction of the sub-atomic particles (mainly the electrons) with the external radiation fields is small compared to the internal interactions, or as a result of strong external radiation fields applied only for a short duration.

The "near-resonance" approximation. Atoms have an infinite number of bound states, some of them occupied, and in principle, an external radiation field at a frequency ω interacts with all of them. However, if there is just one pair of states $|0\rangle$, $|2\rangle$ with an energy separation $\hbar\omega_{02}$ between them such that $\omega \approx \omega_{02}$, we can ignore the interaction of the external radiation field with all other pairs of states. This is the near-resonance approximation. It is valid as long as, for any other pair of states $|m\rangle$, $|n\rangle$ (of which at least one is occupied)

we have $|\omega - \omega_{mn}| \gg \Gamma_m + \Gamma_n + 2|\Omega_{mn}|$, where $\hbar\omega_{mn}$ is the energy separation between the states, Γ_m and Γ_n are the natural linewidths, and $2|\Omega_{mn}|$ is the power broadening width (see Fig. 2.3).

The "small atom" approximation. This is the assumption that the spatial variation of the field inside the atom is small, and so are the spatial derivatives of the field. Those derivatives multiply all the terms in the multipole expansions (Eq. (2.46) and (2.47) with quadrupole or higher moments. As a result, the higher terms are much smaller than the leading terms so that the multipole expansions become very useful tools for such a situation. This approximation is valid as long as the size of the atom is much smaller than the wavelength of the radiation.

The dipole approximation. This approximation is a part of the previous one. In the dipole approximation we ignore all the terms in the multipole expansion [Eq. (2.46) and (2.47)] except the leading dipole term V^{E1}. This approximation is valid as long as the dipole term does not vanish, or as long as we do not care about minute details of the interaction, since the dipole term is at least 2 orders of magnitude larger than any of the following terms.

The rotating wave approximation (RWA). The RWA is useful when an electromagnetic field at an angular frequency ω interacts with an atom and ω is near a transition frequency ω_{nm} between some states $|n\rangle$ and $|m\rangle$ of the atom. Typically it is possible to express the interaction energy as a sum of two types of terms: the "high-frequency terms" that oscillate at the angular frequency of $\omega + \omega_{nm}$, and the "near-resonance terms" that oscillate at $\omega - \omega_{nm}$ [e.g. Eq. (2.64)]. As long as the high angular frequency $\omega + \omega_{nm}$ does not match any other transition frequency of the atom, we can replace such rapidly-oscillating, off-resonant terms with their time-averaged values of zero. This is the RWA.

2.7.5 Optical pumping

Optical pumping is a method to create polarization of a macroscopic substance by electromagnetic radiation. This method was pioneered by Alfred Kastler (Nobel Prize, 1966 [10, 11]). A very detailed review of the optical pumping process was written by W. Happer [34]. Here we will illustrate a very simple example of optical pumping based on the Λ scheme presented by Fig. 2.5. (This scheme may be realized by picking some states of an ensemble of alkali metal atoms, such as vapor in a vapor cell). The separation ω_{01} is on the order of several GHz, while the thermal energy of room-temperature atoms is approximately 1 THz. Thus we can assume that at room-temperature thermal equilibrium (with all the fields turned off) the states $|0\rangle$ and $|1\rangle$ have the same population and there is no coherence between them. On the other hand, both ω_{02} and ω_{12} are in the optical domain – hundreds of THz – so that the population of state $|2\rangle$ is effectively zero.

If we try to utilize the microwave radiation field to induce Rabi oscillations directly between the $|0\rangle$ and $|1\rangle$ states (see Sec. 2.5), no such oscillations will be observed, because the populations are initially equal: the two equal-amplitude Rabi oscillation processes would always have an opposite effect and they would simply cancel.

However, if we turn off the microwave, turn on just the Stokes laser (Fig 2.5) and tune its frequency so that $\omega_{\mathrm{s}} \approx \omega_{12}$, then:

- The Stokes laser will excite $|1\rangle \to |2\rangle$ transitions, while state $|0\rangle$ will not be affected,

since ω_s is too far detuned from both ω_{01} and ω_{02}.

- Atoms that are excited to state $|2\rangle$ may decay spontaneously (at a total rate Γ) either to state $|0\rangle$ or to state $|1\rangle$.
- Those atoms that decay to state $|1\rangle$ will be re-excited to state $|2\rangle$, but those which end up in state $|0\rangle$ will remain there.
- Eventually almost all the atoms will be optically pumped from state $|1\rangle$ to state $|0\rangle$.

If we now turn off the Stokes laser and turn on the microwave radiation, we will be able to observe Rabi oscillations, since all the atoms are in state $|1\rangle$ at the onset of the Rabi process, and the population will oscillate *coherently* between states $|0\rangle$ and $|1\rangle$.

The optical pumping process may be used to modify macroscopic properties of the vapor, such as magnetic moments, via the controlled manipulation of the populations of specific atomic states. Another macroscopic property that may be modified by optical pumping is the optical density of the vapor (see Eq. 4.2): as more and more atoms are pumped to state $|0\rangle$, the density of atoms that can interact with the Stokes laser is reduced, and so is the optical density of the vapor; eventually the vapor becomes transparent.

The optical pumping process of an atomic vapor is governed by several rates:

- the transition rate $\gamma_{1\leftrightarrow 2}$, which is proportional to $|\Omega_s|^2$ (see Sec. 2.12 and note that for optical pumping we tune the Stokes laser frequency so that $\omega_s \approx \omega_{12}$).
- the much smaller transition rate $\gamma_{0\leftrightarrow 2}$, which is proportional to $\gamma_{1\leftrightarrow 2}\cdot|\Omega_s|^2/(|\Omega_s|^2+\omega_{01}^2)$ and to a constant K_{01}, which is the square of the ratio of the dipole matrix elements: $K_{01}=[\langle 0|\boldsymbol{\epsilon}_s\cdot d|2\rangle/\langle 1|\boldsymbol{\epsilon}_s\cdot d|2\rangle]^2$, where $\boldsymbol{\epsilon}_s$ is a unit vector in the direction of the electric field of the Stokes laser beam.
- the spontaneous emission rate Γ of level $|2\rangle$.
- the partial spontaneous emission rates $\gamma_{2\to i}^{sp}$ to level $|i\rangle$; $i=0,1$ ($\gamma_{2\to 0}^{sp}+\gamma_{2\to 1}^{sp}=\Gamma$).
- the thermal relaxation rate $1/T_1$ [see Eq. (2.29)].

The rate equations for the populations p_i ($i=0,1,2$; $\sum p_i=1$) during the optical pumping process are:

$$\begin{aligned}\dot{p}_0 &= (p_2-p_0)\gamma_{0\leftrightarrow 2}+(p_1-p_0)/T_1+p_2\gamma_{2\to 0}^{sp}\\ \dot{p}_1 &= (p_2-p_1)\gamma_{1\leftrightarrow 2}+(p_0-p_1)/T_1+p_2\gamma_{2\to 1}^{sp}\\ \dot{p}_2 &= (p_0-p_2)\gamma_{0\leftrightarrow 2}+(p_1-p_2)\gamma_{1\leftrightarrow 2}-p_2\Gamma.\end{aligned} \tag{2.74}$$

After some time, the system reaches a steady state and we can substitute $\dot{p}_i=0$ in Eqs. (2.74) and solve them. In Fig. 2.7 we plot p_0 and p_1 as a function of the ratio of thermal relaxation rate $(1/T_1)$ to the excitation rate $\gamma_{1\leftrightarrow 2}$. Clearly, to effectively pump most of the population to the state $|0\rangle$, we need to have $1/T_1 \ll \gamma_{1\leftrightarrow 2}$.

Other parameters in Eq. (2.74), beside the ratio $(1/T_1)/\gamma_{1\leftrightarrow 2}$, influence the effectiveness of the optical pumping process. Figure 2.8 shows that increasing the ratio $\gamma_{2\to 0}^{sp}/\gamma_{2\to 1}^{sp}$ reduces the population p_1 (meaning more effective optical pumping). In addition, when the energy separation between states $|0\rangle$ and $|1\rangle$ is several GHz, the ratio $\gamma_{0\leftrightarrow 2}/\gamma_{1\leftrightarrow 2}$ is below 10^{-5}, and its actual value has no significant effect on p_1.

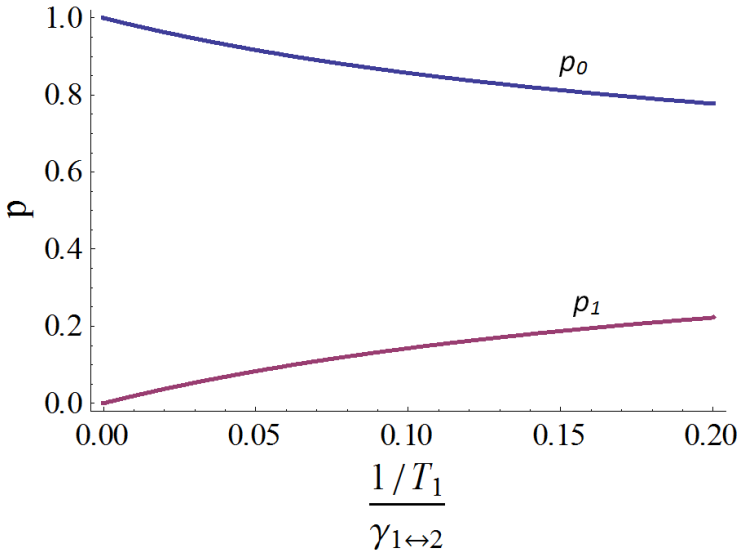

Figure 2.7: Steady-state populations following optical pumping. Plotted are the populations p_0 and p_1 as a function of the ratio of thermal relaxation rate $(1/T_1)$ to the excitation rate $\gamma_{1\leftrightarrow 2}$. (We used the following values: $\gamma_{1\leftrightarrow 2} = 20,000\,\mathrm{s}^{-1}$, $\gamma_{0\leftrightarrow 2} = 3 \cdot 10^{-7} \times \gamma_{1\leftrightarrow 2}$, $\Gamma = 3.77 \cdot 10^7\,\mathrm{s}^{-1}$ and $\gamma^{sp}_{2\to 0} = \gamma^{sp}_{2\to 1} = \Gamma/2$.)

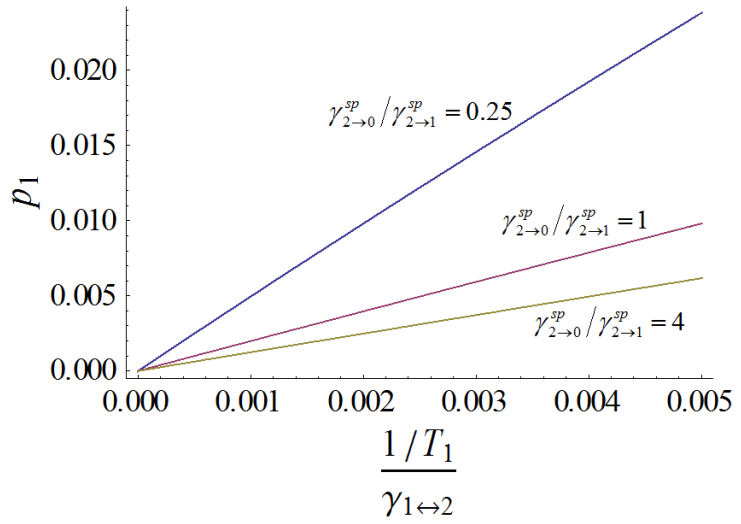

Figure 2.8: Steady-state population p_1 following optical pumping. Plotted are the populations p_1 for three values of $\gamma^{sp}_{2\to 0}/\gamma^{sp}_{2\to 1}$. (The horizontal axis is the ratio of thermal relaxation rate $(1/T_1)$ to the excitation rate $\gamma_{1\leftrightarrow 2}$; other parameters have the same values as given in Fig 2.7).

2.7.6 Raman transitions

Another way to utilize the Λ scheme presented in Fig. 2.5 is to excite $|0\rangle \leftrightarrow |1\rangle$ Rabi population oscillations using the two laser fields that link each of these states to $|2\rangle$. This is known as a Raman transition.

In the scheme shown in Fig. 2.5 the two states $|0\rangle$ and $|1\rangle$ have the same parity, so that the $|0\rangle \leftrightarrow |1\rangle$ transition is dipole-forbidden, and the linewidth of this transition is very narrow. The state $|2\rangle$ is of the opposite parity. Both the laser beams are turned on simultaneously (the microwave field is off), and the two laser beams are coherent. (By "coherent" we mean that the phase of the beat-note of the two light fields is independent of time – see details in the beginning of App. A.) We define here two Rabi frequencies [see Eq. (2.66)]: $\Omega_{\rm p}$ for the $|0\rangle \leftrightarrow |2\rangle$ transition, and $\Omega_{\rm s}$ for the $|1\rangle \leftrightarrow |2\rangle$ transition (we assume here that the phases of the states were chosen so that the Rabi frequencies are real and positive). The energy zero is at level $|0\rangle$, and Δ, δ and Γ are defined in Fig. 2.5. In this section, we assume that $\Delta \gg \Gamma$, so that the probability of populating state $|2\rangle$ by the $|1\rangle \leftrightarrow |2\rangle$ or $|0\rangle \leftrightarrow |2\rangle$ transitions is very small. Following Shore [43] and Dotsenko [56], this system can be described by the wave function

$$\Psi(t) = C_0(t)|0\rangle + C_1(t)|1\rangle + C_2(t)|2\rangle, \tag{2.75}$$

and its Hamiltonian $\widehat{H}$ is given by (using the rotating wave approximation):

$$\widehat{H} = \frac{\hbar}{2}\begin{pmatrix} 0 & 0 & \Omega_{\rm p} \\ 0 & 2\delta & \Omega_{\rm s} \\ \Omega_{\rm p} & \Omega_{\rm s} & 2\Delta \end{pmatrix}. \tag{2.76}$$

Substituting Eq. (2.75) and Eq. (2.76) into the time-dependent Schrödinger equation, we get equations for the $C_i(t)$'s. For $C_2(t)$ we have:

$$i\dot{C}_2(t) = \frac{1}{2}[\Omega_{\rm p}C_0(t) + \Omega_{\rm s}C_1(t)] + \Delta \cdot C_2(t). \tag{2.77}$$

Typically $\Delta \gg \Omega_{\rm s},\ \Omega_{\rm p}$, and we deduce that $C_2(t)$ oscillates at high frequency. Therefore we may replace its time derivative in Eq. (2.77) with its average over a large number of cycles, namely zero (see [56], page 5). Using the modified Eq. (2.77) to calculate (the time averaged) $C_2(t)$ as a function of the other $C_i(t)$'s, we get an effective Hamiltonian:

$$\widehat{H}_{\rm eff} = \frac{\hbar}{4}\begin{pmatrix} \Omega_{\rm p}^2/\Delta & \Omega_{\rm p}\Omega_{\rm s}/\Delta \\ \Omega_{\rm p}\Omega_{\rm s}/\Delta & \Omega_{\rm s}^2/\Delta - 4\delta \end{pmatrix}. \tag{2.78}$$

The off-diagonal elements give the coupling between states $|0\rangle$ and $|1\rangle$ by the Raman beams, while the diagonal elements represent the light shift of the energy levels due to their interaction with the light fields. By solving the time-dependent Schrödinger equation with this effective Hamiltonian, and calculating the population probabilities (with the initial condition $P_0(0) = 1$) , we obtain:

$$\begin{aligned} P_1(t) = 1 - P_0(t) &= \frac{\Omega_R^2}{\Omega_0^2}\sin^2\left(\frac{\Omega_0 t}{2}\right) \\ \text{with} \quad \Omega_R &= \Omega_P\Omega_S/2\Delta \\ \text{and} \quad \Omega_0 &= \sqrt{\Omega_R^2+\delta^2}. \end{aligned} \tag{2.79}$$

Comparing Eq. (2.79) to Eq. (2.32), we see that operating with two light fields in a Λ configuration induces Rabi oscillations between our two states as if we were coupling them with the single δ-detuned microwave field with an interaction strength of Ω_R.

2.7.7 Electromagnetically Induced Transparency – EIT

The Λ scheme presented in Fig. 2.5 can lead to another set of phenomena, known collectively as EIT. A detailed review of EIT can be found in [7] and in references therein. In this section we present a short description of the main features of EIT. Referring to Fig. 2.5, with the MW radiation off, both pump and Stokes lasers on and coherent, we can calculate the eigenstates of the full Hamiltonian of the Λ scheme. We can express these eigenstates (the "dressed states") as linear combinations of the eigenstates of the atomic Hamiltonian H^0 (2.44), (see [7]):

$$\begin{aligned} |a^+\rangle &= \sin\theta\sin\phi|0\rangle + \cos\phi|2\rangle + \cos\theta\sin\phi|1\rangle \\ |a^0\rangle &= \cos\theta|0\rangle - \sin\theta|1\rangle \\ |a^-\rangle &= \sin\theta\cos\phi|0\rangle - \sin\phi|2\rangle + \cos\theta\cos\phi|1\rangle, \end{aligned} \tag{2.80}$$

where the angles θ and ϕ are defined by:

$$\begin{aligned} \tan\theta &= \frac{\Omega_\mathrm{p}}{\Omega_\mathrm{s}} \\ \tan 2\phi &= \frac{\sqrt{\Omega_\mathrm{p}^2+\Omega_\mathrm{s}^2}}{\Delta}. \end{aligned} \tag{2.81}$$

If we choose the beam intensities such that $\Omega_\mathrm{p} \ll \Omega_\mathrm{s}$ and $\Delta \ll \sqrt{\Omega_\mathrm{p}^2+\Omega_\mathrm{s}^2}$, we find that $\sin\theta \to 0$, $\cos\theta \to 1$, $\tan\phi \to 1$, and the eigenstates of the full Hamiltonian become:

$$\begin{aligned} |a^+\rangle &= \frac{1}{\sqrt{2}}(|1\rangle + |2\rangle) \\ |a^0\rangle &= |0\rangle \\ |a^-\rangle &= \frac{1}{\sqrt{2}}(|1\rangle - |2\rangle). \end{aligned} \tag{2.82}$$

The effect of the laser fields on the level structure is presented in Fig. 2.9. We see that while $|a^0\rangle$ remains the ground state, the Stokes laser (ω_s) "combines" states $|1\rangle$ and $|2\rangle$ into the "doublet" $|a^+\rangle$ and $|a^-\rangle$.

Some effects of the modified level structure on the response of the ensemble of "three-level atoms" to the combined light fields are presented in Fig. 2.10. In this figure the susceptibility χ of the ensemble to the "pump" laser field (called also "probe" field) is plotted

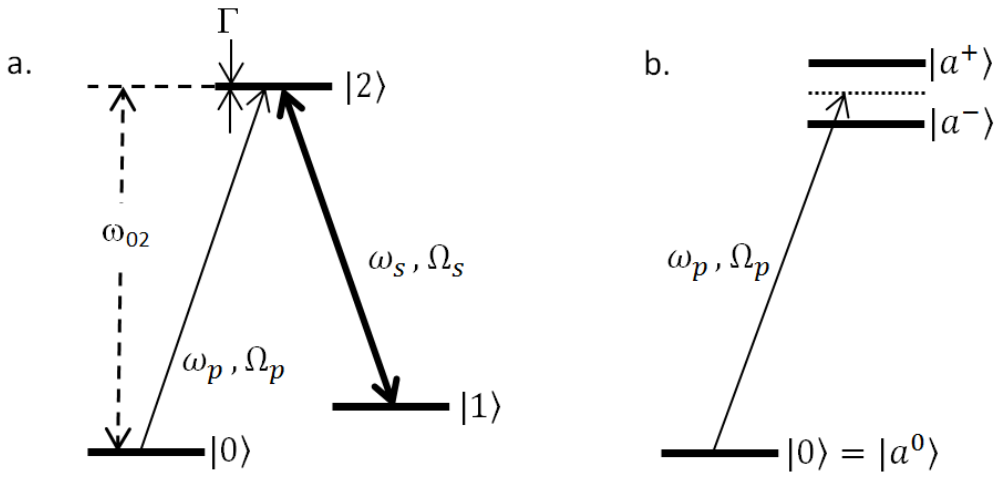

Figure 2.9: a. The Λ scheme with the two laser fields. b. The dressed states. See text for details. (This figure is taken from [7]).

as a function of the detuning. Since the susceptibility is complex, the real and imaginary parts are plotted separately. In the top part we see the absorption [Im(χ)] plotted as a function of the detuning ($\delta = \omega_{\rm p} - \omega_{02}$) of the "pump" beam from resonance. When the Stokes beam ($\omega_{\rm s}$, see Fig. 2.9) is off (dashed line), the absorption reaches a maximum at the resonance ($\delta = 0$). However, when the Stokes beam is on (solid line), the absorption at resonance goes down to zero, and the system becomes transparent – hence the name of the phenomena - "electromagnetically induced transparency". In the bottom part of Fig. 2.10 we see the refractive index [Re(χ)]. Near resonance, (when the Stokes beam is on – solid line) the slope of the refractive index plot in the EIT configuration changes sign, and it is much steeper than the refractive index when the Stokes laser is off (dashed line). This property is the basis for "slow" and "stopped" light (and related phenomena), as is evident from the formula for the light's group velocity $V_{\rm g} = c/(n_{\rm R} + \omega \cdot \partial n_{\rm R}/\partial\omega)$, where $n_{\rm R}$ is the real part of the refractive index (see [7, 57]).

Coherent population trapping. A related phenomenon is coherent population trapping (CPT). While EIT refers to the regime where one of the fields is much stronger than the other ($\Omega_{\rm p} \ll \Omega_{\rm s}$), CPT tends to refer to two fields of approximately equal Rabi frequencies (see [57], § 3.3). In this case it is preferable to study the Λ system using a different basis – replacing the states $|0\rangle$ and $|1\rangle$ with $|+\rangle$ and $|-\rangle$ defined by:

$$\begin{aligned} |+\rangle &= \frac{1}{\sqrt{|\Omega_{\rm p}|^2 + |\Omega_{\rm s}|^2}}(\Omega_{\rm p}^*|0\rangle + \Omega_{\rm s}^*|1\rangle) \\ |-\rangle &= \frac{1}{\sqrt{|\Omega_{\rm p}|^2 + |\Omega_{\rm s}|^2}}(\Omega_{\rm p}|0\rangle - \Omega_{\rm s}|1\rangle). \end{aligned} \tag{2.83}$$

It can be shown [58] that when the Rabi detuning is small, $\delta \to 0$ (see Fig. 2.5), the dipole matrix element for the transition $|-\rangle \leftrightarrow |2\rangle$ vanishes, while the matrix element for the $|+\rangle \leftrightarrow |2\rangle$ transition does not. Thus the $|-\rangle$ state is a "dark state" – atoms which are in

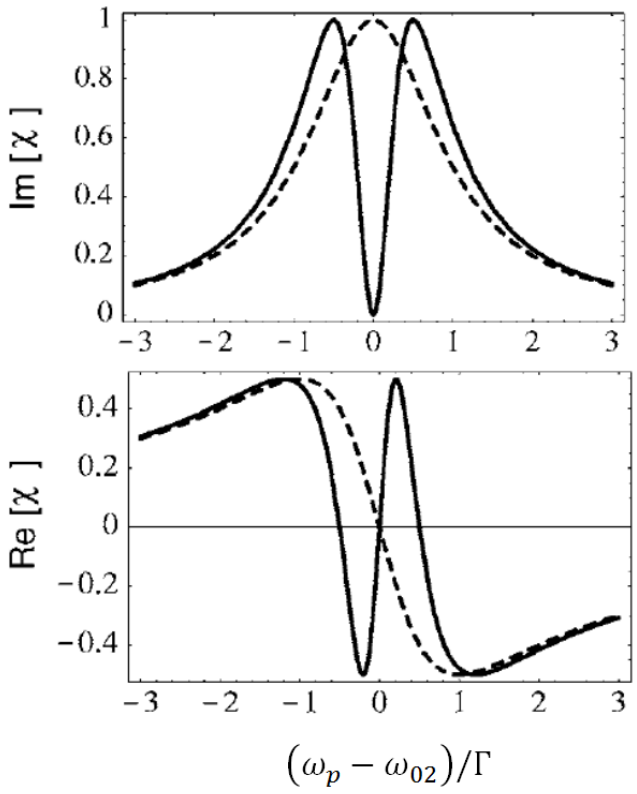

Figure 2.10: Comparison between the susceptibility of a two-level system (dashed line) and that of an EIT system with a resonant coupling field (solid line). The susceptibility is plotted as a function of the detuning $(\omega_p - \omega_{02})$ of the frequency of the pump laser's field from the atomic resonance frequency. Top: imaginary part of the susceptibility, determining absorption. Bottom: real part of the susceptibility, characterizing the refractive properties of the medium. See text for more details. (This figure is taken from [7])

this state cannot interact with the combined field of the two light beams. When these beams are turned on, they induce an optical pumping process that "traps" most of the population in this dark state, and render the system transparent.

The CPT phenomenon has a variety of applications, including several types of atomic clocks (see [58]).

2.8 Angular momentum states

In Sec. 2.7.1 [see Eq. (2.58)], we presented briefly angular momenta as part of the atomic Hamiltonian. For one-electron atoms, there are three relevant angular momenta: **L**, the electron orbital angular momentum, **S**, the electron spin, and **I**, the total nuclear spin. We will just present here some relevant properties of the angular momentum eigenstates. See [46], Ch. 7, for a detailed review.

For any angular momentum operator $\mathbf{J}$ the commutator of any two components is:

$$[J_i, J_j] = i\hbar\epsilon_{ijk}J_k, \tag{2.84}$$

where i, j, k represent x, y, z and ϵ_{ijk} is the Levi-Civita symbol ($\epsilon_{ijk} = 1$ if ijk is a cyclic permutation of $\hat{x}, \hat{y}, \hat{z}$, and equals -1 for an odd permutation and 0 otherwise). $\mathbf{J}^2$ commutes with any component of $\mathbf{J}$, so that we can construct simultaneous eigenstates of $\mathbf{J}^2$ and J_z. We denote these eigenstates $|j, m\rangle$, and we have:

$$\begin{aligned} \mathbf{J}^2|j, m\rangle &= j(j+1)\hbar^2|j, m\rangle \\ J_z|j, m\rangle &= m\hbar|j, m\rangle, \end{aligned} \tag{2.85}$$

where j is a positive integer or half-integer and m can assume values of $m = -j, -j+1, \ldots j$.

2.8.1 Adding angular momentum states

Let $\mathbf{J}_1$ and $\mathbf{J}_2$ be two angular momenta such that their components commute with each other ($[J_{1i}, J_{2j}] = 0$, where i, j can stand for x, y, z). The eigenstates of the two momenta are $|j_1, m_1\rangle$ and $|j_2, m_2\rangle$. Since all the relevant components commute, we can define a combined eigenstate of $\mathbf{J}_1^2, J_{1z}, \mathbf{J}_2^2, J_{2z}$ as:

$$|j_1, m_1; j_2, m_2\rangle \equiv |j_1, m_1\rangle|j_2, m_2\rangle. \tag{2.86}$$

On the other hand, the vector sum of these two momenta, $\mathbf{J} = \mathbf{J}_1 + \mathbf{J}_2$ is also an angular momentum operator, with eigenstates $|j_1, j_2; j, m\rangle$ that can be written as just $|j, m\rangle$. The quantum numbers j, m of the angular momenta sum must obey:

$$\begin{aligned} |j_1 - j_2| \leq j \leq j_1 + j_2 \\ m = m_1 + m_2. \end{aligned} \tag{2.87}$$

The two sets of eigenstates are related by:

$$\begin{aligned} |j, m\rangle &= \sum_{\substack{m_1, m_2 \\ (m=m_1+m_2)}} |j_1, m_1; j_2, m_2\rangle\langle j_1, m_1; j_2, m_2|j, m\rangle \\ |j_1, m_1; j_2, m_2\rangle &= \sum_{\substack{j, m \\ (m=m_1+m_2)}} |j, m\rangle\langle j, m|j_1, m_1; j_2, m_2\rangle. \end{aligned} \tag{2.88}$$

The coefficients $\langle j_1, m_1; j_2, m_2|j, m\rangle = \langle j, m|j_1, m_1; j_2, m_2\rangle^*$ are the Clebsch-Gordan (CG) coefficients. Formulae for the calculation of the values of the CG coefficients can be found, for example, in [46].

2.9 Irreducible tensor operators

The Hamiltonian H^0 describing an isolated one-electron atom possesses spherical symmetry, as it depends just on $\mathbf{p}_i^2$ and $1/|\mathbf{r}_i|$, where the index i indicates the different particles that

compose the atom. However, the eigenstates of the H^0 Hamiltonian are also eigenstates of the angular momentum operators $\mathbf{L}, \mathbf{S}, \mathbf{J}, \mathbf{I}, \mathbf{F}$ and F_z, of which at least one, F_z, points to a preferred direction (the "quantization axis"). When electromagnetic radiation (such as $\mathbf{E}$) interacts with the atom and causes transitions between some atomic states $|\psi_0\rangle$ and $|\psi_2\rangle$, matrix elements such as $\langle\psi_0|\mathbf{d}\cdot\mathbf{E}|\psi_2\rangle$ are needed to calculate transition probabilities and rates [see, for example, Eq. (2.66)]. When transitions take place in an ensemble characterized by mixed angular momentum states, several tools such as the Wigner-Eckart theorem (see Sec. 2.9.4) and the polarization moments (see Sec. 2.11) provide important insight into the ensemble behavior.

In the next sections we briefly review the rotation operators and the definition of the irreducible operators, and then introduce the Wigner-Eckart theorem. However, first we need to introduce a suitable basis – in this case, the spherical basis, which simplifies the relevant mathematical expressions. As an example, it can be shown that when the electric field of light radiation is given in the spherical basis, and this light interacts with an ensemble of atoms, each component of the light induces a transition with a specific change of angular momentum. This is not the case with the Cartesian components.

2.9.1 The spherical basis

The definition of the spherical basis unit vectors (in terms of the Cartesian unit vectors $\hat{x}, \hat{y}, \hat{z}$) is:

$$\begin{aligned} \hat{e}_{\pm} &\equiv \mp\frac{1}{\sqrt{2}}(\hat{x} \pm i\hat{y}) = -(\hat{e}_{\mp})^* \\ \hat{e}_0 &\equiv \hat{z} = (\hat{e}_0)^*. \end{aligned} \tag{2.89}$$

A vector $\mathbf{A}$ (with components A_x, A_y, A_z in the Cartesian basis) has components $A_{\pm}$ and A_0 in the spherical basis given by:

$$\begin{aligned} A_{\pm} &= \mp\frac{1}{\sqrt{2}}(A_x \pm iA_y) \\ A_0 &= A_z, \end{aligned} \tag{2.90}$$

and in the spherical basis the vector A is written as:

$$\mathbf{A} = \sum_q (-1)^q A_q \hat{e}_{-q} = \sum_q A_q \hat{e}_q^*; \quad q = -1, 0, 1. \tag{2.91}$$

The dot product of two vectors $\mathbf{A}$ and $\mathbf{B}$ is, in the spherical basis,

$$\mathbf{A}\cdot\mathbf{B} = \sum_q (-1)^q A_q B_{-q} = \sum_q A_q (B^*)_q^*. \tag{2.92}$$

One example of using this basis is the amplitude of the electric field $\mathbf{E}$ of circularly polarized light propagating in the z direction. Typically it is given as $E(\hat{x} + i\hat{y})$. In the spherical basis it is just $E\hat{e}_+$.

2.9.2 Rotation operators

Let us specify a rotation by a vector $\boldsymbol{\xi}$; the direction of $\boldsymbol{\xi}$ specifies the rotation axis, and its magnitude, the rotation angle. The rotation operators $R(\boldsymbol{\xi})$ rotate the wave function $|\psi\rangle$ in a way that is similar to the rotation of a classical vector: the norm of $|\psi\rangle$ is conserved, and for each rotation $R(\boldsymbol{\xi})$ there is an inverse rotation $R^{-1}(\boldsymbol{\xi}) = R^{\dagger}(\boldsymbol{\xi})$ († indicates Hermitian conjugate) so we have:

$$R^{\dagger}(\boldsymbol{\xi})R(\boldsymbol{\xi}) = 1. \tag{2.93}$$

Using the angular momentum operator $\mathbf{J}$, we define the rotation operator as (see [46], § 7.3):

$$R(\boldsymbol{\xi}) \equiv e^{-\frac{i}{\hbar}\mathbf{J}\cdot\boldsymbol{\xi}}. \tag{2.94}$$

The rotation operator can rotate a state:

$$|\psi'\rangle = R(\boldsymbol{\xi})|\psi\rangle \tag{2.95}$$

or an operator:

$$A' = R^{\dagger}(\boldsymbol{\xi})AR(\boldsymbol{\xi}). \tag{2.96}$$

For angular momentum states $|\psi\rangle = |j, m\rangle$, we can evaluate the rotation matrix as:

$$\begin{aligned} R(\boldsymbol{\xi})|j,m\rangle &= \sum_{m'=-j}^{j} \mathscr{D}^{(j)}_{m',m}(\boldsymbol{\xi})|j,m'\rangle \\ \mathscr{D}^{(j)}_{m',m}(\boldsymbol{\xi}) &\equiv \langle j,m'|e^{-\frac{i}{\hbar}\mathbf{J}\cdot\boldsymbol{\xi}}|j,m\rangle. \end{aligned} \tag{2.97}$$

The matrix $\mathscr{D}^{(j)}_{m',m}(\boldsymbol{\xi})$ is a $(2j+1)\times(2j+1)$ matrix associated with the action of the rotation operator $R(\boldsymbol{\xi})$ on a subspace of angular momentum states with fixed j.

2.9.3 Irreducible operators

The action of an operator A on the quantum states $\{|\Psi\rangle\}$ can be represented by a matrix $A_{n,m}$ via its action of the basis states $|\psi_n\rangle$. In general, all the matrix elements will have non-zero values. However, sometimes the matrix possesses a structure similar to the one presented in Fig. 2.11: blocks of non-zero elements along the main diagonal, and zeros in all other places. If such a structure is maintained under rotations, we say that the operator A is "reducible": we can split the operator A into a sum of other operators A_i (each operating on a separate subset of the basis states $|\psi_n\rangle$) and this splitting does not change under rotations. Otherwise we say that A is irreducible [33].

We can classify the irreducible operators by the way they transform under rotations [see Eq. (2.96)].

Scalar operators. The first type is the scalar operator – it is invariant under rotation:

$$A' = R^{\dagger}(\boldsymbol{\xi})AR(\boldsymbol{\xi}) = A. \tag{2.98}$$

A scaler operator is known also as a rank (0) operator and is labeled $T^{(0)}$. An important example of a scalar operator is the Hamiltonian of an isolated atom (that does not interact

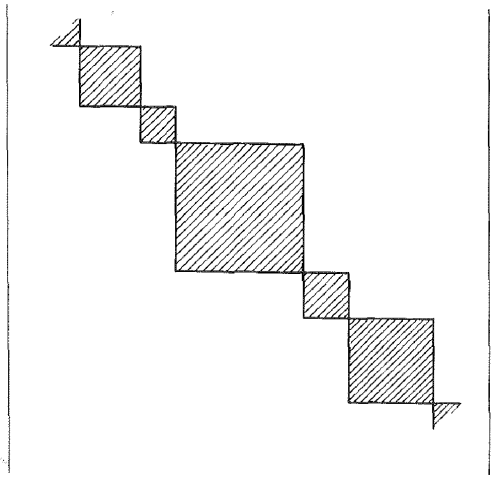

Figure 2.11: Schematic structure of a reducible matrix (from Fano and Racah [33])

with external fields).

Vector operators. Vector operators, or rank (1) operators, have 3 components $\{T_-^{(1)}, T_0^{(1)}, T_+^{(1)}\}$ and transforms under rotation in the same way as the three components of the position operator in the spherical basis ($\{r_-, r_0, r_+\}$).

In general, an irreducible operator of rank (κ) is a set of $2\kappa + 1$ operators, labeled T_q^κ, that transforms under rotation in the same way that the states $\{|j, m\rangle\}$ (with $j = \kappa$) transform:

$$R(\boldsymbol{\xi}) T_q^{(\kappa)} R^\dagger(\boldsymbol{\xi}) = \sum_{q'=-\kappa}^{\kappa} T_{q'}^{(\kappa)} \mathscr{D}_{q',q}^{(\kappa)}(\boldsymbol{\xi}). \tag{2.99}$$

2.9.4 The Wigner-Eckart theorem

The Wigner-Eckart theorem is an important tool when we wish to evaluate the matrix element of an irreducible tensor operator component T_q^κ between two angular momentum states $\langle \alpha, F, m_F|$ and $|\alpha', F', m'_F\rangle$ (α', α, stands for all non-angular-momentum quantum numbers). This theorem states that [46]:

$$\langle \alpha, F, m_F | T_q^{(\kappa)} | \alpha', F', m'_F \rangle = (-1)^{2\kappa} \langle \alpha, F || T^{(\kappa)} || \alpha', F' \rangle \langle F, m_F | F', \kappa, m'_F, q \rangle, \tag{2.100}$$

where

$$\langle \alpha, F || T^\kappa || \alpha', F \rangle \tag{2.101}$$

is the so called "reduced" matrix element, independent of m_F, m'_F and q, and the last expression is the same CG coefficient that appears in the addition of two angular momentum states (see Sec. 2.8.1). Basically, the Wigner-Eckart theorem splits the matrix element of a component of an irreducible tensor operator into two parts:

- A "physical", or "reduced", part that is common to all the possible values of m_F, m'_F and q.
- A purely "geometrical" part that depends on m_F, m'_F and q via the CG coefficients.

The irreducible tensor operator component T^{κ}_{q} transforms under rotation in a way that is similar to the angular momentum state $|F,m\rangle$ ($\kappa = F, q = m$), so that evaluating the matrix element in Eq. (2.100) is similar to combining two angular momenta $|F,m\rangle$ and $|\kappa,q\rangle$ into the final state $|F',m'\rangle$, which explains the appearance of the CG coefficient in Eq. (2.100).

2.10 The rubidium atom

For more than 60 years, alkali metal vapors [lithium (Li), sodium (Na), potassium (K), rubidium (Rb), and cesium (Cs)] have been used intensively both in basic research and in metrology applications, such as atomic clocks, magnetometers and gyroscopes. The alkali atoms are "hydrogen-like" atoms – they have just one electron in their outer shell, thus simplifying the calculation of their Hamiltonians, eigenvalues, eigenstates and their interactions with external fields. They have electric dipole transitions in the optical domain and consequently transitions may be easily excited using commercial. light sources such as diode lasers. In addition, they all have relatively high vapor pressures at room temperature, so there is no problem to maintain a workable vapor concentration. In the work described in this thesis we used ^{87}Rb, a meta-stable isotope of rubidium (half-life of 4.9×10^{10} years). Naturally occurring rubidium contains $\sim 28\%$ ^{87}Rb, while the rest is mostly ^{85}Rb. A detailed description of the properties of ^{87}Rb and its first excited levels is presented in [45]. We will review here some of the relevant details.

The rubidium atom has 37 electrons, of which 36 fill the first four shells, with the single remaining electron in the fifth shell (principle quantum number $n = 5$). The other operators and their quantum numbers specifying the state of the ^{87}Rb atom are:

- $\mathbf{L}$ – The orbital angular momentum operator of the electron, with eigenvalues (quantum numbers) of $\mathbf{L}^2$: $\hbar^2 L(L+1)$; $L = 0, 1, 2 \ldots$. An atom in a state $L = 0$ is denoted "S", an atom in a state $L = 1$ is denoted "P" and an atom in a state $L = 2$ is denoted "D". The operator L_z, the projection of $\mathbf{L}$ on the quantization axis, has eigenvalues $m_L = -L, -L+1, \ldots, L$.

- $\mathbf{S}$ – The spin angular momentum operator of the electron, with a single eigenvalue (quantum number) of $\mathbf{S}^2$: $\hbar^2 S(S+1)$; $S = 1/2$. The operator S_z, the projection of $\mathbf{S}$ on the quantization axis, has two eigenvalues: $m_S = \pm 1/2$.

- $\mathbf{J}$ – The total angular momentum operator of the electron: $\mathbf{J} = \mathbf{L} + \mathbf{S}$, with eigenvalues (quantum numbers) of $\mathbf{J}^2$: $\hbar^2 J(J+1)$; $J = |L-S|, |L-S|+1, \ldots, L+S$. For a single electron, J will always be half-integer. The operator J_z, the projection of $\mathbf{J}$ on the quantization axis, has eigenvalues $m_J = -J, -J+1, \ldots, J$.

- $\mathbf{I}$ – The spin angular momentum operator of the nucleus. For ^{87}Rb, the eigenvalue (quantum number) of $\mathbf{I}^2$ is $\hbar^2 I(I+1)$; $I = 3/2$. The operator I_z, the projection of $\mathbf{I}$ on the quantization axis, has eigenvalues $m_I = -I, -I+1, \ldots, I$.

- $\mathbf{F}$ – The total angular momentum operator of the atom: $\mathbf{F} = \mathbf{J} + \mathbf{I}$, with eigenvalues (quantum numbers) of $\mathbf{F}^2$: $\hbar^2 F(F+1)$; $F = |I-J|, |I-J|+1, \ldots, I+J$. The operator

F_z, the projection of $\mathbf{F}$ on the quantization axis, has eigenvalues $m_F = -F, -F+1, \ldots, F$.

For the ground state of ^{87}Rb, denoted $5^2S_{1/2}$, we have $n = 5,\ L = 0,\ S = 1/2$ and $I = 3/2$. Due to the interaction of the nuclear spin I with the electronic spin S, the ground state is split to two sub-levels:

- $|F = 3/2 - 1/2 = 1\rangle$ (these two spins are anti-parallel)
- $|F = 3/2 + 1/2 = 2\rangle$ (these two spins are parallel)

This is the hyperfine splitting. Both $|F = 1\rangle$ and $|F = 2\rangle$ have the same parity, so there is no electric dipole transition between them. We can induce $|F = 1\rangle \leftrightarrow |F = 2\rangle$ transitions via the magnetic dipole [see Eqs: (2.57), (2.58)] using ∼6.834 GHz microwave radiation. Each of the states $|F = 1\rangle$, $|F = 2\rangle$ has $2F + 1$ Zeeman, or magnetic, sub-level denoted $|F, m_F\rangle$. With no external fields, all the Zeeman sub-levels of a particular $|F\rangle$ state are degenerate (all have the same energy). When the atom is subjected to a direct current (DC) magnetic field, these sub-levels split (see Sec. 2.10.2).

The lowest-energy dipole-allowed transition is from the S ($|L = 0\rangle$) orbital angular momentum state to the P ($|L = 1\rangle$) state. Here, too, we have two options for the value of J: either $J = 1/2$ (the orbital and spin angular momentum of the electron are anti-parallel), or $J = 3/2$ (the orbital and spin angular momentum of the electron are parallel). This is the fine splitting:

- In the first case we get the $5^2S_{1/2} \leftrightarrow 5^2P_{1/2}$, known as the D1 transition, induced by 795nm light.
- In the second case we get the $5^2S_{1/2} \leftrightarrow 5^2P_{3/2}$ transition, known as the D2 transition, induced by 780nm light.

The state $5^2P_{1/2}$ is split into two hyperfine states, typically denoted by F': $|F' = 1'\rangle$ and $|F' = 2'\rangle$. Similarly, the state $5^2P_{3/2}$ is split into four hyperfine states: $|F' = 0'\rangle$, $|F' = 1'\rangle$, $|F' = 2'\rangle$ and $|F' = 3'\rangle$. Similar to the ground states, each of these F' states is further split into $2F' + 1$ Zeeman sub-levels. Diagrams of the D1 and D2 transitions for ^{87}Rb [45] are presented in Figs. 2.12 and 2.13.

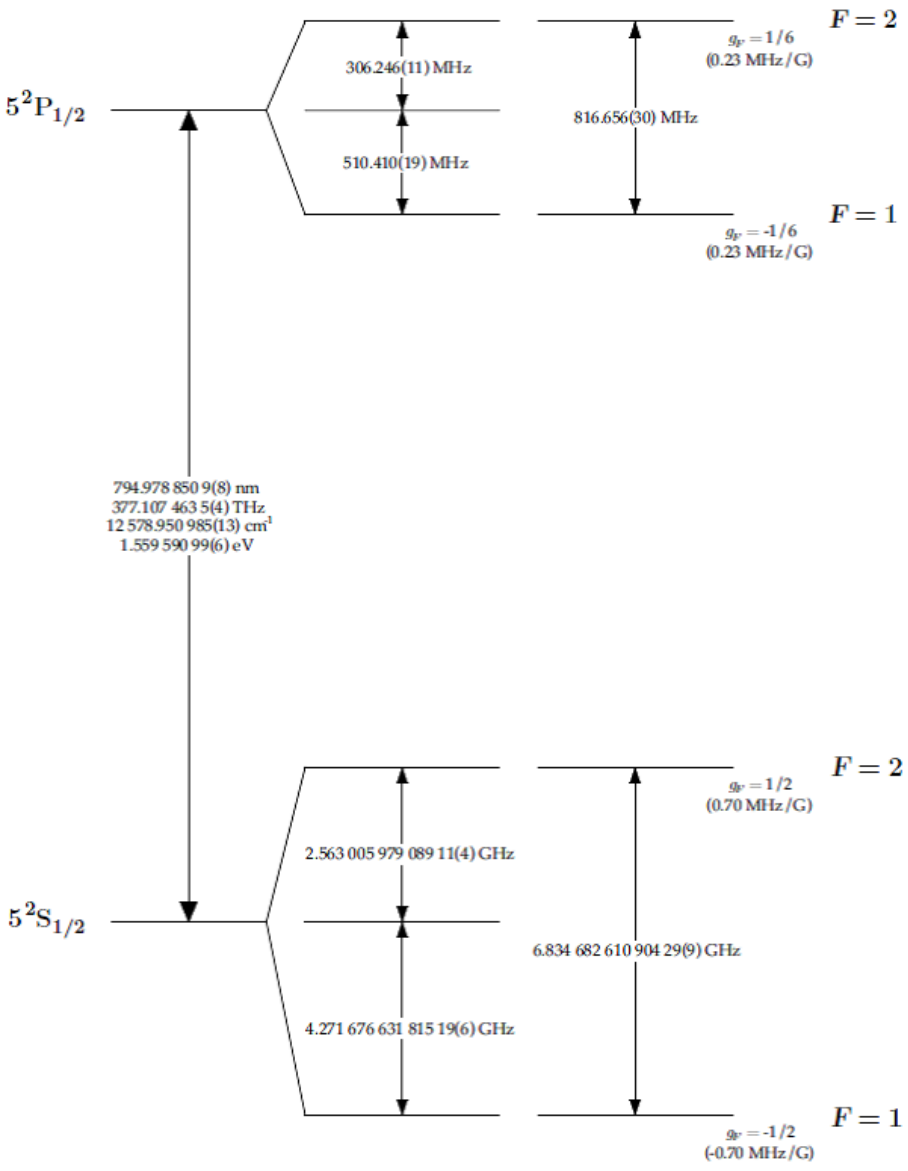

Figure 2.12: ^{87}Rb D1 transition hyperfine structure, with frequency splittings between the hyperfine energy states (taken from [45]). The relative hyperfine shifts are shown to scale within each hyperfine manifold (energy level spacings in the different manifolds and the optical spacing are on different scales). The approximate Landé g_F factors for each state are also given, with the corresponding Zeeman splittings between adjacent magnetic sub-levels.

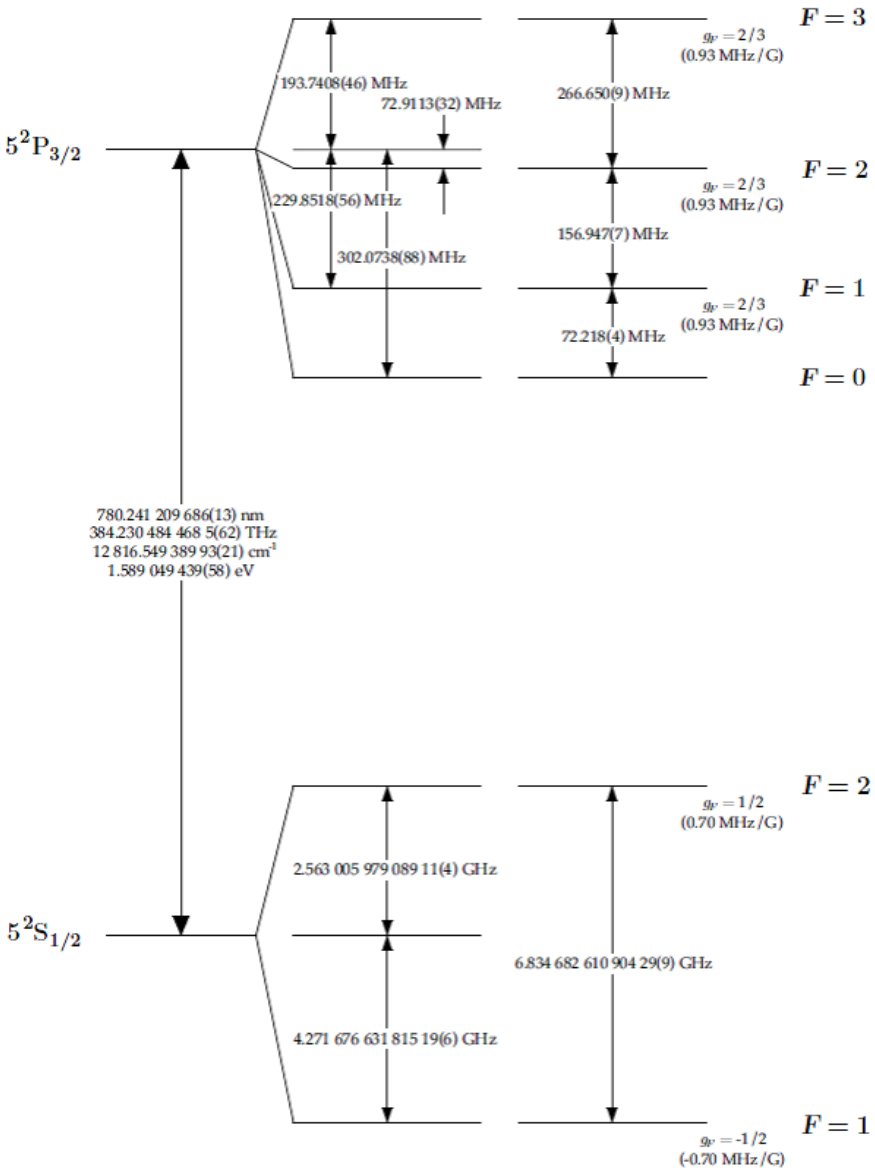

Figure 2.13: ^{87}Rb D2 transition hyperfine structure, with frequency splittings between the hyperfine energy states (taken from [45]). The relative hyperfine shifts are shown to scale within each hyperfine manifold (energy level spacings in the different manifolds and the optical spacing are on different scales). The approximate Landé g_F factors for each state are also given, with the corresponding Zeeman splittings between adjacent magnetic sub-levels.

2.10.1 Doppler broadening

Atomic levels have natural line width (typically noted Γ – see Fig. 2.5) that are related by the uncertainty principle to the level's lifetime. This in turn broadens transitions to this level. Previously we discussed power broadening (see Fig. 2.3); Collisional (pressure) broadening and shifts will be discussed in Sec. 4.1. Here we discuss Doppler broadening, and in particular some of its consequences that will be used in the next chapters.

Let us examine the interaction of near-resonant light at frequency $f_{\rm L}$ with an ^{87}Rb vapor at a temperature T. We assume that the light frequency is near the D2 transition ($f_{\rm L} \sim 384.230\,$THz, see Fig. 2.13). The atoms (of atomic mass m) are in thermal equilibrium, with average (root mean square (RMS)) speed $v_{\rm RMS} = \sqrt{3k_{\rm B}T/m}$ ($k_{\rm B}$ is the Boltzmann constant). For ^{87}Rb at room temperature, $v_{\rm RMS} \approx 300\,$m/s. If an atom has a velocity component v_k parallel to the $\mathbf{k}$ vector of the light, then $f_{\rm rest}$ (the frequency of the light in the rest frame of the atom) is Doppler shifted by $\delta f = f_{\rm L} v_k/c$, so that $f_{\rm rest} = f_{\rm L} + \delta f$. Using the average speed $v_{\rm RMS}$ above, we obtain a Doppler shift of $\delta f_{\rm max} \approx \pm 380\,$MHz.

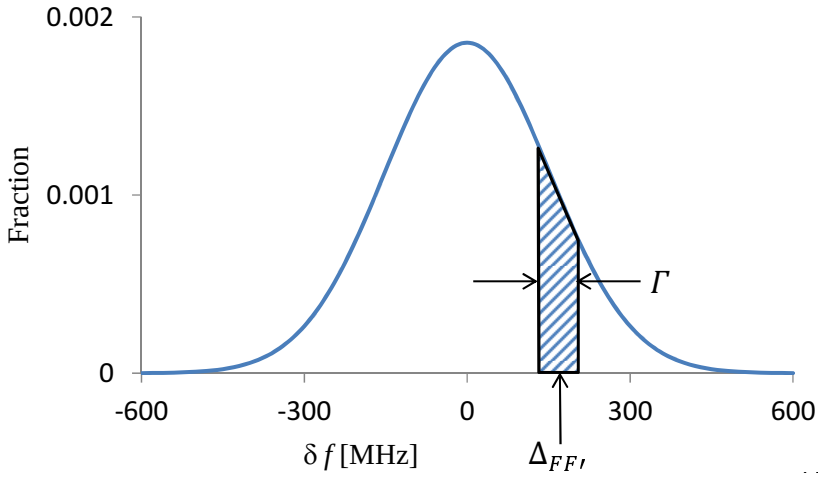

Figure 2.14: Estimation of the fraction of Rb atoms that interact with a light beam via a specific $|F, m_F\rangle \rightarrow |F', m'_F\rangle$ transition (light frequency $f_{\rm L}$, transition frequency $f_{FF'}$, natural linewidth Γ). The quantity $\Delta_{FF'} = f_{FF'} - f_{\rm L}$ is the detuning of laser light from the transition frequency, and the solid curve is a plot of the fraction of room temperature ^{87}Rb atoms that "see" in their rest frame the light Doppler shifted by $\delta f = f_{\rm rest} - f_{\rm L}$. The hatched area marks the fraction of atoms that interact with the light (see text).

One consequence of the Doppler broadening is that only a fraction of the atoms interact with the light. Let us focus our attention on a specific $|F, m_F\rangle \rightarrow |F', m'_F\rangle$ transition (transition frequency $f_{FF'}$, natural linewidth Γ),and further assume that the atoms can absorb light only if its frequency in the atom's rest frame obeys $|f_{\rm rest} - f_{FF'}| \leq \Gamma/2$. The atoms are illuminated by a laser beam with frequency $f_{\rm L}$ which is detuned by $\Delta_{FF'} = f_{FF'} - f_{\rm L}$ from this resonance frequency. Only the fraction $p_{\rm int}$ of the vapor atoms having velocities which Doppler shift the light (in the atom's rest frame) by $\Delta_{FF'} - \Gamma/2 \leq \delta f \leq \Delta_{FF'} + \Gamma/2$ will interact with the laser beam (hatched area in Fig. 2.14). In the case where the Doppler standard deviation (given by $\sigma_{\rm D} = f_{FF'} \cdot \sqrt{k_{\rm B}T/mc^2}$) is much larger the natural linewidth

Γ, we can estimate this fraction as

$$p_{\text{int}} = \frac{1}{2}\int_{f_{FF'}-\Gamma/2}^{f_{FF'}+\Gamma/2} \frac{1}{\sqrt{2\pi}\sigma_{\text{D}}} \exp\left[-\frac{(f_{FF'}-f_{\text{L}})^2}{2\sigma_{\text{D}}^2}\right] df_{\text{L}} \approx \frac{\Gamma}{2\sqrt{2\pi}\sigma_{\text{D}}} \exp\left[-\frac{\Delta_{FF'}^2}{2\sigma_{\text{D}}^2}\right]. \quad (2.102)$$

Another consequence is the merging of several close resonances into one wide resonance unless their separation is much larger than 500 MHz (see Fig. 2.15).

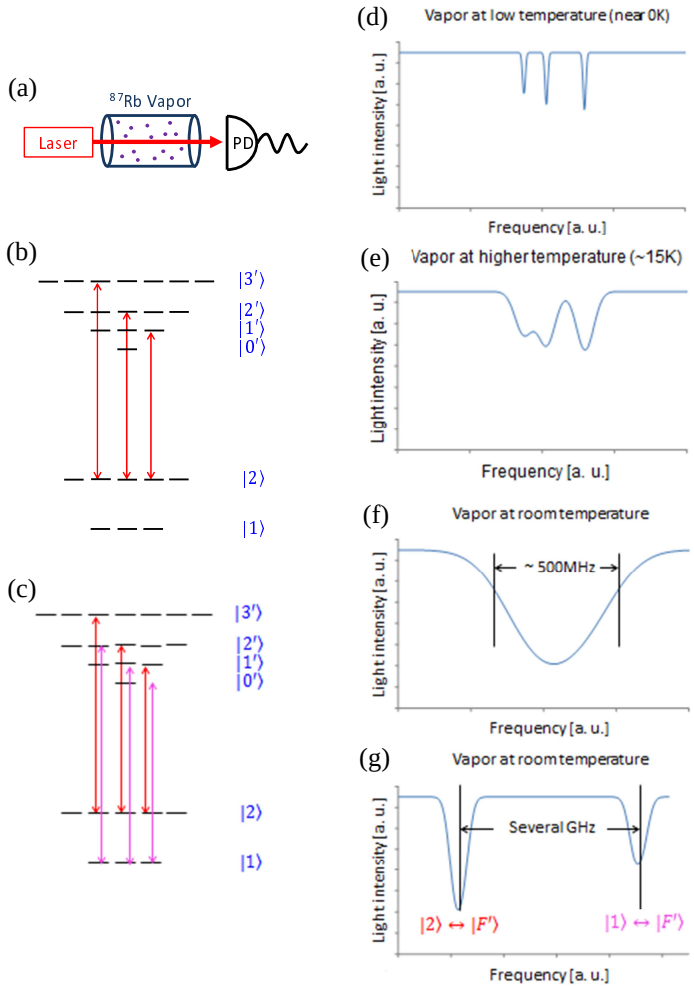

Figure 2.15: Doppler broadening of absorption spectra. (a) The measuring scheme. The laser light passes through the ^{87}Rb vapor, and its exit intensity is measured by a photodiode (PD). (b) Level diagram showing the 3 allowed transitions $|2\rangle \leftrightarrow |F'\rangle$ (in red). (c) Level diagram showing both the 3 allowed transitions $|2\rangle \leftrightarrow |F'\rangle$ (in red), and the additional 3 allowed transitions $|1\rangle \leftrightarrow |F'\rangle$ (in purple). (d-f) schematic plots (at different temperatures) of the exit intensity as the frequency is scanned across the three transitions (b), showing the broadening from three distinct absorption dips to one wide dip. (g) Schematic plot of the exit intensity as the frequency is scanned across the six transitions (c), where the separation between $|1\rangle$ and $|2\rangle$ is resolved, but the finer details are lost in the broadening.

2.10.2 ^{87}Rb interaction with DC magnetic fields

When a ^{87}Rb atom is subjected to a DC magnetic field $\mathbf{B}$, the direction of the magnetic field is chosen as the quantization axis, or the z axis of the atomic coordinate system. Thus the magnetic dipole interaction term V^{M1} [see Eq. (2.58)] can be written as:

$$V^{\mathrm{M1}} = \boldsymbol{\mu} \cdot \mathbf{B} = \mu_B(g_L L_z + g_S S_z + g_I I_Z)|\mathbf{B}| \tag{2.103}$$

since $|\mathbf{B}| = B_z$.

The linear Zeeman shift. When the magnetic field is small, and the resulting magnetic interaction is small compared to the hyperfine splitting ($\sim$ 6.8 GHz), we can assume that $\mathbf{F} = \mathbf{I} + \mathbf{J}$ is a constant of motion, and approximate V^{M1} as:

$$V^{\mathrm{M1}}_{F,m_F} = \mu_B g_F m_F |\mathbf{B}|, \tag{2.104}$$

where μ_B is the Bohr magneton, g_F is the Landé g-factor of the angular momentum state F (see Fig. 2.12 and Fig. 2.13 for the values of g_F), and m_F is the magnetic quantum number. For the ground state of ^{87}Rb we have approximately [59]:

$$\frac{V^{\mathrm{M1}}_{F,m_F}}{\hbar} \approx 2\pi \times 0.7\mathrm{MHz/G}. \tag{2.105}$$

The Briet-Rabi formula. In general, a more accurate calculation of the Zeeman shift involves numerical diagonalization of the interaction Hamiltonian [45]. However, for $J = 1/2$ and any value of I and $|\mathbf{B}|$, the Breit-Rabi formula provides an accurate value of the Zeeman shift [59] (here we express the energy in units of frequency):

$$\begin{aligned} E_{F,m_F} &= -\frac{E_{hfs}}{2(2I+1)} + \frac{\mu_B}{h} g_I m_F |\mathbf{B}| \pm \frac{E_{hfs}}{2}\left(1 + \frac{4m_F\xi}{2I+1} + \xi^2\right)^{1/2}, \\ \text{where} \qquad \xi &= \frac{\mu_B(g_J - g_I)|\mathbf{B}|}{h \cdot E_{hfs}} \end{aligned} \tag{2.106}$$

and where E_{F,m_F} is the energy, in Hz, of the $|F, m_F\rangle$ state relative to a zero set at $E_{hfs}[1 + 1/(2I+1)]/2$, the $\pm$ sign is for $F = I \pm 1/2$, and E_{hfs} is the hyperfine splitting in units of frequency. For the calculations of ^{87}Rb energy level data presented later in this work, we use the following values: $I = 3/2$, $J = 1/2$, $E_{\mathrm{hfs}} = 6,834,682,610.904$Hz, $g_I = -0.0009951414$, $g_J = 2.00233113$, $\mu_B = 9.27400915 \times 10^{-28}$J/G and $h = 6.62606896 \times 10^{-34}$Js.

2.11 Polarization moments

The density operator ρ and the related Liouville equation (see Sec. 2.3) are the tools we need when we describe an ensemble of atoms and its time evolution. Given some basis eigenstates $|\psi_n\rangle$ of the system's Hamiltonian, we can calculate the matrix elements of the density operator:

$$\rho_{n,n'} = \langle\psi_n|\rho|\psi_{n'}\rangle. \tag{2.107}$$

In general the density operator represented by $\rho_{n,n'}$ is a reducible operator in the sense defined in Sec. 2.9.3: it can be converted to a sum of irreducible operators – operators that transform under rotation as defined in Eq. (2.99). We will demonstrate this conversion by an example, using the ground state of ^{87}Rb.

The $5^2S_{1/2}$ ground state of ^{87}Rb is split into two hyperfine states: $|F=1\rangle$ and $|F=2\rangle$ (see Fig. 2.12). The former has 3 Zeeman sub-levels ($m_F=-1,0,1$) and the latter has 5 sub-levels ($m_F=-2,-1,0,1,2$). All in all, we have a set of 8 sub-levels $\{|F,m_F\rangle\}$ that are a basis of the ^{87}Rb ground state. If we use this basis to calculate the elements of the density matrix $\rho_{F,m_F;F'',m'_{F''}}$, we obtain an 8×8 matrix. In the absence of external fields, all the elements with $F\neq F''$ vanish. Thus the structure of this density matrix is similar to the structure presented in Fig. 2.11. We will have one 3×3 block for elements with $F=1$ ($\rho_{1,m_1;1,m'_1}$) and a second 5×5 block with $F=2$ ($\rho_{2,m_2;2,m'_2}$). This structure will not change under rotation, as the rotation operation cannot mix $|F=1\rangle$ and $|F=2\rangle$ states. So the first step in the conversion of the density matrix to an irreducible presentation is to treat each value of F separately.

Let us now focus our attention on an ensemble of atoms that are in the same $|F\rangle$ state. The density operator is defined as (see Sec. 2.3):

$$\rho=\sum_{\mathrm{m,m'=-F}}^{F}\rho_{\mathrm{m,m'}}|m\rangle\langle m'|, \tag{2.108}$$

where the Zeeman sub-levels $\{|m\rangle,\ m=-F,\ -F+1,\cdots,\ F\}$ are a basis of the states in this ensemble. The density matrix elements are then given by:

$$\rho_{m,m'}=\langle m|\rho|m'\rangle. \tag{2.109}$$

This form of the density matrix [Eq. (2.109)] does not have a clear split to irreducible "blocks" (as shown in Fig. 2.11). Such irreducible blocks represent irreducible operators (see Sec. 2.9.3). However, we can express the density operator as a sum of the irreducible operators $T_q^{(\kappa)}$, $\kappa=0,1,\ldots,2F$, $q=-\kappa,-\kappa+1,\ldots,\kappa$ (see [48], §3.7, §5.7 and [35] for the definitions and the properties of these operators and for the following representation of the density operator):

$$\rho=\sum_{\kappa=0}^{2F}\sum_{q=-\kappa}^{\kappa}\rho_q^{(\kappa)}T_q^{(\kappa)}. \tag{2.110}$$

The quantities $\rho_q^{(\kappa)}$ are linear combinations of the elements of the density matrix:

$$\rho_q^{(\kappa)}=\sum_{m,m'=-F}^{F}(-1)^{F-m}\langle F,m',F,-m|\kappa,q\rangle\rho_{m,m'}. \tag{2.111}$$

The $\langle F,m',F,-m|\kappa,q\rangle$ are the CG coefficients, used when two angular momenta are summed (see Sec. 2.8.1). If all the $\rho_q^{(\kappa)}$ are known, the density matrix elements can be calculated:

$$\rho_{m,m'}=\sum_{\kappa=0}^{2F}\sum_{q=-\kappa}^{\kappa}(-1)^{F-m}\langle F,m',F,-m|\kappa,q\rangle\rho_q^{(\kappa)}. \tag{2.112}$$

Thus, the quantities $\rho_q^{(\kappa)}$ serve as a good representation of the density operator ρ and the elements $\rho_{m,m'}$ of the density matrix.

In addition, for each κ, the quantities $\rho_q^{(\kappa)}$ have a direct physical meaning. The set $\{\rho_q^{(\kappa)}\}$, called the κth polarization moment (polarization moments (PM)), represent a physical property of the ensemble of atoms in a particular F state:

- For $\kappa = 0$ we have one element, $\rho_0^{(0)}$. This is the monopole moment, and it is directly related to the population of the state F: $\rho_0^{(0)} = (2F+1)^{-1/2} \times$ population in $|F\rangle$.
- For $\kappa = 1$ we have three elements, $\rho_{-1}^{(1)},\ \rho_0^{(1)},\ \rho_1^{(1)}$, forming a vector. This is the dipole moment, sometimes called "orientation". If we work in the spherical basis (see Sec. 2.9.1), then $\rho_{-1}^{(1)},\ \rho_0^{(1)},\ \rho_1^{(1)}$ are the three components of the macroscopic magnetic dipole moment of the ensemble.
- For $\kappa = 2$ we have five elements, $\rho_{-2}^{(2)},\ \rho_{-1}^{(2)}\ \rho_0^{(2)}\ \rho_1^{(2)},\ \rho_2^{(2)}$, forming a symmetric traceless tensor. This is the quadrupole moment, sometimes called "alignment".

The next moment is the octupole moment, etc.

Below we use the $F = 1$ state to demonstrate some polarization moments. For $F = 1$ we have 3 Zeeman sub-levels: $m_F = -1,\ 0,\ 1$. Thus the density matrix is:

$$\rho = \begin{pmatrix} \rho_{-1,-1} & \rho_{-1,0} & \rho_{-1,1} \\ \rho_{0,-1} & \rho_{0,0} & \rho_{0,1} \\ \rho_{1,-1} & \rho_{1,0} & \rho_{1,1} \end{pmatrix}. \tag{2.113}$$

Using Eq. (2.111) we first calculate the monopole moment:

$$\rho_0^{(0)} = \frac{1}{\sqrt{3}} \sum_{m=-1}^{1} \rho_{m,m} = \frac{1}{\sqrt{3}} \times \text{population in } |F=1\rangle \tag{2.114}$$

(since we know that $\rho_{m,m}$ is the population in the $|1,m\rangle$ sub-level).

Next we calculate the 3 components of the dipole moment, by substituting the values of the CG coefficients (with $F = 1$) in Eq. (2.111):

$$\begin{aligned} \rho_{-1}^{(1)} &= \frac{1}{\sqrt{2}}(\rho_{0,-1} + \rho_{1,0}) \\ \rho_0^{(1)} &= \frac{1}{\sqrt{2}}(-\rho_{-1,-1} + \rho_{1,1}) \\ \rho_1^{(1)} &= -\frac{1}{\sqrt{2}}(\rho_{-1,0} + \rho_{0,1}). \end{aligned} \tag{2.115}$$

Looking at $\rho_0^{(1)}$, the component parallel to the quantum axis z of the ensemble, we see that it is equal to the population of atoms in the $|m = 1\rangle$ sub-level (those with their magnetic moment aligned with z) minus the population of atoms in the $|m = -1\rangle$ sub-level (those with their magnetic moment aligned opposite to z). This is actually the net macroscopic z component of the magnetic moment of the ensemble.

In a similar way one can calculate the five components of the quadrupole moment $\rho_q^{(2)}$.

2.12 Light absorption by alkali atoms

In the next chapter we present our simplified light absorption model, which provides the theoretical basis for the discovery and calculation of the magic frequency (see Sec. 3.1). One of the main assumptions we use to construct the model is this: the absorption (= photon scattering rate) of near-resonant light by a vapor of alkali atoms is proportional to the square of the dipole matrix element. In other words, if the light is tuned near the frequency of some $|0\rangle \leftrightarrow |2\rangle$ electric dipole transition, then

$$\gamma_{\text{scat}} \propto |\langle 0|\hat{\epsilon} \cdot \mathbf{d}|2\rangle|^2 \tag{2.116}$$

where γ_{scat} is the photon scattering rate, $\hat{\epsilon}$ the polarization unit vector of the electric field of the light, $\mathbf{d} = -e\mathbf{r}_e$ is the electric dipole moment of the atom, e is the elementary charge and $\mathbf{r}_e$ is the position of the electron relative to the atomic center of mass. [Note: The value of γ_{scat} is a function of several other physical variables, but in this section we only investigate the validity of Eq. (2.116).]

We start this study by analyzing a two-state excerpt of the Λ system (Fig 2.5), as presented in Fig. 2.16 below for clarity.

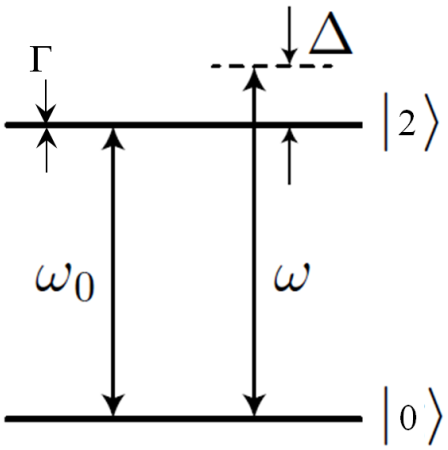

Figure 2.16: Two state system and a single light field with angular frequency ω. (excerpted from Fig. 2.5). The transition's angular frequency is ω_0, Δ is the detuning ($\Delta = \omega - \omega_0$) and Γ is the spontaneous emission rate.

The Rabi frequency for this system is (see Sec. 2.7.2)

$$\Omega = \frac{\langle 0|\hat{\epsilon} \cdot \mathbf{d}|2\rangle E_0}{\hbar}, \tag{2.117}$$

where E_0 is the amplitude of th electric field of the light.

To investigate the situation, we look at the system's density matrix ρ:

$$\rho = \begin{pmatrix} \rho_{00} & \rho_{02} \\ \rho_{20} & \rho_{22} \end{pmatrix}. \tag{2.118}$$

The optical Bloch equations for ρ are (see [60], §2.3):

$$\begin{aligned}
\frac{d\rho_{00}}{dt} &= \frac{i}{2}(\Omega^*\tilde{\rho}_{20} - \Omega\tilde{\rho}_{02}) + \Gamma\rho_{22} \\
\frac{d\rho_{22}}{dt} &= \frac{i}{2}(\Omega\tilde{\rho}_{02} - \Omega^*\tilde{\rho}_{20}) - \Gamma\rho_{22} \\
\frac{d\tilde{\rho}_{02}}{dt} &= -\frac{i\Omega^*}{2}(\rho_{22} - \rho_{00}) - (\gamma + i\Delta)\tilde{\rho}_{02} \\
\frac{d\tilde{\rho}_{20}}{dt} &= \frac{i\Omega}{2}(\rho_{22} - \rho_{00}) - (\gamma - i\Delta)\tilde{\rho}_{20},
\end{aligned} \tag{2.119}$$

where we use the rotating-frame transformation $\tilde{\rho}_{02} = \rho_{02}e^{-i\omega t}$, $\tilde{\rho}_{20} = \rho_{20}e^{i\omega t}$, Γ is the spontaneous emission rate (also termed the "longitudinal decay rate") and γ (typically $\gamma = \Gamma/2$, see [46], § 5.5) is the decoherence rate (also termed the "transverse decay rate").

The formal solution for $\tilde{\rho}_{20}$ is:

$$\tilde{\rho}_{20}(t) = \frac{i\Omega}{2}\int_0^t dt'[\rho_{22}(t') - \rho_{00}(t')]e^{-(\gamma - i\Delta)(t-t')}. \tag{2.120}$$

The integrand in Eq. (2.120) is very small except when $t - t' \sim 1/\gamma$. For the $5^2P_{1/2}$, and $5^2P_{3/2}$ excited states of ^{87}Rb, $1/\gamma \sim 50$ nanoseconds. In addition, $\rho_{22}(t')$ and $\rho_{00}(t')$ are almost constant during the short time interval $t - t' \sim 1/\gamma$, so for times t considerably larger than $1/\gamma \sim 50$ nanoseconds (say 200 nanoseconds, which is the integration time for a single data point in a 5MS/s A/D data acquisition card), we have:

$$\tilde{\rho}_{20}(t) \approx \frac{i\Omega}{2}[\rho_{22}(t) - \rho_{00}(t)]\int_0^t dt' e^{-(\gamma - i\Delta)(t-t')} \approx \frac{i\Omega}{2(\gamma - i\Delta)}[\rho_{22}(t) - \rho_{00}(t)] \tag{2.121}$$

since the integral at the lower limit is negligible. Similarly, we have:

$$\tilde{\rho}_{02}(t) \approx -\frac{i\Omega^*}{2(\gamma + i\Delta)}[\rho_{22}(t) - \rho_{00}(t)]. \tag{2.122}$$

Substituting Eqs. (2.121) and (2.122) into the first line in Eq. (2.119) we have:

$$\begin{aligned}
\frac{d\rho_{00}}{dt} - \Gamma\rho_{22} &= -\frac{|\Omega|^2}{4}\left(\frac{1}{\gamma - i\Delta} + \frac{1}{\gamma + i\Delta}\right)[\rho_{22}(t) - \rho_{00}(t)] = \\
&= \frac{\gamma|\Omega|^2}{2(\gamma^2 + \Delta^2)}[\rho_{00}(t) - \rho_{22}(t)].
\end{aligned} \tag{2.123}$$

The left side of Eq. (2.123) is equal to minus the photon scattering rate (neglecting stimulated emission – justified later): $d\rho_{00}/dt - \Gamma\rho 22 = -\gamma_{\rm scat}$. For low beam intensities ($\Omega \ll \Gamma$) the population in the excited state will not build up (due to the large spontaneous emission rate). Thus $\rho_{22}(t) \approx 0$, $\rho_{00}(t) \approx 1$. Substituting these values in Eq. (2.123) we see that $\gamma_{\rm scat} \propto |\Omega|^2$. In addition, the fact that $\rho_{22}(t) \approx 0$ justifies our assumption that we can neglect stimulated emission.

If the beam intensity is higher ($\Omega \approx \Gamma$) we cannot assume that $\rho_{22}(t) \approx 0$. At the onset of the light field we have $|0\rangle \leftrightarrow |2\rangle$ Rabi population oscillations, but these oscillations decay

to some steady-state population split (see [43], § 3.10). The decay time-constant τ is on the order of $1/\Gamma$, and for ^{87}Rb $\tau \approx 26\,\text{ns}$. Thus we can assume that the system converges to the steady-state some 100 ns after the onset of the light field, so that we can substitute 0 for the time derivatives on the left side of Eqs. (2.119), and get

$$\rho_{22} - \rho_{00} \approx -\frac{\gamma^2 + \Delta^2}{\Omega^2 + \gamma^2 + \Delta^2}. \tag{2.124}$$

or, using $\rho_{22} + \rho_{00} = 1$ and $\gamma_{\text{scat}} = \Gamma\rho_{22}$:

$$\gamma_{\text{scat}} \approx \frac{\Gamma\Omega^2}{2(\Omega^2 + \gamma^2 + \Delta^2)}. \tag{2.125}$$

For a light field detuned by no more than $\pm\Gamma/2$ from resonance, and noting that typically $\gamma \approx \Gamma/2$, we have

$$\gamma_{\text{scat}} \approx \frac{\Gamma\Omega^2}{2(\Omega^2 + \Gamma^2/2)}. \tag{2.126}$$

In Fig. 2.17 we plot γ_{scat} vs. Ω, and we note that the scattering rate of light by a two-state atom is proportional to the square of the Rabi frequency only for $\Omega < \Gamma/3$. On the other hand, for $\Omega > 3\Gamma \approx 18\,\text{MHz}$ we have saturation, and γ_{scat} is almost constant.

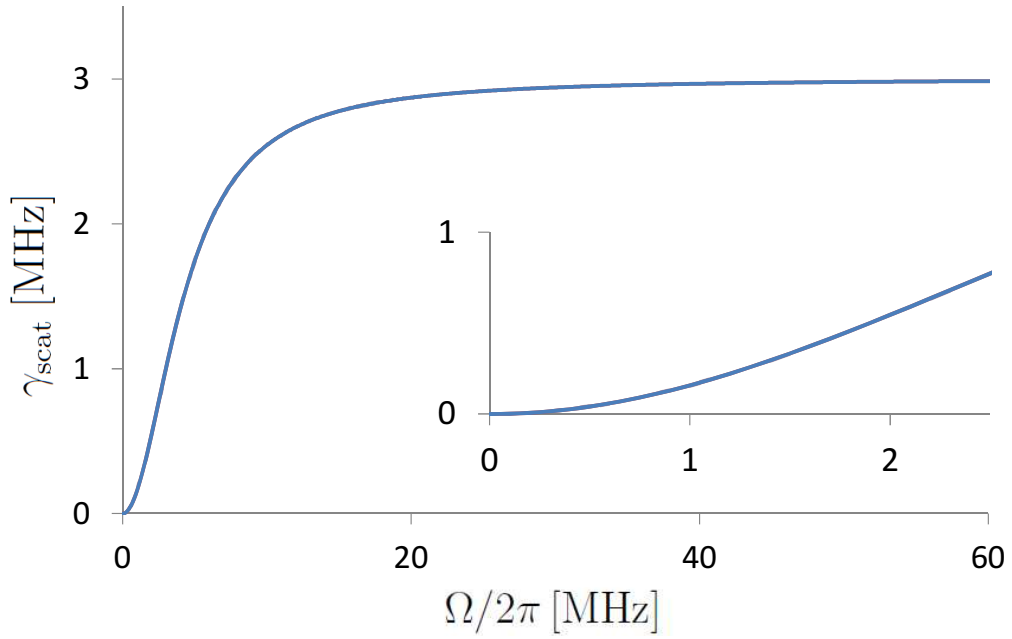

Figure 2.17: Photon scattering rate of near resonant light by a "vapor" of two-state atoms, as a function of the Rabi frequency [Eq. (2.126)]. Inset: zoom on the low Rabi frequency range, showing that approximately $\gamma_{\text{scat}} \propto \Omega^2$ for $\Omega < \Gamma/3 \approx 2\,\text{MHz}$.

So far, we have shown that for a "vapor" of two-state atoms, our assumption [Eq. (2.116)] is valid for light beams with an intensity that produces a Rabi frequency below $\Gamma/3$. In the next paragraphs we try to estimate the assumption's validity for real ^{87}Rb atoms

contained in a vapor cell at room temperature, possibly with some buffer gas or paraffin wall coating.

Three possible transitions. In general, the light can induce up to three types of transitions in real ^{87}Rb atoms: σ^+, σ^- and π. Equation (2.126) provides the scattering rate for each type separately, so for each of these transitions our assumption is valid up to a Rabi frequency of about 2 MHz. However, the intensity of the beam is the sum of the intensities of the components. Thus our assumption [Eq. (2.116)] may be valid for a beam with up to three times the intensity deduced based on Eq. (2.126).

Adding optical pumping. The next difference between the two-state system studied above and real ^{87}Rb atoms is that some of the atoms that are excited to the upper state (state $|2\rangle$, Fig. 2.16) emit photons that relax them to states other then $|0\rangle$. Consequently, we have optical pumping to other hyperfine ground states and sub-levels of the atom. Some of these atoms will be pumped to a state where the beam's frequency is too far detuned for them to be exited again – These atoms are "lost" from the two-state system. Shore ([43], § 3.10) provides a treatment of a two-state system with loss, and shows that for a given light intensity, the population of the upper state is lower when loss is present.

Optical pumping at room temperature. In Sec. 2.10.1 and Fig. 2.14 we show that as a result of the Doppler broadening, only a small fraction of the atoms interacts with a monochromatic laser beam at any given time. If, for example, we assume that:

- at the beginning of the process, all the ^{87}Rb atoms are at the $5^2S_{1/2}|F=2\rangle$ hyperfine ground state;
- the beam is tuned near the $5^2S_{1/2}|F=2\rangle \leftrightarrow 5^2P_{3/2}|F'=2\rangle$ transition;
- the Rabi frequency is on the order of 20 MHz,

then within 1 μs we have several 'excitation $\rightarrow$ spontaneous emission' cycles which lead to considerable optical pumping to the other hyperfine ground state ($5^2S_{1/2}|F=1\rangle$). However, due to the Doppler broadening only a small fraction of the atoms will be pumped, as most of the atoms do not interact with the light. With time, collisions change the velocities of the atoms, and a new group of atoms interacts with the light. As evident from out measurements (see Fig. 4.3) for a vapor cell with 7.5 Torr of Ne buffer gas, the Doppler broadening slows the optical pumping process by at least 2 orders of magnitude: considerable amount of pumping takes $\sim 100\,\mu$s.

All the above indicates that for an actual ^{87}Rb vapor, the range of light intensities for which $\gamma_{\rm scat} \propto |\langle 0|\hat{\epsilon}\cdot\mathbf{d}|2\rangle|^2$ (or equivalently, $\gamma_{\rm scat} \propto |\Omega|^2$) is much larger than the range calculated for a two-state system. Our demonstration of the magic frequency (see Ch. 5) verifies that this is the case.

Chapter 3

The magic frequency

When a near-resonant light passes through an alkali vapor, it is partially absorbed via the process of atomic excitation and subsequent spontaneous emission (at times this processes is also called scattering, although scattering can also be coherent). Figure 3.1 illustrates such a process with ^{87}Rb vapor. Clearly, in this case there is a quantitative relation between the total population in the $|F = 2\rangle$ hyperfine ground state and the absorption. However, in this example there are some 32 possible ways to excite the atom, each with a different rate that depends on several parameters, such as the vapor temperature, the frequency and polarization of the light beam, etc. Because of such differing rates, there has heretofore been no method to accurately deduce the hyperfine population from absorption measurements. This work aims to achieve just that.

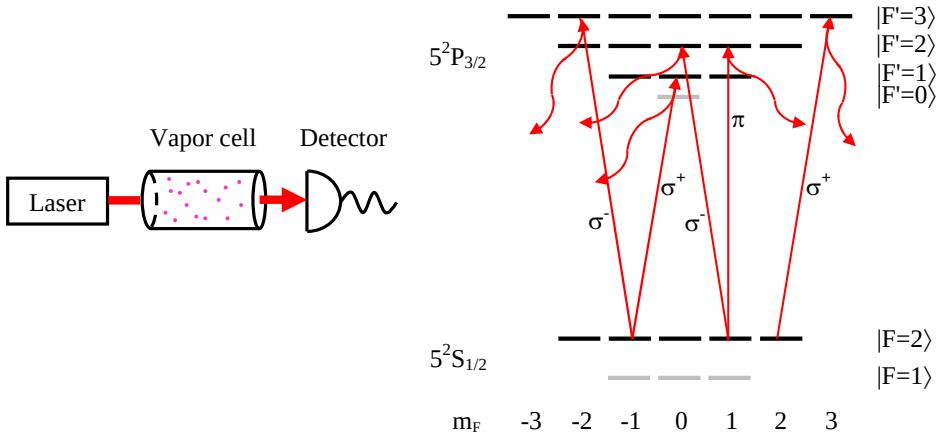

Figure 3.1: Multi-state absorption of a laser beam by room-temperature ^{87}Rb vapor (illustrating only 5 of the 32 possible transitions). Left: experimental configuration. A laser beam tuned near the $5^2S_{1/2}|F = 2\rangle \leftrightarrow 5^2P_{3/2}|F' = 2\rangle$ transition passes through the ^{87}Rb vapor cell and its exit intensity is measured by a detector. Right: the level diagram, showing the relevant hyperfine states and their Zeeman sub-levels (for completeness, other levels of each manifold are displayed in gray). 5 of the 32 possible transitions are indicated by red arrows. Transitions with $\Delta m_F = \pm 1$ are marked $\sigma^{\pm}$; π indicates $\Delta m_F = 0$ transitions. Wavy arrows represent spontaneous emission, which depending on the final state of the atom, may have one of the three polarizations.

3.1 Simplified absorption model

The first step toward our goal is to compare the light absorption rate by two groups of alkali atoms, each in a different Zeeman sub-level of the same hyperfine ground state F. Since we are comparing rates, we may simplify the mathematics by ignoring all common factors and build a model just for the *relative* absorption rates.

Let us examine the absorption of light at frequency $f_{\rm L}$ by an alkali vapor (atomic mass m, temperature T). Note that for any $|F, m_F\rangle \to |F', m'_F\rangle$ transition (of frequency $f_{FF'}$) the light is detuned by $\Delta_{FF'} = f_{FF'} - f_{\rm L}$.

Our model is based on the assumptions that the light absorption rate due to a specific $|F, m_F\rangle \to |F', m'_F\rangle$ transition is proportional to:

- the fraction of vapor atoms having the velocities that Doppler-shift the light by $\Delta_{FF'}$. This fraction is approximately proportional to $\exp[-(\Delta_{FF'}/\sigma_D)^2/2]$, with the Doppler standard deviation $\sigma_D = f_{FF'} \cdot \sqrt{k_B T/mc^2}$ (see Sec. 2.10.1).

- the square of the electric dipole matrix element (see Sec. 2.12). Working in the spherical basis (see Sec. 2.9.1), the Wigner-Eckart theorem (see Sec. 2.9.4) lets us write this matrix element as [45] (see also App. E.1):

$$\begin{aligned}&\langle F, m_F|er_q|F', m'_F\rangle = \\ &\langle J\|e\mathbf{r}\|J'\rangle(-1)^{F'+J+1+I}\sqrt{2J+1}\sqrt{2F'+1}\begin{Bmatrix} J & J' & 1 \\ F' & F & I\end{Bmatrix}\langle F, m_F|F', 1, m'_F, q\rangle,\end{aligned} \tag{3.1}$$

  where $q = -1, 0, 1$ is the spherical basis index, $\langle J\|e\mathbf{r}\|J'\rangle$ is the reduced matrix element, J - the total electron angular momentum number, I - the nuclear spin number, the curly brackets hold the Wigner's $6J$ symbol, and the last factor is the Clebsch-Gordan (CG) coefficient.

- the intensity of the relevant light component $|E_q|^2$.

Based on these assumptions, we define $\Gamma^{rel}_{m_F}$, the *relative* light absorption rate by atoms in a particular m_F sub-level as a sum (over all possible transitions) of products of the above mentioned fraction of atoms, the square of the matrix element, and the intensity of the light component related to each of these transitions:

$$\Gamma^{rel}_{m_F} \equiv \sum_{F'=F-1}^{F'=F+1} e^{-\frac{1}{2}\left(\frac{\Delta_{FF'}}{\sigma_D}\right)^2}(2F'+1)\begin{Bmatrix} J & J' & 1 \\ F' & F & I\end{Bmatrix}^2 \sum_{q=-1}^{q=1}|E_{-q}|^2\langle F, m_F|F', 1, m'_F, q\rangle^2, \tag{3.2}$$

where we sum first over all the allowed transitions ($\Delta F = 0, \pm 1$) from a particular hyperfine ground state F, and then over the three components q of the light's electric field, corresponding (in the spherical basis) to the three possible transition types (π, $\sigma^{\pm}$) from a given $|F, m_F\rangle$ sub-level. Since we are interested only in *relative* light absorption rates, we ignore all factors in the electric dipole matrix element [Eq. (3.1)] that are independent of m_F, m'_F and F'. We also ignore the natural line width, the laser line width and the Zeeman splitting, as these are all much smaller than the Doppler broadening; for cases in which the pressure shift

and broadening are significant (e.g. in vapor cells containing buffer gas), we would modify the transition frequencies $f_{FF'}$ with the relevant shifts [61] and replace the Doppler term in Eq. (3.2) with the appropriate Voigt function [62].

The normalized spherical components E_q ($|\mathbf{E}|^2 = 1$) of the light's electric field are evaluated in a coordinate system where $\hat{e}_0$ is in the direction of the DC magnetic field $\mathbf{B}$ (the quantization axis). We call this system the "atomic coordinate" or "atomic frame".

In the lab we typically control and evaluate the components of the light's electric field in a coordinate system where $\hat{e}_0$ (or $\hat{e}_z$, if we are using Cartesian coordinates) is parallel to the $\mathbf{k}$ vector of the light. We call this coordinate system the "light coordinate" or "light frame". Thus, we need to transform the components of the light from the light coordinate system to the atomic one before we can substitute them in Eq. (3.2).

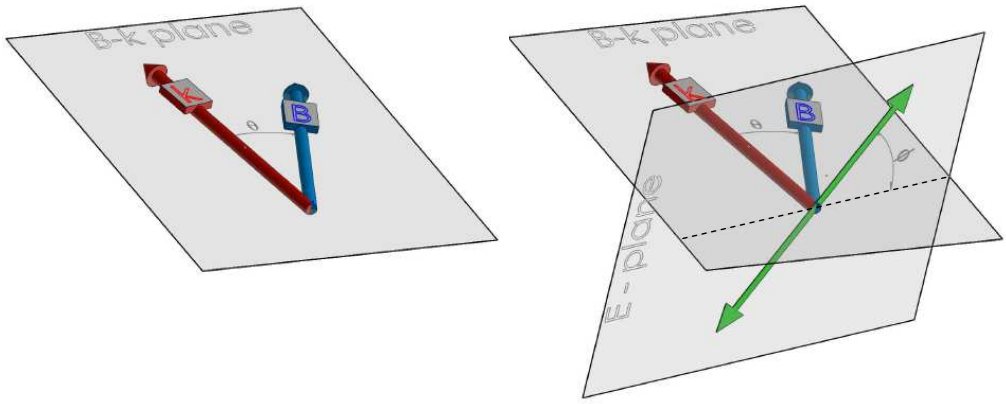

Figure 3.2: Relation between the light's $\mathbf{k}$ vector, the DC magnetic field $\mathbf{B}$ and the electric field $\mathbf{E}$ of the light. Left: the light's $\mathbf{k}$ vector and the DC magnetic field $\mathbf{B}$ define the B-k plane, and θ is the angle between them. Right: in addition to $\mathbf{k}$ and $\mathbf{B}$, we show the E-plane – a plane perpendicular to $\mathbf{k}$ – in which the light's electric field oscillates. The dashed line indicates the intersection of the B-k and E planes, and the green arrow indicates the direction of the oscillating electric field of linearly polarized light. The angle ϕ is measured in the E-plane between the dashed intersection line and the green arrow.

Figure 3.2 presents the relation between the light's $\mathbf{k}$ vector, the DC magnetic field $\mathbf{B}$ and the electric field $\mathbf{E}$ of the light. We use this figure to illustrate the relation between the two coordinate systems. The $\hat{e}_z^{\mathrm{L}}$ unit vector (the superscript "L" indicates the light coordinate system) is parallel to $\mathbf{k}$, and without loss of generality we choose $\hat{e}_x^{\mathrm{L}}$ to be in the B-k plane. Thus, $\hat{e}_y^{\mathrm{L}}$ is perpendicular to the B-k plane. The $\hat{e}_z^{\mathrm{A}}$ unit vector (the superscript "A" indicates the atomic coordinate system) is parallel to $\mathbf{B}$ (the quantization axis) and without loss of generality we choose $\hat{e}_x^{\mathrm{A}}$ to be in the B-k plane. Thus, $\hat{e}_y^{\mathrm{A}}$ is also perpendicular to the B-k plane. Since both $\hat{e}_y^{\mathrm{A}}$ and $\hat{e}_y^{\mathrm{L}}$ are perpendicular to the B-k plane, they are parallel to each other and we can transform any vector from one system to the other by a rotation $\mathrm{R_y}(\pm\theta)$ around the common y axis.

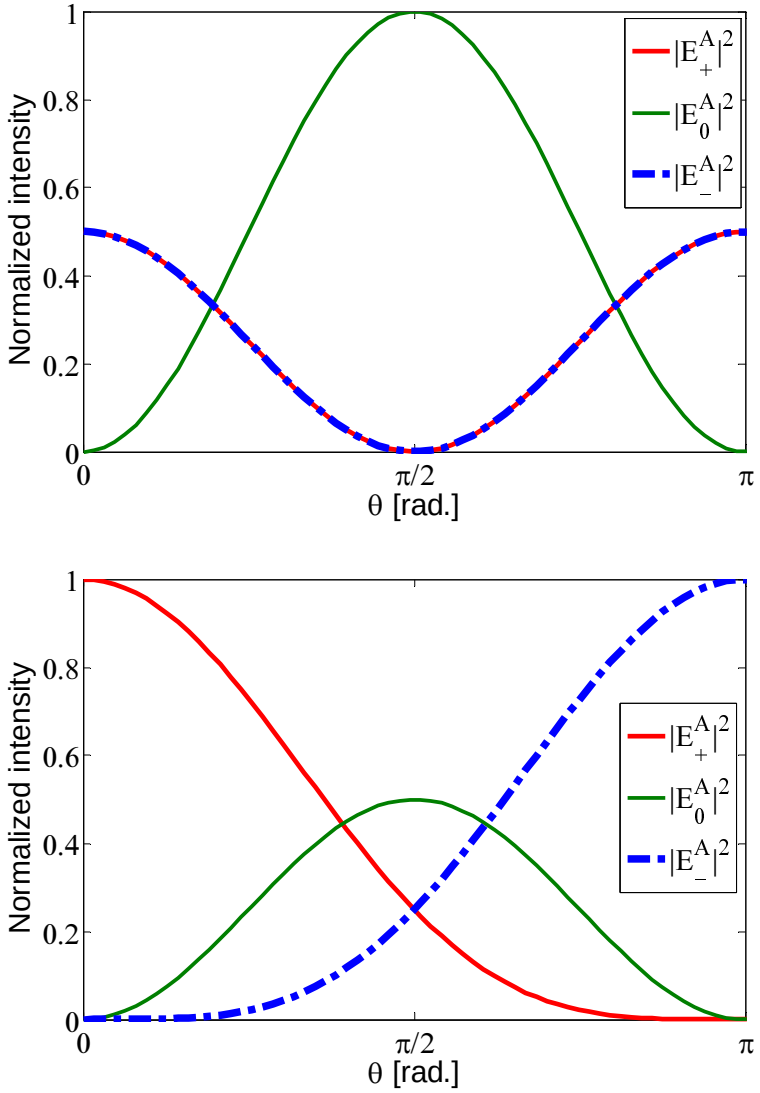

Figure 3.3: Normalized ($|\mathbf{E}^A|^2 = 1$) intensity components of the light's electric field in the atomic spherical basis as a function of the angle θ between $\mathbf{B}$ and $\mathbf{k}$ with $\phi = 0$ (Fig. 3.2). Top: components of light that is linearly polarized in the light coordinate system. Note that $|E^A_+|^2 = |E^A_-|^2$, and that there are two values of θ for which all three components are equal. Bottom: components of light that is circularly (+) polarized in the light coordinate system.

The light's electric field vector in the light coordinate system, $\mathbf{E}^{\mathrm{L}}$, may be specified either in the Cartesian basis or in the spherical basis, but $\mathbf{E}^{\mathrm{A}}$ should be specified in the spherical basis so that we can substitute its components in Eq. (3.2). Thus, if $\mathbf{E}^{\mathrm{L}}$ is specified in the Cartesian basis we have:

$$\begin{pmatrix} E^{\mathrm{A}}_+ \\ E^{\mathrm{A}}_- \\ E^{\mathrm{A}}_0 \end{pmatrix} = U^{C\to s} R_y(\theta) \begin{pmatrix} E^{\mathrm{L}}_x \\ E^{\mathrm{L}}_y \\ E^{\mathrm{L}}_z \end{pmatrix}, \tag{3.3}$$

and if $\mathbf{E}^{\mathrm{L}}$ is specified in the spherical basis:

$$\begin{pmatrix} E_+^{\mathrm{A}} \\ E_-^{\mathrm{A}} \\ E_0^{\mathrm{A}} \end{pmatrix} = U^{C\to s} R_y(\theta) U^{s\to C} \begin{pmatrix} E_+^{\mathrm{L}} \\ E_-^{\mathrm{L}} \\ E_0^{\mathrm{L}} \end{pmatrix}, \tag{3.4}$$

where $R_y(\theta)$ is the rotation matrix and $U^{C\to s}$, $U^{s\to C}$ are the transformation matrices between the Cartesian and the spherical basis:

$$R_y(\theta) = \begin{pmatrix} \cos(\theta) & 0 & \sin(\theta) \\ 0 & 1 & 0 \\ -\sin(\theta) & 0 & \cos(\theta) \end{pmatrix}; \quad U^{C\to s} = \begin{pmatrix} -1/\sqrt{2} & i/\sqrt{2} & 0 \\ 1/\sqrt{2} & i/\sqrt{2} & 0 \\ 0 & 0 & 1 \end{pmatrix}, \quad U^{s\to C} = (U^{C\to s})^{-1} \tag{3.5}$$

In Fig. 3.3 we present the intensity components $|E_q^A|^2$ of the light's electric field in the atomic coordinate system for linearly polarized light and for circularly (+) polarized light (as seen in the light coordinate system) as a function of θ – the angle between the light's $\mathbf{k}$ vector and the DC magnetic field $\mathbf{B}$.

Note: in the next sections we will drop the superscripts A and L, and unless otherwise indicated, the components $|E_q|$ are evaluated in the atomic coordinate system.

3.2 Numerical study of the absorption model

The value of $\Gamma_{m_F}^{rel}$, the relative light absorption rate by atoms in a particular m_F sub-level [Eq. (3.2)], depends on several variables, as we detail below. For the reader's benefit, we repeat the definition:

$$\Gamma_{m_F}^{rel} \equiv \sum_{F'=F-1}^{F'=F+1} \exp\left[-\frac{\Delta_{FF'}^2}{2\sigma_{\mathrm{D}}^2}\right] (2F'+1) \begin{Bmatrix} J & J' & 1 \\ F' & F & I \end{Bmatrix}^2 \sum_{q=-1}^{q=1} |E_{-q}|^2 \langle F, m_F | F', 1, m'_F, q\rangle^2. \tag{3.6}$$

Beside the magnetic quantum number m_F, we have the quantum numbers F and I, which change from one alkali atom to the other (we are interested in the ground state for which $J = 1/2$, so that $F = I \pm 1/2$). The mass of the alkali atom and the vapor temperature enter $\Gamma_{m_F}^{rel}$ via the value of Doppler standard deviation σ_D (see Sec. 2.10.1). The polarization of the light, as well as the angle θ between the light's $\mathbf{k}$ vector and the DC magnetic field $\mathbf{B}$ affect the value of the components of light intensity $|E_q|^2$. The last variable is the light frequency f_{L}, which fixes the value of $\Delta_{FF'} = f_{FF'} - f_{\mathrm{L}}$ (see Sec. 2.10.1).

For the alkali atoms, the frequency f_{L} of the light that can drive transitions from a ground state F to an excited-state manifold is on the order of few hundreds of terahertz. On the other hand, the separation between the hyperfine states within the excited-state manifold is on the order of few hundreds of megahertz – six orders of magnitude smaller. For ease of presentation, we denote the light frequency by:

$$\Delta_{\mathrm{L}} = f_{\mathrm{L}} - f_{\mathrm{manifold}} \tag{3.7}$$

where f_{manifold} is the energy difference (in Hertz) between ground state F and the lowest hyperfine state in the excited manifold.

Plots of $\Gamma^{rel}_{m_F}(\Delta_{\rm L})$ for several alkali atoms are presented in Fig. 3.4. These plots are calculated for linearly polarized light exciting room temperature vapor, with both angles θ, ϕ (see Fig. 3.2) equal zero. Note that $\Gamma^{rel}_{m_F} = \Gamma^{rel}_{-m_F}$ [see Eq. (3.16) and the subsequent discussion]. One notices clearly that for each alkali vapor there is at least one frequency ($\Delta^{\rm M}_{\rm L}$) where all the $\Gamma^{rel}_{m_F}(\Delta^{\rm M}_{\rm L})$ rates are equal. Here we have an indication that these frequencies may possess special properties, and we label them the *magic frequencies*.

To further study the magic frequencies we define several functions of the relative absorption rate $\Gamma^{rel}_{m_F}$. The first one is $S_F(\Delta_{\rm L})$, which is the light absorption rate when the population is equally distributed amongst the $2F+1$ Zeeman sub-levels:

$$S_F(\Delta_{\rm L}) \equiv \frac{1}{2F+1}\sum_{m_F=-F}^{F}\Gamma^{rel}_{m_F}(\Delta_{\rm L}). \tag{3.8}$$

Since $S_F(\Delta_{\rm L})$ is the total absorption rate when all the Zeeman sub-levels are equally populated, there is no preferred direction, and $S_F(\Delta_{\rm L})$ should be independent of both θ and ϕ. We have studied the quantity $S_F(\Delta_{\rm L})$ numerically, and found that indeed this is the case. Thus it can serve as a figure of merit of the atom-light interaction strength at a given light frequency $\Delta_{\rm L}$.

A related value is $S^{\rm M}_F$:

$$S^{\rm M}_F = \max(S_F), \tag{3.9}$$

where max indicates the maximal value of S_F when varying the frequency Δ_L.

We use $S^{\rm M}_F$ to normalize the quantity $\Delta\Gamma_F$, defined below:

$$\Delta\Gamma_F \equiv \left[\max(\Gamma^{rel}_{m_F}) - \min(\Gamma^{rel}_{m_F})\right]/S^{\rm M}_F \quad (\text{max/min scan the } m_F \text{ space}). \tag{3.10}$$

The quantity $\Delta\Gamma_F$ is a measure of the maximal difference (span) between the relative absorption rates $\Gamma^{rel}_{m_F}$. Clearly, when $\Delta\Gamma_F = 0$, all the $\Gamma^{rel}_{m_F}$ are equal. A three-dimensional plot of $\Delta\Gamma_F$ as a function of $\Delta_{\rm L}$ and θ is presented in Fig. 3.5. This plot reveals that there are 4 lines in the $\Delta_{\rm L} - \theta$ plane along which $\Delta\Gamma_F = 0$.

Two of these lines, at $\theta = 0.62$ and at 2.53 rad, correspond to the values of θ at which the intensity of all the three components of the light are equal (see top right plot at Fig. 3.5). It has been known for a long time [45] that when all three light components are equal, the absorption of light by the atoms is independent of the Zeeman sub-level these atoms are in (see the discussion following Eq. (3.16) for a mathematical proof of this statement).

However, to the best of our knowledge, the existence of the other two lines, at frequencies $\Delta_{\rm L} = 385$ and -318 MHz for ^{87}Rb (or any similar lines for other alkali atoms), is shown here for the first time. For now, we will term the first one (at 385 MHz) the "upper magic frequency" and the second one the "lower magic frequency".

Next, we wish to analyze the dependence of the magic frequencies on the vapor temperature (the vapor temperature enters $\Gamma^{rel}_{m_F}$ and $\Delta\Gamma_F$ via the Doppler standard deviation $\sigma_{\rm D}$ – see Eq. (3.6) and Sec. 2.10.1). Figure 3.6 presents calculated values of both the "upper" magic frequency and the "lower" one as a function of the vapor temperature. Clearly, the "upper" magic frequency is almost independent of the temperature, while the "lower"

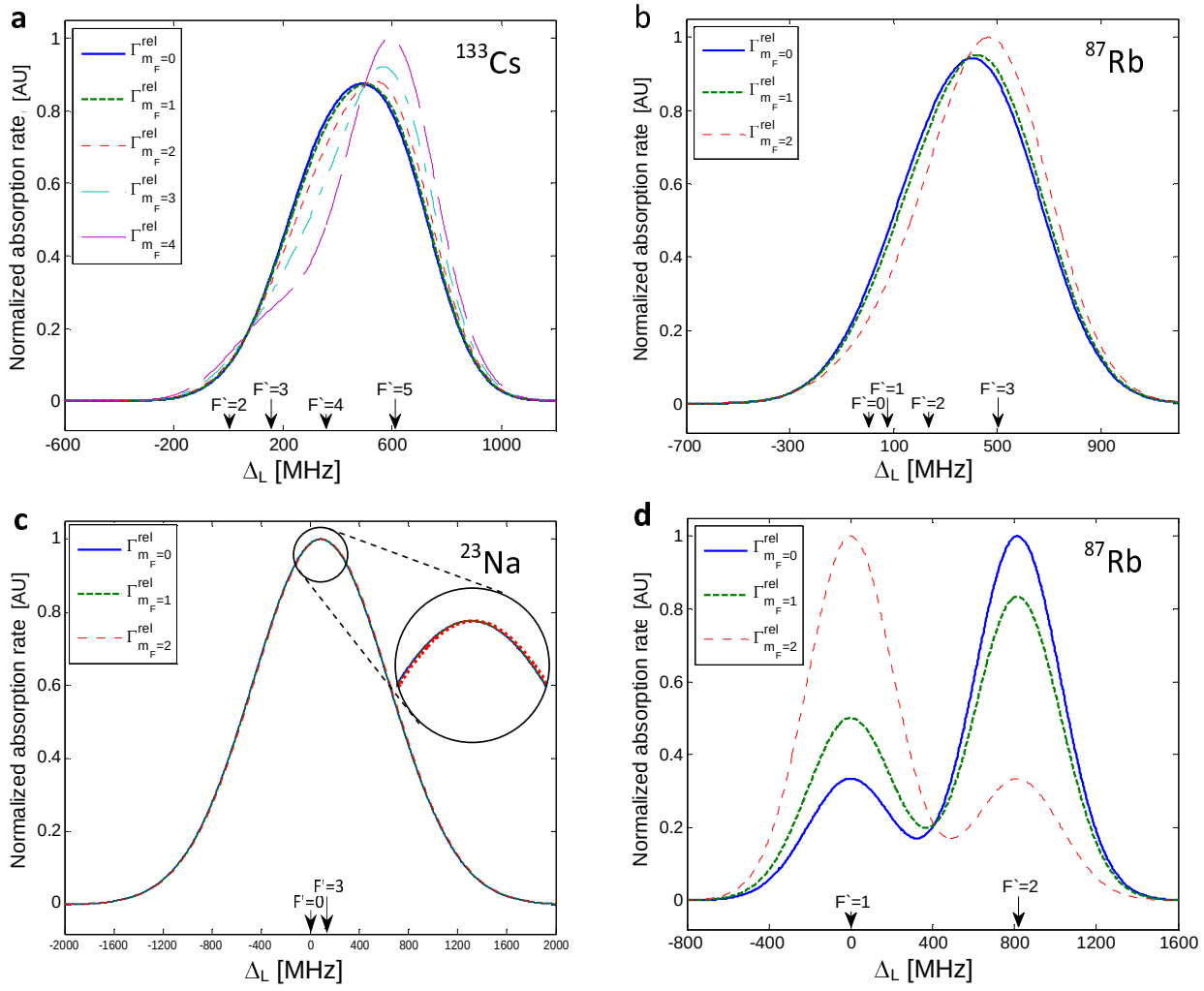

Figure 3.4: Plots of $\Gamma^{rel}_{m_F}$ (the relative absorption rate by atoms in a specific m_F state) as a function of the light frequency $\Delta_{\rm L}$ [see Eq. (3.7)] for different alkali atoms. These relative absorption rates are calculated using Eq. (3.6) for linearly polarized light exciting room temperature vapor. The values of both angles θ, ϕ (see Fig 3.2) is zero. The rates are normalized so that for each alkali atom $\max(\Gamma^{rel}_{m_F}) = 1$. Note that $\Gamma^{rel}_{m_F} = \Gamma^{rel}_{-m_F}$.
a. Five plots for ^{133}Cs: $6^2S_{1/2}|F=4\rangle \rightarrow 6^2P_{3/2}$ (D2 transition)
b. Three plots for ^{87}Rb: $5^2S_{1/2}|F=2\rangle \rightarrow 5^2P_{3/2}$ (D2 transition)
c. Three plots for ^{23}Na: $3^2S_{1/2}|F=2\rangle \rightarrow 3^2P_{3/2}$ (D2 transition; note the added zoom)
d. Three plots for ^{87}Rb: $5^2S_{1/2}|F=2\rangle \rightarrow 5^2P_{1/2}$ (D1 transition)
The frequencies of the transitions $F \rightarrow F'$ are marked with arrows on the horizontal axis. (For ^{23}Na, only $F'=0$ and $F'=3$ are shown explicitly, because the separation of the hyperfine states is too small to show all four). Note that as the separation between the excited F' states grows (relative to the Doppler broadening), so does the difference between the $\Gamma^{rel}_{m_F}$. However, there is always at least one frequency – the *magic frequency* $\Delta^M_{\rm L}$– where all the plots intersect (this intersection also exists for ^{23}Na even though the overlap of all three curves makes it difficult to see in this plot).

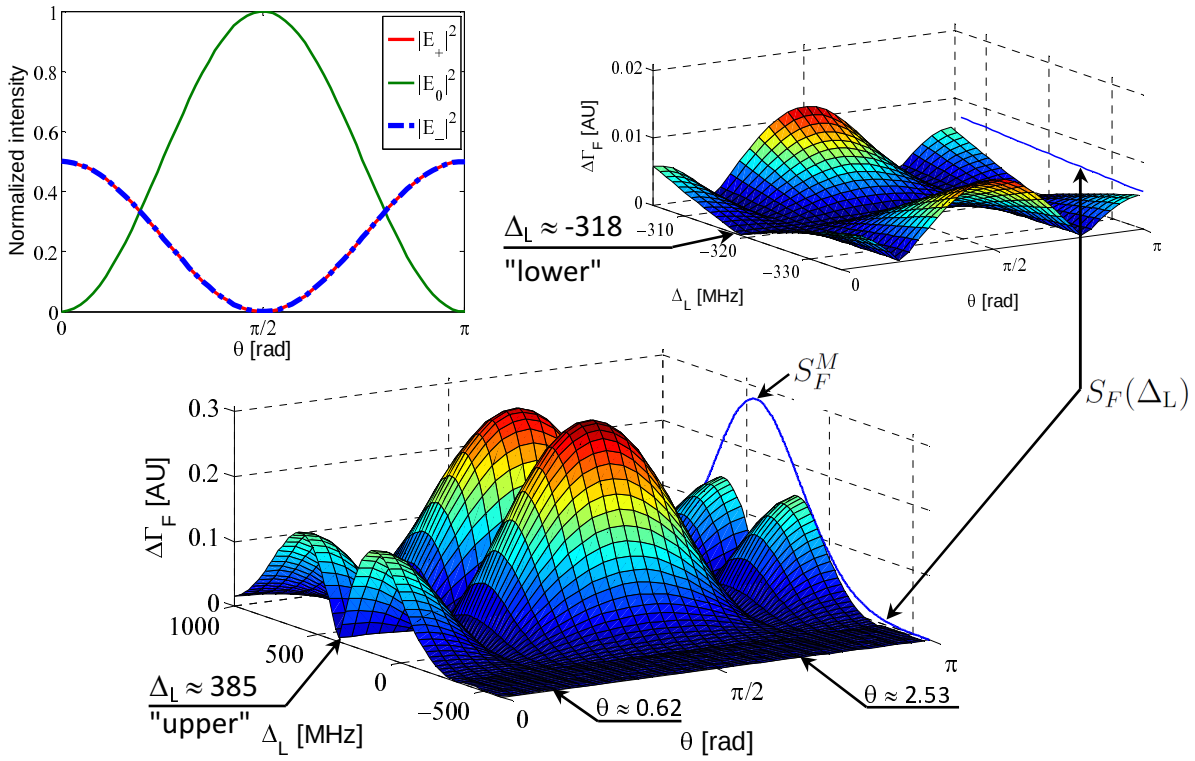

Figure 3.5: Three-dimensional plot of $\Delta\Gamma_F(\Delta_{\rm L},\theta)$ for the $5^2S_{1/2}|F=2\rangle \rightarrow 5^2P_{3/2}$ transition in room temperature ^{87}Rb induced by linearly polarized light with $\phi = 0$ (see Fig. 3.2). Bottom: plot of $\Delta\Gamma_F$ as a function of the light frequency $\Delta_{\rm L}$ [see Eq. (3.7)] and the angle θ between $\mathbf{B}$ and $\mathbf{k}$ (see Fig. 3.2). The quantity $S_F(\Delta_{\rm L})$ is plotted in blue on the $\theta = \pi$ plane, its maximum $S_F^{\rm M}$ is indicated by an arrow. Note that $\Delta\Gamma_F = 0$ along 4 lines in the $\Delta_{\rm L} - \theta$ plane, marked with arrows: two lines with $\theta = 0.62$ or 2.53 rad, and two with $\Delta_{\rm L} = 385$ or -318 MHz. Top right: a scaled up (x10) portion of the $\Delta\Gamma_F$ plot. Top left: plots of the normalized intensities of the light components (in the atomic frame) as a function of θ for $\phi = 0$.

one varies considerably with it. In addition we note that the "upper" magic frequency is located near the peak of $S_F(\Delta_{\rm L})$ (see Fig. 3.5), indicating strong atom-light interaction, while the "lower" one is located where $S_F(\Delta_{\rm L})$ is small, meaning weak interaction between the (detuned) light and the atoms. For these reasons we focus our attention henceforth on the "upper" magic frequency – the *magic frequency* $\Delta_{\rm L}^{\rm M}$.

Figure 3.7 provides information on the behavior of the quantity $\Delta\Gamma_F \cdot S_F^M$ near the magic frequency. We see that there is a frequency range of about ± 15 MHz within which the variation of the absorption rate by atoms at different Zeeman sub-levels is less than 1%. This is a relatively wide frequency range, which means that the probe laser's accuracy and stability can easily be achieved, for example by a locked ECDL (see [63]).

In Fig. 3.8 we show how $\Delta\Gamma_F$ changes when the light's polarization angle ϕ (see Fig. 3.2) is modified. Note that although the general shape of $\Delta\Gamma_F$ changes considerably, and for

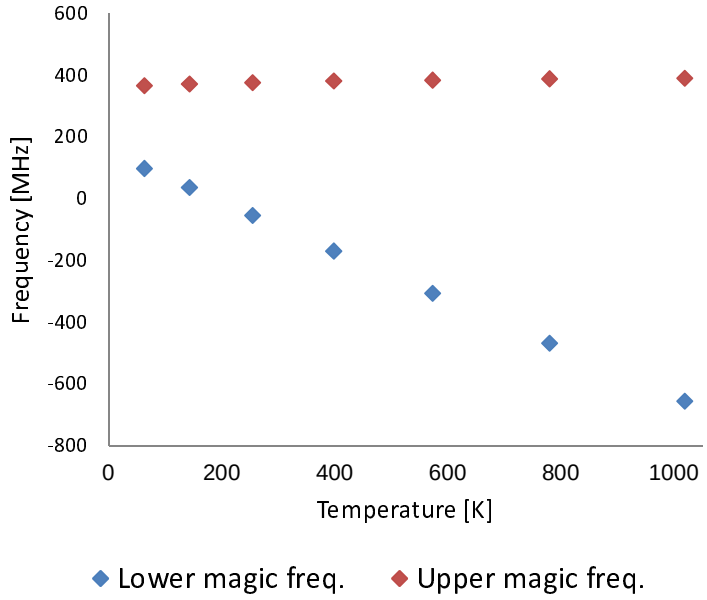

Figure 3.6: Calculated magic frequencies (see Fig. 3.5) as a function of the temperature of ^{87}Rb vapor for the $5^2S_{1/2}|F=2\rangle \rightarrow 5^2P_{3/2}$ transition induced by linearly polarized light with $\phi = 0$ (see Fig. 3.2). Note how the "upper" magic frequency remains almost constant ($< 0.025\,\mathrm{MHz/K}$) over a wide range of temperatures.

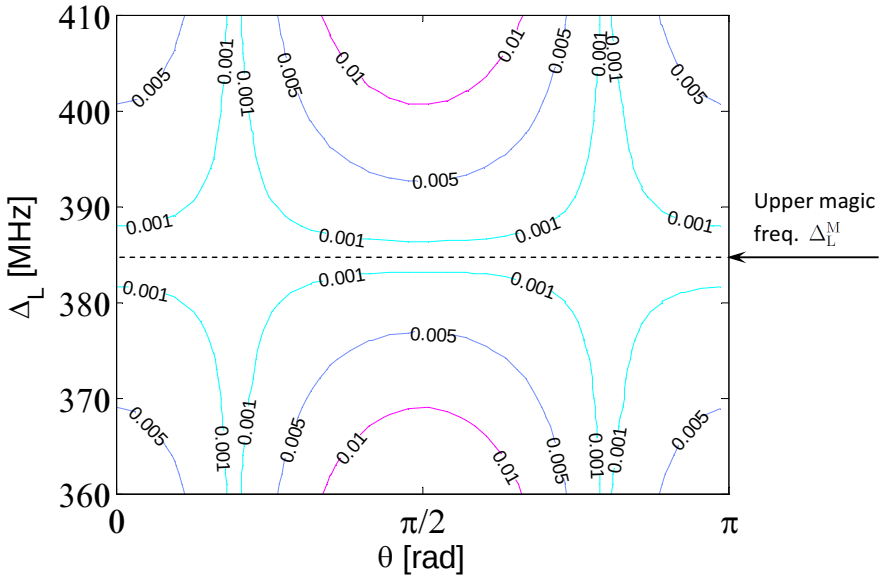

Figure 3.7: Contours of $\Delta\Gamma_F \cdot S_F^M$ [see Eq. (3.10)] over the $\Delta_L - \theta$ plane near the magic frequency Δ_L^M. The contours are plotted for the $5^2S_{1/2}|F=2\rangle \rightarrow 5^2P_{3/2}$ transition in room temperature ^{87}Rb vapor induced by a linearly polarized light with $\phi = 0$ (see Fig. 3.2). In the $\Delta_L^M \pm 15\,\mathrm{MHz}$ frequency range $\Delta\Gamma_F \cdot S_F^M = \left[\max(\Gamma_{m_F}^{rel}) - \min(\Gamma_{m_F}^{rel})\right] < 0.01$, meaning that the variation in absorption rate by atoms in different Zeeman sub-levels is less than 1%.

$\phi \geq 55°$ there are no points where the intensity of all light components is equal, one feature remains fixed for all values of ϕ: the magic frequency $\Delta_{\mathrm{L}}^{\mathrm{M}}$ at which $\Delta\Gamma_F(\Delta_{\mathrm{L}}^{\mathrm{M}}) = 0$.

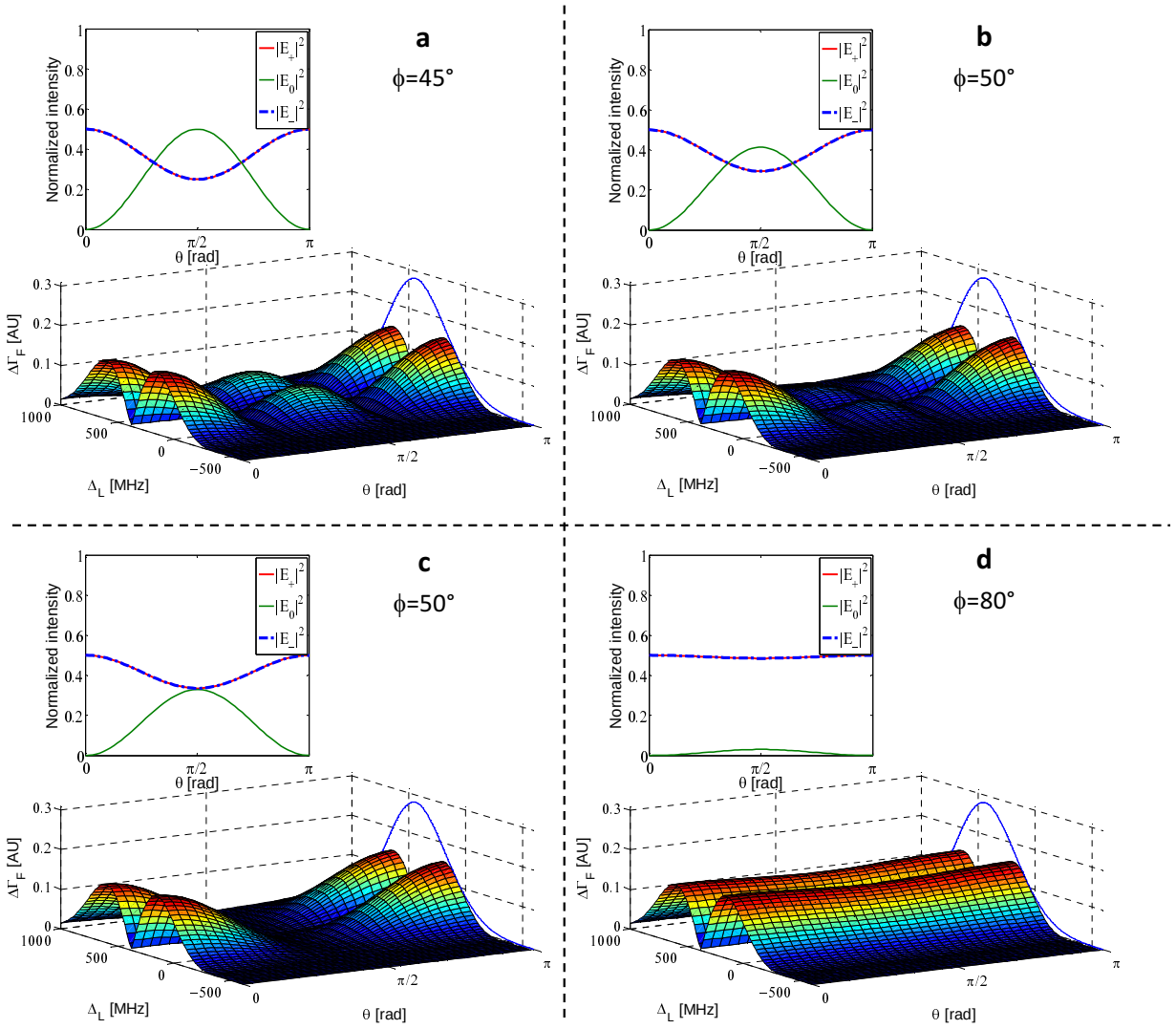

Figure 3.8: Plots of $\Delta\Gamma_F$ for the $5^2S_{1/2}|F = 2\rangle \rightarrow 5^2P_{3/2}$ transition in room temperature ^{87}Rb induced by linearly polarized light with ϕ ranging from 45° to 80° (a-d), plotted as in Fig. 3.5. Note that there are two types of lines along which $\Delta\Gamma_F = 0$. Those parallel to the Δ_{L} axis change position with the value of ϕ, merge into one line at $\phi \approx 55°$ and disappear for $\phi > 55°$. In contrast, the line at the magic frequency $\Delta_{\mathrm{L}}^{\mathrm{M}}$ is independent of ϕ.

The magnitude of the DC magnetic field is not a variable of our simplified absorption model. In fact, our model is based on the assumption that we can neglect the matrix elements of the magnetic interaction which mix between the different hyperfine states of the ground state. Thus we can use the Wigner-Eckart theorem (see Sec. 2.9.4) to get Eq. (3.1) which is the starting point of our model. To estimate the influence of the magnitude of the magnetic field on our model, we adapt a numerical tool (based on the methods developed by W. Happer [64]) that diagonalizes the full Hamiltonian of the system including the magnetic

field. We compare the predictions of our model with the numerical calculation and find that:

- For negligible DC magnetic fields ($|\mathbf{B}| < 0.01\,\mathrm{G}$) the predictions of our model are identical with those of the numerical calculation.
- For small magnetic fields ($|\mathbf{B}| \sim 1\,\mathrm{G}$) the numerical calculation predict a shift of $\sim 1\,\mathrm{MHz}$ in the value of the magic frequency compared to the result of our model. Also, the calculated $\Delta\Gamma_F(\Delta_{\mathrm{L}}^{\mathrm{M}})$ does not vanish completely, but it is still well below 0.01.
- For larger magnetic fields, ($1\,\mathrm{G} < |\mathbf{B}| < 10\,\mathrm{G}$), the numerical calculation predict a shift of $\sim 1.5\,\mathrm{MHz/G}$ in the value of the magic frequency compared to the result of our model. Also, the value of calculated $\Delta\Gamma_F(\Delta_{\mathrm{L}}^{\mathrm{M}})$ is now up to 0.05.
- Changing the angle θ between $\mathbf{B}$ and $\mathbf{k}$ and the polarization angle ϕ (see Fig. 3.2) does not affect on the values of either the magic frequency or of $\Delta\Gamma_F(\Delta_{\mathrm{L}}^{\mathrm{M}})$.

These results confirm that our model is sufficiently accurate for small magnetic fields.

3.3 Mathematical study of the absorption model

The aim of this section is to prove the existence of the *magic frequency*, at which the absorption of linearly polarized light by alkali atoms is independent of:

- the specific Zeeman sub-level m_F state the atoms are in;
- the angle θ between the external magnetic field $\mathbf{B}$ and the light propagation vector $\mathbf{k}$;
- the light polarization angle ϕ (see Fig 3.2).

To this end, let us take two Zeeman sub-levels of the hyperfine ground-state, $|F, m_{1F}\rangle$ and $|F, m_{2F}\rangle$, and look for a frequency f_{L} of the light beam so that absorption rate by atoms in these two Zeeman sub-levels will be the same. By definition, we must have $\Gamma^{rel}_{m_{1F}} = \Gamma^{rel}_{m_{2F}}$, or [see Eq. (3.2)]:

$$\sum_{F'=F-1}^{F'=F+1} \exp\left[-\frac{\Delta_{FF'}^2}{2\sigma_{\mathrm{D}}^2}\right](2F'+1)\begin{Bmatrix} J & J' & 1 \\ F' & F & I \end{Bmatrix}^2 \cdot \sum_{q=-1}^{q=1} |E_{-q}|^2 \langle F, m_{1F}|F', 1, m'_{1F}, q\rangle^2$$

$$= \sum_{F'=F-1}^{F'=F+1} \exp\left[-\frac{\Delta_{FF'}^2}{2\sigma_{\mathrm{D}}^2}\right](2F'+1)\begin{Bmatrix} J & J' & 1 \\ F' & F & I \end{Bmatrix}^2 \cdot \sum_{q=-1}^{q=1} |E_{-q}|^2 \langle F, m_{2F}|F', 1, m'_{2F}, q\rangle^2. \quad (3.11)$$

Note that the beam's frequency enters Eq. (3.11) three times (for $F' = F-1$, F, $F+1$) via the terms $\Delta_{FF'} = f_{FF'} - f_{\mathrm{L}}$, where $f_{FF'}$ is the frequency of the $|F\rangle \to |F'\rangle$ transitions. Proving the existence of the magic frequency is equivalent to showing that the solution(s) f_{L} of Eq. (3.11) exist and are independent of m_{1F}, m_{2F} and $|E_q|^2$ ($q = -1, 0, 1$).

Equation (3.11) can be simplified:

$$\sum_{F'=F-1}^{F'=F+1} \exp\left[-\frac{\Delta_{FF'}^2}{2\sigma_{\mathrm{D}}^2}\right](2F'+1)\begin{Bmatrix} J & J' & 1 \\ F' & F & I \end{Bmatrix}^2 \times \sum_{q=-1}^{q=1}\left(|E_{-q}|^2\langle F, m_{1F}|F', 1, m'_{1F}, q\rangle^2 - |E_{-q}|^2\langle F, m_{2F}|F', 1, m'_{2F}, q\rangle^2\right) = 0. \tag{3.12}$$

Given that our light is linearly polarized and normalized, we know that $|E_{+1}|^2 = |E_{-1}|^2$ and $|E_0|^2 = 1 - 2|E_{+1}|^2$. This enables us to write Eq. (3.12) as:

$$\begin{aligned}&\sum_{F'=F-1}^{F'=F+1} \exp\left[-\frac{\Delta_{FF'}^2}{2\sigma_{\mathrm{D}}^2}\right](2F'+1)\begin{Bmatrix} J & J' & 1 \\ F' & F & I \end{Bmatrix}^2 \\ &\times\Bigg[\Big(1-2|E_{+1}|^2\Big)\Big(\langle F, m_{1F}|F', 1, m_{1F}, 0\rangle^2 - \langle F, m_{2F}|F', 1, m_{2F}, 0\rangle^2\Big) \\ &+ |E_{+1}|^2\Big(\langle F, m_{1F}|F', 1, m_{1F}+1, -1\rangle^2 - \langle F, m_{2F}|F', 1, m_{2F}+1, -1\rangle^2 \\ &+ \langle F, m_{1F}|F', 1, m_{1F}-1, 1\rangle^2 - \langle F, m_{2F}|F', 1, m_{2F}-1, 1\rangle^2\Big)\Bigg] = 0.\end{aligned} \tag{3.13}$$

Let us examine the factor that multiplies $(1-2|E_{+1}|^2)$ in Eq. (3.13). Using the explicit expression for the Clebsch-Gordan coefficients we can show (App. E.2) that this factor equals $(m_{1F}^2 - m_{2F}^2)\cdot G(F, F')$ where $G(F, F')$ is given by:

$$G(F,F') = \begin{cases} 1/(F-2F^2), & F' = F-1 \\ 1/(F+F^2), & F' = F \\ -1/(3+5F+2F^2), & F' = F+1. \end{cases} \tag{3.14}$$

In addition, we can also show (App. E.2) that the factor that multiplies $|E_{+1}|^2$ in Eq. (3.13) equals $(m_{1F}^2 - m_{2F}^2)\cdot(-G(F, F'))$ – exactly the negative of the previous factor!
Using these results we can re-write Eq. (3.13) as:

$$\begin{aligned}&(m_{1F}^2 - m_{2F}^2)\cdot\sum_{F'=F-1}^{F'=F+1} \exp\left[-\frac{\Delta_{FF'}^2}{2\sigma_{\mathrm{D}}^2}\right](2F'+1)\begin{Bmatrix} J & J' & 1 \\ F' & F & I \end{Bmatrix}^2 \\ &\times\Big[(1-2|E_{+1}|^2)\cdot G(F,F') - |E_{+1}|^2 G(F,F')\Big] = 0,\end{aligned} \tag{3.15}$$

which can be further simplified to:

$$\begin{aligned}&(1-3|E_{+1}|^2)\cdot(m_{1F}^2 - m_{2F}^2) \\ &\times\sum_{F'=F-1}^{F'=F+1} \exp\left[-\frac{\Delta_{FF'}^2}{2\sigma_{\mathrm{D}}^2}\right](2F'+1)\begin{Bmatrix} J & J' & 1 \\ F' & F & I \end{Bmatrix}^2 \cdot G(F,F') = 0.\end{aligned} \tag{3.16}$$

Equation (3.16) is equivalent to Eq. (3.11); Since its left-hand-side is the product of three factors, there are three possible circumstances in which it vanishes as we require:

1. $m_{1F} = -m_{2F}$, so $\Gamma^{rel}_{m_F} = \Gamma^{rel}_{-m_F}$ for all frequencies and intensities of the different light components. This is a trivial solution which is to be expected from symmetry considerations.

2. $|E_{+1}|^2 = 1/3$ (i.e., all light components have the same intensity), so that $\Gamma^{rel}_{m_{1F}} = \Gamma^{rel}_{m_{2F}}$ for every choice of m_{1F}, m_{2F} and for every frequency $f_{\rm L}$ of the laser light: the absorption of such light is independent of the population distribution amongst the Zeeman sub-levels [45]. (This case corresponds to the $\Delta\Gamma_F = 0$ lines at $\theta = 0.62$ or $2.53\,$rad in Fig. 3.5.)

3. $m^2_{1F} - m^2_{2F} \neq 0$ and $1 - 3|E_{+1}|^2 \neq 0$, so we can divide Eq. (3.16) by these two factors and get:

$$\sum_{F'=F-1}^{F'=F+1} \exp\left[-\frac{\Delta^2_{FF'}}{2\sigma^2_{\rm D}}\right](2F'+1)\begin{Bmatrix} J & J' & 1 \\ F' & F & I \end{Bmatrix}^2 \cdot G(F,F') = 0. \tag{3.17}$$

Remembering that the solutions $f_{\rm L}$ of Eq. (3.17) are the light frequencies at which $\Gamma^{rel}_{m_{1F}} = \Gamma^{rel}_{m_{2F}}$, and noting that Eq. (3.17) is equivalent to Eq. (3.11), it is clear that the solutions $f_{\rm L}$ are independent of the particular choice of m_{1F}, m_{2F} and of the value of $|E_{+1}|^2$ (i.e. the angle θ between $\mathbf{B}$ and $\mathbf{k}$ and the polarization angle ϕ – see Fig. 3.2). To see that such solutions exist, note that the left hand side of Eq.(3.17) is a sum of three Gaussian functions of $f_{\rm L}$, each with a peak at a different value of $f_{\rm L}$ [see the discussion following Eq. (3.11)]. Each of these Gaussian functions is multiplied by some expressions of F, F', I, J, and J' which are always positive, and by $G(F,F')$ [see Eqs. (E.19) and 3.17)]. The function $G(F,F')$ is always positive for $F' = F$ and negative for $F' = F \pm 1$ [see Eqs. (E.19)]. Consequently the left hand side will vanish for at least one value of $f_{\rm L}$. Thus, we have shown that there exists a *magic frequency* at which absorption of linearly polarized light by alkali atoms is independent of the distribution of that population among the Zeeman sub-levels and of the angles θ and ϕ.

Chapter 4

Measuring hyperfine populations

At the magic frequency, the absorption of the light by a vapor is not affected by the distribution of the population of a hyperfine state amongst its Zeeman sub-levels. Thus, light at that frequency can be used to measure the total population of an hyperfine state. (For ease of presentation , we will use throughout this chapter the phrase "hyperfine population" instead of "population of a hyperfine state").

The basic principle is very simple:

- tune a laser beam to the magic frequency;
- irradiate the vapor with the beam;
- measure the absorbance of the beam by the vapor;
- from the absorbance, deduce the hyperfine population (calibration required).

Note that only when the light is tuned to the magic frequency there is a one to one correspondence between the absorbance and the total population in the hyperfine state.

The rest of this chapter is devoted to the description of the measurement method. Before we go into the method's finer details, we review (Sec. 4.1) several issues related to decoherence and relaxation in vapor cells. Then, in Sec. 4.2, we describe the measurement system, the tuning of its components and the calibration procedure. Several fine-tuning methods are presented in Sec. 4.3, followed by a review of a measuring example (Sec. 4.4). We conclude this chapter (Sec. 4.5) with a discussion of the advantages and limitations of our measurement method.

4.1 Decoherence and relaxation in vapor cells

Most of the discussion in Ch. 3 does not include interactions of the alkali metal atoms with their environment – the vapor cell, buffer gas, other alkali atoms, etc. In this section we provide a short review of these interactions and introduce some results that are needed for the presentation of our hyperfine population measuring method.

Alkali metal atoms in room-temperature vapor cells are in constant thermal motion at average speeds ranging from 200 to 600 m/s (depending on the mass of the alkali atom). Their vapor pressure is on the order of 10^{-6} Torr or less, and if no other gases are present, the mean free path for atom-atom collision is tens or even hundreds of meters. However, a typical vapor cell is only a few centimeters long, so the alkali atom collides with the cell walls within few hundred μs. The atom has a high probability of adsorbing on the cell wall (typically made of glass) for a time of up to few milliseconds. During that time the alkali atom interacts with the cell wall so that when the alkali atom desorbs its internal state is unrelated to its initial state. We say that the internal state has been *relaxed* by the wall collision, and consequently the coherence is destroyed (see [38, 65]).

If alkali atoms can be approximated as two-state systems, we can use the T_1 and T_2 relaxation times of Eq. (2.29) to characterize the effect of atom-wall collisions (and also atom-atom collisions) on an ensemble of alkali atoms. Let us assume that at $t = 0$ the atoms in the ensemble are all in the same coherent superposition $|\Psi\rangle(0) = C_0(0)|0\rangle + e^{i\phi(0)}C_1(0)|1\rangle$ of the two states [both C_0 and C_1 can be real – see Eq. (2.21)]. Collisions cause two processes:

- "thermal relaxation" during which the coefficients $C_0(t)$ and $C_1(t)$ will change so that the ratio of their squares will approach the ratio of the thermal-equilibrium populations of the two states. T_1 is the thermal relaxation time.

- "dephasing" (or "decoherence") of the phase $\phi_i(t)$ of each atom i in the ensemble so that after a time $t \gg T_2$ the value of $\phi_i(t) - \phi(0)$ is equally distributed between 0 and 2π. T_2 is the coherence time.

We note here that alkali atoms are not two-state systems, and typically several relaxation and decohernece processes occur simultaneously, each with different time constants [34]; the relaxation times T_1 and T_2 nevertheless provide a good starting point.

For ^{87}Rb room-temperature vapor in a glass cell, both T_1 and T_2 are on the order of 10^{-5} s (assuming that coherence is completely lost in a single wall collision). However, more than 60 years ago, two methods were found to lengthen both the relaxation and the coherence times. One such method is to add a diamagnetic gas (such as noble gases) to the cell (introduced by A. Kastler and J. Brossel [11]), and the other consists of coating the inner walls of the cell with paraffin wax. A detailed study of the effect of paraffin coating on the relaxation and coherence can be found, for example, in a paper by M. Bouchiat [38]. Below we describe in some detail the effects of adding a buffer gas at low to moderate pressure (1 to 100 Torr) to the vapor cell.

On the one hand, collisions with the buffer gas atoms drastically reduce the mean free path of the alkali atoms, thus the alkali-wall and alkali-alkali collision rates decrease, increasing the relaxation and coherence times. On the other hand, we typically have a large rate of collisions between alkali and buffer gas atoms. Although an alkali atom can maintain its coherence through millions of collisions with buffer gas atoms, eventually, at high enough buffer gas pressure, these collisions will accelerate the relaxation and decoherence processes. These two opposite effects on the relaxation time are expressed in Eq. (4.1) (see [34, 66, 67]):

$$T_1 = \frac{1}{AD_0\frac{p_0}{p} + N_0\bar{v}_r\sigma_1\frac{p}{p_0}}, \tag{4.1}$$

where p the buffer gas pressure, $p_0 = 760\,\text{Torr}$ is the reference pressure, D_0 is the diffusion constant of the alkali atoms in the buffer gas (at p_0), N_0 is the Loschmidt's constant, $\bar{v}_r$ is the relative velocity of the alkali and the buffer gas atoms, σ_1 is the cross section for collisions that change the internal state of the alkali atoms (see Table 4.1) and A is a factor that only depends on the geometry of the cell [34].

Buffer gas	D_0 ($\mathbf{cm^2/sec}$)	σ_1 ($\mathbf{cm^2}$)
Ne	0.31	$1.6 \cdot 10^{-22}$
Ar	0.22	$9 \cdot 10^{-22}$

Table 4.1: Diffusion coefficient D_0 and cross section σ_1 for rubidium atoms in some buffer gases [67].

The first term in the denominator of Eq. (4.1) describes the relaxation caused by the diffusion of the rubidium atoms through the buffer gas to the cell walls. This term is inversely proportional to the buffer gas pressure p. The second term describes relaxation by collisions between the rubidium atoms and buffer gas atoms; it is proportional to the buffer gas pressure and can be neglected for buffer gas pressures below $\sim 100\,\text{Torr}$ [34].

Adding buffer gas to alkali vapor cells gives rise to several additional phenomena:

- **Pressure shift and pressure broadening**. When we excite an alkali atom with a light beam (e.g., a 780 nm light beam driving the $5^2S_{1/2}|F = 2\rangle \rightarrow 5^2P_{3/2}$ transition of ^{87}Rb), the frequent collisions with buffer gas atoms cause a shift in the resonance frequency of the transition, as well as its broadening. The shift and broadening are both linear functions of the buffer gas pressure. Coefficients for the pressure shift and broadening for the D2 line of ^{87}Rb by the noble gases are presented in Table 4.2. In some applications, such as atomic clocks, a mixture of buffer gases (e.g. helium and neon) is used to minimize the resulting shift.

- **Line narrowing (Dicke narrowing)**. Collisions with buffer gas atoms reduce the mean free path of the alkali atoms, and cause frequent abrupt velocity changes. When near-resonance radiation that excites alkali atoms has a wavelength that is comparable or larger than the mean free path of the alkali atoms, the Doppler broadening of the transition linewidth is significantly reduced. This "narrowing" of the linewidth results from the frequent velocity changes that occur while the alkali atoms interact with the light, so that the "average" speed of the atoms during the interaction is close to zero (see [16, 68]).

A ^{87}Rb vapor cell we frequently used in the work is a borosilicate glass cylinder (I.D. 22 mm, length 38 mm) with 7.5 Torr Ne buffer gas. For this cell, the estimated thermal relaxation time is on the order of 10 ms [see Eq. (4.1)], the pressure shift is $28 \pm 4\,\text{MHz}$ and the pressure broadening (FWHM) is $70 \pm 3\,\text{MHz}$ (see Table 4.2).

The Doppler broadening of the D2 transition is much larger than this pressure broadening and we assume that the total broadening in our cell is adequately described by the Doppler profile of Sec. 2.10.1 with a FWHM of $\sqrt{70^2 + 505^2} \simeq 510\,\text{MHz}$, where 505 MHz is the room-temperature Doppler FWHM (σ_D increased from 215 to 217 MHz).

Buffer gas	Shift (MHz/Torr)	Broadening (MHz/Torr)
He	2.2 ± 0.5	22.5 ± 1.1
Ne	-3.7 ± 0.5	9.4 ± 0.4
Ar	-7.1 ± 0.8	19.8 ± 0.5
Kr	-8.4 ± 1.0	17.5 ± 1.0
Xe	-7.0 ± 1.1	19.8 ± 0.9

Table 4.2: Pressure shift and broadening of the $5^2S_{1/2}|F = 2\rangle \rightarrow 5^2P_{3/2}$ (D2) transition frequencies in room-temperature ^{87}Rb due to several buffer gases [61].

4.2 Detailed description of the population measuring method

Our population measuring method evaluates the population distribution (p_1 and $p_2 = 1-p_1$) between the two hyperfine ground states of alkali atoms in a vapor cell. These populations are directly related to the zero-order polarization moment (see Sec. 2.11). Typically such measurements are needed to assess the results of some other manipulations that are performed on the alkali vapor. The method is a destructive one, it applies to that part of the cell that is illuminated by the measuring light beam (i.e., within the red arrow on Fig. 4.1), and we assume that just prior to the measurement the values of p_1 and p_2 are independent of the position inside the cell.

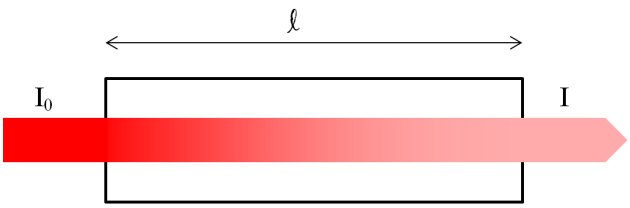

Figure 4.1: Absorption of a laser beam as it passes through an alkali-metal vapor-cell of length l. If the density n of the atoms that can interact with the beam is constant across the cell, and is not affected by the beam, then the Beer-Lambert law [Eq. (4.2)] is valid.

Below we present our method as it applies to ^{87}Rb vapor in 7.5 Torr of Ne buffer gas (it can easily be modified for every other alkali atom in any other buffer gas or in a paraffin coated cell). We use the concept of the optical density (OD) which characterizes the absorption of the light by a substance, such as alkali vapor: when a beam of light of intensity I_0 passes through an alkali-metal vapor-cell of length l (see Fig. 4.1) then the intensity I of the light as it emerges from the cell is given by the Beer-Lambert law:

$$I = I_0 e^{-\mathrm{OD}} = I_0 e^{-\sigma \cdot l \cdot n \cdot p_i} \tag{4.2}$$

where OD is the optical density, n is the density of alkali atoms, p_i is the relative population of the atoms in the hyperfine state $|F = i\rangle$ that can interact with the light and σ is the cross section for interaction of an atom with the light. It is important to note that the

Beer-Lambert law as given in Eq. (4.2) is valid only if the density $n \cdot p_i$ is constant along the length of the cell and is independent of the light intensity.

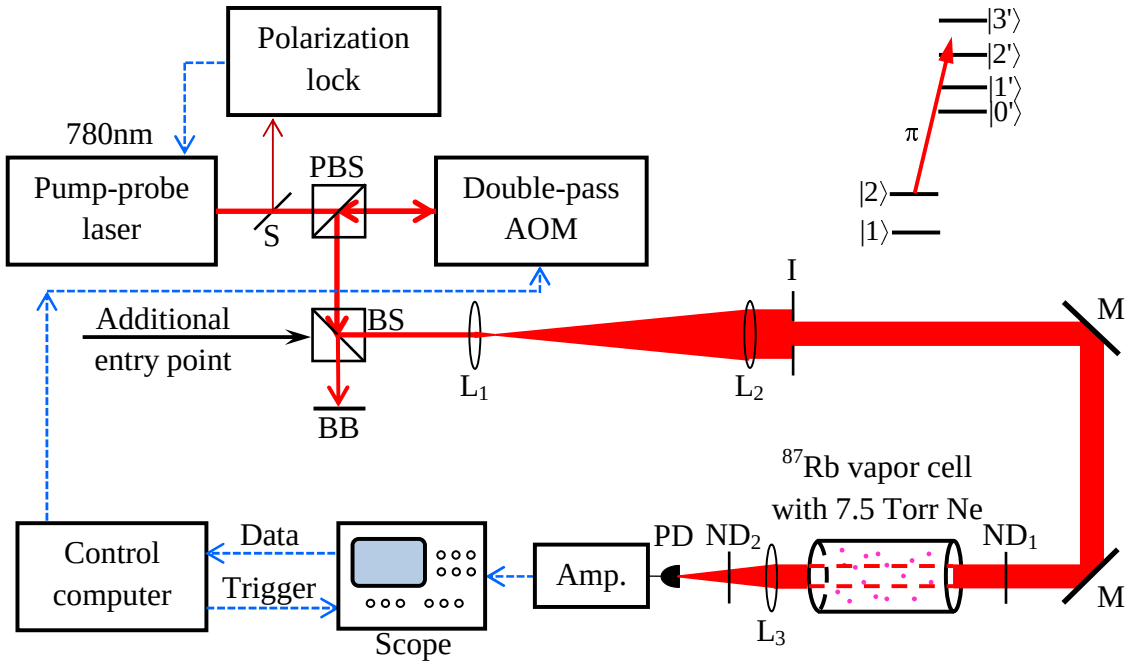

Figure 4.2: Details of the population measurement scheme. BB – Beam blocker; BS – non-polarizing beam splitter cube; I – iris; L_1, L_2, L_3 – lenses; M – mirror; ND_1, ND_2 – neutral density filters; PBS – polarizing beam splitter cube; PD – Photodiode; S – beam sampler. Red arrows and lines indicate the laser beam; the beam is tuned to the magic frequency for the $5^2S_{1/2}|F = 2\rangle \rightarrow 5^2P_{3/2}$ transition in ^{87}Rb (schematic level diagram is presented in the top right corner). Dashed blue arrows indicate data and control lines. The measuring beam is produced by the pump-probe laser (so named since, as explained in this chapter, it probes the population using optical pumping). The polarization-lock sub-system [69, 70] and the double-pass AOM (see App. B.2) enable tuning of the beam to the magic frequency, and switching it on and off within 1 μs. The lenses L_1 and L_2 and the iris control the diameter and the intensity profile of the beam (see Fig. B.3). The beam then passes through the cell and its exit intensity recorded as a function of time. (The scope is triggered simultaneously with the onset of the pump-probe laser beam.) This data are used to calculate (see text) the distribution of the population amongst the two hyperfine ground states (only atoms contained in the volume of the cell between the dashed red lines are measured). The additional entry point on the left facet of the non-polarizing beam splitter is used to direct other laser beams to the cell prior to the measurement (e.g., for optical pumping).

A detailed scheme of the population measurement system is presented in Fig. 4.2. The value that we wish to measure is p_2^s – the relative population of ^{87}Rb atoms in the $|F = 2\rangle$ state just prior to the start of the measuring procedure. (The total population of ^{87}Rb atoms in the $|F = 2\rangle$ state is $p_2^s \cdot n \cdot V$, where V is the volume of the vapor and n is the density of the ^{87}Rb atoms). The measuring beam is produced by the pump-probe laser (so named since, as explained in this chapter, it probes the population using optical pumping). When

we turn on the pump-probe laser beam, it starts pumping atoms from the $|F=2\rangle$ state to the $|F=1\rangle$ state (see Sec. 2.7.5). Once this process starts, the relative population $p_2(t)$ of ^{87}Rb atoms in the $|F=2\rangle$ state depends on the optical pumping rate, which depends on the local light intensity, which in turn decreases along the length of the cell due to absorption. So for any time $t>0$, the relative population $p_2(t)$ is also a function of the location along the cell. Since $p_2(t)$ is part of the exponent of the Beer-Lambert law [Eq. (4.2)], this law is not valid. However, there are two instances where it is valid:

- at $t=0+\epsilon$ (just after the pump-probe beam is turned on) the density $n\cdot p_2(\epsilon)$ of ^{87}Rb atoms in the $|F=2\rangle$ state is constant along the cell if the time ϵ is small enough that we can neglect the amount of optical pumping during that time. For small enough ϵ we have
$$n\cdot p_2^{\mathrm{s}}\simeq n\cdot p_2(\epsilon), \tag{4.3}$$
In addition, as our beam is tuned to the *magic frequency*, the distribution of the population between the Zeeman sub-levels of the $|F=2\rangle$ state does not affect the absorption. Thus the intensity I_{s} of the light emerging from the vapor cell at the start of the optical pumping process is related to p_2^{s} by the Beer-Lambert law and we have [see Eq. (4.2)]:
$$I_{\mathrm{s}}\simeq I_0 e^{-\sigma\cdot l\cdot n\cdot p_2^{\mathrm{s}}}\Rightarrow p_2^{\mathrm{s}}\simeq -\frac{\ln(I_{\mathrm{s}}/I_0)}{k};\ k=\sigma\cdot l\cdot n. \tag{4.4}$$
We evaluate the calibration constant k as described in Sec. 4.2.3.

- Asymptotically as $t\to\infty$, provided that the intensity of the pump-probe beam is strong enough that we can assume
$$n\cdot p_2(t)_{t\to\infty}\simeq 0. \tag{4.5}$$
In this case the light absorption is very small, so we can neglect its variation along the cell, and we have:
$$I(t)_{t\to\infty}\simeq I_0 e^{-\sigma ln\cdot p_2(t)}\simeq I_0 e^{-\sigma ln\cdot 0}=I_0. \tag{4.6}$$

Thus, by measuring I_{s} and I_0 of Eqs. (4.4),(4.6) (and evaluating the calibration constant k) we can calculate the hyperfine populations p_1 and p_2.

4.2.1 Tuning the beam's intensity

Our first task is to tune the intensity of the pump-probe beam so that both Eqs. (4.3) and (4.5) are valid. The value of ϵ is taken to be the integration time of a single data point in our scope. Based on the considerations to be presented in Sec. 4.2.2, this integration time is 200 ns. The effect of the optical pumping process on the intensity of the pump-probe beam as it emerges from the vapor cell can be approximated as:
$$I(t)=I_0(1-a\cdot e^{\frac{t}{\tau_{\mathrm{p}}}}), \tag{4.7}$$
where τ_{p} is the time constant of the optical pumping process (see Fig. 4.3). This time constant increases as the light intensity decreases. If we tune the light so that $\tau_{\mathrm{p}}\gg\epsilon$, then

Eq. (4.3) holds. On the other hand, to satisfy Eq. (4.3) we need to have a strong enough pumping process so that at steady state the remaining population in the $|F = 2\rangle$ can be neglected. The main competing process to the optical pumping is the thermal relaxation, with time constant T_1 (see Sec. 2.7.5) so if we have $\tau_p \ll T_1$ then the optical pumping will be strong enough, and Eq. 4.5 holds. For ^{87}Rb vapor with 7.5 Torr Ne buffer gas, $T_1 \approx 10\,\text{ms}$ (see end of Sec. 4.1). Thus we need to tune the intensity of the light so that:

$$200\,\text{ns} \approx \epsilon \ll \tau_p \ll T_1 \approx 10\,\text{ms}. \tag{4.8}$$

Tuning the light intensity is done with a variable neutral-density filter (ND_1 in Fig. 4.2). The value of τ_p is estimated based on light intensity plot (e.g. Fig. 4.3), and we aim at $50\,\mu\text{s} < \tau_p < 100\,\mu\text{s}$.

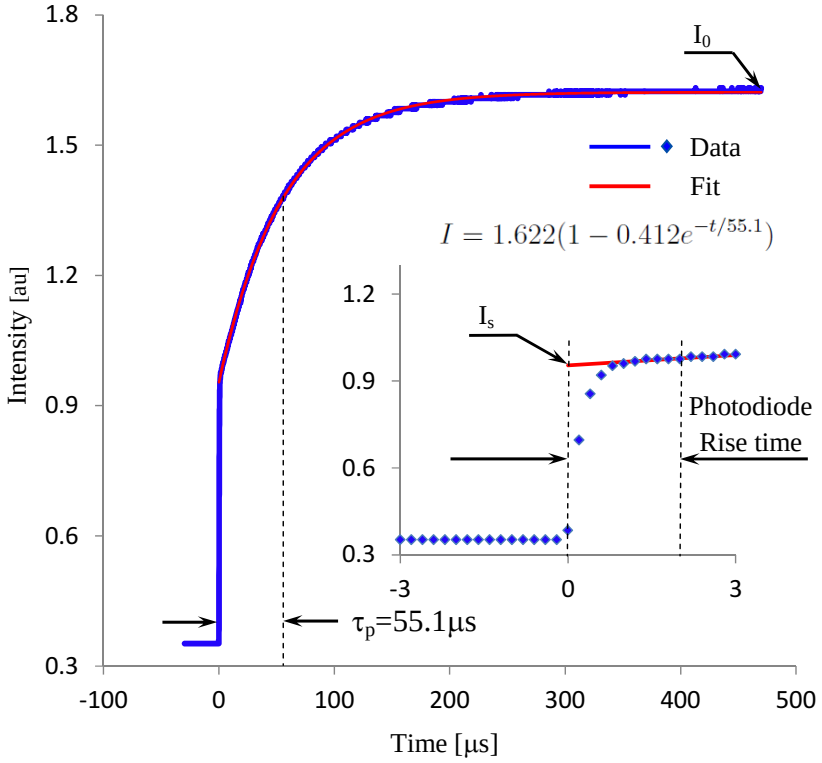

Figure 4.3: Typical plot of the intensity of the pump-probe laser beam as it emerges from the vapor cell (Fig. 4.2). The starting time ($t = 0$) is at the simultaneous onset of the pump-probe laser and the trigger of the scope (see Fig 4.2). Data is shown in blue, fitted to an exponential function having the form of Eq. (4.7) shown in red with a time constant $\tau_p = 55.1\,\mu\text{s}$. The inset magnifies the plot during the first few μs. The data recorded during the photodiode rise time (the first 2 or 3 μs) is excluded from the fitting process. I_s, the intensity at the start of the process, is estimated by extrapolating the fit to $t = 0$; I_0, the intensity at the end of the optical pumping process, is estimated by extrapolating the fit to $t \to \infty$.

4.2.2 Tuning the amplifier and the scope

Once the light intensity that enters the cell is tuned, we need to make sure that our photodiode (Thorlabs DAT210, PD in Fig. 4.2) is not saturated. We use a variable neutral-density filter (ND_2 in Fig. 4.2) to adjust the light intensity that reaches the photodiode. The photodiode produces a photocurrent of $\sim 0.45\,\mathrm{A/W}$. Thus, at the typical light intensity of less than 1 mW the photocurrent is in the range of a few hundred μA. We use a transimpedance amplifier (Fig. 4.4) to convert this current to a voltage, so that we can record it on the scope. The capacitor C1 and the resistor R1 are chosen so that the combined rise time of the photodiode will be minimal while avoiding overshoot.

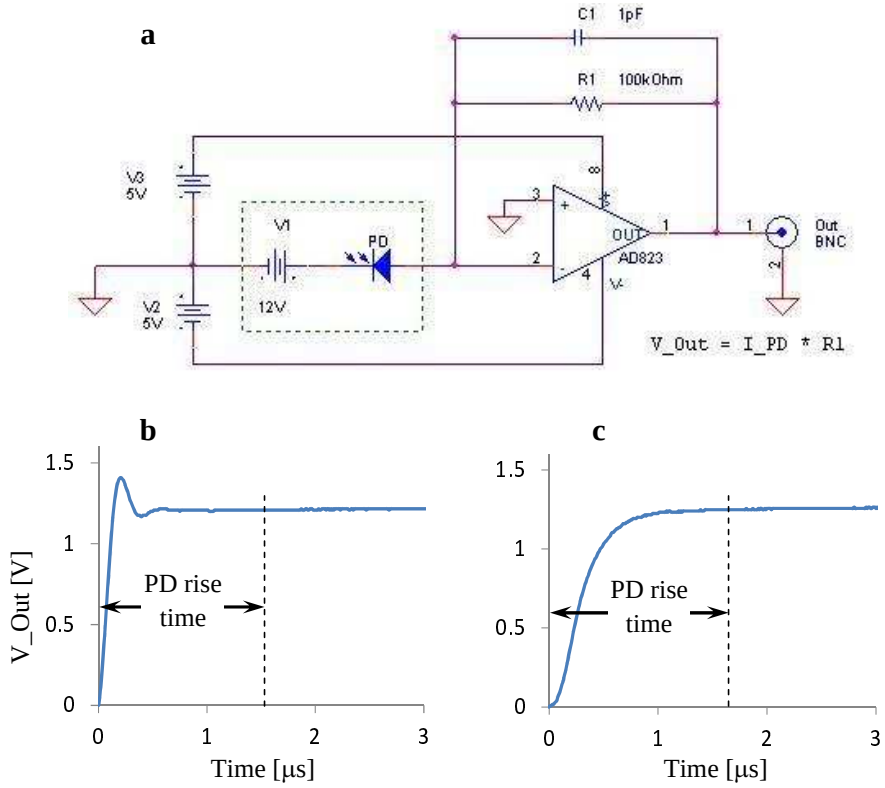

Figure 4.4: The transimpedance amplifier. a: circuit diagram; b,c: plots of the response of the amplifier to turning the light on at $t = 0$ (for different combinations of R1 and C1). The plot in (b) shows an overshoot, while the plot in (c) does not. The output voltage in the first 1 or 2 μs (photodiode rise time) is not proportional to the light intensity.

Next, we choose the time scale of the scope. Since we need to estimate the intensity both at $t = 0$ and at $t \to \infty$, we typically choose it so that a full scale equals $\sim 10\tau_P$. In Fig. 4.3 (which is typical of our measurements) the full scale is set to 500 μs. With 2500 data points for a full screen, each data point represents an integration time of 200 ns. (This is the source of the value of the short time ϵ in Eq. (4.8).

4.2.3 Calibrating the measurement system

Recoding the intensity of the light as it emerges from the vapor cell (such as the plot presented in Fig 4.3), fitting the plot with the functional form of Eq. (4.7) and extrapolating to $t = 0$ and $t \to \infty$ provides us with both I_s and I_0 (see Fig. 4.3). Using Eq. (4.4) we can calculate p_2^s (the hyperfine population in the $|F = 2\rangle$ just before the state at the start of the measuring process) provided that we can evaluate k. To that end, we developed a calibration process that is a variation of Franzen's "evolution in the dark" method [37]. The time sequence of this process is presented in Fig. 4.5. As described in this figure caption, setting $T \gg T_1$ (T is the dark time and T_1 is the thermal relaxation time constant) ensures that at the start of the intensity data recording, the vapor is at thermal equilibrium.

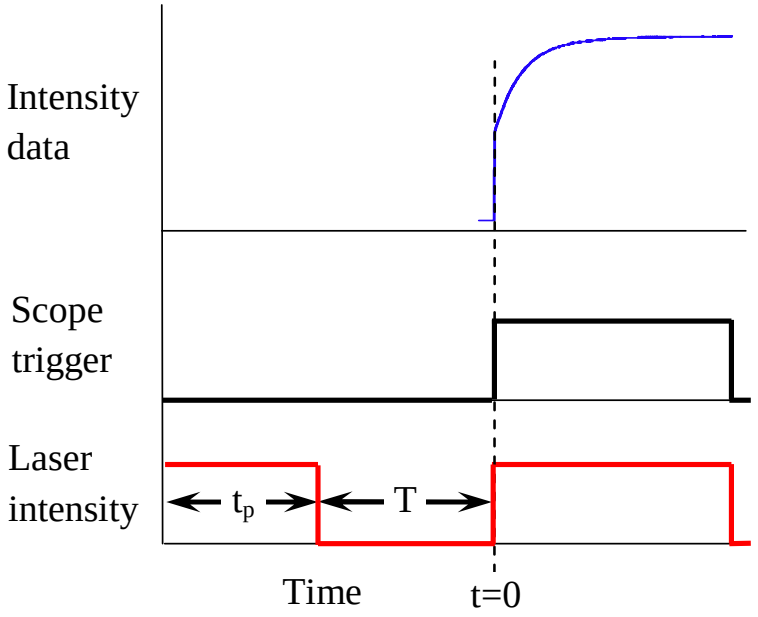

Figure 4.5: Calibration time sequence. At the beginning of the sequence, the pump-probe laser (see Fig. 4.2, used in this stage for pumping only) is turned on for time t_p that is long enough to pump all the population to the $|F = 1\rangle$ state. Then it is turned off for a time T during which the thermal relaxation processes return some of the population back to the $|F = 2\rangle$ state. The laser (now pumping and probing) is turned on again at $t = 0$ and simultaneously the scope is triggered to record the transmitted laser intensity. Note that the population $|F = 2\rangle$ returns to its thermal equilibrium value if the time T is long enough.

The thermal energy of alkali atoms at room temperature (in units of frequency) is on the order of a THz. The ground state hyperfine splitting, which is $< 10\,\text{GHz}$, is negligible in comparison. Based on the Boltzmann distribution we know that the population will be equally distributed between all the sub-levels of the ground state. On the other hand, a transition from the ground state to the first excited P state is in the optical range – hundreds of THz. Thus without external excitation, the population of the excited states is nil.

The $|F = 1\rangle$ hyperfine ground state of a ^{87}Rb atom has 3 Zeeman sub-levels, while the $|F = 2\rangle$ state has 5 sub-levels. At room-temperature thermal equilibrium all the population is equally distributed between these 8 sub-levels. Thus for p_2^{TE}, the relative population of

the $|F = 2\rangle$ hyperfine state at thermal equilibrium is:

$$p_2^{\mathrm{TE}} = \frac{5}{8} = 0.625. \tag{4.9}$$

To proceed, we run the calibration sequence with $\mathrm{T} \gg T_1$. We record the intensity of the light emerging from vapor cell to produce a plot similar to the one presented in Fig. 4.3, and extract I_s and I_0 at thermal equilibrium. We mark these values with superscript TE – "thermal equilibrium", and substitute them in Eq. (4.4):

$$0.625 = p_2^{\mathrm{TE}} \simeq -\frac{\ln(I_\mathrm{s}^{\mathrm{TE}}/I_0^{\mathrm{TE}})}{k} \Rightarrow k \simeq -\frac{\ln(I_\mathrm{s}^{\mathrm{TE}}/I_0^{\mathrm{TE}})}{0.625}. \tag{4.10}$$

Once the value of the calibration constant k is calculated, we can use our method to measure p_2 for any state of the vapor.

Important notes.

1. The quantities I_0 and I_s that we extract from the intensity plots are only proportional to the actual light intensities in the vapor cell, since there is absorption by the vapor cell wall, by the filter ND_2 (Fig. 4.2) and amplification by the photodiode-amplifier combination. However, in Eqs. (4.4) and (4.10) we only have the ratio I_s/I_0, which is independent of these factors.

2. In most cases the ratio I_s/I_0 is close to 1. Taking the first term of the Taylor expansion:

$$\ln(x) = \sum_{n=1}^{\infty} (-1)^{n-1} \frac{(x-1)^n}{n}, \tag{4.11}$$

   we get

$$\ln(I_\mathrm{s}/I_0) \simeq \frac{I_\mathrm{s} - I_0}{I_0} \quad \text{and} \quad \ln(I_\mathrm{s}^{\mathrm{TE}}/I_0^{\mathrm{TE}}) \simeq \frac{I_\mathrm{s}^{\mathrm{TE}} - I_0^{\mathrm{TE}}}{I_0^{\mathrm{TE}}}. \tag{4.12}$$

   In some instances (see Sec. 4.3) it may be preferable to replace $\ln(I_\mathrm{s}/I_0)$ with $(I_\mathrm{s}-I_0)/I_0$ in Eqs. (4.4) and (4.10).

4.3 Fine tuning of the population measuring method

We developed several procedures to fine tune our population measuring method and fit it to a specific alkali, a specific vapor cell and varied experimental conditions. The flexible experimental control system (detailed in App. B.4) provides us with the ability to choose how the population measurement is performed. There are several options for this fine tuning, as described below:

- **Averaging the plots.** Recording a plot such as the one presented in Fig 4.3 may be done repeatedly and the results are averaged automatically by the scope's internal averaging feature. The operator can choose the number of repetitions: if the particular environment is noisy, more repetitions are needed; however, this will obviously increase the overall measurement time.

- **Choosing the fit type.** In Fig. 4.3 we illustrated the fitting of the intensity plot to the functional form of Eq. (4.7): $I(t) = I_0[1-a\cdot\exp(-t/\tau_{\rm p})]$, which is a single-exponential fit. However, due mainly to the variation in the intensity profile of the laser beam, atoms that are close to the edge of the beam will be optically pumped at a different rate. Thus, fitting to a function of the type $I(t) = I_0[1-a\cdot\exp(-t/\tau_{\rm p1})-b\cdot\exp(-t/\tau_{\rm p2})]$ may provide a more accurate estimation of $I_{\rm s}$ and I_0. This fit is the "double-exponential fit". Another option is to fit to the double-exponential function, but with a pre-determined ratio of the time constants $\tau_{\rm p1}/\tau_{\rm p2}$.

- **Choosing the calculation method.** The operator can choose whether to calculate the population by Eqs. (4.4) and (4.10), using $\ln(I_{\rm s}/I_0)$ – the "ln route", or by the "difference route" – using $I_{\rm s}-I_0$ – as modified by Eq. (4.12). The "difference route" may be preferred if the anticipated values of p_2 are small so that $I_{\rm s}/I_0 \simeq 1$. This is because in such a case the "ln route" requires to strongly zoon-in on the vertical axis of the scope around I_0, and consequently we will not be able to measure the amplifier output when the light is off, and variation of the ambient light may introduce noise to the estimation of I_0.

- **Adjusting the zero point.** The calibration process described in Sec. 4.2.3 is based on the assumption that the pump-probe laser can, given a sufficiently long time, pump all the population from the $|F=2\rangle$ state. However, this is not always the case. The remaining steady-state population can be estimated using the method presented in the last part of Sec. 2.7.5. If this remaining population is not negligible compared to the anticipated population to be measured, the system can modify I_0 and/or k accordingly.

The experimental control system includes a calibration section that runs the sequence presented in Fig. 4.5. The operator can choose up to 4 values of T and the system runs the sequences, downloads and analyzes the data, presents a statistical summary, and then pauses to let the operator choose the preferred mode of operation.

4.4 Measurement examples

An example of the population measurement method is presented in Fig. 4.6 by plotting the thermal relaxation process of ^{87}Rb vapor contained in a vapor cell with 7.5 Torr Ne buffer gas. At $t=0$ the vapor is optically pumped by the pump-probe laser to $p_2=0$. Following calibration and fine tuning, we run a sequence similar to the one presented in Fig. 4.5 sixty times, with $T = 0.2 + n\cdot 1\,\text{ms}, \quad n = 1, 2, \ldots 60$. We calculate p_2 for each such run and then fit the results to a function of the type $p_2 = p - a\cdot e^{-t/\tau_1}$; we find a fit goodness of $R^2 = 0.9992$. We then fit the results to a function of the type $p_2 = p - a\cdot e^{-t/\tau_1} - b\cdot e^{-t/\tau_1}$, this time with $R^2 = 0.9998$. The second fit is presented in Fig. 4.6. As detailed in previous studies [71, 72], the "two exponent" behavior is to be expected. The average deviation of the data points from the fit is 0.0015, or 0.15% of the full scale. Another measurement example is presented in App. B.5 for two-photon Rabi oscillations induced in a vapor cell by RF and MW fields.

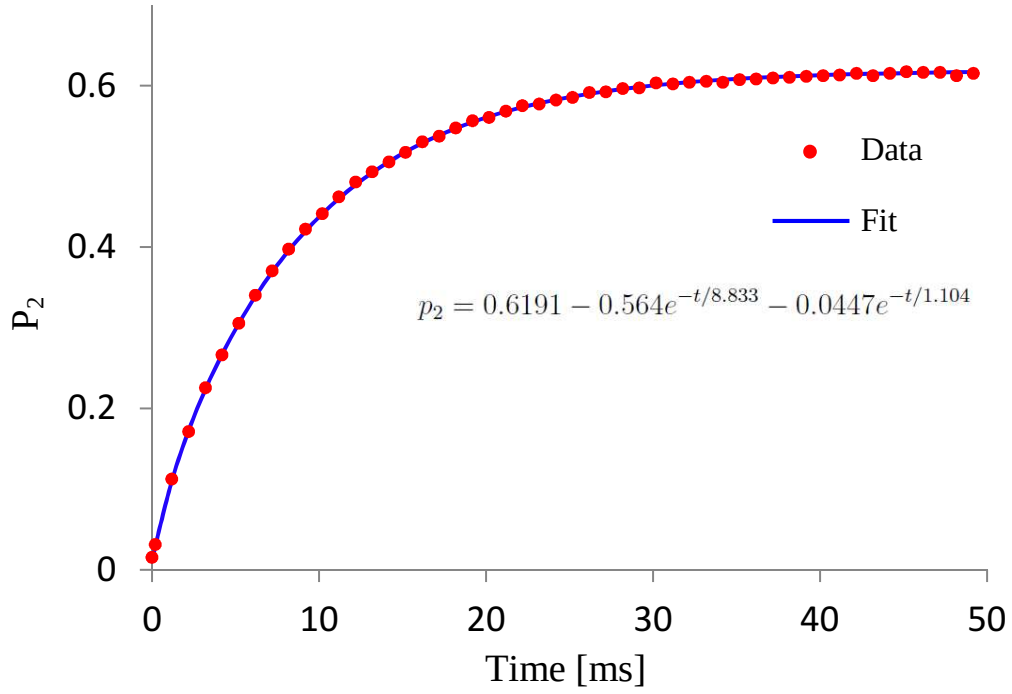

Figure 4.6: Thermal relaxation plot of the relative population in the $|F = 2\rangle$ hyperfine ground state of ^{87}Rb vapor contained in a vapor cell with 7.5 Torr Ne buffer gas. The data points are measured by the population measurement method. The fitted function ($R^2 = 0.9998$) is displayed below the plot. As detailed in previous studies of the thermal relaxation process [71, 72], the double-exponential behavior, as well as the 1 to 8 ratio of the time constants of the exponents, is to be expected. The average deviation of the data points from the fit is 0.15% of the full scale.

4.5 Advantages and limitations of the population measurement method

The main advantages of our population measurement method is that it is accurate and fast. In its current form, it can provide population data with a time resolution of 1 μs. However, the limiting factors are our National Instruments NI PCI 6733 control card and the photodiode amplifier. Both can be replaced with faster hardware, bringing the time resolution down to 200 ns.

Our measurement method is very stable, as demonstrated by the excellent fit to the thermal relaxation data of Fig. 4.6. The ability to fine tune the method to each particular cell and experiment, and to calibrate it prior to each run, enhances this stability. The method is also insensitive to the fluctuation of the laser power, since each measurement evaluates both I_s and I_0 within $\sim$ 500 μs [see Eqs. (4.4), (4.6)]. To further improve accuracy and stability, we can repeat the measurement several times and average the results.

One important limitation of this method is that it is destructive. We cannot continuously measure the population; if we wish to provide a plot of the population as a function of some other parameter, we need to prepare the vapor with different values of that parameter

and then measure the population each time.

Another limitation is our need to use a linearly polarized beam in a π configuration – having the DC magnetic field parallel to the direction of the electric field of the light. This is because the magic frequency is valid only for a linealy polarized beam. If we use a linearly polarized beam whose electric field is not parallel to the magnetic field, the absorption of the E_+ component might not be equal to the absorption of E_- component (see discussion of light components in Sec. 3.1). Thus, even though the light that enters the cell is linearly polarized, it may acquire elliptical polarization as it propagates through the cell. This limitation can be avoided if we analyze the light that emerges from the cell by a system that is capable of separately measuring the intensity of each light component (such as Schäfter & Kirchhoff Polarization Analyzer SK010PA). We would then be able to use the measured absorption of the E_0 component to calculate p_2, the total population in the $|F = 2\rangle$ state, in a manner similar to the one detailed in this chapter. While the linear component deals with the zero order polarization moment (see Sec. 2.11), we may be able to deduce from the absorption of the $E_\pm$ components more information on the state of the vapor, and specifically the value of higher order polarization moments (see also Ch. 6)

Chapter 5

Demonstration of the magic frequency

The experimental demonstration of the magic frequency is based on the hyperfine population measurement method described in Ch. 4. The idea is simple: we create Rabi population oscillations between Zeeman sub-levels of the $5^2S_{1/2}|F=2\rangle$ hyperfine ground state of ^{87}Rb vapor, and then measure the hyperfine population p_2. We repeat this procedure while detuning the frequency of the measuring beam from the magic frequency. The measurement results should show Rabi oscillations unless the measuring laser beam is at the magic frequency. This confirms that at the magic frequency, the interaction with light is independent of the population distribution among the Zeeman sub-levels.

We use our versatile experimental system, described in App. B, to realize this idea. Table 5.2 shows a brief description of each experimental step (detailed descriptions follow). For ease of presentation, we use the short form $|i,j\rangle$ for the Zeeman sub-level $|F=i,m_F=j\rangle$.

5.1 The magnetic and RF fields

In this section we describe the parts of the experimental setup needed for the demonstration of the magic frequency. We then proceed with the description of the demonstration itself.

Our vapor cell is 38 mm long, and the diameter of the laser beams we use in this experiment is 12 mm. We refer to the illuminated cylindrical volume (diameter 12 mm, length 38 mm) inside the cell as the "active volume" (this volume is indicated by the dashed red lines in Fig. 4.2). We subject the Rb atoms in the active volume to an axial DC magnetic field of 26 G (Table 5.2, step 1). The purpose of the field is to induce a second-order Zeeman shift between the Zeeman sub-levels, so that each transition between these sub-level has a distinct frequency. At this field the $|2,2\rangle \leftrightarrow |2,1\rangle$ transition frequency is 18.057 MHz (calculated by the Briet-Rabi formula, see Sec. 2.10.2). The next transition, $|2,1\rangle \leftrightarrow |2,0\rangle$, is at 18.153 MHz – separated by 96 kHz and easily resolvable in our system.

To estimate the required homogeneity of the magnetic field note that in step 3 (Table 5.2) we induce Rabi oscillations for up to 400 μs by an RF field at 18.057 MHz (we limit the Rabi oscillations time to 400 μs so that the thermal relaxation, with a time constant of ~ 10 ms, will not reduce the oscillation's visibility). Since we wish to estimate visibility of the Rabi oscillations, we need to have several cycles within those 400 μs, and consequently, the Rabi frequency should be ~ 10 kHz. The resulting power broadening is ~ 20 kHz (see

Step	Details	Section
1	We subject a cylindrical ^{87}Rb vapor cell (with 7.5 Torr Ne buffer gas) to a DC magnetic field of ~ 26 G along the axis of the cell.	5.1
2	We optically pump the ^{87}Rb vapor population to the $\|2,2\rangle$ Zeeman sub-level, using two circularly polarized laser beams.	5.2
3	We induce Rabi population oscillations between the $\|2,2\rangle$ and the $\|2,1\rangle$ Zeeman sub-levels with an RF field for a Rabi time t.	5.3
4	We turn off the RF field and adiabatically reduce the DC magnetic field to 1 G perpendicular to the axis of the cell. The 90° rotation of the field is intended to enable the same optical axis as before to be used for the production of π polarized light.	5.1
5	We perform a hyperfine "population measurement" sequence as described in Sec. 4.2, using a measuring beam detuned by Δf from the magic frequency. We denote the measurement result $\mathrm{OD}(t,\Delta f)$.	5.4
6	We repeat steps 2 to 5 for several values of t ($0 \le t \le 400\,\mu$s) and produce a plot of $\mathrm{OD}(t,\Delta f)$ as a function of t (with Δf as a parameter), to produce a Rabi oscillation plot.	5.4
7	We repeat steps 2 to 6 for several values of the frequency detuning Δf ($-120 \le \Delta f \le 120$ MHz) and estimate for each plot the visibility of the Rabi population oscillations.	5.5

Table 5.2: Brief descriptions of the steps of the experimental demonstration.

Fig. 2.3). Since a change of the axial DC magnetic field by 0.015 G shifts the transition frequency by ~ 10 kHz, we conclude that the uniformity of the magnetic field in the active volume should be within ± 0.015 G, or $\pm 0.06\%$. Under this condition, most of the Rb atoms in the active volume can interact with the RF field.

The axial DC magnetic field. The required axial magnetic field is produced by the axial coil arrangement (Fig. 5.1). This arrangement consists of a main coil and a pair of auxiliary coils with an adjustable separation. When this distance is larger than the coils' radius, the field of the auxiliary coils has a dip in its center, which can be adjusted to cancel the central peak in the field of the main coil (Fig. 5.1b). Magnetic field measurements using a Lake Shore 460 3-channel Gauss-meter allowed us to ensure field uniformity within the active volume. In addition, three pairs of compensation coils and an auxiliary pair for the y axis (shown in Fig. 5.3) are used to cancel the ambient magnetic field (due to the earth's field and other sources).

The RF field. As mentioned above, an RF field at 18.057 MHz is needed to induce Rabi oscillation between the $|2,2\rangle$ and $|2,1\rangle$ Zeeman sub-levels (Table 5.2, step 3). This transition is a magnetic dipole transition [see Sec. 2.7.1 and Eq. (2.57)], so that the magnetic component of the RF field should be perpendicular to the quantization axis (z axis). We use two rectangular loops located above and below the cell to produced the required field (see Fig. 5.2). The RF signal is produced by an Agilent 33220A 20 MHz function generator and is fed directly to the loops without any impedance-matching circuit. Since the wavelength of the RF field (~ 17 m) is much larger than the size of our loops, we can treat its magnetic

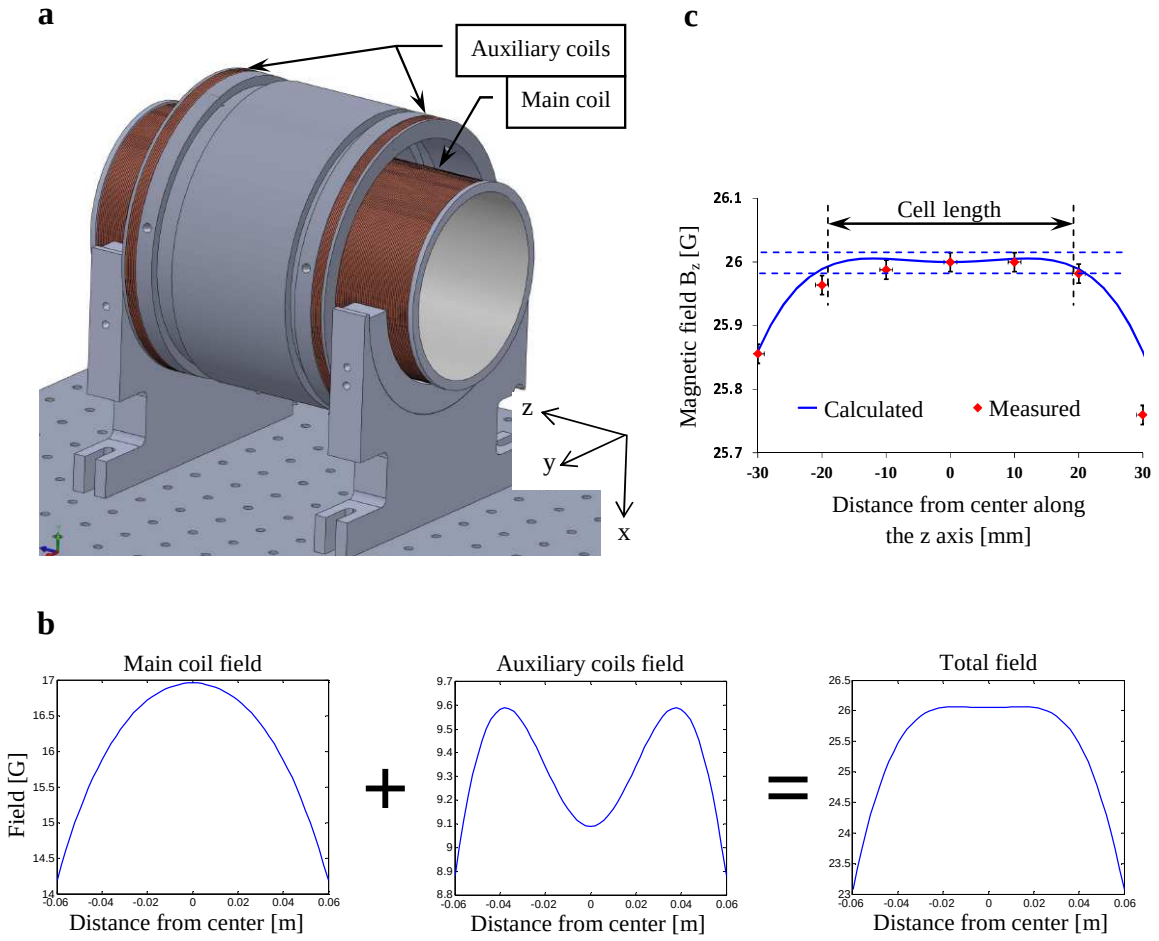

Figure 5.1: The axial coils arrangement. a: Arrangement overview; the main coil is a single-layer coil (length 180 mm, inner diameter 106 mm, wire diameter 1 mm); the auxiliary coils are 36-turns six-layer coils (length 6 mm each, inner diameter 148 mm, wire diameter 1 mm). The distance between the coils is adjustable. The vapor cell (not shown) is located at the center of the main coil. b: Calculation of the combined magnetic field of the coils (current 2.6 A in all the coils). The distance between the auxiliary coils is adjusted so that the total field is uniform along the length of the cell (38 mm). c: Comparison between the calculated and the measured magnetic fields. The dashed blue lines indicate our $\pm 0.015\%$ tolerance for the field magnitude along the length of the cell (z axis), and the vertical error bars represent the ± 15 mG repeatability of the Gauss-meter. Both the calculated and the measured fields are within the acceptable limits (except one measured point at the edge of the cell).

component as near field, i.e. it will be similar to a magnetic field that a DC current in the loops will produce – almost uniform along the length of the vapor cell. Using a pick-up loop and a spectrum analyzer we measured the intensity of the RF in the active area (the vapor cell was not installed during this measurement). We found a uniform intensity to within $\pm 2\%$, and as the Rabi frequency is proportional to the square root of the intensity, we expect a $\sim 1\%$ variation in the Rabi frequency of atoms in different areas of the vapor cell. Since we have only few Rabi cycles, this variation is acceptable.

Adiabatic change of the DC magnetic field. During the first three experimental steps we have an axial DC magnetic field of 26 G. In the fifth we perform a hyperfine-population measurement with the measuring beam tuned to or near the magic frequency. We know that the DC magnetic field should not be larger than few Gauss (see discussion at the end of Sec. 3.2). In addition the beam has to be in a π configuration (see Sec. 4.5) which means that during this step the DC magnetic field must have only transverse components to the light propagation axis.

The DC magnetic field must be changed adiabatically to avoid perturbing the population distribution between the Zeeman sub-levels. For the change to be adiabatic, it's rate should be negligible compared to the transition frequency between the Zeeman sub-levels. In our case the lowest magnetic field is 1 G, driving the transition frequency to 700 kHz. Thus changing the magnetic field during more than $\sim 100\,\mu$s is adiabatic. On the other hand, we wish to perform the change in a time that is considerably shorter than the 10 ms thermal relaxation time for this cell (see 4.2.1). In addition, for a typical current driver limited to voltage $V_{\max}$, its ability to rapidly raise the current in an inductive load L is limited by $dI/dt = V_{max}/L$. Conversely, turning off the current completely can be done much faster, with the help of specially designed fast current shutters (see App. D). Taking all the above into consideration, we perform the adiabatic change in the following way:

- The system is initially prepared by tuning the current in the three pairs of the compensation coils so that the magnetic field in the cell is $\mathbf{B}_{\text{comp}} = 1\hat{y}\,\text{G}$. We tune the current in the auxiliary y-axis coils (Fig. 5.3), which are connected to their current driver via a fast current shutter, to produce a magnetic field of $\mathbf{B}_{\text{aux}} = -1\hat{y}\,\text{G}$. Thus when the current in all these coils is on, the total DC magnetic field in the cell is zero.

- In addition to the above currents, we turn on the current in the axial coils (Fig. 5.1) at the beginning of the sequence (see Table 5.2, step1), producing a magnetic field of $\mathbf{B} = 26\hat{z}\,\text{G}$. The axial coils are also connected via a fast current shutter.

- The current shutter of the auxiliary y-axis coils is tuned to shut down the current within $\sim 200\,\mu$s, while the current in the axial coils arrangement is turned off within $\sim 400\,\mu$s. At the beginning of step 4 (see Table 5.2) we activate both current shutters, so that after $\sim 400\,\mu$s the magnetic field is equal to $\mathbf{B}_{\text{comp}} = 1\hat{y}\,\text{G}$.

The total magnetic field is always above 1 G during the shutting process, so that the transition frequency between the Zeeman sub-levels is higher than 700 kHz. Thus the change is adiabatic, and its $\sim 400\,\mu$s duration is short compared to the 10 ms thermal relaxation time, as required.

Following the above description of the parts of the experimental setup required for the demonstration of the magic frequency, let us now detail the demonstration steps (Table 5.2) one by one.

5.2 Optical pumping to a Zeeman sub-level

In step 1 (Table 5.2) we turn on the currents just described to produce the DC magnetic field $\mathbf{B} = 26\hat{z}\,\text{G}$. A level diagram describing the beams, polarizations and levels of optical

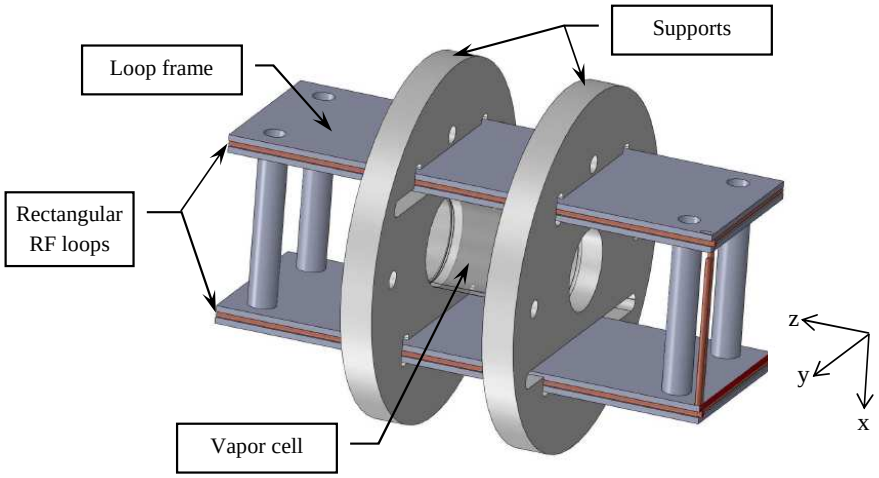

Figure 5.2: The RF loops arrangement. The RF field is created by the two rectangular loops, held in place by the loop frames. The supports hold the RF loop coils and the vapor cell together. The whole RF loops arrangement is inserted into the axial coil arrangement (see Fig. 5.1). Note that the RF magnetic field oscillates along the x direction, while the DC magnetic field is along the z axis.

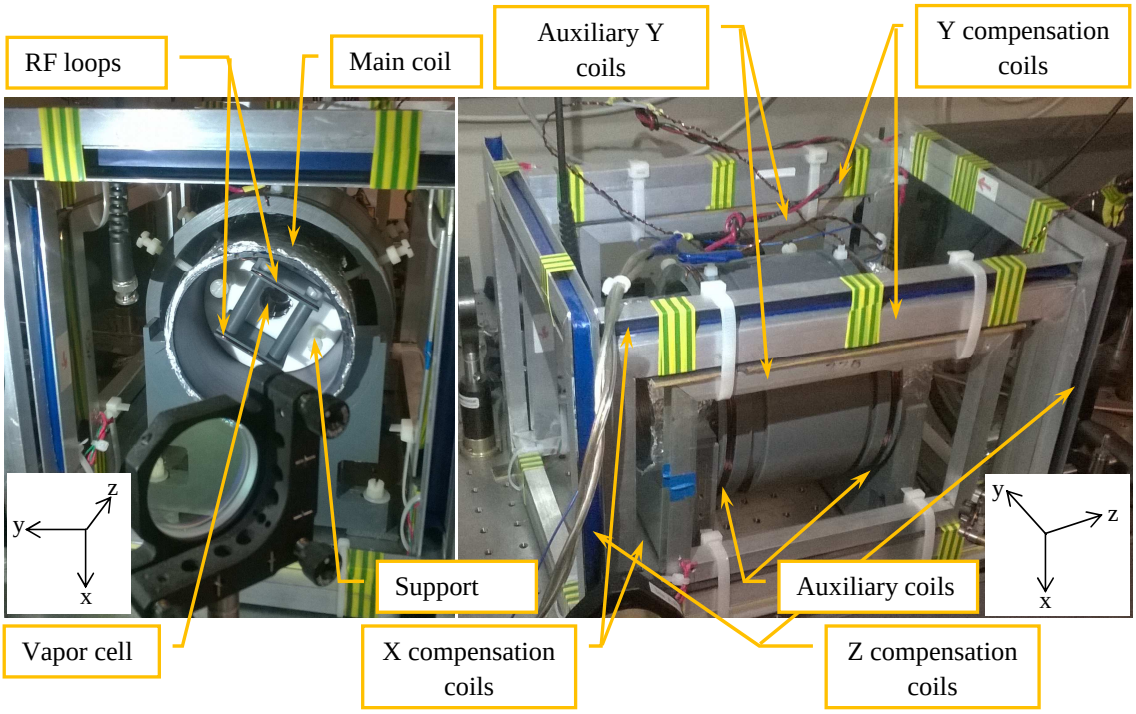

Figure 5.3: Front view (left) and side view (right) of the vapor cell environment prepared for the demonstration of the magic frequency. In the front view, we label the supports that hold the vapor cell and the RF loop arrangement (see Fig. 5.2) inside the main coil. In the side view we label the auxiliary coils, the compensation coils, and the auxiliary coils for the y axis.

pumping process in step 2 is presented in Fig 5.4. We excite the Rb atoms with two circularly polarized laser beams. Beam 1 is tuned to the $5^2S_{1/2}|F=2\rangle \leftrightarrow 5^2P_{1/2}|F'=2\rangle$ transition, and it can excite Rb atoms that are in the $|F=2\rangle$ state except those in the $|2,2\rangle$ Zeeman sub-level. Beam 2, which is tuned to the $5^2S_{1/2}|F=1\rangle \leftrightarrow 5^2P_{3/2}|F'=2\rangle$ transition, is too far detuned to excite atoms that are in the $|2,2\rangle$ sub-level, so this sub-level is a "dark state". Atoms that reach this dark state via excitation and subsequent spontaneous emission would remain there indefinitely, but the thermal relaxation processes cause a "leak" characterized by the 10 ms thermal relaxation time. If the pumping rate of the two laser beams is fast enough compared with this relaxation, most of the population will accumulate in the $|2,2\rangle$ Zeeman sub-level. The efficiency of this optical pumping depends on two additional factors:

- The ellipticity of the Beam 1 polarization which would pump population away from the $|2,2\rangle$ sub-level so that it would not be "dark" any more. We measured the beam ellipticity by passing Beam 1 via a linear polarizer, rotating it and measuring the emerging power as a function of the polarizer angle. For a perfectly circularly polarized beam, the power should be independent of the angle. In our setup this variation was less than $\pm 1.5\%$.

- The angle between the DC magnetic field and the $\mathbf{k}$ vector of the light. Since the magnetic field defines the quantization axis, any non-zero angle leads to the appearance of both π and σ^- components in the atomic coordinate system (see Fig. 3.3), and again the $|2,2\rangle$ sub-level will not be a dark state. During the optical pumping step, the DC magnetic field is in the axial (z) direction, and we keep both beams parallel to this field to within 0.002 radian.

We produce the two pumping laser beams using the lasers described in App. B.1 – "The laser module". The auxiliary laser produces Beam 1, and the (un-modulated) Raman laser produces Beam 2. The "Beam management module" (App B.2) is used to combine the beams, make their polarization circular and turn them on and off. We then use the "Additional entry point" (Fig. 4.2) to feed the pumping beams to the vapor cell. Based on arguments to be presented in Sec 5.6, we pump more than 90% of the population to the $|2,2\rangle$ Zeeman sub-level.

5.3 RF induced Rabi oscillations

Once a large part of the population is pumped to the $|2,2\rangle$ Zeeman sub-level, we move to step 3 (Table 5.2) – Rabi oscillations. We keep the DC magnetic field on at $\mathbf{B} = 26\hat{z}$ G, turn off the pumping beams and turn on the Agilent 33220A 20 MHz function generator. This generator feeds an RF signal at 18.057 MHz to the RF loops arrangement (Fig. 5.2) that induces the $|2,2\rangle \leftrightarrow |2,1\rangle$ Rabi population oscillations. The RF is turned off after a time t.

In general, these population oscillations affect the absorption of light by the vapor; the absorption by atoms in $|2,1\rangle$ is not equal to the absorption by atoms in $|2,2\rangle$ unless the light is tuned to the magic frequency. Thus we can observe the oscillations by measuring the absorbance of the vapor with a laser beam tuned away from the magic frequency (see Sec. 5.4 and Fig. 5.5). We use this data to tune the power of the function generator so that the Rabi frequency will be ~ 10 kHz.

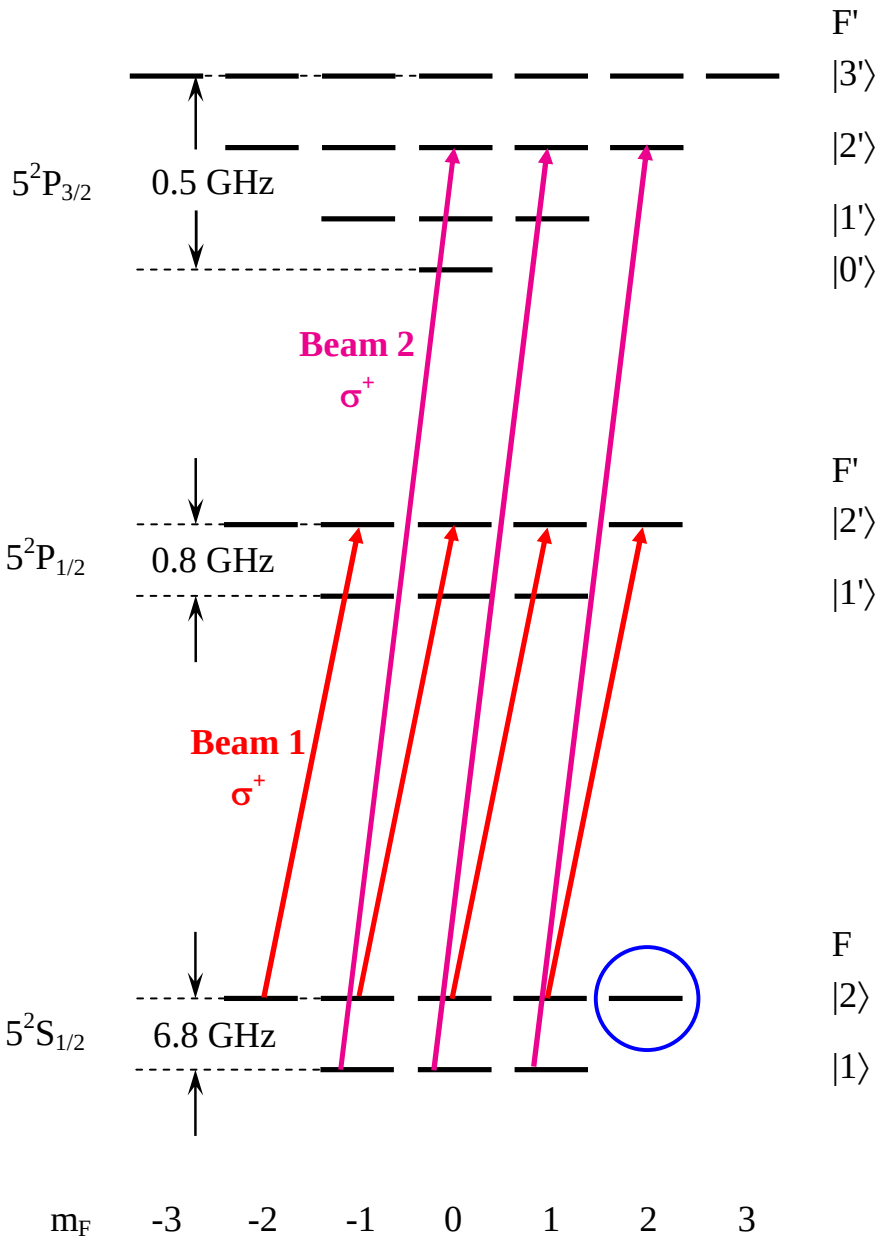

Figure 5.4: Optical pumping to a Zeeman sub-level. We use two circularly polarized laser beams. Beam 1 is tuned to the $5^2S_{1/2}|F=2\rangle \leftrightarrow 5^2P_{1/2}|F'=2\rangle$ transition and beam 2 to the $5^2S_{1/2}|F=1\rangle \leftrightarrow 5^2P_{3/2}|F=2\rangle$ transition. The Zeeman sub-level $|2,2\rangle$ (marked by a blue circle) is a "dark state": Beam 1 cannot excite atoms that are in this state because the $5^2P_{1/2}|F'=2\rangle$ does not have an $|m_F=3\rangle$ sub-level, which is necessary to conserve the angular momentum, and beam 2 is too far detuned. The optical pumping cycle includes spontaneous emission back down to the $5^2S_{1/2}$ ground state that *does* populate the dark state

5.4 Absorbance (optical density) measurements

Following the end of the Rabi oscillations step (Sec. 5.3) we adiabatically change the DC magnetic field from $\mathbf{B} = 26\hat{z}\,\mathrm{G}$ to $\mathbf{B} = 1\hat{y}\,\mathrm{G}$ as described in the last part of Sec. 5.1. This is step 4 (Table 5.2). Then we move on to step 5 – performing a population measurement sequence as described in Ch. 4.

The frequency of the measuring beam (pump-probe laser, Fig. 4.2) is set by a combination of the polarization locking point and the frequency of the double-pass AOM (see App. B.2). The beam is linearly polarized in the y direction, parallel to the DC magnetic field – thus the beam is in the π configuration, as required. Note (see Fig. 3.5) that the magic frequency for the $|F = 2\rangle$ hyperfine state of ^{87}Rb vapor is at $\Delta_{\mathrm{L}} = 385\,\mathrm{MHz}$. In addition, we have 7.5 Torr of Ne buffer gas in the cell, which shifts the transition frequencies by $7.5 \cdot (-3.7) = -28\,\mathrm{MHz}$ (see Table 4.2), so the calculated magic frequency for our cell is:

$$\text{Magic frequency}_{7.5\,\text{Torr Ne}} = 385 - 28 = 357\,\mathrm{MHz}. \tag{5.1}$$

For ease of presentation, we denote the frequency of the measuring beam by its detuning Δf from the magic frequency:

$$\Delta f = \text{Measuring beam frequency} - \text{Magic frequency}_{7.5\,\text{Torr Ne}}. \tag{5.2}$$

The population measurement sequence (step 5, Table 5.2) produces a value which we denote $\mathrm{OD}(t, \Delta f)$. This value is a "calibarted" absorbance of the vapor [absorbance divided by the calibration constant k of Eq. (4.4)]. We then modify the Rabi oscillation time t and repeat steps 2 to 5 for several values of t, $0 \le t \le 400\,\mu\mathrm{s}$ (this is step 6, Table 5.2).

In Fig. 5.5 we present such a plot of $\mathrm{OD}(t, \Delta f)$ as a function of t for a measuring beam detuned by $\Delta_f = -125\,\mathrm{MHz}$ from the magic frequency. Each data point is an average of 6 measurements, and we fit the data to the functional form below:

$$\mathrm{OD}(t) = a + b \cdot t + c \cdot e^{-t/\tau_1} \sin(t/\tau_2 + \phi); \quad t \text{ in } \mu\mathrm{s}. \tag{5.3}$$

The fitted parameters are listed in Table 5.4:

In Fig. 5.5 we clearly notice the Rabi oscillations since the measuring beam is detuned from the magic frequency. The parameter "c" (Table 5.4) is the main parameter of interest here: it is expected go to zero as the measuring beam's frequency approaches the magic frequency.

5.5 Rabi visibility vs. the measuring beam detuning

In the last step of our demonstration (step 7, Table 5.2) we repeat the absorbance measurement as described in Sec. 5.4, each time changing the detuning Δf of the measuring beam and recording optical density plots such as the one presented in Fig. 5.5. Several such plots are shown in Fig. 5.6. We then modify the entire procedure described in this chapter by pumping the population to $|2, -2\rangle$ instead of $|2, 2\rangle$. This is done by reversing the direction of the magnetic field produced by the axial coils arrangement (Fig. 5.1), causing the σ^+ polarized beams to become σ^- polarized. The dark-state is now $|2, -2\rangle$ (see Fig. 5.4) and

Parameter	Value	Notes
a	0.947 ± 0.001	a-c/2 is the calibrated optical density at the beginning of the Rabi oscillations ($t = 0$). Note that $\phi \approx \pi/2$. When the measuring beam is tuned to the magic frequency, "a" becomes the relative population in the $\|F = 2\rangle$ hyperfine state.
b	$(3.57 \pm 0.5) \cdot 10^{-5} (\mu s)^{-1}$	b approximates the thermal relaxation rate of the population in the $\|F = 2\rangle$ hyperfine state.
c	0.0209 ± 0.0021	this parameter defines the visibility, or contrast, of the Rabi oscillations.
τ_1	$(212 \pm 35)\mu s$	τ_1 characterizes the decay, or decoherance, of the Rabi oscillations
τ_2	$(15.73 \pm 0.2)\mu s$	τ_2 defines the frequency of the Rabi oscillations. For this plot we have: $f_{\text{Rabi}} = 1/(2\pi \cdot 15.73 \cdot 10^{-6}) = 10.1\,\text{kHz}$
ϕ	$1.86 \pm 0.1\,\text{rad.}$	ϕ is the phase of the oscillations, which is the case is a 0.6π – slightly higher than $\pi/2$, as is clear from the plot.

Table 5.4: List and description of the parameters fitted to the calibrated OD plot in Fig. 5.5 according to the functional form given by Eq. 5.3. Note that OD, as well as a and c are pure numbers (no units).

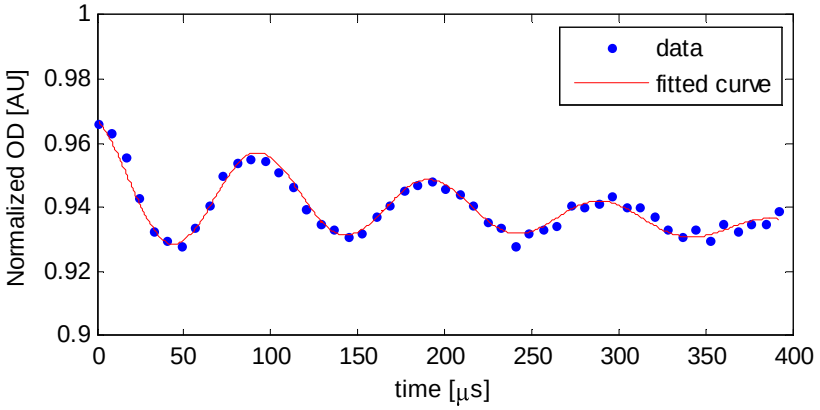

Figure 5.5: Absorbance plot showing Rabi oscillations. Plotted is the calibrated absorbance vs. the Rabi time t for a measuring beam detuned by $\Delta f = -125\,\text{MHz}$ from the magic frequency. The blue data points are the average of 6 runs of the experiment, and the average standard deviation is 0.003. The fit has the functional form given by Eq. (5.3), and the fit parameters are listed in Table 5.4.

the pumping is therefore to this sub-level. The $|2, -2\rangle \leftrightarrow |2, -1\rangle$ Rabi oscillations are now induced by an 18.34 MHz RF field. The plots resulting from this modified procedure are presented in Fig. 5.7.

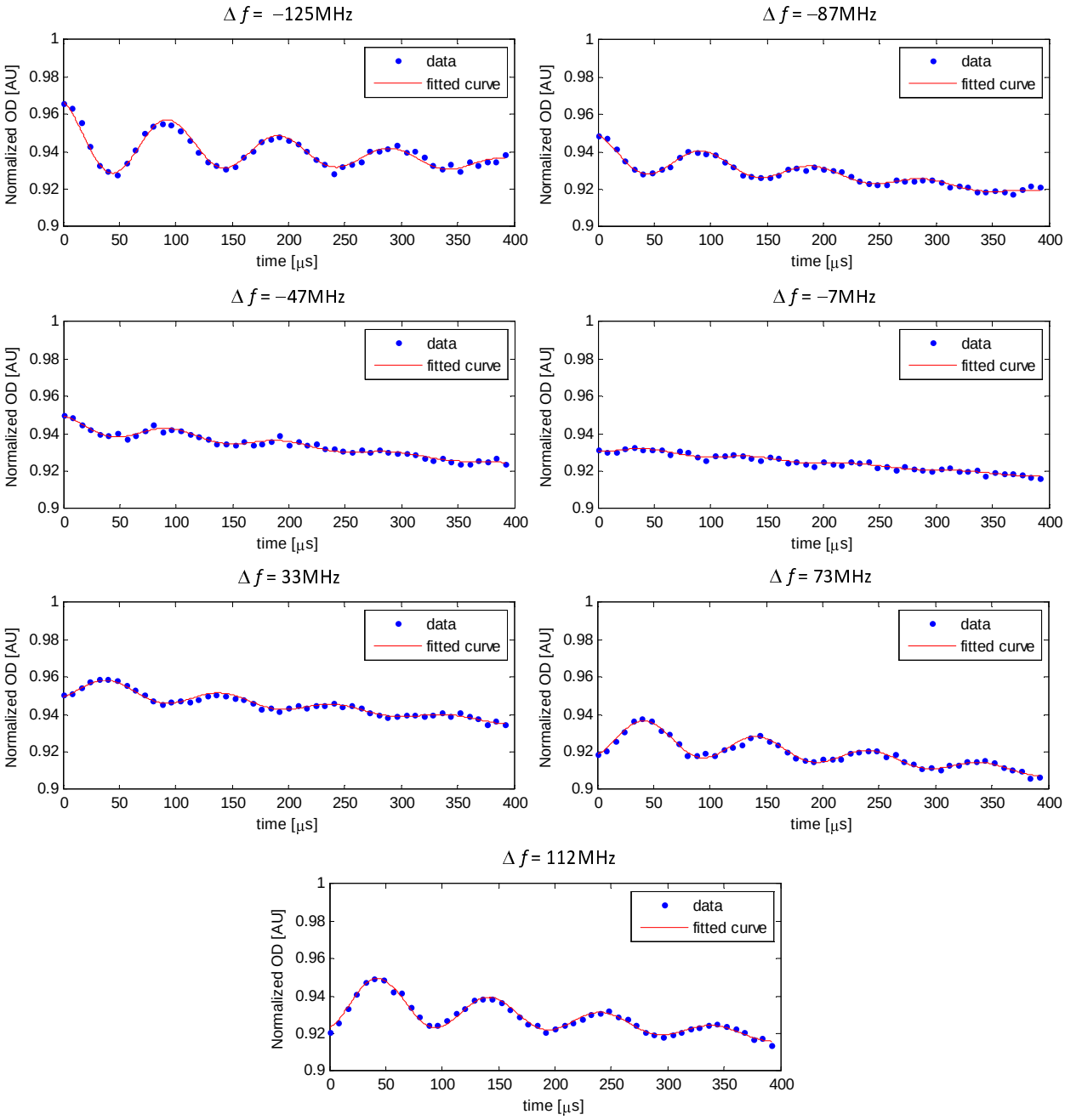

Figure 5.6: Several optical density plots showing $|2,2\rangle \leftrightarrow |2,1\rangle$ Rabi oscillations. Each plot is recorded as described in Sec. 5.4 with the measuring beam detuned from the magic frequency by Δf (the magic frequency is 357 MHz). This detuning is noted above each plot. The data points are the average of 6 runs of the experiment, and the standard deviation is 0.003 for most of the plots, except for those with $\Delta f = -47$ and -7 MHz, where it is 0.005. The data are fitted to the functional form of Eq. (5.3). The plots show that the Rabi visibility, or contrast, decreases almost to zero as the frequency of the measuring beam approaches the magic frequency ($\Delta f \to 0$).

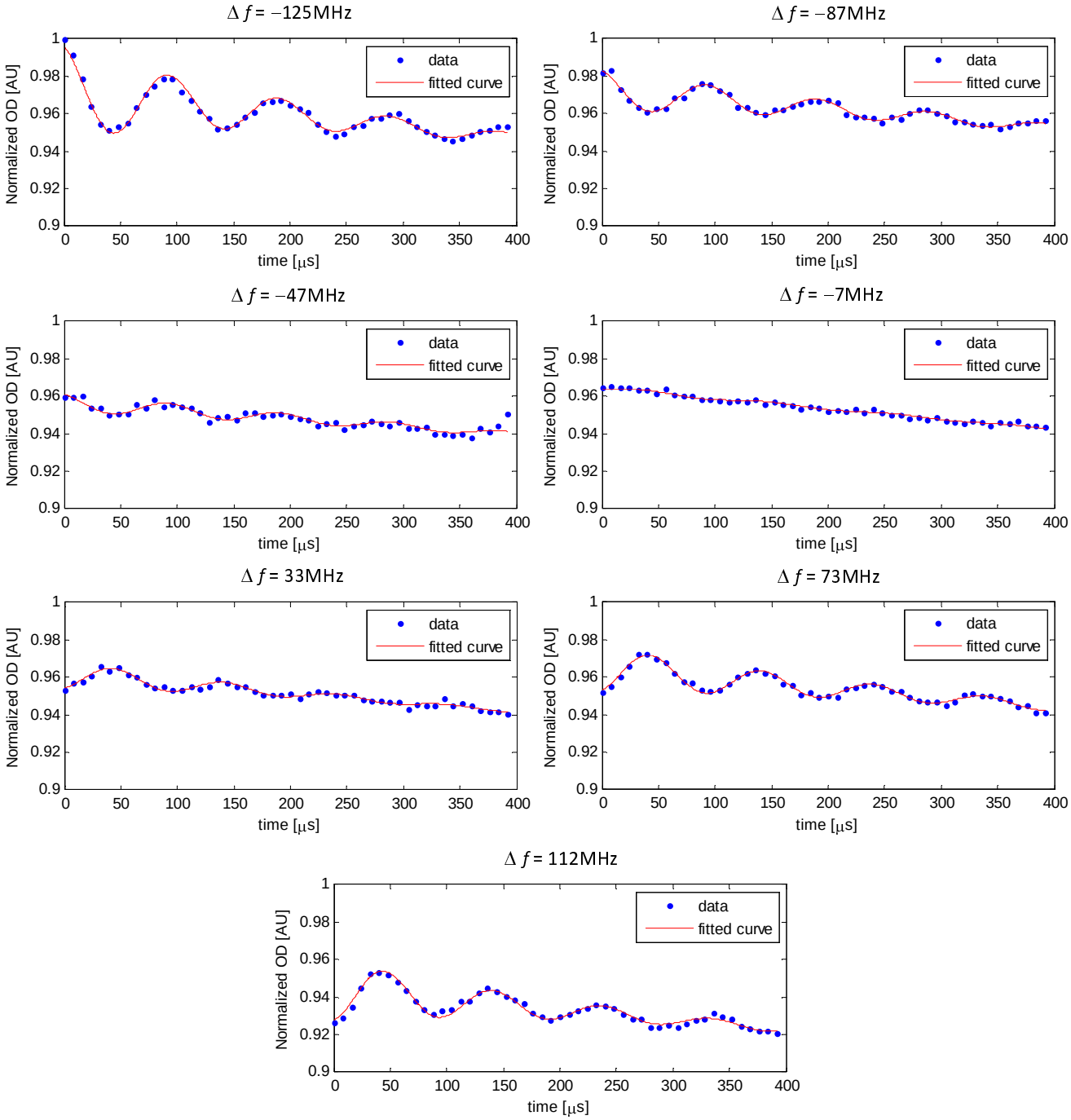

Figure 5.7: Several optical density plots showing $|2,-2\rangle \leftrightarrow |2,-1\rangle$ Rabi oscillations, obtained as in Fig. 5.6, with with two changes: At step 2 (see Table 5.2) the direction of the magnetic field is reversed to optically pump the population to the $|2-2\rangle$, and the frequency of the RF field that induces the Rabi oscillations is changed to 18.34 MHz (step 3, Table 5.2)

Our aim in this demonstration is to show that when the measuring beam is tuned to the magic frequency, the Rabi oscillations are not noticeable, although they do exist. The plots in Figs. 5.6 and 5.7 clearly show that. In addition, in Fig. 5.8 we plot the Rabi contrast

(parameter "c", Table 5.4) as a function of the detuning Δf of the measuring beam from the magic frequency. We see indeed that the Rabi contrast, or visibility, vanishes near the magic frequency. We also note that it flips sign at the magic frequency which is equivalent to the π phase shift in the optical density plots (Figs. 5.6 and 5.7) at the same point. This happens because when the frequency of the measuring beam is lower than the magic frequency the absorption by atoms in $|2,2\rangle$ is higher than by those in the $|2,1\rangle$ sub-level, and the reverse is true when the frequency of the measuring beam is higher than the magic frequency.

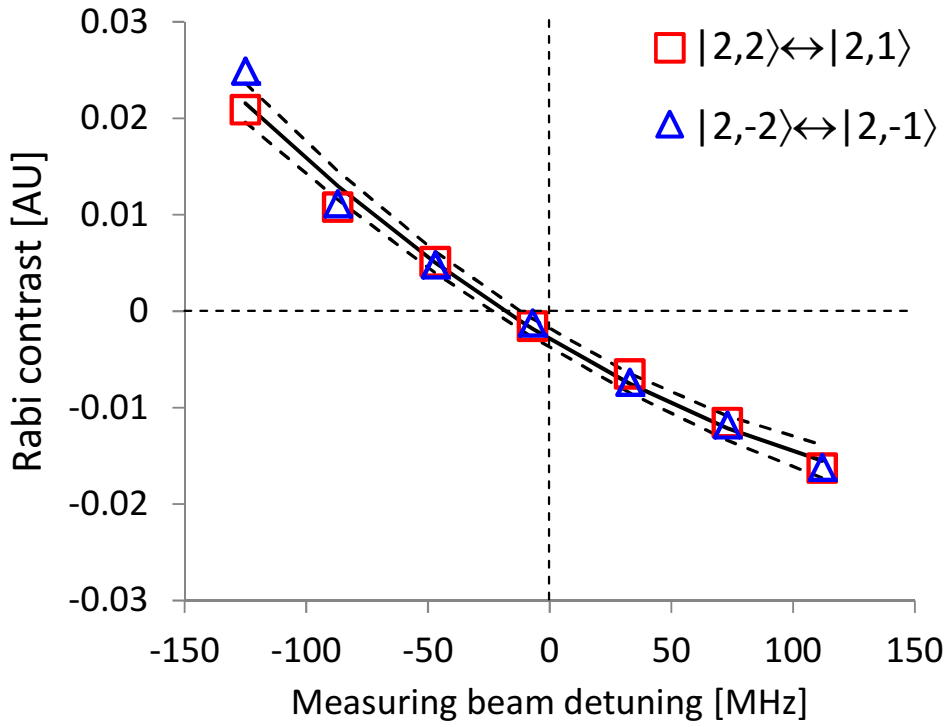

Figure 5.8: Rabi contrast vs. measuring beam detuning Δf. The Rabi contrast is defined as the parameter "c" [Eq. (5.3)] in the functional form of the curves fitted to the data presented in Figs. 5.6 and 5.7. The solid line is a 2^{nd} order polynomial fit to the data; the two dashed lines are fitted to the upper and lower $\pm 10\%$ uncertainty limits of c (see Table 5.4). At vanishing contrast, the detuning of the measuring beam is $\Delta f = -18 \pm 5$ MHz. Note that the contrast flips sign at the magic frequency, which reflects the π phase shift observed in the optical density plots (Figs. 5.6 and 5.7) when Δf changes sign (see text).

Figures 5.6 and 5.7 validate qualitatively our theory: the absorbance of a light beam tuned within ± 15 MHz of the magic frequency is independent of the distribution of the population amongst the Zeeman sub-levels (see Fig. 3.7). Figure 5.8 lets us measure the magic frequency by fitting a curve to the Rabi contrast data (the parameter "c" - see Table 5.4) and finding its intersection with the horizontal axis (vanishing contrast). The result is that the contrast vanishes at $\Delta f = -18$ MHz. The two dashed lines on Fig. 5.8 represent the upper and lower limits of the parameters "c" (see Table 5.4), and their intersections with the horizontal axis provide the upper and lower error on the measured magic frequency: ± 5 MHz. Thus there is a difference of $\Delta f = -18 \pm 5$ MHz between the measured magic frequency and the calculated value.

Let us now estimate the possible sources of this difference.

- **Uncertainty of the measuring beam frequency**. We estimate the uncertainty of the frequency of the measuring beam at ± 2 MHz due to uncertainty in the laser locking point.

- **Uncertainty of the pressure shift**. The pressure shift is part of the calculation of the magic frequency [see Eq.(5.1) and preceding text]. There are two ways to estimate the uncertainty in the pressure shift:

  1. Calculation. Based on supplier data, we estimate the Ne pressure at 7.5 ± 0.5 Torr; the shift/Torr data are given by Table 4.2: -3.7 ± 0.5 MHz/Torr, thus the pressure shift is -28 ± 4.2 MHz (summing in quadrature the fractional uncertainties).
  2. Independent measurement. The pressure shift can be measured; such a measurement was performed [73]. The resulting pressure shift is -26 MHz and the estimated overall uncertainty is ± 10 MHz.

Using a middle value of ± 7 MHz for the uncertainty of the pressure shift, and summing in quadrature all uncertainties, we get that the difference between the calculated and measured magic frequency is -18 ± 8.8 MHz, or a deviation of about 2σ. Thus we can conclude that we have observed a good (but not perfect) agreement between our theory and the experimental results.

5.6 Final notes on our population measurement method

We have seen in this section that our measuring method is capable of providing absorbance data with a temporal resolution of $\sim 5\,\mu$s, and clearly noticing variations of less than 1% in the measured absorbance. We also validated our theory that at or near the magic frequency the absorbance of an alkali vapor is independent of the distribution of population amongst the Zeeman sub-levels.

Furthermore we note that at the magic frequency (when $\Delta f \approx 0$) the calibrated absorbance data in Figs. 5.6 and 5.7 is equal to the value of p_2, the population in the $|F = 2\rangle$ hyperfine state. Thus we see that the optical pumping process manages to raise the population of the $|F = 2\rangle$ hyperfine state to 93% (Fig. 5.6, $\Delta f = -7$ MHz) and 96% (Fig. 5.7, $\Delta f = -7$ MHz). Since only the external $|2, 2\rangle$ Zeeman sub-level is a dark state, it is reasonable to assume that most of the population is accumulated there. So we have an indication that our pumping process is effective.

Chapter 6

Conclusions and outlook

In this thesis we present a simple model for the interaction of linearly polarized light with alkali atoms. The model reveals a *magic frequency* for which light is equally scattered by all the Zeeman sub-levels of the hyperfine ground state. We show analytically that such a magic frequency always exists based on the Wigner-Eckart theorem and on inherent properties of Clebsch-Gordan (CG) coefficients. We explore numerically the properties of the model, and use an exact calculation to determine its validity in the presence of a magnetic field. We experimentally demonstrate the magic frequency. We expect the magic frequency to be useful in a wide range of applications, in addition to the robust measurement of the hyperfine population $\rho^{(0)}$. From a fundamental point of view, the magic frequency represents a unique cancellation effect in which light-matter interaction becomes rotationally invariant although the atomic sample as well as the light beam and its polarization all have a well defined direction. As $\rho^{(0)}$ is the only polarization moment which is a scalar, this means that the contributions of all other polarization moments cancel out, a phenomenon which may shed interesting new light in the realm of group theory.

Note: After this thesis was completed, our attention was drawn to previous works by W. Happer and B. S. Mathur. In a 1967 paper [74] Happer and Mathur present an effective operator formalism for optical pumping, and later [75] Mathur, Tang and Happer apply this formalism to study light propagation in optically pumped alkali vapors (focusing on ^{87}Rb). From the results of these works one may infer the existence of such a magic frequency. Taking the above into account, the novelty in our work is the development of the simplified model which predicts the phenomenon and enables a direct calculation of the role of different parameters. Furthermore, our work provides the first experimental confirmation of the effect. We survey the previous work in App. F.

Our work may have opened the way for several interesting studies. Below we briefly outline some suggestions.

Upgrade of the measurement method. The population measuring scheme we developed utilizes a π polarized light beam and a single photodiode that records the intensity of that beam as it emerges from the vapor cell (Fig. 4.2). Note that the emerging beam remains π polarized. (Reminder: in a π configuration, the electric field of the light oscillates parallel to the direction of the DC magnetic field: $\theta = \pi/2$ and $\phi = 0$ in Fig. 3.2).

A possible upgrade of the measuring method may include:

- using a linearly polarized light that is not in the π configuration ($\theta \neq \pi/2$ and/or $\phi \neq 0$);
- using a polarization analyzer that can measure the intensity of each component of the light emerging from the vapor cell.

We know the angles θ and ϕ, and with the polarization analyzer (or similar equipment) we may be able record the intensity of each of the emerging light components. Using the transformations of Sec. 3.1 [Eqs. (3.3) and (3.4)] we may be able the produce intensity plots similar to Fig. 4.3 for each of the light components E_0, E_+ and E_-.

As can be seen by inspection of Eqs (3.13), the same magic frequency exists separately for the absorption of the E_0 component and separately for absorption of the sum of the E_+ and E_- components. Thus we will by able to use the plot of E_0 to measure the hyperfine population in a manner similar to that described in Ch. 4. In addition, we probably will be able to deduce additional information of the state of the vapor from the plots of the E_+ and E_- components.

Magic frequencies for other atoms. Our simple model (Sec. 3.1) is developed for alkali atoms, which have just one valance electron in a $|J = 1/2\rangle$ ground state. Exploring such models for atoms with more complex electronic structure may reveal similar magic frequencies, representing possible invariance in the interaction of light with these atoms.

Study of the CG coefficients. Although these coefficients were introduced more than 60 years ago, there is still an ongoing research into their properties and calculation methods (see [76] and references therein). We have seen in Eqs. (3.13) and (E.19) that two completely different sums of CG coefficients cancel: one was equal to the negative of the other. This may be an isolated case, but it can also points to more fundamental properties of the CG coefficients. A detailed study into the source of this cancellation may shed new light on some hidden properties of the the CG coefficients.

Appendices

Appendix A

The modulated laser subsystem

Two coherent laser beams with a fixed frequency difference are an important spectroscopy tool. Such beams are needed to induce Raman transitions (see Sec. 2.7.6) or to investigate EIT phenomena (see Sec. 2.7.7). In this appendix we will review the design, setup and performance of the "Raman system", a system capable of producing such a pair of coherent beams − the "Raman beams". Before we describe the system, we need to define what we mean by the coherence of two beams with different frequencies, and describe a method to measure it. For this purpose, let the electric field of one beam be $\mathbf{E}_1 = \mathbf{E}_1^0 \sin[\omega_1 t + \phi_1(t)]$ and the second $\mathbf{E}_2 = \mathbf{E}_2^0 \sin[\omega_2 t + \phi_2(t)]$, where $\mathbf{E}_i^0$ describe the amplitudes and polarizations, ω_i the angular frequencies and $\phi_i(t)$ are the random phases. For ease of presentation, we assume that $\mathbf{E}_1^0 = \mathbf{E}_2^0$, and both beams propagate collinearly to a fast photodiode. The combined electric field on the photodiode is the sum of the two fields:

$$\begin{aligned}\mathbf{E}_1 + \mathbf{E}_2 &= \mathbf{E}_1^0\big(\sin[\omega_1 t + \phi_1(t)] + \sin[\omega_2 t + \phi_2(t)]\big) \\ &= \mathbf{E}_1^0 \sin\frac{(\omega_1+\omega_2)t + \phi_1(t) + \phi_2(t)}{2} \cos\frac{(\omega_1-\omega_2)t + [\phi_1(t) - \phi_2(t)]}{2}.\end{aligned} \tag{A.1}$$

The sine factor in Eq. (A.1) oscillates at a frequency $\sim (\omega_1 + \omega_2)/2$, which is the average of the two frequencies and is in the optical domain. The argument of the cosine factor is $\big([\omega_1 - \omega_2] + [\phi_1(t) - \phi_2(t)]\big)/2$. When this factor vanishes, the two beams interfere destructively, and the total amplitude is 0. When it equals 1, the two beams interfere constructively, and the total amplitude is maximal. These amplitude oscillations are termed the "beat-note", and if $\phi_1(t) - \phi_2(t) =$ constant then the amplitude oscillation frequency is the beat frequency ω_{beat}:

$$\omega_{\text{beat}} = |\omega_1 - \omega_2|, \tag{A.2}$$

which is twice the argument of the cosine in Eq. (A.1).

We are now in a position to both define and measure the coherence of two laser beams: two laser beams of frequencies ω_1 and ω_2 are coherent if their beat-note frequency ω_{beat} [see Eq. (A.2)] is time independent. In other words, the beams are coherent if $\phi_1(t) - \phi_2(t) =$ constant independent of time. To measure the coherence of the two beams, we aim the beams at an AC photodiode fast enough to respond at the frequency $|\omega_1 - \omega_2|$, feed the output of the photodiode to a spectrum analyzer, and measure the width of the beat signal.

Since we work with ^{87}Rb, both the Raman beams' wavelengths are near 780nm (the wavelength of the D2 transitions), and their frequency difference equals the ^{87}Rb hyperfine splitting frequency : $f_{\mathrm{HS}} = 6,834,682,610\mathrm{Hz}$ (see Fig. 2.13).

The Raman system includes three lasers: A modulated master laser and two slave lasers.

A.1 The modulated master laser

The modulated master laser is an ECDL (See [63]) where the DC current input to the laser diode is modulated by a microwave signal at a frequency $f_{\mathrm{HS}}/2$, and where the grating assembly is mounted on a 25 mm micrometric translation stage (see Fig. A.1).

Similar to other ECDLs, when only DC current is fed to the laser diode, and the grating is properly aligned, the beam generated by the laser diode bounces back and forth between the grating and the back facet of the laser diode, creating the external cavity. (The back facet is the uncoated facet of the laser diode, see bottom part of Fig. A.1.) The wavelength λ of the laser beam is given by the constructive interference condition of the grating (d_{grating} is the grating spacing):

$$\sin\alpha = \frac{\lambda}{2d_{\mathrm{grating}}}. \tag{A.3}$$

Tuning of the beam's wavelength is possible by adjusting the angle α. Coarse tuning is done by a tuning screw, and fine tuning by a piezoelectric transducer (PZT) (not shown).

The anti-reflection (AR) coating on the front facet of the laser diode eliminates the internal cavity, so that the resonance condition of the external cavity dominates the possible (un-modulated, or "carrier") frequencies f_{cr} of the laser beam:

$$f_{\mathrm{cr}} = M\frac{c}{2l_{\mathrm{eff}}}, \tag{A.4}$$

where M is an integer, c is the speed of light and l_{eff} is the effective cavity length that is related to the refractive index n_{LD} of the laser diode (see Fig. A.1):

$$l_{\mathrm{eff}} = L_1 \times n_{\mathrm{LD}} + (L_2 - L_1) \times n_{\mathrm{air}}. \tag{A.5}$$

Since the refractive index n_{LD} is a function of both the laser diode temperature and the DC current through it, the current and temperature must be stabilized. Modifying any of them can be used to tune the laser frequency. The free spectral range (FSR) of this laser, which is the difference, in frequency, between two consecutive modes [two consecutive values of M in Eq. (A.4)], is:

$$\mathrm{FSR} = \frac{c}{2l_{\mathrm{eff}}}. \tag{A.6}$$

In our system we use AR-coated laser diodes (Eagleyard Photonics EYP-RWL-0780-00100-1000-SOT01). To modulate the master laser beam we superimpose on the DC input current a microwave current at frequency f_{MW} via the "MW feed" port of the bias T (see Fig. A.1). The resulting spectral composition of the laser beam now includes, in addition

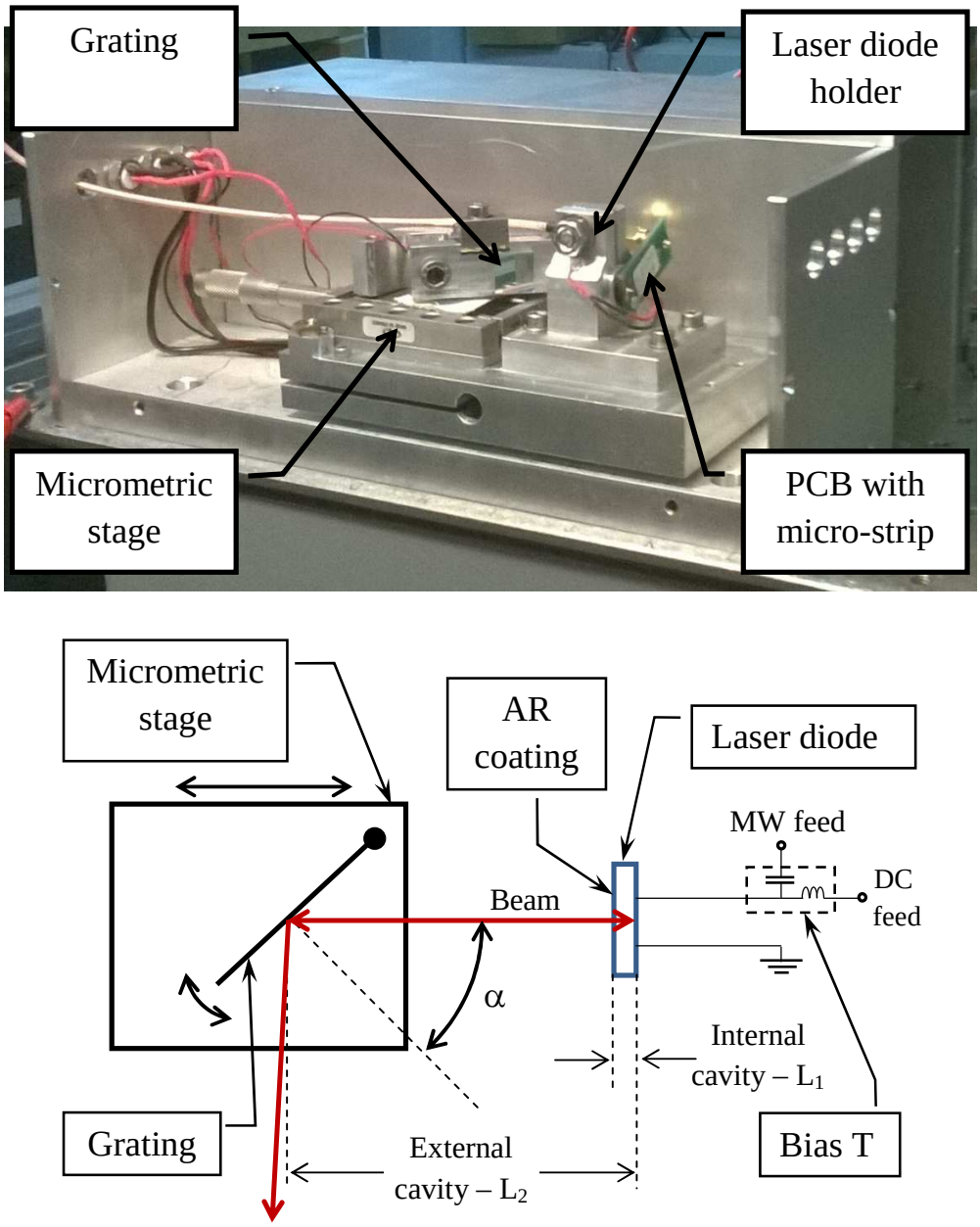

Figure A.1: The modulated master laser. Top: picture of the laser. Bottom: schematic diagram of the main components. AR coating – anti-reflection coating. See text for details.

to the main (also called the "carrier") frequency $f_{\rm cr}$, sidebands at frequencies $f_{\rm cr} \pm k \times f_{\rm MW}$, where k is an integer.

The laser beam modulation is of a type known as phase modulation, and the electric field of the light is given by:

$$E = E_0 e^{i\omega_{\rm cr} t + m\sin(\Omega_{\rm MW} t)};\ \omega_{\rm cr} = 2\pi f_{\rm cr},\ \Omega_{\rm MW} = 2\pi f_{\rm MW}, \tag{A.7}$$

where m is the modulation index – a parameter that indicates the depth, or strength, of the modulation. We can develop Eq. (A.7) and have (for simplicity, we dropped the

subscripts $_{\rm cr}$, $_{\rm MW}$):

$$E = E_0\left(\sum_{k=0}^{\infty} J_k(m)e^{i(\omega+k\Omega)t} + \sum_{k=0}^{\infty}(-1^k)J_k(m)e^{i(\omega-k\Omega)t}\right), \tag{A.8}$$

where $J_k(m)$ is the k^{th} Bessel function of the first kind. Each term in Eq. (A.8) with $k \geq 1$ represents a "sideband" – a part of the beam that oscillates at the frequency $f_{\rm cr} \pm k \times f_{\rm MW}$, with a relative sideband amplitude of $J_k(m)$. In Fig. A.2 we plot the first three Bessel functions as a function of the modulation index m. We see that as the modulation index increases, the amplitude of the carrier (J_0) decreases while the amplitudes of the first and second sidebands go up. For a modulation index of 2.4, the amplitude of the carrier goes down to zero. This point is called "full carrier suppression".

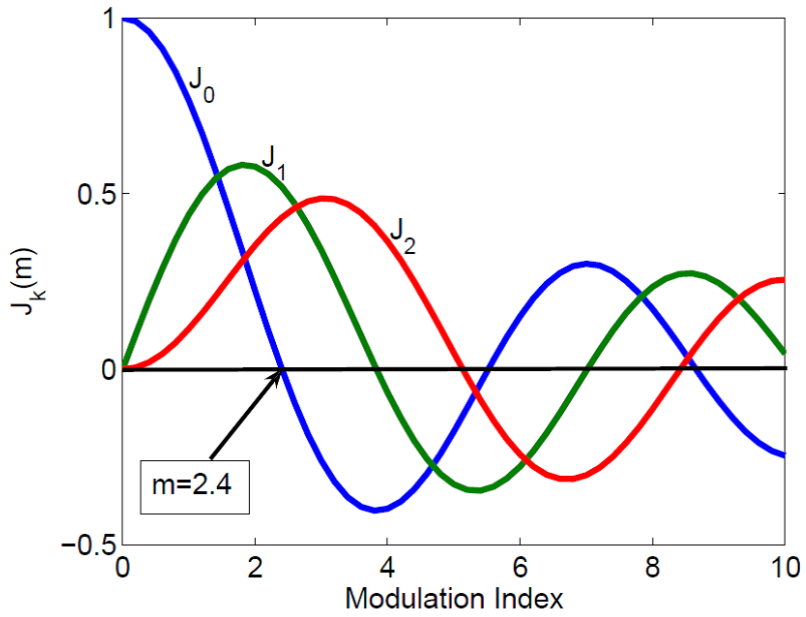

Figure A.2: The first three Bessel functions of the first kind, as a function of the modulation index m. Note that $J_0(2.4) = 0$, which means that the amplitude of the carrier (the component with the unmodulated frequency) is zero. This point is known as "full carrier suppression".

A.2 Enhanced modulation method

Typically, as the modulation frequency goes up, the modulation index goes down, for several reasons.

One reason is the decay of the MW component of the feed current as it flows through several wires and connectors from the bias T to the laser diode. To overcome this problem, we prepared a 50 Ω microstrip on a printed circuit board (PCB), welded a "subminiature version a (SMA)" connector on one side of the microstrip, and welded the laser diode leads

directly to the other side of the microstrip. We used an SMA–SMA 10GHz coaxial cable to connect the output of the bias T to the microstrip's connector. The PCB and the cable are visible in the top part of Fig. A.1.

Another reason that the modulation index degrades is the fact that as the modulation frequency goes up, the sideband frequency gets further away from the carrier frequency, which is the resonance frequency of the external cavity. Thus, the cavity suppresses the sidebands, and their amplitude goes down rapidly. In our setup, as the modulation frequency approaches 1GHz, the modulation index almost vanishes. Since we need to modulate at about 3.4GHz, this obstacle seems almost prohibitive.

We found an innovative solution to this problem. Our grating assembly is mounted on a 25 mm micrometric translation stage, and we have several locations to connect the grating assembly to the stage, so that we are able to vary L_1, the length of our external cavity, from 12 mm to about 50 mm. Thus we were able to tune the external cavity so that its FSR [see Eq. (A.6)] is equal to our modulation frequency. Now the cavity supports both the carrier frequency as well as the sidebands, and the modulation index goes up dramatically.

We published a detailed description of this method and its results [77], and submitted a patent application for this modulation enhancement method [78].

A.3 The full Raman laser system

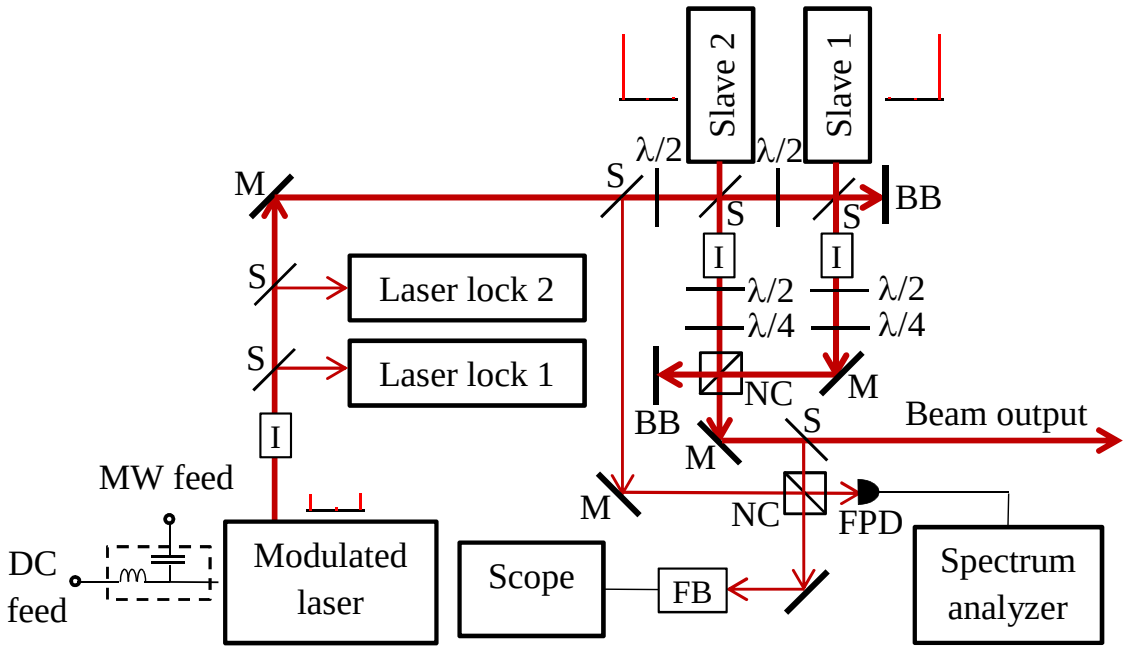

Figure A.3: The full Raman laser system. BB – beam blocker; DC – direct current; FB – Fabry-Perot interferometer; FPD – fast photodiode (10GHz); I – optical isolator; M – mirror; MW – microwave NC– non-polarizing beam-splitter cube; S – beam sampler (5%); $\lambda/2$, $\lambda/4$ – wave plates. Laser beams are marked in red. Schematic spectra are shown above the modulated laser, beside the slave lasers and above the beam output.

The full Raman laser system includes three lasers: the modulated master laser and two slave lasers. This system is presented in Fig. A.3. The modulated laser, operating using the enhanced modulation method (see Sec. A.2), produces two frequency sidebands, as shown by the schematic spectra drawn above it in Fig. A.3. These beams pass via the optical isolator to the slave lasers. Three beam samplers deflect small portions of this double-frequency beams; two of those go to the laser lock units (see Sec. A.5) and the third goes to the beam analysis part of the system (see Sec. A.4). Two additional beam samplers direct part of the double-frequency beam to each of the slave lasers. The slave lasers each contain a single-mode $\sim 780\,\mathrm{nm}$ edge-emitting diode lasers (such as Thorlabs L785P090) in a temperature-controlled collimation tube with a collimation lens (Thorlabs LT230P-B) and a combination temperature controller/DC current driver (such as Thorlabs ITC 510).

When free-running, the slave laser produces a beam with a width of several tens of MHz – quite broad, compared to the 1MHz width of each of the components of the modulated beam. The slave laser frequency is controlled by the current and temperature of the laser. To inject the slave laser with the modulated beam, we need to match their modes. First, both beams must be co-linear (we achieve co-linearity $< 1\,\mathrm{mrad}$). Then, using a $\lambda/2$ wave-plate, we align the linear polarization of the modulated beam to be parallel to the polarization of the slave laser beam. The last step in the injection of the slave laser is to scan the current of the laser diode until the slave's free-running frequency is close to one of the frequencies of the modulated beam. When this happens, the slave laser "locks" on to one of the components of the modulated beam and produces a strong and narrow ($\sim$1MHZ) beam that is coherent with one of the components of the modulated beam. In the same manner, the second slave laser is locked to the other component of the modulated beam. This is shown in the schematic spectra beside each of the slave lasers in Fig. A.3. Note that the "locking" can occur for only one frequency, so each slave current is tuned so that it selectively amplifies only one of the sidebands.

While each component of the modulated beam has a power of about 1-2mW, each slave produces a beam of about 70mW. Consequently we now have two 70mW, spatially separated coherent laser beams with a fixed frequency difference. We can tailor their polarization separately with the $\lambda/2$ and the $\lambda/4$ wave-plates. The two slave laser beams are then combined in the non-polarizing beam-splitter cube to produce the output beam.

A.4 Analysis of the Raman beams

The Raman beam analysis section is shown at the bottom of Fig. A.3. A beam sampler deflects part of the output Raman beam to the top facet of a non polarizing beam splitter cube (lower NC in Fig. A.3). This cube serves as the "input" of the analysis section of the system. Another sampler directs a part of the modulated beam to the left facet of the same cube. Each of these beams emerges from the two remaining facets: one facet is aimed at a fast photodiode (EOT ET-4000, labeled FPD in Fig. A.3) and the other at a scanning Fabry-Perot interferometer (Toptica FP 100, labeled FP in Fig. A.3). The Fabry-Perot interferometer produces the spectral composition of its input beam(s). By blocking/unblocking any of the input beams we can get a combined spectrum of all the beams, a spectrum of just the modulated beam, or a spectrum of just the the output beam.

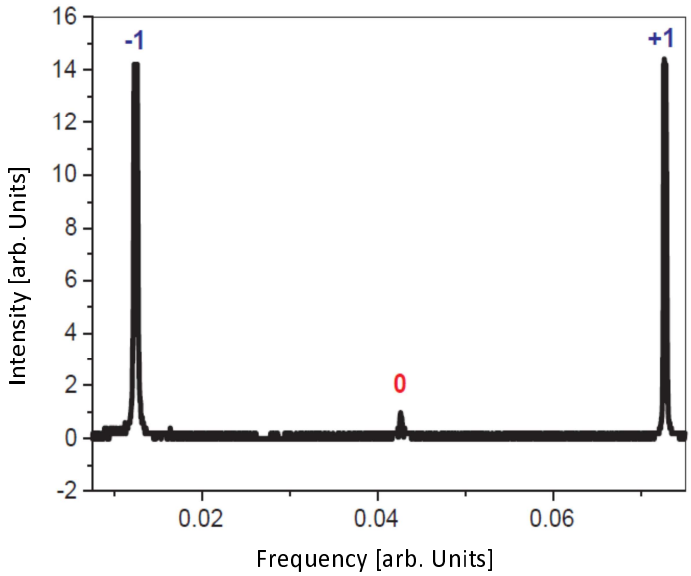

Figure A.4: Spectrum of the output beam of the Raman laser system registered by the Fabry-Perot interferometer (FP in Fig. A.3). The un-modulated beam ("carrier", labeled "0") is at 780.24 nm, the modulation MW frequency is 3.417GHz, and the MW power is 17dBm ($\sim$0.06mW). Note that the intensity of the two side bands (labeled -1 and $+1$) is much higher that that of the carrier, which is almost completely suppressed. (Taken from [70].)

A spectrum of the output beam is presented in Fig. A.4. Note that most of the intensity is in the two sidebands (marked -1 and $+1$) , while the carrier (marked "0") is almost completely suppressed.

The two sidebands in the output beam reach the fast photodiode together, resulting in a beat-note [see Eq. (A.2)]. The fast photodiode signal is fed to the spectrum analyzer, and results in a beat-note spectrum. Such a spectrum is presented in Fig. A.5. The beat-note width as seen in this spectrum is $\sim$ 1Hz, which is 6 orders of magnitude lower than the few MHz spectral width of each of the side bands. This narrow beat-note width verifies that the term $[\phi_1(t) - \phi_2(t)]$ [see Eq. (A.2)] is independent of time to within 1Hz and the two sidebands can be regarded as coherent for any process having a time scale not larger than 1 second. We note that the observed width of 1Hz is probably determined by the spectrum analyzer capabilities rather then the true width of the beat-note.

A.5 The Raman laser lock units

The modulated laser, like any other ECDL, needs a locking unit if we wish to stabilize its frequency. To lock an ECDL we typically use a method based on Doppler-free spectroscopy in a vapor cell [69, 79]. "Laser lock 1" (see Fig. A.3) is based on polarization Doppler-free spectroscopy in a Rb vapor cell, known as a "polarization lock" [69, 70]. Later, we added "Laser lock 2", which is based on a retro-reflecting polarization Doppler-free spectroscopy method developed in our group [80]. We evaluated the performance of "Laser lock 2", and verified that it was as effective as the more traditional "Laser lock 1".

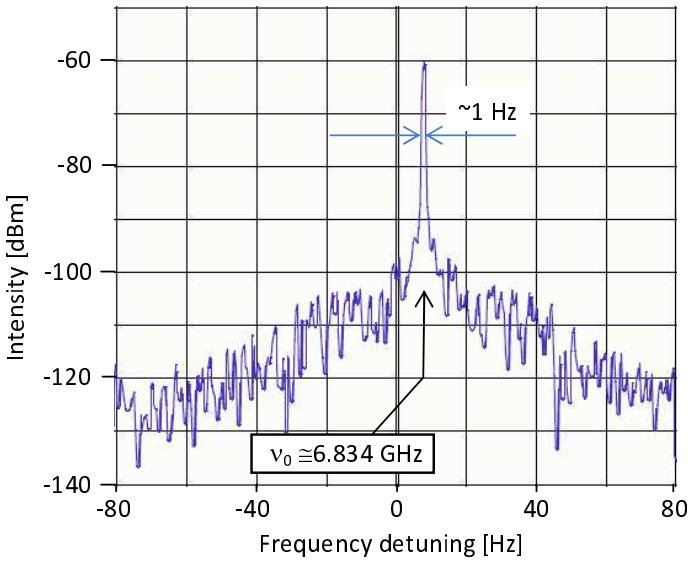

Figure A.5: Spectrum of the beat-note of the two sidebands in the output beam of the Raman laser system (see Fig. A.4), as registered by the fast photodiode labeled FPD in Fig. A.3. The narrow width (1Hz) of the beat-note confirms that the two sidebands are coherent.

A.6 Future work on the Raman system

The combination of the modulated laser and the retro-reflecting polarization Doppler-free spectroscopy section ("Laser lock 2") opens some interesting possibilities. A minor modification to the "Laser lock 2" subsystem can add CPT [58] capabilities to the system. This may lead to the utilization of the retro-reflecting polarization spectroscopy unit both for laser locking and for CPT-based magnetometry.

Appendix B

Details of the experimental system

The experimental system is a versatile system aimed at the study of the response of a variety of rubidium vapor cells to several types of radiation and fields. The system has four main modules, listed briefly below:

- The laser module. In addition to the modulated laser system (see App. A) operating at ∼780nm, we have two additional lasers: the auxiliary laser, operating at ∼795nm, and the pump-probe laser, operating at ∼780nm (see Sec. B.1).

- The beam management module. This module includes means for switching the laser beams on and off, for controlling the beams' size, shape and polarization, and for combining beams and directing them to the vapor cell (see Sec. B.2).

- The vapor cell environment. This module includes the mechanical holder of the cell, enabling accurate positioning and easy replacement of vapor cells. In this module we control the magnetic field in the cell, and transmit electromagnetic radiation (from 1MHz up to 6.8GHz) to the cell (see Sec. B.3).

- The experimental control and data acquisition system. This module controls the experimental sequence including light, RF and MW fields as well as static magnetic fields, which the cell is exposed to. It also acquires and analyzes the data (see Sec. B.4).

A schematic description of the four modules of the experimental system is presented in Fig. B.1. In general, the pump-probe laser is utilized to initiate the state of the vapor by optically pumping all the population to one of the hyperfine ground states, and then it is switched off. Two lasers are required to pump the entire population to a specific Zeeman sub-level, for which we add the auxiliary laser. Next, the vapor atoms are irradiated by light, MW, or RF or by some combination of them. Vapor properties such as the internal state population distribution, its polarization, etc. are determined using the pump-probe laser and the measuring method described in Ch. 4.

Sections B.1 - B.4 provide descriptions of each module, while in Sec. B.5 we present an illustrative example. The experimental system is very flexible and was frequently reconfigured for different studies of atom-light interaction.

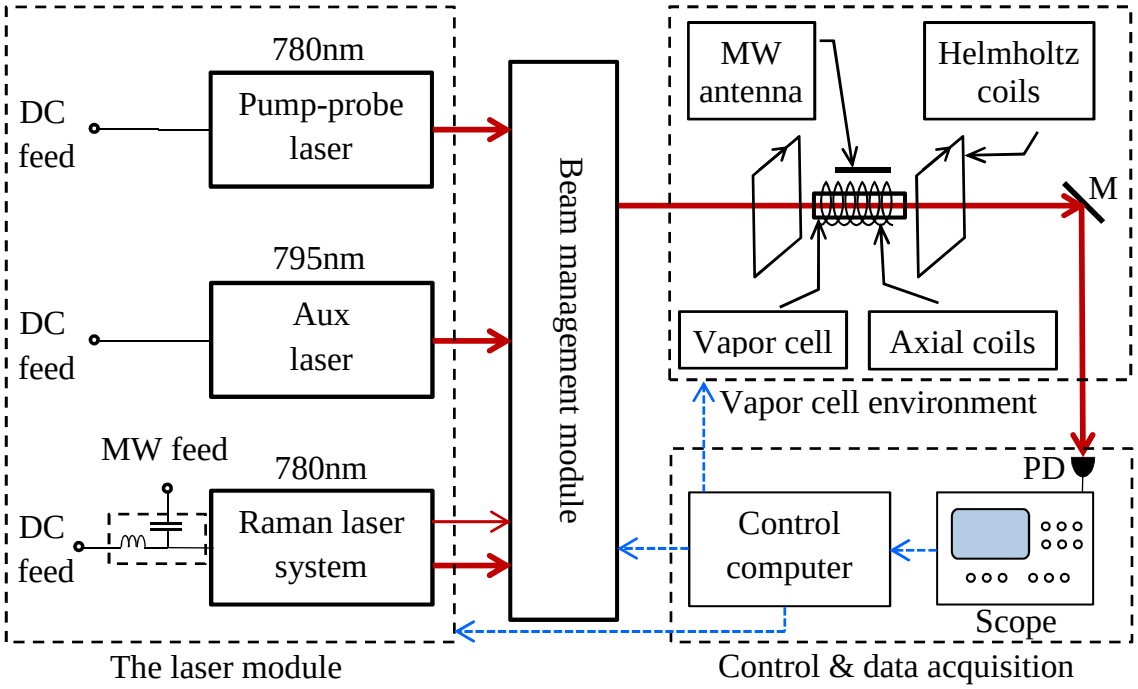

Figure B.1: Schematic of the experimental system. The **laser module** includes the Raman laser system, operating at 780nm and producing two beams (see App. A and Sec. B.1), an auxiliary laser operating at 795nm, and the pump-probe laser, operating at 780nm. The **beam management module** contains: (a) passive optical elements such as wave plates, lenses, mirrors, filters etc. that tailor the shape, size, intensity and polarization of each beam; (b) polarizing and non-polarizing beam splitter cubes used to combine beams; (c) acousto-optic modulators (AOMs), capable of blocking each beam and modifying the beam frequencies. The overall role of the beam management module is to produce a tailored sequence of beam pulses to the vapor cell (see details in Sec. B.2). The **vapor cell environment** produces and controls the DC magnetic field inside the cell, as well as provides means to transmit to the cell both RF radiation via an axial coil and MW radiation via a MW patch antenna (see details in Sec. B.3). The **control and data acquisition module** controls the other modules, and analyzes the data received via the photodiode PD (see details in Sec. B.4).

B.1 The laser module

the laser module includes three continuous wave (CW) laser sources, as shown in Fig. B.1

- the Raman laser system, operating at $\sim 780\,\mathrm{nm}$, is capable of producing either a $\sim 30\,\mathrm{mW}$, un-modulated laser beam or a double-frequency laser beam (see App. A);
- the auxiliary laser, operates at $\sim 795\,\mathrm{nm}$ and produces a $\sim 50\,\mathrm{mW}$ beam;
- the pump-probe laser, operating at $\sim 780\,\mathrm{nm}$, producing a $\sim 50\,\mathrm{mW}$ beam.

The auxiliary and the pump-probe lasers are ECDLs [63], each equipped with a polarization lock based on a Rb vapor cell [69, 70]. The auxiliary laser may be locked on any of the hyperfine $5^2S_{1/2} \leftrightarrow 5^2P_{1/2}$ (D1) transitions (see Fig. 2.12), and the pump-probe laser may be independently locked on any of the hyperfine $5^2S_{1/2} \leftrightarrow 5^2P_{3/2}$ (D2) transitions (see Fig. 2.13). When locked, these lasers provide stable single-frequency light with spectral widths of $\sim 1\,\mathrm{MHz}$.

B.2 Beam management module

The experimental system was designed to be flexible so that it may easily accommodate different experimental schemes. The beam management module provides this flexibility. The module includes three acousto-optic modulator (AOM)s, two of which are used in a double-pass configuration [81]. Each double-pass AOM is capable of switching a beam on and off within less than a microsecond and with an extinction ratio of 10^{-7}. The double-pass AOM shifts the beam's frequency by $\pm 2 \times (100 \pm 20)\,\mathrm{MHz}$. Thus, combining the AOM's shift with the transition used to lock the laser (see Fig. B.2), we can tune its frequency to any value within a few hundred MHz around the D1 and D2 transition frequencies of ^{87}Rb (the accuracy of the beam's frequency is $\pm 2\,\mathrm{MHz}$). The third AOM is a single-frequency, single-pass AOM used to switch the modulated beam on and off. The AOMs enable precise timing of the laser beams directed into the vapor cell via commands from the control computer (see Fig. B.1 and Sec. B.4).

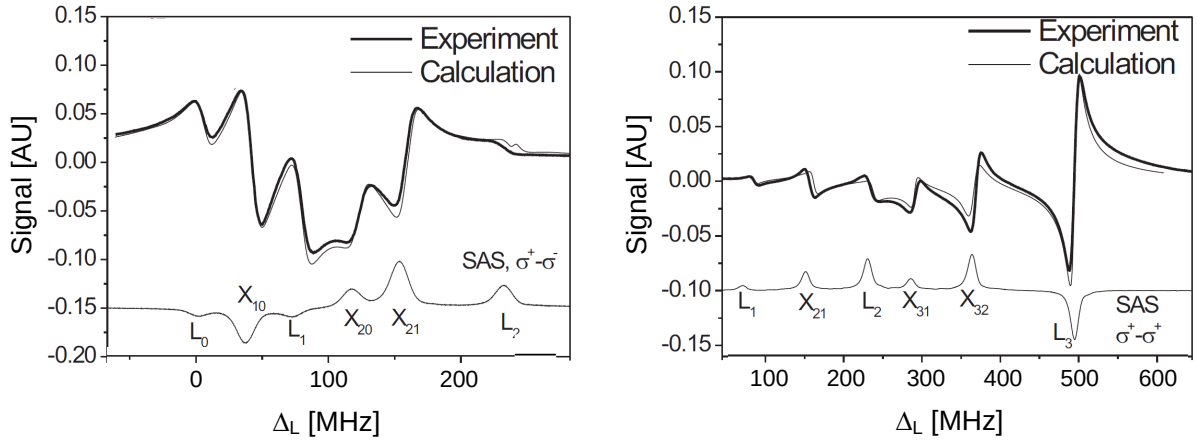

Figure B.2: Polarization spectroscopy plots, providing laser locking frequencies (adapted from [82]). Left: polarization spectroscopy of transitions from the $5^2S_{1/2}|F=1\rangle$ hyperfine ground state to the excited $5^2P_{3/2}$ manifold. The laser frequency is denoted by Δ_L as defined in Eq. (3.7). L_i denotes the transition to the $|F'=i\rangle$ excited state and X_{ij} denotes the crossover frequencies. Right: polarization spectroscopy from the $5^2S_{1/2}|F=2\rangle$ state to the $5^2P_{3/2}$ manifold. We can lock the laser on the zero-crossing point of any of the slopes (see [80, 82] for additional details).

In addition to the AOMs, the beam management system includes:

- wave plates for adjusting the required polarization of each beam;

- filters for managing the intensity of the beams;
- mirrors and cubes to combine the beams and direct them to the vapor cell;
- beam expanders and irises to improve the uniformity of the beam's intensity (see Fig. B.3).

The specific arrangement of these elements changes from experiment to experiment.

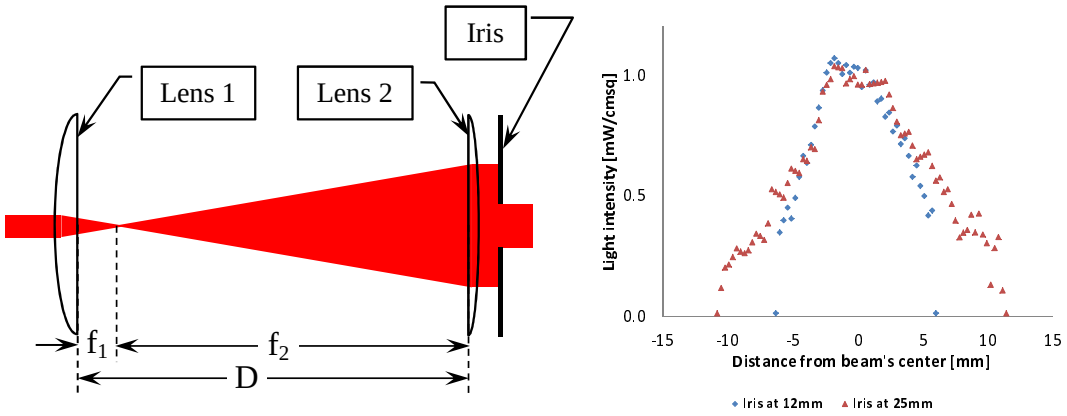

Figure B.3: Improving beam uniformity with a beam expander. Left – optical arrangement ($f_1/f_2 \approx 20$, iris aperture is 1 to 25 mm). Right – beam intensity profiles for two values of the iris setting. With the iris set to 25 mm, only about 25% of the cross section of the beam has a light intensity above 0.5 mW/cm^2. With the iris set to 12 mm, 50% of the beam's cross section has a light intensity above 0.5 mW/cm^2.

B.3 The vapor cell environment

A general view of the vapor cell environment is presented in Fig. B.4 with a more detailed view shown in Fig. B.5. The vapor cell environment enables us to control and modify the magnetic field as well as to irradiate the vapor cell with both MW and RF fields and with a combination of laser beams.

Magnetic fields. Three pairs of square Helmholtz coils produce fields of up to ± 1.5 G along each axis of the cell (Fig. B.4). Each pair is connected to an independent DC current source. The magnetic field (measured by a Lake Shore 460 3-channel Gauss-meter) is uniform to within 0.005G over the dimensions of the cell [diameter – 25 mm (along $\hat{x}$ and $\hat{y}$), length – 40 mm (along $\hat{z}$)]. Thus, the earth magnetic field can be compensated, bringing the total magnetic field inside the cell to $|\mathbf{B}| = 0 \pm 0.005$G. Alternatively, we can set the magnetic field components inside the cell to any value -1G$< B_i <$ 1G, where i can stand for x, y, z. The current drivers that supply these coils are manually controlled, so the above mentioned magnetic fields are fixed throughout the experimental sequence. In addition, we have two computer-controlled current drivers. One of them is connected to a fourth set of Helmholtz coils aligned in the y direction, producing a controllable -1G$< B_y <$ 1G component. The other current driver feeds an axial coil (see Fig. B.5). We have several such axial coils,

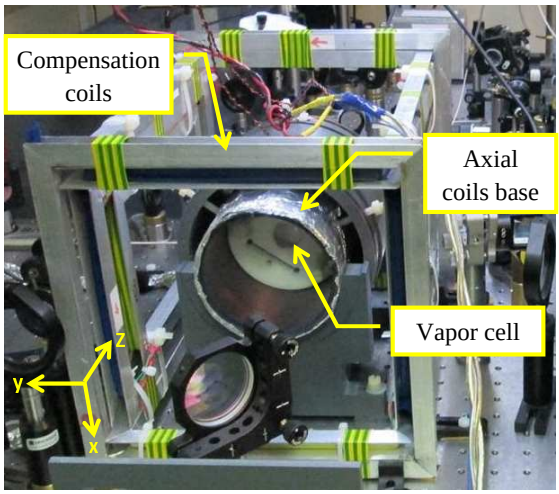

Figure B.4: General view of the vapor cell environment. The outermost parts of this environment are the compensation coils: one pair of square Helmholtz coils for each axis and an additional pair for the y axis. The mirror seen at the bottom of the photograph directs the laser beams through the cell.

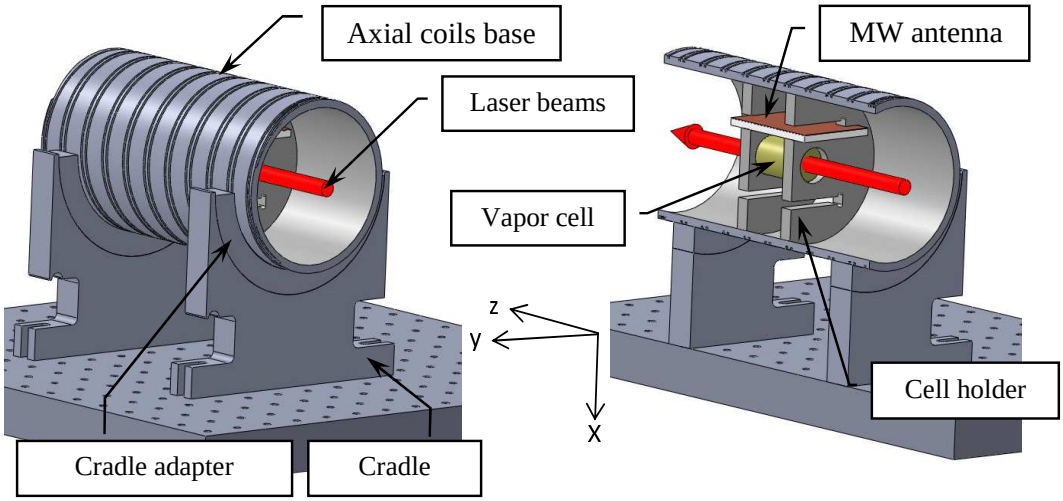

Figure B.5: Detailed schematic of the vapor cell environment. Left – full view of the axial coils base. Right – a cut through the axial coils base. For reference, the length of the axial coil base is 200 mm. The aim of the design is to assure easy and accurate positioning of the vapor cells. The two cradles (left) are positioned and locked such that the laser beam will pass through the centers of their semi-circle top part. The cradle adapters interface with the base of the axial coils such that its axis is co-linear with the beam's center. The cell holders (right) position the cell so that the cell's axis is also co-linear with the beam. This enables us to replace cells and/or axial coils bases, with no need to realign the beam direction or to re-adjust the magnetic fields. The axial coils base seen contains two parallel spiral slots for two separate, but coaxial, coils: one for DC current, and one for RF ($\sim$ 1MHz). Also seen is the "patch type" MW antenna ($\sim$6.8GHz).

capable of producing a field of up to $B_z = \pm 30$G. The computer-controlled current drivers are equipped with specially designed current shutters (see App. D), capable of cutting the current to an inductive load with adjustable (few microseconds to few milliseconds) shutting time.

RF and MW fields. The MW field is transmitted by the MW patch antenna (see Fig. B.5), located about 2 cm above the vapor cell axis. There are several arrangements for transmitting RF. In the one presented in Fig. B.5, one of the two axial coils is used to generate RF radiation along the axis of the vapor cell.

B.4 Control and data acquisition

The control system is based on a National Instrument NI PCI 6733 high-speed analog output card, installed on a desktop computer with a Windows 7 operating system. The main control program (MCP) of the experimental system was developed on the LabView 2010 graphical programming platform. The PCI 6733 card includes its own memory, a central processing unit (CPU) and a clock which enables "real time" operation of some parts of the experimental sequence (time resolution of $1\,\mu$s). The MCP provides the required man-machine interface, coordinates and sequences the operation of all the other devices, and controls the transfer of digital data to and from these devices via the digital communication provided by the general-purpose interface bus (GPIB). However, while the card's outputs can be programmed with a time resolution of $1\,\mu$s, the GPIB-based data transfer may take a few milliseconds, much too slow for accurate experimental control and furthermore it may be interrupted by the Windows operating system.

The PCI 6733 card's analog outputs directly control the following elements:

- AOM 1: AOM type 3080-122, with 1080AF-AENO 2.0W AOM driver, both made by Crystal Technology Inc. Frequency range is 50 to 100 MHz. One analog output controls the driver's frequency, and another controls the driver's power. This second output is also used to switch the AOM driver on and off.

- AOM 2: AOM type 3110-140, with 1110AF-DEFO 1.5W AOM driver, both made by Crystal Technology Inc. Frequency range is 110 ± 25 MHz. One analog output controls the driver's frequency, and another controls the driver's power. This second output is also used to switch the AOM driver on and off.

- AOM 3: AOM type 3080-125, with 1080AF-AIFO 1.0W AOM driver, both made by Crystal Technology Inc. Operating at a fixed frequency of 80 MHz only one analog output is needed to control both the AOM power and to switch it on and off.

- Current shutters: Our current shutters are made in-house, and are capable of switching off an inductively-loaded current within $\sim 2\,\mu$s. The shutting time can be lengthened up to several milliseconds by changing some internal components. The current shutters are activated by a transistor-transistor logic (TTL) digital signal from the digital outputs of the NI PCI 6733 card.

The following devices are primarily controlled via digital communication provided by the GPIB. Some of the devices are controlled both by GPIB based data transfer and by digital and/or analog signals provided by the NI PCI 6733 card.

- Agilent 66312A 20V, 2A DC current source: The MCP sets the current and the voltage of the source and turns it on and off. This current source supplies current (via a current shutter) to the additional y-axis Helmholtz coils (see caption of Fig. B.4).

- HP 6632A 20V, 5A DC power supply: The MCP sets the current and the voltage of the power supply and turns it on and off. This power supply supplies current (via a current shutter) to the axial coil (see Fig. B.5).

- Rodhe & Schwarz SMR 20 (10 MHz to 20 GHz) signal generator: The MCP sets the frequency and amplitude of the signal, turns it on and off, and selects modes of operation (CW, pulsed, frequency sweep etc.). The digital output of the PCI 6733 card provides accurate triggering of pulses and frequency sweeps.

- Agilent 33220A 20 MHz arbitrary waveform generator: The MCP sets the frequency and amplitude of the signal, turns it on and off, and selects modes of operation (CW, pulsed, frequency sweep etc.). The digital output of the PCI 6733 card provides accurate triggering of pulses and frequency sweeps.

- Tectronix TDS 1002 60 MHz 2-channel 8-bit digital oscilloscope: This scope reads the current of the photodiode marked "PD" (see Fig. B.1). The MCP can, via the GPIB digital communication, set the modes of operation and download waveform data from the scope. A digital output of the PCI 6733 card is connected to the external trigger port of the scope, providing accurate triggering.

- Accubeat AR40A 10 MHz frequency standard (Allan deviation below 3×10^{-12} @100 s, aging $< 1 \times 10^{-9}$/year). The standard produces an accurate 10 MHz signal, serving as an external reference to the signal generators and to other devices.

The experiment's control system is based on the PCI 6733 and on the independent control features of the above mentioned devices, all coordinated by the MCP. The purpose of the MCP is to subject the vapor cell to a predetermined sequence of different fields (DC, RF, MW and optical light) and measure and analyze the light intensity emerging from the vapor cell (see Fig B.1). The MCP is flexible and can be easily modified to fit different experiments. The general structure of the MCP is listed below (see also the flowchart in Fig. B.6). An example illustrating the operation of the control system is presented in Sec. B.5.

- **Parameters input.** All the experimental parameters are loaded via the control panel [graphical user interface (GUI)] of the LabView based MCP.

- **Initiation.** This sequence initiates, via GPIB, all the external devices to the correct modes of operation and sets relevant parameters, such as current levels for DC power supplies or frequencies for signal generators.

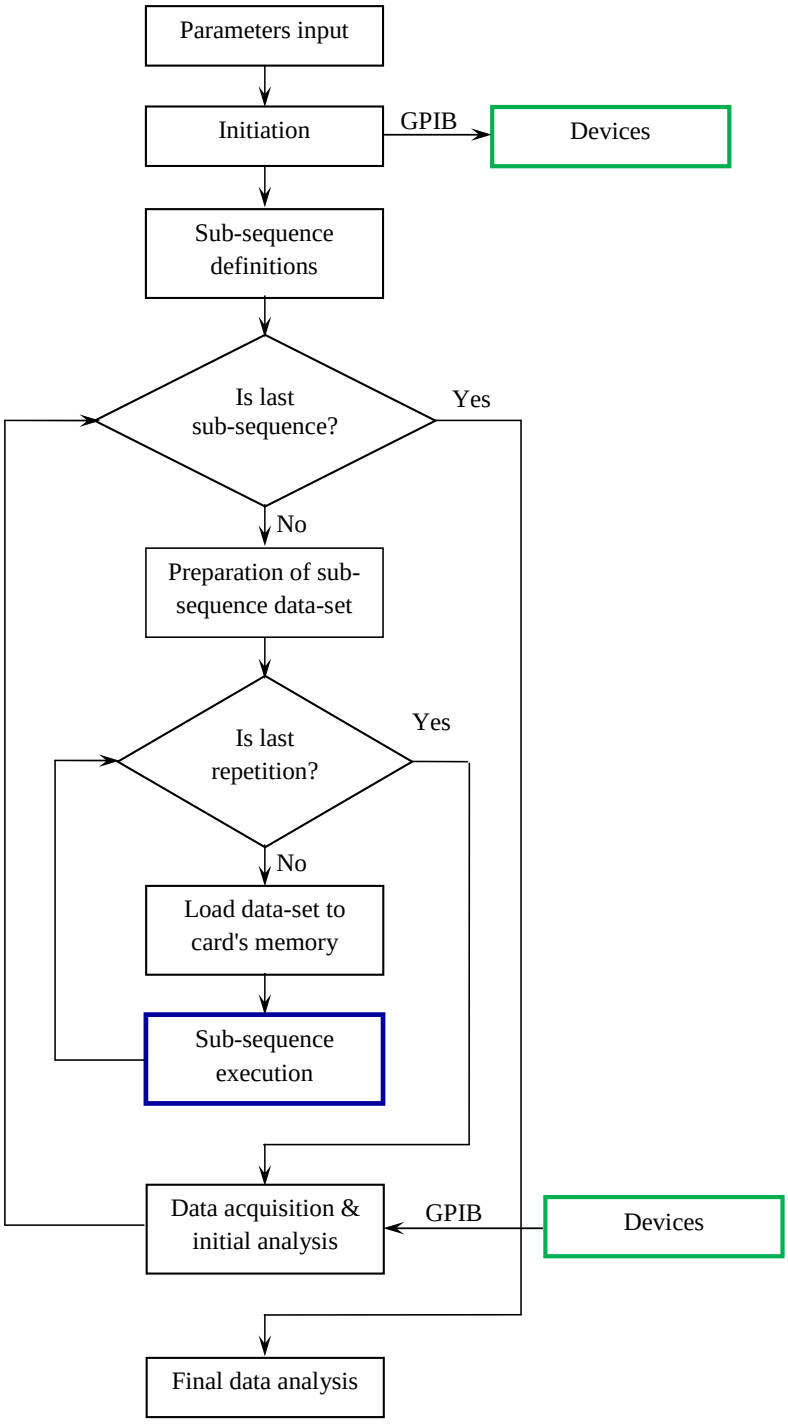

Figure B.6: Flowchart of the main control program (MCP). The black color refers to the parts of the flowchart that are executed by the Windows based desktop computer; the blue – to the real-time segments executed by the CPU of the PCI 6733 card and the green color indicates the control features of the external devices, such as the averaging feature of the scope. See text for details.

- **Sub-sequence definitions.** Based on the experimental parameters, the MCP defines experimental sub-sequences needed to perform the full experiment. One or more of the experimental parameters (e.g. time, length or frequency of a MW pulse) change from one experimental sub-sequence to the next. These sub-sequences are performed as follows:

  1. **Preparation of sub-sequence data-set.** Based on the sub-sequence definitions, the MCP calculates the data-set, which includes timed sets of output voltages of the PCI 6733 needed to perform the required experimental sub-sequence. This data-set is then uploaded to the card's memory.
  2. **Sub-sequence execution.** Control is transferred to the PCI 6733 card's CPU, and the experimental sub-sequence is performed in "real time" with 1μs resolution. During the execution of the sub-sequence, the response of the photodiode PD (see Fig. B.1) is recorded in the scope memory. The experimental sub-sequence may be repeated several times, using the scope to average the photodiode response.
  3. **Data acquisition and initial analysis.** The MCP downloads (via GPIB) the recorded data from the scope and saves it in the main computer's memory. Initial data analysis may be performed to produce values needed for the next experimental sub-sequence.

- **Repeat sub-sequences operation.** Steps 1–3 are repeated until the last experimental sub-sequence is executed.

- **Final data analysis.** Following the execution of the last experimental sub-sequence, final data analysis is performed. See next section (Sec. B.5) for an example of the operation of the MCP and of the data analysis.

B.5 Example: Detecting two-photon transitions

In this section we illustrate the operation of the experimental system with an example in which we study two-photon transitions between Zeeman sub-levels of the ground-state of ^{87}Rb atoms in a room-temperature vapor cell filled with 70 Torr of Ne buffer gas. In this experiment we apply a DC magnetic field of $B_z = 3.23\,\mathrm{G}$, produced by the compensation coils and the axial coil of the vapor cell environment (see Figs. B.4 and B.5), inducing a Zeeman sub-level splitting of 2.1 MHz.

The aim of the experiment is to induce Rabi population oscillations between the $|1,-1\rangle$ and the $|2,1\rangle$ Zeeman sub-levels, as shown in Fig. B.7. In total, three radiation fields are used:

- MW radiation is transmitted via the MW antenna (see Fig. B.5) and is blue detuned by $\Delta \approx 1\,\mathrm{MHz}$ from the $|0\rangle \leftrightarrow |2,0\rangle$ transition frequency (~ 6.8GHz).

- RF radiation is transmitted by the second axial coil (see Fig. B.5) and is chosen so that the sum $(\omega_{MW} + \omega_{rf})/2\pi$ is δ detuned from the $|0\rangle \leftrightarrow |1\rangle$ transition frequency ($\omega_{rf}/2\pi \approx 1\,\mathrm{MHz}$).

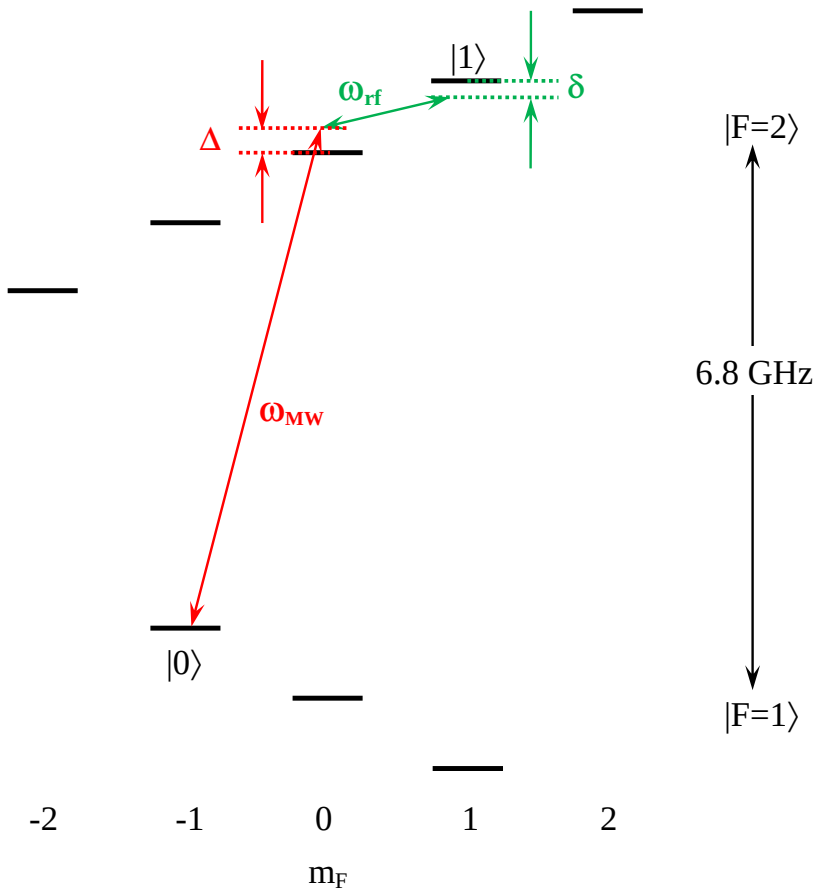

Figure B.7: Zeeman sub-levels of the ground state of ^{87}Rb subjected to a DC magnetic field of 3.23 G. All three sub-levels of the $|F = 1\rangle$ hyperfine state and all five sub-levels of the $|F = 2\rangle$ state are shown. The separation between two adjacent Zeeman sub-levels is ~ 2.1 MHz. The transition studied is from the $|1, -1\rangle$ sub-level (marked $|0\rangle$) to the $|2, 1\rangle$ sub-level (marked $|1\rangle$). This is a $\Delta m_F = 2$ transition, requiring two photons to provide two angular momentum quanta. The two-photon transition is driven coherently by MW and RF sources at frequencies $\omega_{\rm MW}$ and $\omega_{\rm rf}$, respectively.

- The pump-probe laser beam (see Sec. B.1) is tuned near the frequency of the D2 $5^2S_{1/2}|F = 2\rangle \leftrightarrow 5^2P_{3/2}|F = 3\rangle$ transition. The beam management module of the experimental system (see Sec. B.2) expands the beam and directs it to the vapor cell via a double-pass AOM that can switch the beam on and off. The pump-probe laser beam is used both to initiate the experiment by pumping all the population to the $|F = 1\rangle$ hyperfine state and to probe the population in the $|F = 2\rangle$ hyperfine state after the interaction of the vapor with the combined RF and MW radiation (for details of the population measurement method see Ch. 4).

Both the MW and the RF signal generators are synchronized to an external 10MHz rubidium frequency standard with 5×10^{-11} relative frequency accuracy (AccuBeat AR40A), making the MW and RF radiation coherent in the sense described at the beginning of App. A. Thus the combined radiation can induce Raman transitions (see Sec. 2.7.6). This experiment has

three stages that need to be performed in "real time":

Stage 1: **Initiation.** Optically pumping all the vapor atoms to the $|F = 1\rangle$ hyperfine state.

Stage 2: **Evolution.** Turning on the RF and MW radiation for a "evolution time" t_{evol}.

Stage 3: **Evaluation.** Measuring the population in the $|F = 2\rangle$ hyperfine state.

These three stages are repeated N times for different values of the "evolution time"

$$t_{evol_n} = t_{start} + n\Delta t, \quad n = 0, 1, 2 \ldots N. \tag{B.1}$$

The experiment is performed as follows:

- **Parameters input.** The experimental parameters (such as t_{start}, N, Δt of Eq. (B.1), and the MW and RF frequencies) are loaded via the control panel [GUI] of the LabView based MCP.

- **Initiation.** The relevant external devices (signal generators, scope) are initiated via GPIB to the correct modes of operation.

- **Sub-sequence definitions.** Based on the experimental parameters, the MCP defines experimental sub-sequences that include states 1–3 defined above. The value of t_{evol_n} changes from one sub-sequence to the next as defined by Eq. (B.1).

    1. **Preparation of sub-sequence data-set.** Based on the sub-sequence definitions, the MCP calculates the data-set, which includes timed sets of output voltages of the PCI 6733 needed to perform the required experimental sub-sequence. This data-set is then uploaded to the card's memory.
    2. **Sub-sequence execution.** Control is transferred to the PCI 6733 card's CPU, and the experimental sub-sequence is performed in "real time". During the evaluation stage (stage 3 above - measuring the population in the $|F = 2\rangle$ hyperfine state) the response of the photodiode PD (see Fig. B.1) is recorded in the scope memory. The experimental sub-sequence may be repeated several times, using the scope to average the photodiode response.
    3. **Data acquisition and initial analysis.** The MCP downloads (via GPIB) the recorded data from the scope and calculates the population in the $|F = 2\rangle$ hyperfine state (see Ch. 4)

- **Repeat sub-sequences operation.** Steps 1–3 are repeated for $n = 0, 1, 2 \ldots N$ [Eq. (B.1)].

- **Final data analysis.** Following the execution of the last experimental sub-sequence, final data analysis is performed, producing a plot of the population in the $|F = 2\rangle$ hyperfine state vs. t_{evol_n}

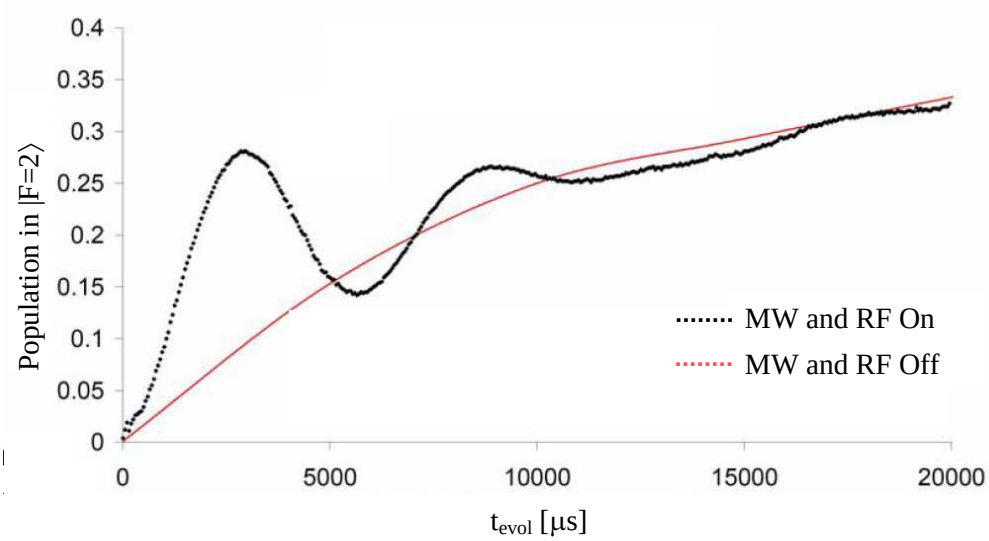

Figure B.8: Typical plots of the ^{87}Rb vapor population in the $|F = 2\rangle$ hyperfine state (see Fig. B.7) as a function of the evolution time t_{evol} [see Eq. (B.1)]. The vapor cell contains neon buffer gas at 70 Torr. Red plot: $|F = 2\rangle$ population when the evolution stage (Stage 2) is "in the dark" (all fields off). This red plot shows the thermalization process, with a relaxation time of about 30 ms. Black plot: $|F = 2\rangle$ population when the RF and MW fields are on during the evolution stage, showing two-photon Rabi oscillations at about 170Hz superimposed upon the thermalization process. The thermalization process is also responsible for the fast decay of the oscillations.

The full experimental sequence is run twice: once with the RF and MW radiation turned on during stage 2 above, and once when these fields off, so that we can measure the evolution of the population in $|F = 2\rangle$ "in the dark". With all fields off, we can observe the thermalization process, causing the return of the population in $|F = 2\rangle$ to its thermal equilibrium value of $5/8 = 0.625$. Typical results of such an experiment are presented in Fig. B.8. For a full review of this experiment, see [83].

Appendix C

Vapor cell filling system

Alkali vapor cell filling, and in particular, filling cells with paraffin wall coating, is a difficult art, mastered in only a few places. Apart from standard cells, the lead time for vapor cells purchasing is long, and the quality of commercially available cells is not always good. We therefore built our own vapor cell filling system as described below.

Figure C.1 displays the system in its final stage of construction and its schematic design.

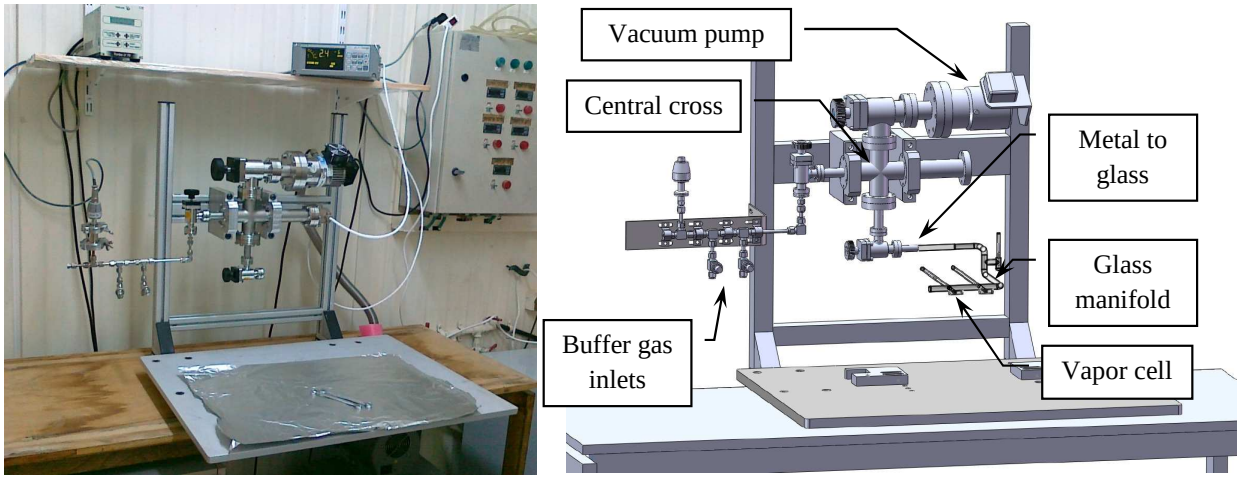

Figure C.1: Left: the vapor cell filling system in its final stage of construction. Right: vapor cell filling system schematic. The central cross is connected to the vacuum pump (top), to the glass manifold that contains the cells (bottom), to the buffer gas inlets (left) and to a vacuum gauge (right, not shown). Details of the glass manifold are presented in Fig. C.2.

The central cross serves both as the mechanical support for the system and as the connector between all other parts of the system. The vacuum pump (Varian Turbo V70LP) provides vacuum down to 10^{-7} Torr. The buffer gas inlets allow mixing of up to two buffer gases, and can easily be expended to allow mixing of more buffer gases. The glass manifold with the vapor cells (see details in Sec. C.1) is connected to the system via a valve and a metal-to-glass connector.

C.1 Glass manifold for paraffin coating

A typical design of a glass manifold is presented in Fig. C.2. In this design two vapor cells are connected to the main pipe and both may be filled with Rb and coated with paraffin. The glass manifold is connected to the vacuum system via a metal to glass connector (see Fig. C.1). Once the glass manifold is under vacuum, a removable oven (not shown) "bakes" the vapor cells at a temperature of about 200°C for six to eight hours, until a stable vacuum of below 5×10^{-7} Torr is reached. During baking, the needles (see Fig. C.2) are in the "retracted" position, so that the paraffin (tetracontane) on their tips will not melt.

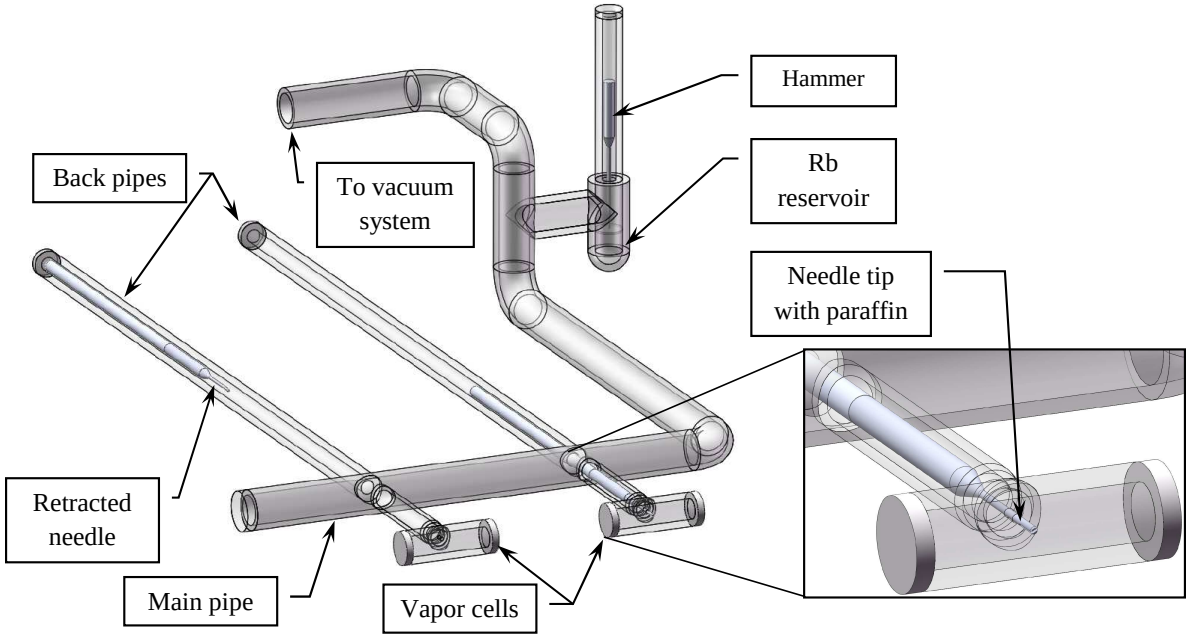

Figure C.2: Design of the glass manifold for paraffin coating. Two vapor cells are connected by a short glass pipe to the main pipe. Two "back pipes" (with a movable needle placed inside each of them) are connected to the main pipe so that the internal needle can move freely from the retracted position (shown in the left back pipe) to the forward position where the needle tip is inside the cell (right back pipe). When the the glass manifold is constructed, a drop of paraffin is applied to each tip. The needles are made of copper with a short iron end, so that they can be manipulated by an external magnet. A sealed Rb reservoir is also connected to the main pipe, with an iron hammer, that is later used to break the seal of the Rb reservoir.

Then we proceed according to the following stages:

Filling stage 1: **Paraffin evaporation.** After backing, the needles are moved (with a hand-held magnet next to the back pipe) so that their tips are inside the cells. We then insert a coil around the back pipe, and use an induction-heating system to heat the needle until the paraffin on the tip evaporates and covers the inner cell walls (see Fig. C.3). Then we move the needles back to the retracted position (see Fig. C.2).

Filling stage 2: **Opening the rubidium reservoir.** An iron hammer is located above the sealed rubidium reservoir (see Fig. C.2). Using a magnet, we lift the hammer and let it fall on the seal several times, until it breaks.

Filling stage 3: **"Chasing" rubidium.** We use an hot air fan to heat the rubidium in the reservoir and "chase" some of the rubidium into the main pipe towards the vapor cells until some is deposited on the walls of the short pipe connecting the vapor cells to the main pipe. Care is taken to ensure that no rubidium metal is deposited on the vapor cell walls.

Filling stage 4: **Vapor cell sealing.** We wrap a wet cloth around both cells, and using a torch, start heating the short pipe connecting the vapor cell to the main pipe until it becomes flexible. (We keep the vapor cell itself cold by a constant drip of ice cold water on the cloth wrapped around the cell). Pulling the cell gently away from the main pipe while heating the short pipe, the short pipe becomes narrower until it completely seals the vapor cell and disconnects from the main pipe.

Filling stage 5: **Final baking.** We bake the cells in an oven for two days at a temperature of 45°C.

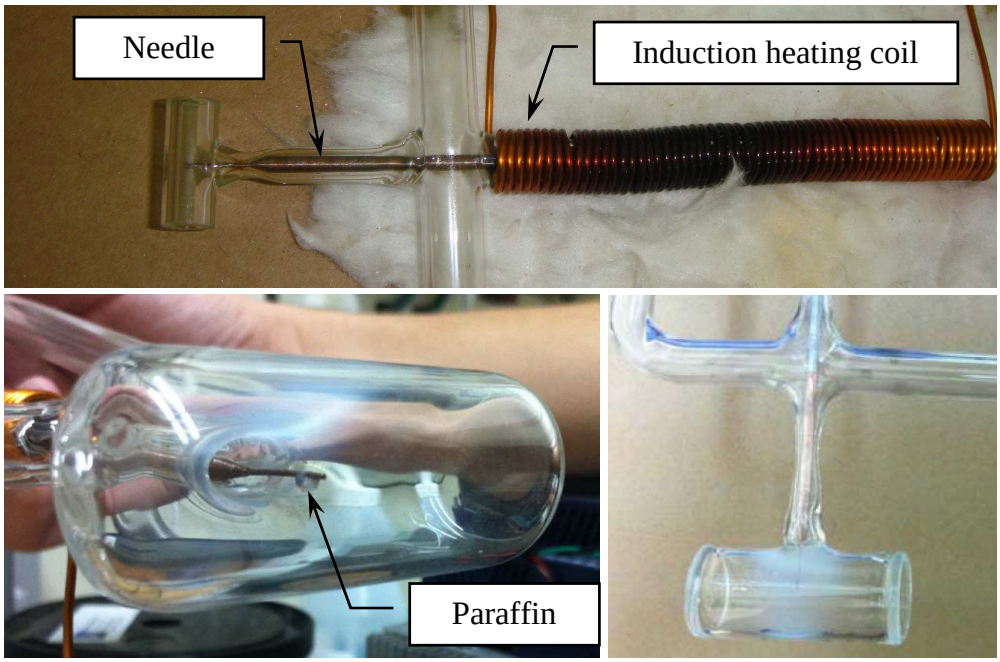

Figure C.3: Paraffin evaporation method. Top: the induction heating coil wrapped around the glass pipe with the needle inside. The tip of the needle is inside the vapor cell. (This picture was taken during heating tests). Bottom left: drop of molten paraffin hanging from the tip of the needle inside the vapor cell, just before it evaporates. Bottom right: vapor cell after paraffin evaporation. (The coating is not uniform, but it does cover all the inner walls of the cell.)

C.2 The moving plug method

The paraffin coating and Rb filling method described in the previous section is very similar to most vapor cell filling methods described in the scientific literature (see, for example, [84] and references therein). These methods involve significant manual labor and require highly experienced glass-blowers. We have developed a novel vapor cell filling method, which can streamline the vapor cell production and considerably reduce the required labor. (A patent application [85] was submitted.) Cell production according to the new method is split into two separate procedures:

- preparation of rubidium coated glass plugs.
- production of the vapor cells, utilizing the coated glass plugs

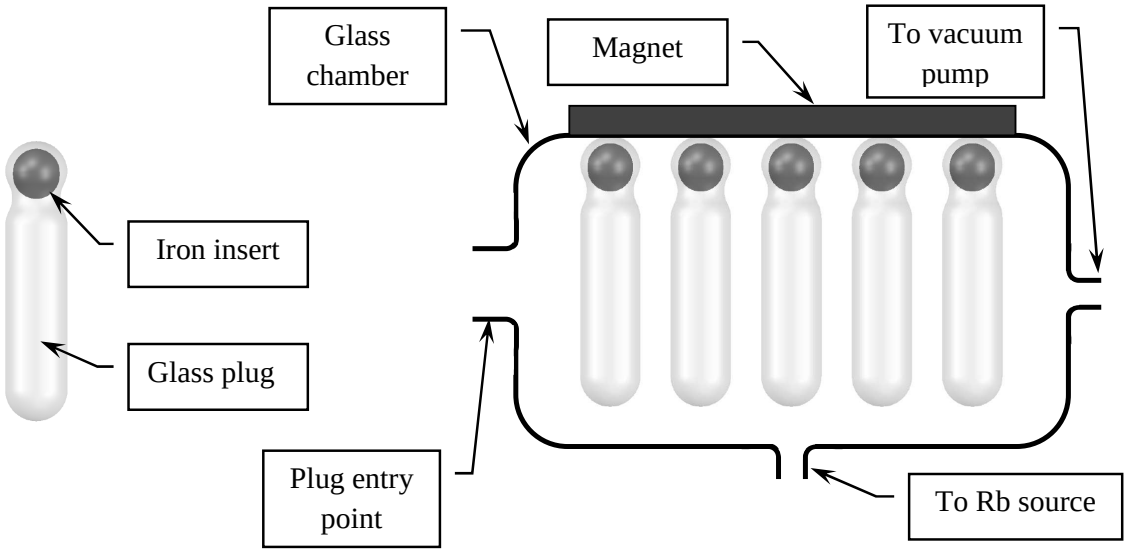

Figure C.4: Plugs for vapor cells production. Left: a glass plug. The plug diameter is 2−3mm, length $\sim$ 15mm. The iron insert enables manipulation of the glass plug inside the glass piping of the vapor filling system (using an external magnet). The iron insert is covered completely by glass, to avoid contamination of the inside volume of the vapor filling system. Right: several glass plugs hanging (magnetically) from the ceiling of the glass chamber. The glass plugs can be moved in and out of the chamber via the "Plug entry point".

Figure C.4 illustrates the plugs' coating procedure. Several glass plugs are suspended magnetically from the ceiling of an evacuated glass chamber. Rubidium is chased from a reservoir (not shown) into the chamber so that rubidium is deposited on the lower part of the glass plugs. Then the top magnet is removed and an additional small hand-held magnet (not shown) is used to manipulate the rubidium coated glass plugs out of the chamber.

The next step in the procedure is the preparation of a glass manifold similar to the one presented in Fig. C.2. The only difference is the replacement of the Rb reservoir with a reservoir of rubidium-coated glass plugs. Then paraffin evaporation is performed as described earlier (Sec. C.1). A magnet is then used to transfer a rubidium-coated glass plug from its

reservoir to the short pipe connecting the vapor cell to the main pipe, positioning the glass plug as shown in Fig. C.5. The rubidium coated side of the glass plug faces the hole in the cell wall, and the iron insert is located away from the cell. Then a torch is used to the separate the vapor cell from the glass manifold along the separation position (Fig. C.5) so that the iron insert is not part of the separated vapor cell.

We position an additional glass ball between the glass plug and the hole in the wall of the vapor cell and verify during the separation of the vapor cell that the ball remains pressed against the hole. The purpose of the glass ball is to reduce the cross section area for rubidium vapor to move between the cell and the rubidium deposited on the glass plug in the cell's stem (see [40] on the importance of reducing this cross section). Since the flow of atoms that leave the vapor cell to the stem (as well as atoms that enter the cell from the stem) reduce the coherence time of rubidium vapor in the cell, this arrangement may increase the coherence time of the vapor cell.

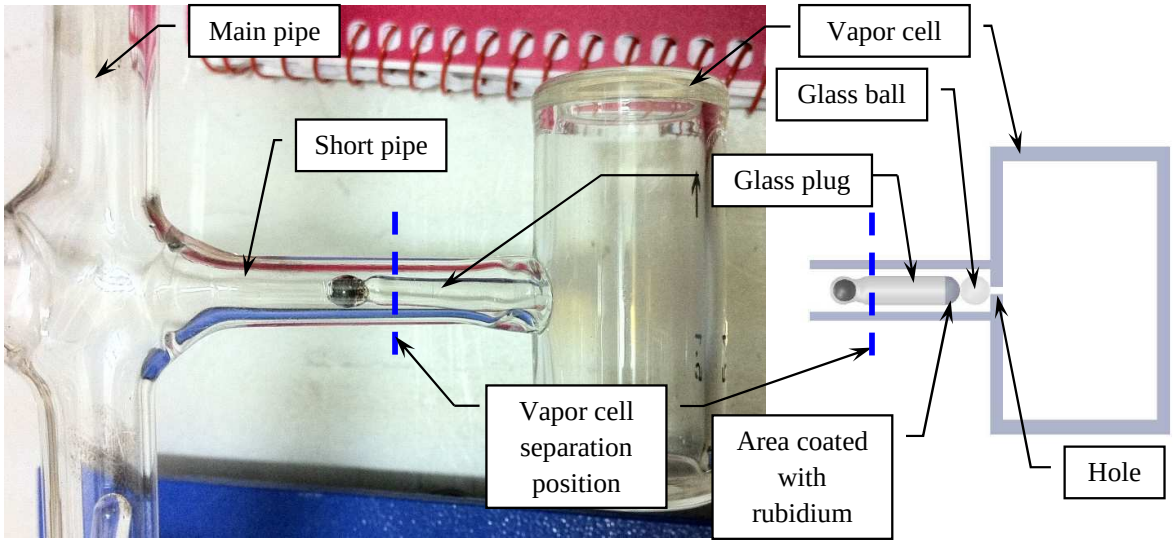

Figure C.5: Location of a glass plug in the vapor cell. Left: vapor cell with a glass plug just before the vapor cell separation from the glass manifold. Right: schematic diagram of the vapor cell and the glass plug. A glass ball is located between the hole in the wall of the vapor cell and rubidium coated on the glass plug (not realized in the picture for the actual setup). This arrangement limits the diffusion of rubidium atoms between the vapor cell and the rubidium deposited in the cell's stem – after the completion of the production process.

The combination of the glass plug and the induction heating methods described in this appendix may lead to a reliable vapor cell production technology that can produce high quality, low cost vapor cells for quantum metrology applications (such as optical magnetometers and atomic clocks). However, so far we have done only preliminary tests showing that a vapor cell can be produced in this way. Additional tests and characterization work, as well as a major engineering effort, are required in order to develop a reliable production and quality assurance procedures based on this technology.

Appendix D

Fast current shutter

The vapor cell environment (App. B.3) includes coils producing DC magnetic fields. During the current shutting time a voltage $V = L \cdot dI/dt$ develops across the coil (L is the coil's inductance). Typically, the voltage of a commercial power supply is limited, and the current shutting time may be too long. Our current shutters (Fig. D.1) provide fast and adjustable current shutting time.

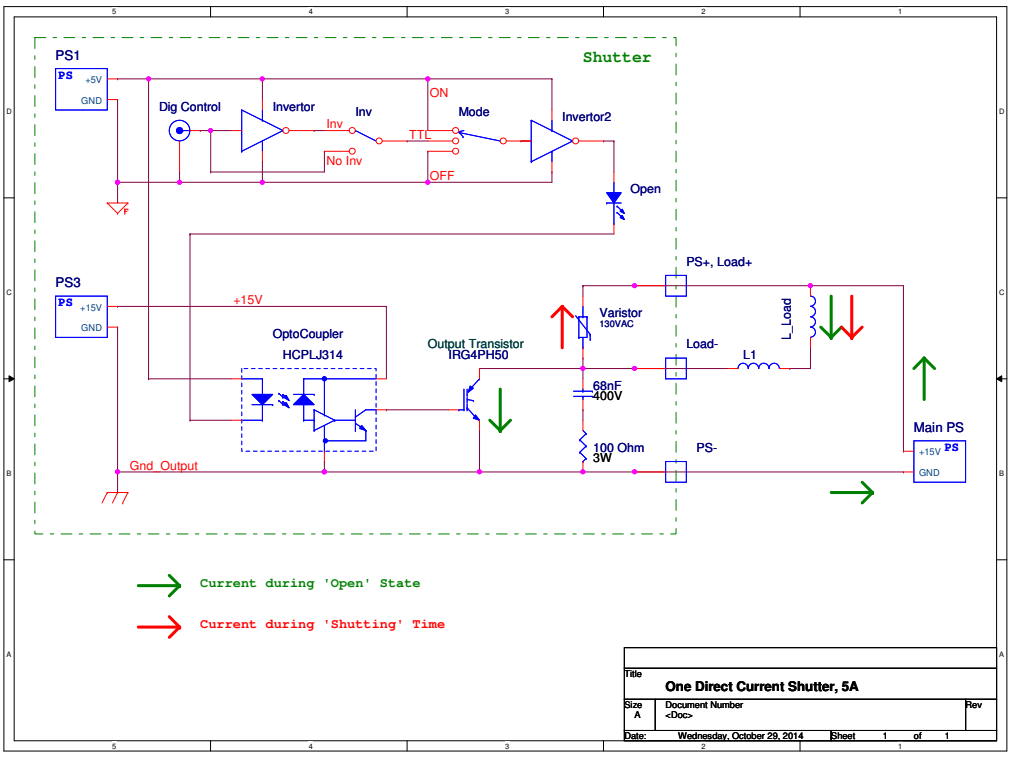

Figure D.1: Fast current shutter circuit. PS – power supply. The current shutter is operated by a digital output. Green arrows indicate the current route when the shutter is open; red arrows show the route of the transient current during the current shutting time. Current shutting time is inversely proportional to the varistor voltage rating. The L1 coil (optional) increases the shutting time.

Appendix E

Supplementary algebraic calculations

In Ch. 3 we develop our simplified absorption model and prove the existence of the magic frequency. For clarity, we did not include all the algebraic calculations in the body of the text. The required calculations are detailed in this appendix.

E.1 Derivation of the dipole matrix element

The expression of the matrix element $\langle F, m_F|er_q|F', m'_F\rangle$ for an $|F, m_F\rangle \rightarrow |F', m'_F\rangle$ dipole transition [Eq. (3.1)] is the basis of our simplified absorption model (Sec. 3.1). Our aim here is to detail the derivation of this expression:

$$\begin{aligned}&\langle F, m_F|er_q|F', m'_F\rangle = \\ &\langle J\|e\mathbf{r}\|J'\rangle(-1)^{F'+J+1+I}\sqrt{2J+1}\sqrt{2F'+1}\begin{Bmatrix} J & J' & 1 \\ F' & F & I\end{Bmatrix}\langle F, m_F|F', 1, m'_F, q\rangle,\end{aligned} \tag{E.1}$$

and we will follow the derivation presented by Stack [46]. We start with the Wigner-Eckart theorem [see [46], § 7.3.4 and Eq.(2.100] which states that

$$\langle \alpha, F, m_F|T^{(\kappa)}_q|\alpha', F', m'_F\rangle = (-1)^{2\kappa}\langle \alpha, F||T^{(\kappa)}||\alpha', F'\rangle\langle F, m_F|F', \kappa, m'_F, q\rangle, \tag{E.2}$$

where α stands for the quantum numbers that are not related to angular momentum, $T^{(\kappa)}$ is a tensor operator of rank κ, and $\langle \alpha, F||T^{(\kappa)}||\alpha', F'\rangle$ is the reduced matrix element:

$$\langle \alpha, F||T^{(\kappa)}||\alpha', F'\rangle = (-1)^{2\kappa}\sum_{m'_F, q}\langle \alpha, F, m_F|T^{(\kappa)}_q|\alpha', F', m'_F\rangle\langle F, m|F', \kappa, m'_F, q\rangle, \tag{E.3}$$

For a two-component system with electron angular momentum J and nuclear angular momentum I, a resultant angular momentum F, and a tensor $T^{(\kappa)}(J)$ that acts only on J (I and m_I are not affected) we can transform Eq. (E.3) into the uncoupled states (see [46], § 7.3.6.1):

$$\begin{aligned}\langle F||T^{(\kappa)}(J)||F'\rangle = (-1)^{2\kappa}\sum&\langle F, m_F|J, m_J, I, m_I\rangle\langle J', m'_J, I, m_I|F', m'_F\rangle\times \\ &\langle F, m_F|F', m'_F, \kappa, q\rangle\langle J, m_J|T^{(\kappa)}_q(J)|J', m'_J\rangle,\end{aligned} \tag{E.4}$$

where the summation is over m_F, q, m_J, m'_J and m_I, and we have dropped α ($T^{(\kappa)}(J)$ does not act on the part of the state represented by α). We now apply the Wigner-Eckart theorem to the matrix elements in Eq. (E.4), and use the symmetry relation ([46], § 7.1.3.5)

$$\langle J_1, m_1, J_2, m_2 | J_3, m_3 \rangle = (-1)^{J_1+J_2-J_3} \langle J_2, m_2, J_1, m_1 | J_3, m_3 \rangle \tag{E.5}$$

to get:

$$\begin{aligned} \langle F||T^{(\kappa)}(J)||F'\rangle = \sum & \langle J, m_J, I, m_I | F, m_F\rangle \langle J', m'_J, I, m_I | F', m'_F\rangle \times \\ & (-1)^{F'+\kappa-F} (-1)^{J'+\kappa-J} \langle \kappa, q, F', m'_F, | F, m_F\rangle \times \\ & \langle \kappa, q, J', m'_J, | J, m_J\rangle \langle J||T^{(\kappa)}(J)||J'\rangle. \end{aligned} \tag{E.6}$$

Next, we use the relation ([46], § 7.1.4.1)

$$\begin{aligned} \begin{Bmatrix} j_1 & j_2 & j_{12} \\ j_3 & j & j_{23} \end{Bmatrix} = \frac{(-1)^{j_1+j_2+j_3+j}}{\sqrt{(2j_{12}+1)(2j_{23}+1)}} \sum & \langle j_{12}, m_{12}, j_3, m_3 | j, m\rangle \langle j_1, m_1, j_2, m_2 | j_{12}, m_{12}\rangle \\ & \langle j_1, m_1, j_{23}, m_{23} | j, m\rangle \langle j_2, m_2, j_3, m_3 | j_{23}, m_{23}\rangle, \end{aligned} \tag{E.7}$$

where the term in the curly brackets is the $6J$ symbol, and the summation is over m_1, m_2, m_3, m_{12} and m_{23}. Identifying $\kappa \to j_1$, $J' \to j_2$, $I \to j_3$, $F \to j$, $J \to j_{12}$, $F' \to j_{23}$ and exchanging the first and last columns of the $6J$ symbol, we get:

$$\langle F||T^{(\kappa)}(J)||F'\rangle = (-1)^{F'-J+\kappa-I-2F} \sqrt{(2F'+1)(2J+1)} \begin{Bmatrix} J & J' & \kappa \\ F' & F & I \end{Bmatrix} \langle J||T^{(\kappa)}(J)||J'\rangle. \tag{E.8}$$

Using the fact that $F + J + I$ must be an integer (otherwise the 6J symbol vanishes), we can add $2(F + J + I)$ to the exponent of (-1) in Eq. (E.8), and we obtain:

$$\langle F||T^{(\kappa)}(J)||F'\rangle = (-1)^{F'+J+\kappa+I} \sqrt{(2F'+1)(2J+1)} \begin{Bmatrix} J & J' & \kappa \\ F' & F & I \end{Bmatrix} \langle J||T^{(\kappa)}(J)||J'\rangle. \tag{E.9}$$

Noting that the $\kappa = 1$ dipole operator $e\mathbf{r}$ operates only on J, it can replace $T^{\kappa}(J)$ in Eq. (E.9) to get an expression for the reduced matrix element $\langle F||e\mathbf{r}||F'\rangle$. Substituting it in the Wigner-Eckart theorem [Eq. (E.2)] we then obtain Eq. (E.1).

E.2 Calculation of Clebsch-Gordan (CG) coefficients

One of the necessary steps for proving the existence of the magic frequency involves factoring the dependence on m_{1F} and m_{2F} out of the CG coefficients in Eq. (3.13). For clarity, we rewrite this equation:

$$\sum_{F'=F-1}^{F'=F+1} \exp\left[-\frac{\Delta_{FF'}^2}{2\sigma_{\mathrm{D}}^2}\right](2F'+1)\begin{Bmatrix} J & J' & 1 \\ F' & F & I \end{Bmatrix}^2$$
$$\times\Bigg[\Big(1-2|E_{+1}|^2\Big)\Big(\langle F,m_{1F}|F',1,m_{1F},0\rangle^2-\langle F,m_{2F}|F',1,m_{2F},0\rangle^2\Big)$$
$$+|E_{+1}|^2\Big(\langle F,m_{1F}|F',1,m_{1F}+1,-1\rangle^2-\langle F,m_{2F}|F',1,m_{2F}+1,-1\rangle^2$$
$$+\langle F,m_{1F}|F',1,m_{1F}-1,1\rangle^2-\langle F,m_{2F}|F',1,m_{2F}-1,1\rangle^2\Big)\Bigg]=0. \tag{E.10}$$

Our specific aim is to factor the dependence on m_{1F} and m_{2F} out of the expression in the square brackets in Eq. (E.10). To this end, we use an explicit expression for the CG coefficients [86]:

$$\langle j,m|j_1,j_2,m_1,m_2\rangle=\delta_{m,m_1+m_2}\sqrt{\frac{(2j+1)(j_1+j_2-j)!(j+j_1-j_2)!(j+j_2-j_1)!}{(j_1+j_2+j+1)!}}\times$$
$$\sqrt{(j+m)!(j-m)!(j_1+m_1)!(j_1-m_1)!(j_2+m_2)!(j_2-m_2)!}\times$$
$$\sum_k\frac{(-1)^k}{k!(j_1+j_2-j-k)!(j_1-m_1-k)!(j_2+m_2-k)!(j-j_2+m_1+k)!(j-j_1-m_2+k)!} \tag{E.11}$$

where the summation is over all integers k for which all the factorials have a non-negative argument, and it is assumed that $m\geq 0$ and $j_1\geq j_2$. In case we have CG coefficients with $m<0$ and/or $j_1<j_2$, we use the following relations to convert them to CG coefficients that can be calculated by Eq. (E.11):

$$\begin{aligned}\langle j,m|j_1,j_2,m_1,m_2\rangle&=(-1)^{j-j_1-j_2}\langle j,-m|j_1,j_2,-m_1,-m_2\rangle\\ \langle j,m|j_1,j_2,m_1,m_2\rangle&=(-1)^{j-j_1-j_2}\langle j,m|j_2,j_1,m_2,m_1\rangle.\end{aligned} \tag{E.12}$$

In the square brackets in Eq (E.10) we have 6 CG coefficients, and we need to calculate each of them 3 times: for $F'=F-1$, $F'=F$ and $F'=F+1$. In total, we need to calculate 18 CG coefficients. Let us start by calculating the first pair of CG coefficients that appears in the first large brackets in Eq. (E.10): $\langle F,m|F',1,m,0\rangle$ for the case $F'=F$. Substituting $j=j_1=F$, $j_2=1$, $m_1=m$ and $m_2=0$ in Eq. (E.11) we get:

$$\langle F,m|F,1,m,0\rangle=\sqrt{\frac{(2F+1)(1)!(2F-1)!(1)!}{(2F+2)!}}\times$$
$$\sqrt{(F+m)!(F-m)!(F+m)!(F-m)!(1)!(1)!}\times \tag{E.13}$$
$$\sum_k\frac{(-1)^k}{k!(1-k)!(F-m-k)!(1-k)!(F-1+m+k)!(k)!}.$$

Noting that only for $k = 0, 1$ the arguments of all the factorials in Eq. (E.13) are non-negative, we get:

$$\langle F, m|F, 1, m, 0\rangle = \sqrt{\frac{1}{2F(2F+2)}}(F+m)!(F-m)! \times \left(\frac{-1}{(F-m)!(F+m-1)!} + \frac{1}{(F-m-1)!(F+m)!}\right) \tag{E.14}$$

which can be further simplified to:

$$\langle F, m|F, 1, m, 0\rangle = -\sqrt{\frac{1}{2F(2F+2)}}2m = -\sqrt{\frac{1}{F^2+F}}m. \tag{E.15}$$

Using Eq. (E.15) we can now evaluate the first large brackets in Eq. (E.10) for the case $F' = F$:

$$\langle F, m_{1F}|F, 1, m_{1F}, 0\rangle^2 - \langle F, m_{2F}|F, 1, m_{2F}, 0\rangle^2 = (m_{1F}^2 - m_{2F}^2)\frac{1}{F^2+F}. \tag{E.16}$$

In the square brackets in Eq (E.10) we have 6 CG coefficients, and we need to calculate each of them 3 times: for $F' = F-1$, $F' = F$ and $F' = F+1$. In total, we need to calculate 18 CG coefficients. So far we have calculated just 2 CG coefficients for the case $F' = F$. The algebraic calculation of the other 16 CG coefficients in Eq. (E.10) was done using the "Wolfram Mathematica" software. The results are:

$$\langle F, m_{1F}|F', 1, m_{1F}, 0\rangle^2 - \langle F, m_{2F}|F', 1, m_{2F}, 0\rangle^2 = (m_{1F}^2 - m_{2F}^2)G(F, F'), \tag{E.17}$$

and

$$\begin{aligned}&\langle F, m_{1F}|F', 1, m_{1F}+1, -1\rangle^2 - \langle F, m_{2F}|F', 1, m_{2F}+1, -1\rangle^2 + \\ &\langle F, m_{1F}|F', 1, m_{1F}-1, 1\rangle^2 - \langle F, m_{2F}|F', 1, m_{2F}-1, 1\rangle^2 = -(m_{1F}^2 - m_{2F}^2)G(F, F'),\end{aligned} \tag{E.18}$$

where $G(F, F')$ is given by:

$$G(F, F') = \begin{cases} 1/(F-2F^2), & F' = F-1 \\ 1/(F+F^2), & F' = F \\ -1/(3+5F+2F^2), & F' = F+1. \end{cases} \tag{E.19}$$

Appendix F

An additional explanation of the magic frequency

In a 1967 paper [74] Happer and Mathur present an effective operator formalism for optical pumping, and later [75] Mathur, Tang and Happer (M&H) apply this formalism to study light propagation in optically pumped alkali vapors (focusing on ^{87}Rb). Their results can be used to explain the existence of the magic frequency, as detailed below.

At that time the available light source for optical pumping experiments was a resonance lamp which has a spectral width much larger than the hyperfine splitting. M&H represent this kind of light by an ensemble of many monochromatic plane waves at different frequencies and with random phases. The light was considered weak (the rate of induces absorption is much smaller than the spontaneous decay rate). Under this condition, a plane wave $\vec{\mathcal{E}}$ induces in the vapor a dipole moment $\vec{\mathcal{P}}$:

$$\vec{\mathcal{P}} = \langle \overleftrightarrow{\alpha} \rangle \vec{\mathcal{E}}, \tag{F.1}$$

where $\overleftrightarrow{\alpha}$ is the polarizability tensor of the atom, and its expectation value is given by:

$$\langle \overleftrightarrow{\alpha} \rangle = Tr[\overleftrightarrow{\alpha} \rho], \tag{F.2}$$

where ρ is the density matrix of the atomic ground state [see Eqs. (4), (5) in M&H] .

The polarizability $\overleftrightarrow{\alpha}$ determines the way in which light propagates through a vapor. Working in the spherical basis (see 2.9.1) and utilizing the polarization moments (see 2.11), M&H write the polarization operator as a sum of four components [Eq. (39) in M&H]:

$$\overleftrightarrow{\alpha} = \alpha_{eq} + \alpha_{hps} \vec{I} \cdot \vec{J} + i \sum_{f,f'} \alpha_{gt}(f,f') \vec{J}(f,f') \times + \sum_{f,f'} \alpha_{br}(f,f') \overleftrightarrow{Q}(f,f') \tag{F.3}$$

where the $\times$ sign after the third term indicates the vector cross product (note that $\overleftrightarrow{\alpha}$ operates on $\vec{\mathcal{E}}$), and f, f' are the ground state hyperfine quantum numbers. Terms with $f \neq f'$ are relevant only if hyperfine coherences are present in the ground-state density matrix of the vapor (see M&H for more details).

This polarizability tensor operator includes isotropic, or scalar component (the first two terms), dipolar component and quadrupolar component. Since photons have spin 1,

higher order atomic density matrix multipole components do not affect the way in which light propagates through a vapor.

The first term, α_{eq}, is a complex scalar response function of the light frequency, representing a state-independent interaction of the light with the atoms. The second term, $\alpha_{hps}\vec{I}\cdot\vec{J}$, has a nonzero expectation only when some population imbalance $\langle\vec{I}\cdot\vec{J}\rangle$ exists between the population of the lower and upper hyperfine states.

Together the first two terms compose the isotropic polarizability operator α_0 [see Eq. (40) in M&H], which transforms under rotations as a scalar (tensor of rank 0). The absorption of the light due to α_0 is independent of the light polarization.

The third term, the "gyrotropic polarizability", which transforms under rotations as a vector (rank 1 tensor) is related to the absorptivity of circularly polarized light (see M&H). Since in this thesis we work exclusively with linearly polarized light, this term does not contribute to the absorption of the light that we use.

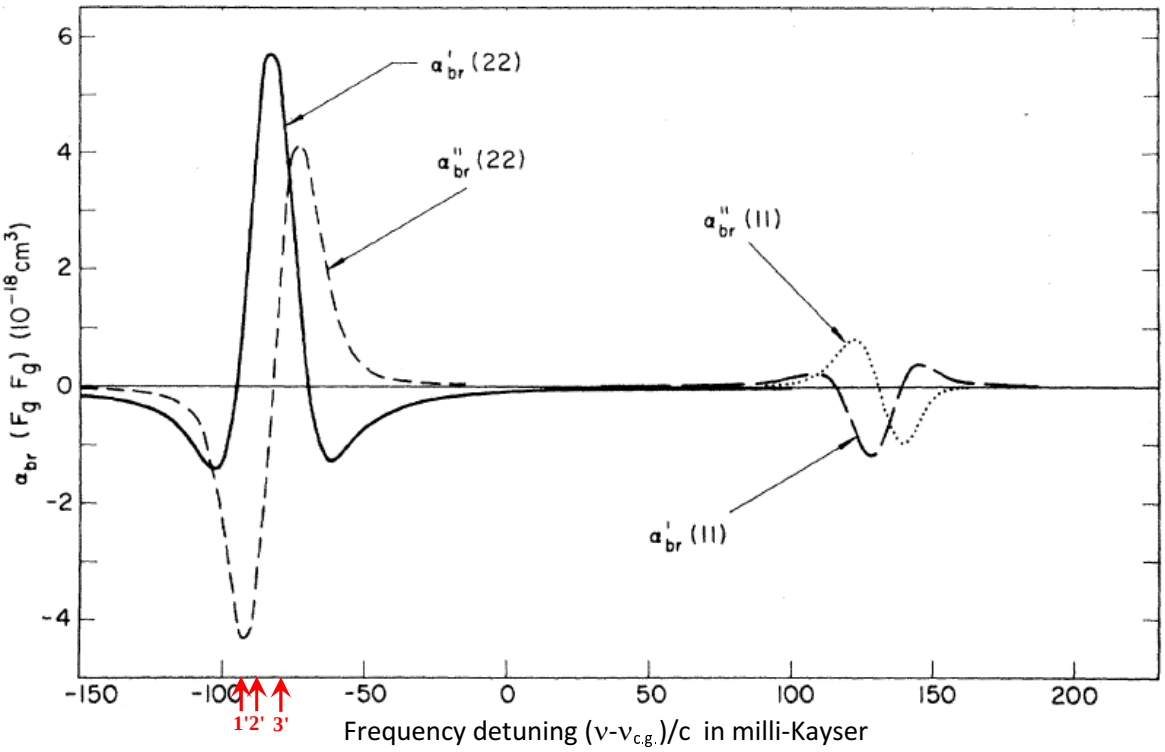

Figure F.1: This figure is a slightly modified copy of Fig. 10 of M&H [75]. Plotted are the real (') and imaginary (") parts of the birefringent response functions $a_{br}(1,1)$ and $a_{br}(2,2)$ for the D2 transition in ^{87}Rb. The horizontal axis is the detuning of the light frequency, in milli-Kayser (1 Kayser=1 cm^{-1}) from $\nu_{c.g.}$, the "center of gravity" of the D2 transition (This frequency is the $5^2S_{1/2} \leftrightarrow 5^2P_{3/2}$ transition frequency given in Fig. 2.13). The three red arrows marked 1', 2', 3' indicate the location of the $|5^2S_{1/2}, F=2\rangle \leftrightarrow |5^2P_{3/2}, F'=1,2,3\rangle$ transition frequencies, respectively.

The fourth term, the "birefringent polarizability" is related to the quadrupolar absorption [see Eq. (58) in M&H for the definition of the quadrupole operators $\overleftrightarrow{Q}(f,f')$], and it transforms under rotations as a rank 2 tensor. Plots of two of the birefringent response

functions, $a_{br}(1,1)$ and $a_{br}(2,2)$ [see Eq. (F.3)] for the D2 transition in ^{87}Rb are presented in Fig. F.1. We note that the imaginary part of each of them has a zero crossing near the center of the transition. In particular, the zero crossing of $a''_{br}(2,2)$ is located at a detuning of 82 milli-Kayser, (1 Kayser=1 cm^{-1}) which agrees to within 1 milli-Kayser (~ 30 MHz) with the location of the magic frequency evaluated in Sec. 3.2.

It can be seen from Eq. (61) in M&H that in the absence of hyperfine coherences, the quarupolar absorptivity of a monochromatic light tuned near the transition frequency from a hyperfine ground state f to an excited state is proportional to the imaginary part of the relevant birefringent response function $a_{br}(f,f)$. Thus for a light tuned to the magic frequency, the imaginary part of the relevant birefringent response function is zero and the quarupolar absorptivity vanishes. We note here that a DC magnetic field introduces hyperfine coherences to the density matrix of the ground state of alkali vapor, and as shown in the end of Sec. 3.2, at large enough magnetic field the magic frequency phenomenon disappears – i.e. the $\Gamma^{rel}_{m_F}$ curves (see Fig. 3.4) do not all intersect at the same point.

The arguments presented above show that in the absence of hyperfine coherences, the absorption of linearly polarized light tuned to the magic frequency by ^{87}Rb vapor transforms under rotations as a scalar, so that this absorption is independent of the direction of the polarization and of the distribution of the vapor amongst the sub-levels of the ground state – a conclusion similar to the results detailed in Ch. 3 of this thesis.

We note here that the simplified model developed in this thesis addresses each Zeeman sub-level separately, so that it can support a more detailed study of the interaction of lineally polarized light with the vapor.

Bibliography

[1] R. Folman, "The Atom Chip Lab website," `http://www.bgu.ac.il/atomchip` (2014).
One citation on page vi.

[2] C. E. Wieman, D. E. Pritchard, and D. J. Wineland, "Atom cooling, trapping, and quantum manipulation," Rev. Mod. Phys. **71**, S253 (1999).
One citation on page vi.

[3] C. N. Cohen-Tannoudji, "Manipulating atoms with photons," Rev. Mod. Phys. **70**, 707 (1998).
One citation on page vi.

[4] R. Folman, P. Krüger, J. Schmiedmayer, J. Denschlag, and C. Henkel, "Microscopic atom optics: from wires to an atom chip," Adv. At. Mol. Opt. Phys. **48**, 263 (2002).
One citation on page vi.

[5] T. David, "Magnetic interactions of ultra-cold atoms near surfaces," Ph.D. thesis, Ben-Gurion University of the Negev, Beer-Sheva, Israel (2009).
One citation on page vi.

[6] R. Salem, "Bose-Einstein condensate on the atom chip," Ph.D. thesis, Ben-Gurion University of the Negev, Beer-Sheva, Israel (2010).
One citation on page vi.

[7] M. Fleischhauer, A. Imamoglu, and J. P. Marangos, "Electromagnetically induced transparency: Optics in coherent media," Rev. Mod. Phys. **77**, 633 (2005).
5 citations on pages vi, 1, 28, 29, and 30.

[8] I. Dotsenko, W. Alt, S. Kuhr, D. Schrader, M. Müller, Y. Miroshnychenko, V. Gomer, A. Rauschenbeutel, and D. Meschede, "Application of electro-optically generated light fields for Raman spectroscopy of trapped cesium atoms," Appl. Phys. B **78**, 711 (2004).
One citation on page vi.

[9] D. Budker and M. V. Romalis, "Optical magnetometry," Nat. Phys. **3**, 227 (2007).
3 citations on pages vi, 1, and 3.

[10] A. Kastler, "Some suggestions concerning the production and detection by optical means of inequalities in the populations of levels of spatial quantization in atoms. Application to the Stern and Gerlach and magnetic resonance experiments," J. Phys. Radium **11**,

255 (1950).
2 citations on pages 1 and 24.

[11] A. Kastler, "Optical methods for studying hertzian resonances," Science **158**, 214 (1967).
3 citations on pages 1, 24, and 62.

[12] J. P. Barrat, J. Brossel, and A. Kastler, "Production optique d'une orientation atomique dans la vapeur saturante de sodium," C.R. Acad. Sci. **239**, 1196 (1954).
One citation on page 1.

[13] H. G. Dehmelt, "Modulation of a light beam by precessing absorbing atoms," Phys. Rev. **105**, 1924 (1957).
One citation on page 1.

[14] W. E. Bell and A. L. Bloom, "Optical detection of magnetic resonance in alkali metal vapor," Phys. Rev. **107**, 1559 (1957).
One citation on page 1.

[15] W. E. Bell and A. L. Bloom, "Optically detected field-independent transition in sodium vapor," Phys. Rev. **109**, 219 (1958).
One citation on page 1.

[16] R. H. Dicke, "The effect of collisions upon the Doppler width of spectral lines," Phys. Rev. **89**, 472 (1953).
2 citations on pages 1 and 63.

[17] N. F. Ramsey, "History of early atomic clocks," Metrologia **42**, S1 (2005).
One citation on page 1.

[18] S. Knappe, V. Shah, P. D. D. Schwindt, L. Hollberg, J. Kitching, L. A. Liew, and J. Moreland, "A microfabricated atomic clock," Appl. Phys. Lett. **85**, 1460 (2004).
One citation on page 1.

[19] S. Micalizio, A. Godone, F. Levi, and C. Calosso, "Medium-long term frequency stability of pulsed vapor cell clocks," IEEE T. Ultrason. Ferr. **57**, 1524 (2010).
One citation on page 1.

[20] B. H. McGuyer, "Atomic physics with vapor-cell clocks," Ph.D. thesis, Princeton University (2012).
One citation on page 1.

[21] R. Boudot, X. Liu, P. Abbé, R. Chutani, N. Passilly, S. Galliou, C. Gorecki, and V. Giordano, "A high-performance frequency stability compact CPT clock based on a Cs-Ne microcell," IEEE T. Ultrason. Ferr. **59**, 2584 (2012).
One citation on page 1.

[22] R. Straessle, M. Pellaton, C. Affolderbach, Y. Pétremand, D. Briand, G. Mileti, and N. F. de Rooij, "Low-temperature indium-bonded alkali vapor cell for chip-scale atomic clocks," J. Appl. Phys. **113**, 064501 (2013).
One citation on page 1.

[23] D. Budker, D. F. Kimball, S. M. Rochester, V. V. Yashchuk, and M. Zolotorev, "Sensitive magnetometry based on nonlinear magneto-optical rotation," Phys. Rev. A **62**, 043403 (2000).
One citation on page 1.

[24] C. Affolderbach, M. Stähler, S. Knappe, and R. Wynands, "An all-optical, high sensitivity magnetic gradiometer," Appl. Phys. B **75**, 605 (2002).
One citation on page 1.

[25] I. K. Kominis, T. W. Kornack, J. C. Allred, and M. V. Romalis, "A subfemtotesla multichannel atomic magnetometer," Nature **422**, 596 (2003).
One citation on page 1.

[26] D. Sheng, S. Li, N. Dural, and M. V. Romalis, "Subfemtotesla scalar atomic magnetometry using multipass cells," Phys. Rev. Lett. **110**, 160802 (2013).
One citation on page 1.

[27] B. Patton, E. Zhivun, D. C. Hovde, and D. Budker, "All-optical vector atomic magnetometer," Phys. Rev. Lett. **113**, 013001 (2014).
One citation on page 1.

[28] B. Julsgaard, A. Kozhekin, and E. S. Polzik, "Experimental long-lived entanglement of two macroscopic objects," Nature **413**, 400 (2001).
One citation on page 1.

[29] L. V. Hau, S. E. Harris, Z. Dutton, and C. H. Behroozi, "Light speed reduction to 17 metres per second in an ultracold atomic gas," Nature **379**, 594 (1999).
One citation on page 1.

[30] D. F. Phillips, A. Fleischhauer, A. Mair, R. L. Walsworth, and M. D. Lukin, "Storage of light in atomic vapor," Phys. Rev. Lett. **86**, 783 (2001).
One citation on page 1.

[31] M. Shuker, O. Firstenberg, R. Pugatch, A. Ron, and N. Davidson, "Storing images in warm atomic vapor," Phys. Rev. Lett. **100**, 223601 (2008).
One citation on page 1.

[32] U. Fano, "Description of states in quantum mechanics by density matrix and operator techniques," Rev. Mod. Phys. **2**, 74 (1957).
One citation on page 1.

[33] U. Fano and G. Racah, *Irreducible tensorial sets* (Academic Press, New York, 1959), 1st ed.
3 citations on pages 1, 33, and 34.

[34] W. Happer, "Optical pumping," Rev. Mod. Phys. **44**, 169 (1972).
5 citations on pages 1, 2, 24, 62, and 63.

[35] A. Omont, "Irreducible components of the density matrix. Applications to optical pumping." Prog. Quant. Electron. **5**, 69 (1977).
2 citations on pages 1 and 42.

[36] H. G. Dehmelt, "Slow spin relaxation of optically polarized sodium atoms," Phys. Rev. **105**, 1487 (1957).
One citation on page 2.

[37] W. Franzen, "Spin relaxation of optically aligned rubidium vapor," Phy. Rev. **115**, 850 (1959).
2 citations on pages 2 and 69.

[38] M. A. Bouchiat and J. Brossel, "Relaxation of optically pumped Rb atoms on parrafin coated walls," Phys. Rev **147**, 41 (1966).
2 citations on pages 2 and 62.

[39] M. V. Balabas, K. Jensen, W. Wasilewski, H. Krauter, L. S. Madsen, J. H. Müller, T. Fernholz, and E. S. Polzik, "High quality anti-relaxation coating material for alkali atom vapor cells," Opt. Express **18**, 5825 (2010).
One citation on page 2.

[40] M. V. Balabas, T. Karaulanov, M. P. Ledbetter, and D. Budker, "Polarized alkali-metal vapor with minute-long transverse spin-relaxation time," Phys. Rev. Lett. **105**, 070801 (2010).
2 citations on pages 2 and 114.

[41] V. V. Yashchuk, D. Budker, W. Gawlik, D. F. Kimball, Y. P. Malakyan, and S. M. Rochester, "Selective addressing of high-rank atomic polarization moments," Phys. Rev. Lett. **90**, 253001 (2003).
One citation on page 2.

[42] M. T. Graf, D. F. Kimball, S. M. Rochester, K. Kerner, C. Wong, D. Budker, E. B. Alexandrov, M. V. Balabas, and V. V. Yashchuk, "Relaxation of atomic polarization in paraffin-coated cesium vapor cells," Phys. Rev. A **72**, 023401 (2005).
One citation on page 2.

[43] B. W. Shore, *The theory of coherent atomic excitation*, vol. 1 (Wiley, New York, 1990), 1st ed.
10 citations on pages 3, 5, 10, 17, 18, 21, 22, 27, 46, and 47.

[44] B. W. Shore, *The theory of coherent atomic excitation*, vol. 2 (Wiley, New York, 1990), 1st ed.
One citation on page 3.

[45] D. A. Steck, "Rubidium 87 D line data," `http://steck.us/alkalidata/rubidium87numbers.pdf` (2010).
10 citations on pages 3, 20, 35, 36, 37, 38, 41, 49, 53, and 60.

[46] D. A. Steck, "Quantum and atom optics," `http://atomoptics.uoregon.edu/~dsteck/teaching/quantum-optics/` (2011).
11 citations on pages 3, 6, 19, 23, 30, 31, 33, 34, 45, 116, and 117.

[47] D. Budker, W. Gawlik, D. F. Kimball, S. M. Rochester, V. V. Yashchuk, and A. Weis, "Resonant nonlinear magneto-optical effects in atoms," Rev. Mod. Phys. **74**, 1153 (2002).
One citation on page 3.

[48] M. Auzinsh, D. Budker, and S. M. Rochester, *Optically polarized atoms: understanding light-atom interactions* (Oxford U. Press, 2010).
2 citations on pages 3 and 42.

[49] L. I. Schiff, *Quantum mechanics* (McGraw-Hill, 1968).
One citation on page 4.

[50] H. Mabuchi, "On-line physics course notes (Caltech)," `http://minty.caltech.edu/Ph195` (2001).
2 citations on pages 6 and 9.

[51] Y. Y. Jau, "New studies of optical pumping, spin resonances, and spin exchange in mixtures of inert gases and alkali-metal vapors," Ph.D. thesis, Princeton University (2004).
One citation on page 9.

[52] S. Kuhr, "A controlled quantum system of individual neutral atoms," Ph.D. thesis, Bonn University (2003).
One citation on page 12.

[53] J. R. Rubbmark, M. M. Kash, M. G. Littman, and D. Kleppner, "Dynamical effects at avoided level crossing: A study of the Landau-Zener effect using Rydberg atoms," Phys. Rev. A **23**, 3107 (1981).
One citation on page 15.

[54] R. L. Sutherland, *Handbook of nonlinear optics* (CRC Press, 2003).
One citation on page 16.

[55] R. D. Cowen, *The theory of atomic structure and spectra* (University of California Press, 1981).
One citation on page 21.

[56] I. Dotsenko, "Raman spectroscopy of single atoms," Master's thesis, Bonn University (2002).
One citation on page 27.

[57] G. T. Purves, "Absorption and dispersion in atomic vapours: applications to interferometery," Ph.D. thesis, Durham University (2006).
One citation on page 29.

[58] R. Wynands and A. Nagel, "Precision spectroscopy with coherent dark states," Appl. Phys. B **68**, 1 (1999).
3 citations on pages 29, 30, and 97.

[59] P. Treutlein, "Coherent manipulations of ultracold atoms on atom chips," Ph.D. thesis, Ludwig Maximilians University Munich (2008).
One citation on page 41.

[60] H. J. Metcalf and P. van der Straten, *Laser cooling and trapping* (Springer Verlag, New York, 1999).
One citation on page 45.

[61] M. D. Rotondaro and G. P. Perram, "Collisional broadening and shift of the rubidium D1 and D2 lines ($5^2S_{1/2} \rightarrow 5^2P_{1/2}$, $5^2P_{3/2}$) by rare gases," J. Quant Spectrosc. Ra. **54**, 497 (1997).
2 citations on pages 50 and 64.

[62] S. R. Drayson, "Rapid computation of the Voigt profile," J. Quant Spectrosc. Ra. **66**, 611 (1976).
One citation on page 50.

[63] S. Petra, "Development of frequency stabilised laser diodes for building a magneto-optical trap," Ph.D. thesis, Universiteit van Amsterdam (1998).
3 citations on pages 55, 91, and 100.

[64] W. Happer, Y. Y. Jau, and T. Walker, *Optically Pumped Atoms* (Wiley-VCH Verlag, Weinheim, 2010), 1st ed.
One citation on page 57.

[65] M. Stephens, R. Rhodes, and C. Wieman, "Study of wall coatings for vapor-cell laser traps," J. Appl. Phys. **76**, 3479 (1994).
One citation on page 62.

[66] S. Brattke, U. Kallmann, and W. D. Hartmann, "Coherent dark states of rubidium 87 in a buffer gas using pulsed laser light," Eur. Phys. J. D **3**, 159 (1998).
One citation on page 62.

[67] M. Arditi and T. R. Carver, "Hyperfine relaxation of optically pumped ^{87}Rb atoms in buffer gases," Phys. Rev. **136**, A643 (1964).
2 citations on pages 62 and 63.

[68] R. P. Frueholz and C. H. Volk, "Analysis of Dicke narrowing in wall-coated and buffer-gas-filled atomic strorage cells," J. Phys. B **18**, 4055 (1985).
One citation on page 63.

[69] Y. Yoshikawa, T. Umeki, T. Mukae, Y. Torii, and T. Kuga, "Frequency stabilization of a laser diode with use of light-induced birefringence in an atomic vapor," Appl. Opt. **42**, 6645 (2003).
3 citations on pages 65, 96, and 100.

[70] A. Waxman, "Coherent manipulations of the rubidium atom ground state," Master's thesis, Ben-Gurion University of the Negev, Beer-Sheva, Israel (2007).
3 citations on pages 65, 96, and 100.

[71] H. Gibbs, "Importance of nuclear-spin effects in extracting alkali spin-exchange cross-sections from Zeeman optical-pumping signals," Phys. Rev. **139**, A1374 (1965).
2 citations on pages 71 and 72.

[72] M. V. Balabas, M. I. Karuzin, and A. S. Pazgalev, "Experimental investigation of the longitudinal relaxation time of electronic polarization of the ground state of potassium atoms in a cell with an antirelaxation coating on the walls," JETP Lett. **70**, 196 (1999).
2 citations on pages 71 and 72.

[73] Y. Margalit, "Measuring hyperfine population of hot alkali vapor using a magic frequency," Master's thesis, Ben-Gurion University of the Negev, Beer-Sheva, Israel (2014).
One citation on page 86.

[74] W. Happer and B. S. Mathur, "Effective operator formalism in optical pumping," Phys. Rev. **163**, 163 (1967).
2 citations on pages 87 and 120.

[75] B. S. Mathur, H. Y. Tang, and W. Happer, "Light propagation in optically pumped alkali vapors," Phys. Rev. A **2**, 648 (1970).
3 citations on pages 87, 120, and 121.

[76] S. B. Doma and M. M. Hammad, "Classification, selection rules, and symmetry properties of the Clebsch-Gordan coefficients of symmetric group," J. Math. Phys. **53**, 033511 (2012).
One citation on page 88.

[77] A. Waxman, M. Givon, G. Aviv, D. Groswasser, and R. Folman, "Modulation enhancement of a laser diode in an external cavity," Appl. Phys. B **95**, 301 (2009).
One citation on page 94.

[78] M. Givon and A. Waxman, "WO2010041158 PCT patent application: Phase locked sideband beams by bias modulation of an external cavity laser diode having a grating," (2008).
One citation on page 94.

[79] D. W. Preston, "Doppler-free saturation spectoscopy: laser spectroscopy," Am. J. Phys. **64**, 1432 (1996).
One citation on page 96.

[80] D. Groswasser, A. Waxman, M. Givon, G. Aviv, Y. Japha, M. Keil, and R. Folman, "Retroreflecting polarization spectroscopy enabling miniaturization," Rev. Sci. Instrum. **80**, 093103 (2009).
2 citations on pages 96 and 100.

[81] E. A. Donley, T. P. Heavner, F. Levi, M. O. Talaw, and S. R. Jefferts, "Double-pass acousto-optic modulator system," Rev. Sci. Instrum. **76**, 063112 (2005).
One citation on page 100.

[82] H. D. Do, G. Moon, and H. R. Noh, "Polarization spectroscopy of rubidium atoms: theory and experiment," Phys. Rev. A **77**, 032513 (2008).
One citation on page 100.

[83] G. Aviv, "Two-photon coherent manipulation of an atomic two-state system," Master's thesis, Ben-Gurion University of the Negev, Beer Sheva, Israel (2009).
One citation on page 109.

[84] D. F. Phillips, A. Boca, and R. L. Walsworth, "Evaporative coating of Rb maser cells," `http://walsworth.physics.harvard.edu/publications/1999_Phillips_otherdoc.pdf` (1999).
One citation on page 113.

[85] Y. Bar-Haim, M. Givon, and T. David, "Israeli patent application 227584: A vapor cell and a method and system for fabrication thereof," (2013).
One citation on page 113.

[86] G. W. F. Drake, *Springer Handbook of Atomic, Molecular, and Optical Physics* (Springer, 2006).
One citation on page 118.

תקציר

בתזה זו אני מנתח באופן תאורטי ומדגים נסיונית את הקיום של תדר קסום, שבו הבליעה של אור מקוטב לינארית ע״י אדים של מתכת אלקלית היא בלתי תלויה בפילוג האוכלוסייה בין תת-רמות זימן השונות, ובזווית בין קרן האור לשדה מגנטי חיצוני. אני מראה כי התופעה נובעת מביטול התרומות של מומנטים גבוהים של מטריצת הצפיפות האטומית, והיא מתוארת באמצעות משפט ויגנר-אקרט והתכונות של מקדמי קלבש-גורדן.

פיתחתי מודל פשוט לבליעת קרן אור על ידי אדים של אטומים אלקליים, ואני משתמש בו כדי לאפיין את התדר הקסום: אני מוצא תלות חלשה מאד של התדר הקסום בטמפרטורה, ומדגים כי גם בתחום של כ 10 מגה-הרץ סביב התדר הקסום הבליעה אינה תלויה בהתפלגות האוכלוסייה בקרב תת-רמות זימן או בזווית בין קרן האור לשדה מגנטי חיצוני.

בהתבסס על התדר הקסום פיתחתי ומימשתי שיטה למדידת כמות האוכלוסייה בכל אחת משתי רמות היסוד של האטומים האלקליים, הוכחתי שהשיטה יכולה למדוד את האוכלוסייה ברזולוצית זמן של מספר מיקרו-שניות, ומצאתי שהיציבות והרגישות של השיטה טובים מ 1%.

כמו כן בניתי מערכת ניסיונית גמישה וניתנת בקלות להתאמה לניסויים שונים לצורך בחינת האינטראקציה של אדי רובידיום 87 עם מגוון רחב של שדות אלקטרומגנטיים (אור, קרינת מיקרוגל וקרינה בתדר רדיו), וזאת בסביבה מבוקרת היטב של שדות מגנטיים קבועים. אני מתאר את התכנון, את ההקמה והתפעול של המערכת, הכוללת מקור קרינה בתדר רדיו, גנרטור מיקרוגל, מספר סלילים המייצרים שדות מגנטיים קבועים וכן שלושה לייזרים - שאחד מהם הוא לייזר רמן המסוגל לייצר שתי אלומות אור קוהרנטיות כאשר הפרש התדרים בין הקרניים מגיע למספר ג׳יגה הרץ. לייזר רמן זה מבוסס על שיטה חדשנית שפיתחתי המגבירה את עוצמת פסי הצד הנוצרים כתוצאה של מודלוציה של זרם ההזנה של דיודת הלייזר ע״י זרם בתדר מיקרוגל.

כמו כן אני מתאר את התכנון, הבנייה וההפעלה של מערכת למילוי תאי אדים המסוגלת לייצר תאי אדים של צזיום ורובידיום עם ציפוי פראפין על הקירות הפנימיים ו/או עם גזים אצילים. המערכת כוללת הדגמה של שיטה חדשנית למילוי תאי אדים, שיכולה להיות בסיס לשיטת ייצור תעשייתית של תאי אדים אמינים במחיר סביר.

<u>הצהרת תלמיד המחקר עם הגשת עבודת הדוקטור לשיפוט</u>

אני החתום מטה מצהיר/ה בזאת: (אנא סמן):

√ חיברתי את חיבורי בעצמי, להוציא עזרת ההדרכה שקיבלתי מאת המנחה.

√ החומר המדעי הנכלל בעבודה זו הינו פרי מחקרי <u>מתקופת היותי תלמיד/ת מחקר</u>[1].

√ בעבודה נכלל חומר מחקרי שהוא פרי שיתוף עם אחרים, למעט עזרה טכנית הנהוגה בעבודה ניסיונית. לפיכך מצורפת בזאת הצהרה על תרומתי ותרומת שותפי למחקר, שאושרה על ידם ומוגשת בהסכמתם[2].

4 בנובמבר 2014, על החתום: מנחם גבעון. חתימה _____

[1] חלק מעבודת המחקר בוצע במשך ההפסקה המיוחדת שאושרה לי לצורך השתתפות במחקר אחר שהתנהל באוניברסיטה (ראה ה Preface באנגלית).

[2] ראה תצהיר באנגלית המפרט את תרומת שותפי למחקר.

העבודה נעשתה בהדרכת פרופ׳ רון פולמן

במחלקה לפיסיקה

בפקולטה למדעי הטבע

תדר קסום באינטראקצית אור עם חומר
הכולל מערכות שתי-רמות עם ניוון מרובה

מחקר לשם מילוי חלקי של הדרישות לקבלת תואר "דוקטור לפילוסופיה"

מאת

מנחם גבעון

הוגש לסינאט אוניברסיטת בן גוריון בנגב

אישור המנחה _____, תאריך:_____

אישור דיקן בית הספר ללימודי מחקר מתקדמים ע"ש קרייטמן _____

י"ח חשון תשע"ה **11 לנובמבר 2014**

באר שבע

תדר קסום באינטראקצית אור עם חומר
הכולל מערכות שתי-רמות עם ניוון מרובה

מחקר לשם מילוי חלקי של הדרישות לקבלת תואר "דוקטור לפילוסופיה"

מאת

מנחם גבעון

הוגש לסינאט אוניברסיטת בן גוריון בנגב

י"ח חשון תשע"ה **11 לנובמבר 2014**

באר שבע